LEVERAGING AUTOMATED FIBER PLACEMENT COMPUTER AIDED PROCESS PLANNING FRAMEWORK FOR DEFECT VALIDATION AND DYNAMIC LAYUP STRATEGIES

by

Joshua Allen Halbritter

Bachelor of Engineering
University of South Carolina 2017

Master of Science
University of South Carolina 2020

Submitted in Partial Fulfillment of the Requirements

for the Degree of Doctor of Philosophy in

Mechanical Engineering

College of Engineering & Computing

University of South Carolina

2023

Accepted by:

Ramy Harik, Major Professor

Brian Tatting, Committee Member

August Noevere, Committee Member

David Rocheleau, Committee Member

Tracey L. Weldon, PhD, Interim Dean of the Graduate School and Vice Provost for Graduate Education

ABSTRACT

Process planning represents an essential stage of the Automated Fiber Placement (AFP) workflow. It develops useful and efficient machine processes based upon the working material, composite design, and manufacturing resources. The current state of process planning requires a high degree of interaction from the process planner and could greatly benefit from increased automation. Therefore, a list of key steps and functions are created to identify the more difficult and time-consuming phases of process planning. Additionally, a set of metrics must exist by which to evaluate the effectiveness of the manufactured laminate from the machine code created during the Process Planning stage.

Layup strategies, in addition to dog ears, stagger shifts, steering constraints, and starting points, represented the group of functions labeled as process optimization and ranked the highest in terms of priority for automation. The laminates resulting from the selected parameters are evaluated through the occurrences of principal defect metrics such as fiber gaps, overlaps, angle deviation and steering violations.

This document presents an automated software solution to the layup strategy and starting point selection phase of process planning. A series of ply scenarios are generated with variations of these ply parameters and evaluated according to a set of metrics entered by the Process Planner. These metrics are generated through use of the Analytical Hierarchy Process (AHP), where relative importance between each of the fiber features are defined. The ply scenarios are selected which reduce the overall fiber feature scores based on the defects the Process Planner wishes to minimize.

An extensive evaluation of the ply scoring algorithms was performed with various tool surfaces. The evaluation provided insight into the interaction of the different layup strategies and the underlying geometry of the tool surface. Additionally, the relationship of the various fiber defects with the tool surface curvature were also investigated.

Furthermore, the document covers the incorporation of inspection data for the validation of fiber defect predictions, in addition to a new laminate evaluation technique which begins to consider how undesirable features within the composite may interact through the thickness of the laminate. Utilizing the in-depth understanding of fiber path generation with the evaluation methods within CAPP, a new dynamic layup strategy is devised which considers the assigned relative importance of various defect types to take some of the guess work out of layup strategy selection, which can be a challenging task when complex tool geometry is involved.

TABLE OF CONTENTS

LIST OF TABLES

List of Figures

List of Abbreviations

ACSIS	Advanced Composite Structures Inspection System
AFP	Automated Fiber Placement
AHP	Analytical Hierarchy Process
ARAP	As Rigid as Possible
CAD	Computed Aided Design
CAPP	Computed Aided Process Planning
CO	Central Optimizer
FEM	Finite Element Method
LSCM	Least Squares Conformal Mapping
NURBS	Non-uniform rational B-spline
STEP	Standard for the Exchange of Product model data
VCP	VERICUT Composite Programming

CHAPTER 1

INTRODUCTION

Automated Fiber Placement (AFP) is increasingly utilized for manufacturing composite materials into useful parts [1]. An AFP machine is typically comprised of a robotic arm/gantry and a fiber placement head that can layup multiple strips of primarily carbon fiber reinforced polymer-matrix material. These strips of carbon fiber material, known as tows, are often laid up in differently oriented layers, known as plies, to increase the strength and isotropy of the part [2]. To secure adhesion of these tows, the fiber placement head must have a method of heating the resin and compacting it down to the surface. This is accomplished by using a controlled amount of heat and compaction load supplied by the AFP end-effector [3]. After placing the first ply to the tool, subsequent plies can be added until the desired shape and strength of the part has been achieved.

AFP brings a more efficient and productive method of composite manufacturing, however, the automated manufacturing process is far from optimized, and defects can persist throughout the products created with AFP manufacturing. The defects found in the layup portion of the AFP process are often an unintended part of the layup process and forced by the nature of the geometrical shape. Therefore, it is critical to understand what these defects are and how they interact with the part. Tow gaps/overlaps and wrinkles represent some of the most common defects for composite parts. These defects have been investigated in previous work. For example, tow gaps/overlaps, have been found to result in reduction in laminate strength in the work by [4]. Additionally, it has been shown that gap/overlap defects lead to a decrease in strength at the site of the defect, whereas an overlap is shown to increase the strength at that site in a constant stiffness laminate [4, 5]. The geometric effect of these defects and their potential consequence, such as strength reduction, were detailed in [6]. It has also been determined that gaps and overlaps can lead to resin-rich and fiber-rich areas in the part is left untreated [7]. The wrinkle defect has also been investigated. The effects of minimum turning radius on tow-wrinkling were presented in [8]. Another paper detailed the reduction in strength that resulted from wrinkling and identified it to be as high as 36% [9]. Finally, the detrimental effects of the defects on the final laminate's structural properties are included [10, 11].

1.1 Process Development for AFP

Since AFP is an automated process, it is necessary to create numerical control (NC) code which defines the creation of the laminate part. The development of this NC code is known as process planning, which creates an AFP manufacturing plan based on the working material, composite design, and manufacturing resources. Process planning (figure 1.1) represents one of the most critical and user-interactive portions of the AFP process. In this step, a process planner will use a multitude of different functions to prepare the design for layup by the machine. To use these functions, a process planner must use his knowledge of the part being made, the tool being laid up on, and the machine.

The economic impacts of process planning for AFP arise from the reduction in time it takes to program the machine prior to manufacturing by embedding design for manufacturing concepts well ahead in the product lifecycle. It also reduces the labor and material cost that may result during manufacturing due to poor and/or inefficient programming. Therefore, improving process planning will allow for more cost efficient and faster manufacturing using AFP, leading to faster certification cycles. To improve AFP process planning, the functions that make up the process planning stage must

Figure 1.1 Primary considerations for AFP process planning [12]

first be identified and discretized. By defining these individual functions, their total contribution to the result can be interpreted and steps can be taken to automate the most important and time-consuming functions.

CHAPTER 2

LITERATURE REVIEW

This literature review intends to provide a background into relevant topics for the content presented in throughout the remaining chapters of this document. These topics include the primary methods for the development of fiber paths, issues of concern both when devising fiber paths and during layup, inspection techniques for identify defects during and after fiber placement, and current techniques that exist to improve fiber paths and manufacturing quality. Together, these topics provide insight into the considerations that need to be taken during the development stage of composite structures, and how both planned and manufactured defects can be leveraged in such a way to improve future manufacturing cycles and even revise the manufacturing plans to further reduce fiber defects.

2.1 FIBER PLACEMENT DEFECTS

AFP defects represent a disparity between the idealized laminate design and the manufactured structure. To understand AFP defects, the source of the defect and how the part geometry influences the defect formation must be investigated. A subset of these defects can be predicted and modeled through the interaction of the tool surface geometry and the fiber tows alone, while others may occur due to manufacturing conditions, machine errors, or material quality. The ability to model some of these defects enables an entire virtual layup to be built and analyzed before any manufacturing, so that processing parameters and fiber paths can be adjusted to minimize the occurrence these predictable defects.

The following sections define the distinct types of defects which may be present in fiber placed composite structures. Each defect is presented with a graphical representation and the various conditions which may lead to an occurrence of that defect with respect to surface geometry and material placement are discussed.

2.1.1 Gap/Overlap

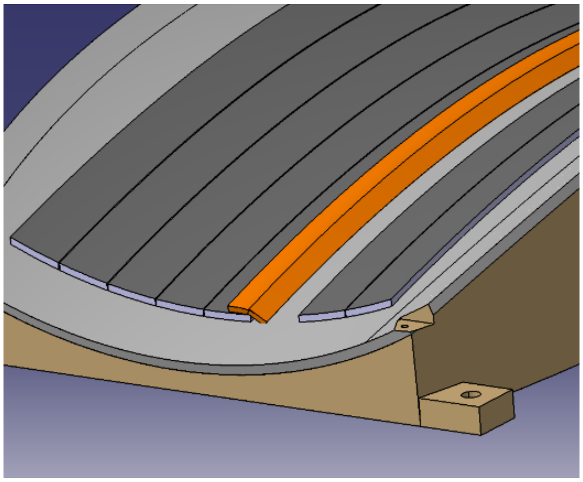

Figure 2.1 Gap/Overlap CAD Representation

A gap occurs when two adjacent tows are not perfectly laid up adjacent to each other resulting in a gap between the tows. An overlap is when the two adjacent tows are overlapping onto each other. The most common cause of gaps and overlaps is steering during layup since, the tows in a course will not fit together perfectly, especially when adopting a parallel coverage strategy. However, gaps and overlaps can naturally occur outside of steering if laying up over a complex 3D tool surface.

Gaps and overlaps are well anticipated in areas of purposeful steering, or on doubly curved surfaces where adequate roller compaction is not guaranteed. From the geometry of these situations, the gaps and overlaps can be directly computed. The measurement of gaps and overlaps are generally easy to detect due to the build-up or lack of material along the course. As successive plies are laid up over overlaps, consistently at the same location at each layer, significant thickness buildup will be visible. A gap and/or overlap may become a site for failure initiation under loads. Gaps would create resin rich regions for crack growth while overlaps create undulation in the fiber that can lead to compressive failures. They may also become a site for wrinkling in the layers placed over them in the succeeding layer.

2.1.2 PUCKER

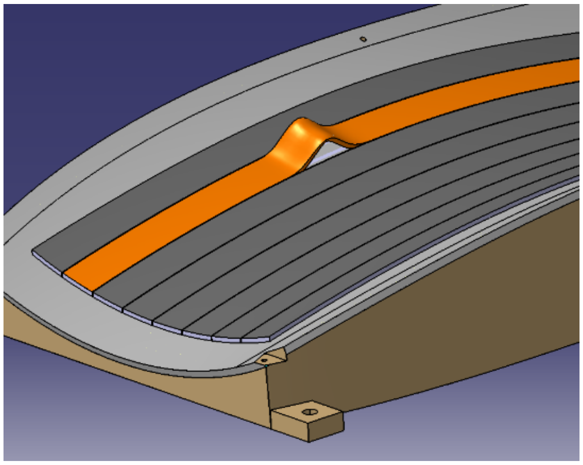

Figure 2.2 Pucker CAD Representation

Puckers initiate at the inside radius of a steered tow, resulting in the tow lifting from the tool surface either partially or across the entire tow width forming an arch of excess material that is not adhered to the underlying substrate material. Puckered tows are caused by excess length of tow due to steering. This excess length of tow increases shear stress at the tow to substrate boundary overcoming the tack adhesion strength. If placement is over a compliant surface, with the force of the compaction roller, longer tows may be deposited that can form the pucker after the surface spring backs to its original shape.

Puckers can be prevented through appropriate towpath planning, since thickness buildup in concave shapes may cause shortening of the surface length, and the tow length fed out by the machine head may need to be shortened to compensate for the reduced length. Small puckers may be difficult to detect visually due to lack of contrast, so instead profilometry-based sensor detection system can be utilized to identify the puckered tow. Puckered tows are typically flattened by successive layers placed over them and by debulking. However, if the puckers are not properly compacted, it may result in a significant loss of strength.

2.1.3 Wrinkle

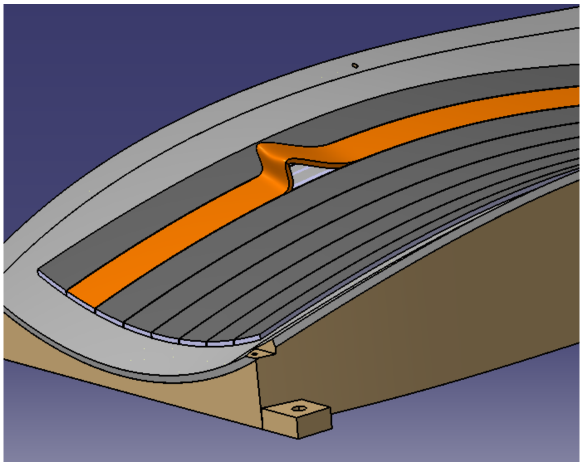

Figure 2.3 Wrinkle CAD Representation

A wrinkle is typically indicated by a wavy pattern of puckering along the edge of a tow when it is steered through a non-geodesic path over a complex (potentially doubly curved) surface or following a steered path on a flat surface. These types of defects occur on the inner radius and remain out-out-plane after compaction and curing. Wrinkles are often caused by placing tows at small steering radii, which can lead to excessive differential length between the two edges of the projection of the tow on the part surface. The two edges of a tow delivered from the machine head are of equal length, hence part of the excessive differential length presents itself as puckers and/or wrinkles.

The steering radius definition and the complexity of the tool surface being laid up on are the main ways to anticipate a wrinkle. Tow path definition during design phase can have a strong influence on wrinkling behavior. Process parameters and tow material properties are also influential. Wrinkles can be detected either visually or using automated inspection systems but can be difficult to distinguish from puckers as the tow is overhanging along its orientation. Wrinkled tows covered by layers that are laid on top, force them to flatten during which in-plane fiber waviness or folded fibers may be caused. Additionally, wrinkles can cause gaps and folded tows which can result in a loss of strength.

2.1.4 BRIDGING

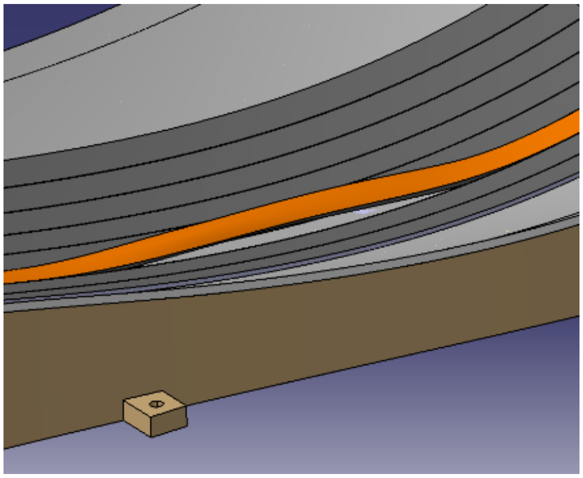

Figure 2.4 Bridging CAD Representation

A bridged tow does not fully adhere to the concave surface (female tool portion) or a re-entrant corner or ramp-up area over which the tows are being laid up on, leaving a gap between the radius of the concave tool surface and the tow. The main causes of a bridged tow are too much tension on the tow, which will force the tow to lift, or insufficient tack adhesion to the surface being laid up on because the roller does not provide full contact with the substrate material.

The main ways to anticipate this defect are to ensure that the roller has the best contact coverage possible when going over a complex tool surfaces, especially concave portions. Overfeeding of the tow may eliminate bridging in re-entrant corners and ramps. Bridging is often readily identified visually and by automated inspection systems since the tow in question will be raised about the concave portion of the tool being laid up on. Successive passes of the roller to place additional layers with different orientations or de-bulking step with a vacuum may push the bridged tow to re-adhere to the substrate. However, the bridging could leave resin rich areas at best, or delamination at worst.

2.1.5 BOUNDARY COVERAGE

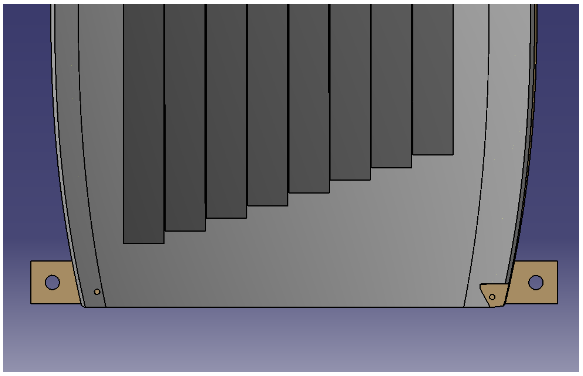

Figure 2.5 Boundary Coverage CAD Representation

A boundary gap/overlap occurs when the material cannot perfectly meet up with the edge of a part when laying up at off-axis orientation such as ±45° in rectangular parts. Since the tows do not meet up perfectly with the edge, this will result in either an excess of material along that edge or a shortage between the tow-end and the boundary edge. This can be at the boundary of any coverage zone, be it internal to the part inducing ply drop-offs, or at the external boundary.

This defect is a direct result of the chosen percentage of boundary gap and overlap defined during process planning and are additionally influence by the ply angle. These defects are clearly visible on the edges of any variable angle laminates and will be visible post-cure. A boundary gap and/or overlap can influence the shape of the part since the course will not line up with the desired geometry. If the edges are trimmed to ensure accuracy the part may be more likely to fail in the spots where the trimming occurred.

2.1.6 ANGLE DEVIATION

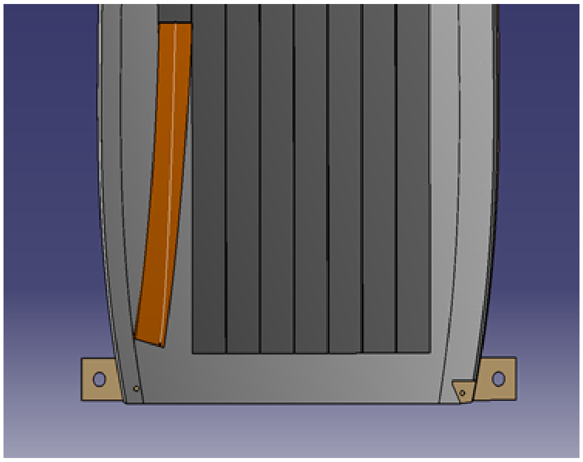

Figure 2.6 Angle Deviation CAD Representation

Angle Deviation is when the angle of the as-manufactured layup deviates from the as-designed one. Angle deviation can be caused by incorrect roller coverage or small radius steering as the tow may move after being steered. It also may result from necessary concessions made by the layup strategy in order to create coherent fiber paths.

The main way to anticipate angle deviation is through defining the steering radius for any required steering throughout the layup, since a smaller radius can cause angle deviation. Angle deviation is observed by visual inspection, but it requires further processing and comparison with the as-designed angles. Inspection systems alone cannot confirm the angle deviation without a benchmark for comparison. Angle deviation can cause overlap on portions of the ply when a course will be laid up on top of the deviated tows. This can lead to an undesired shape in the laminate and can be a cause of failure due to resin rich areas on the counter side. This is a similar effect to overlap and gaps and can lead to delamination in the resin rich areas due to improper course coverage.

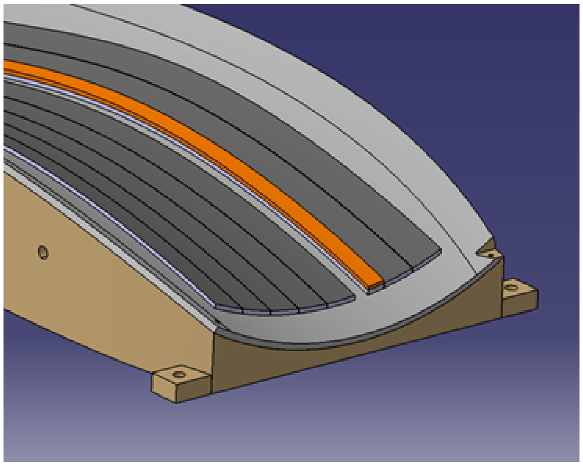

Figure 2.7 Fold CAD Representation

2.1.7 FOLD

This defect occurs when the tow folds in the transverse direction onto itself, creating a gap in the surface coverage and doubling the tow thickness over the folded part. An extension (and probably the worst-case scenario) of the folding could be rolling (or completely twisting) of the tow to become "rope" like. Lack of or too much tension could increase the propensity of the tow to fold. Long unsupported/complex towpaths from the spools to the head can also result in folding. In a steered/curved towpath, the outer segment of the tow may fold towards the inner side after the compaction roller nip point due to tension on the outer edge of the tow and improper tack adhesion.

The quality of the slit-tape or tow will have a large influence on the folding defect, in addition to the machine's type and calibration (health). Design has some influence if the towpath is steered. Process parameters influence the tack adhesion, where speed, compaction pressure and temperature dominate. These defects can either be visually detected from variations in the courses surface, or via automated inspection systems. Twist are one of the more serious defect types for cured laminates due to increased thickness right next to a reduced thickness region. Substantial influence on local fiber volume fraction variation, and creation of resin rich areas for failure initiation. These may also serve as sites for delamination initiation following the crack growth from the resin rich defect sites.

2.1.8 Twist

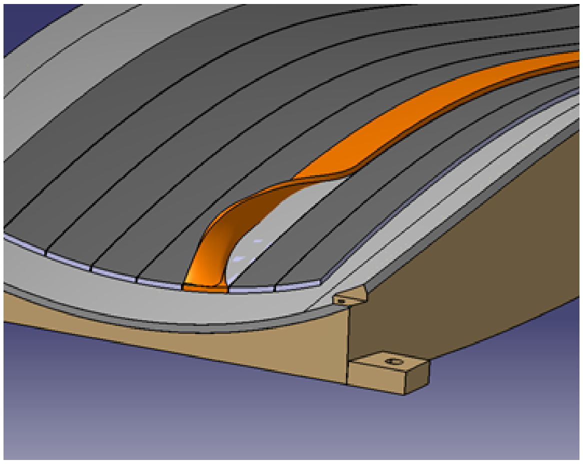

Figure 2.8 Twist CAD Representation

For this type of AFP defect, the tow is rolled axially 180º onto itself and then flattened by the compaction roller. Depending on the length over which the twisting occurs, the shape may be like a bowtie with bunching of the fibers and increased thickness at the center. For long twists, L>5tw, the sides are simply folded. Twisted tow could be initiated by folding, in which the fold grows and completes a full turn rather than unfold (folded tow could be considered incomplete twist). Friction between guide holes, where material is fed from the material roll to the head, along a long/complex tow path and a tacky tow may cause twisting due to head rotation during bi-directional layups.

Twist may occur from the rotation of the machine head, the geometry of the part, or the tows not being properly fed into the machine. The geometry of the part contributes since a head rotation may be necessary on some portions of the part surface. Can be detected either visually or via automated inspection systems. Machine learning algorithms can be useful in classifying the defect as twist. Like folded tows, twisting roots causes a portion of the part surface to not be covered with fiber, especially for long twists, and parts with increased thickness. A twist may be more damaging than a fold, as structural load may cause scissoring deformation. Aside from being a source for cracking and delamination, severe deviation of the fiber paths within the tow from being straight will cause kinking failure of tows under compressive loads.

2.1.9 Wandering Tow

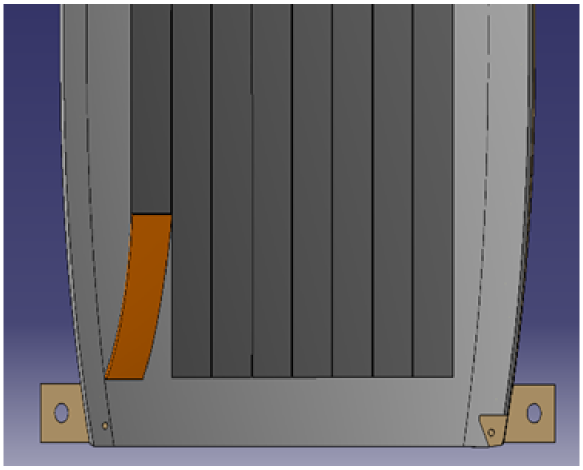

Figure 2.9 Wandering Tow CAD Representation

A wandering tow is when the portion of the tow between the roller and the cutter wanders from the original fiber path after being cut. Similar to “angle deviation”, wandering tows can be attributed to having an unsupported portion of the tow between the compaction roller and the tow cutter. Therefore, the angle deviation will only be of the dimension of this un-supported tow length.

The main approach to prevent a wandering tow would be to ensure that any steering has an appropriate radius or that the roller coverage is maximized to ensure proper adhesion. Wandering tows can be visually observed since they are typically located at the ends of a course. These defective tows can lead to a gap/overlap between tows which can result in a resin rich area and ultimately a higher chance of failure.

2.1.10 Loose Tow

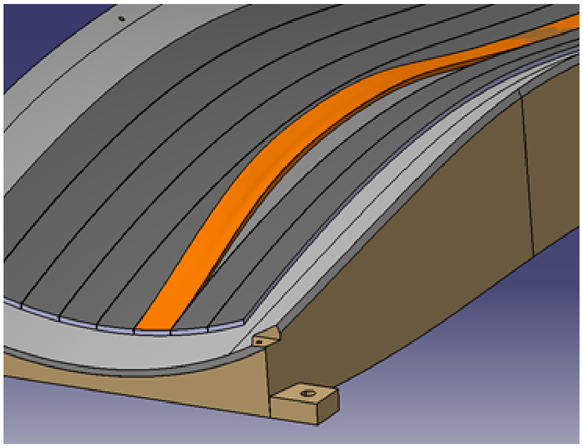

Figure 2.10 Loose Tow CAD Representation

A loose tow generally refers to a section of a tow (or tows) that the machine head attempts to place on a part without having complete and precise control over where it is placed, causing the tow to meander. A tow is completely loose when the length of a tow is shorter than the length between the cutters and the compaction roller. In this case, the tow is free to land on an arbitrary position. If at the end of a course the fiber path is still steered, the section of the tow before the compaction roller may not follow the defined steered path.

If the loose tow results in significant gap in the laminate, or a completely missing tow, then it can be detected visually or by automated vision systems. For steered tows, it will not be obvious if the tow is floating because of precision or because of course steering. If the loose tows are caused by steering, then their consequences have to be accounted for by using tools appropriate for it (if/when they exist) and may additionally cause unanticipated gap or overlap.

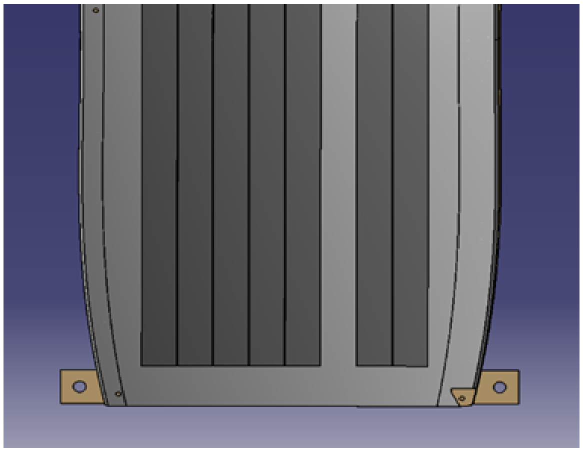

Figure 2.11 Missing Tow CAD Representation

2.1.11 Missing Tow

This defect typically occurs when an entire tow does not correctly adhere and falls off the surface or is not successfully fed onto a surface from the spools. The resulting missing tow is very similar to a gap, and in fact can be considered as a gap with a size equal to a tow width. Missing tows are caused by either discontinued material feeding into the machine head or layup of a tow with insufficient tack adhesion.

Missing tows are not related to any designed features. Ensuring proper splices, and full material spools will eliminate accidental missing tow. On complex surfaces, providing enough compaction pressure, and ensuring sufficient material tack with proper temperature will preclude long bridged tows that may fall off the surface. The gaps created by missing tows are easy to detect either visually or through automated hardware. Like a gap, missing tows will cause local thickness variation, and potential resin rich pockets in the layup that can serve as a failure initiation point. This defect is a potential site for progressive delamination failure with the adjacent layers.

2.1.12 Splice

When two tows are joined by the material or slitting supplier end-to-end in a spool by overlapping 1 to 3 inches over each other and tacking them together. This results

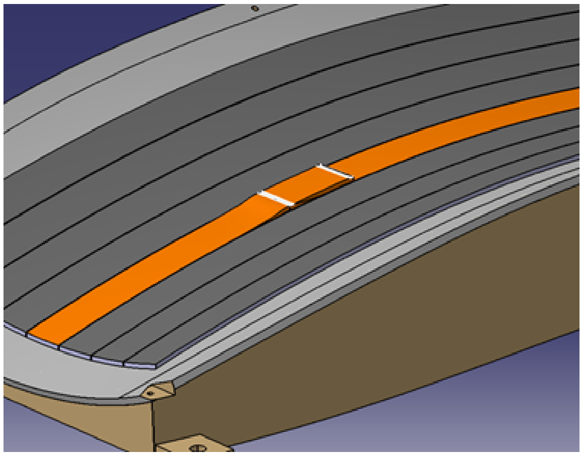

Figure 2.12 Splice CAD Representation

in a portion of the spool that is thicker than the rest and is usually marked by white dashes for detection. Theoretically, carbon fibers can be drawn infinitely long. However, most AFP pre-impregnated tows are slit tape that are cut from a roll of finite length unidirectional tape. These slit tapes are spliced and spooled based on customer specifications.

Monitoring and keeping track of spool length for the splice locations with respect to the part size may eliminate the spliced tow from the part. Splices are difficult to detect visually if not marked. The thickness increase over the splice allows detection with a detection system. Thickness change over a small area may be insignificant for stiffness change. This site may become a location for failure initiation especially under compressive loads. Splices are possible sites for fiber kinking progression under compressive loads.

2.1.13 Position Error

A position error is when a tow is placed in a wrong location in reference to the end or beginning of a course. This results in a tow that is misaligned with the rest of the tows in the boundary. Main causes of this defect are either obstruction of the tow during feeding (such as building up of fuzz in one of the guide chutes of the

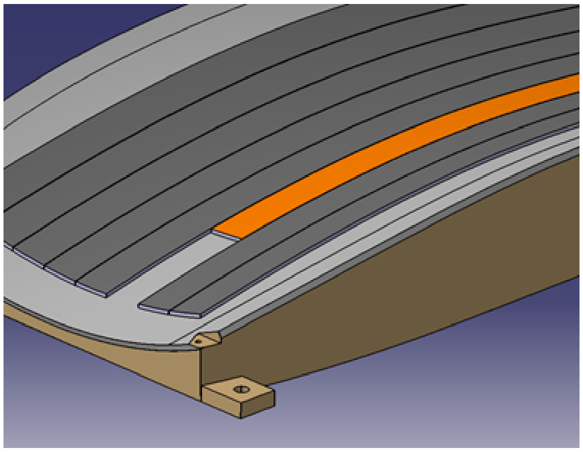

Figure 2.13 Position Error CAD Representation

machine head), or incorrect machine reference points with respect to the part for a particular course. Sometimes they are due to machine control issues and auto tuning requirements.

Position errors are arbitrary, and there is no way to anticipate them. However, ensuring that there is no material build up in the head of the machine that can cause resistance during layup and monitoring the accuracy of the layup simulation will reduce the possibility of an occurrence. These are similar to a tow gap near the part boundary, hence their influence compared to the regular defects are expected to be more pronounced due to edge-effect failures observed in multi-layered composites.

2.1.14 Foreign Object Detection

A foreign object debris (FOD) defect is when a small piece of composite material, either carbon fiber "fuzz-ball" or "resin ball or other debris from the production area fall onto the part during layup. This results in a small excess volume of material on the ply if laid up over.

Monitoring the head of the machine and the production area for FOD and routine cleaning of surfaces are the appropriate ways to anticipate this defect. Large objects may be visually detected as it will be an irregular shape out of thickness along the

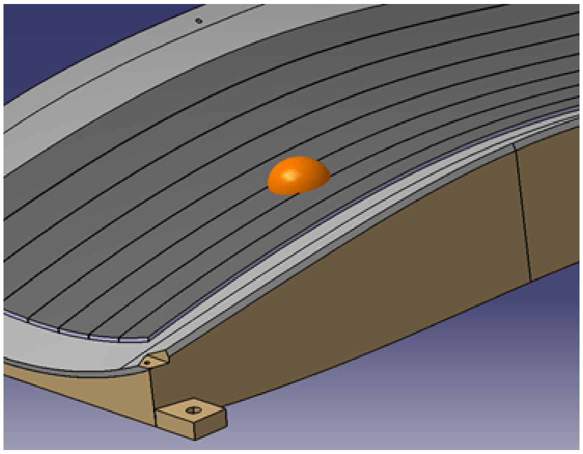

Figure 2.14 Foreign Object CAD Representation

same layer. A FOD defect in layup can cause the portion of the next ply above the defect to improperly adhere to the defect's ply. This will lead to an undesired shape and strength of the part being made.

2.2 Effects of Fiber Defects

Composite laminate theory (CLT) provides the fundamental form of evaluation for the strength and failure forms for a composite structure. Modern composite design tools enable the creation and design of complex composite structures by leveraging fundamental theories like CLT. However, additive manufacturing technologies such as AFP are relatively young and resist efforts for material characterization, when compared to the mature field of subtractive manufacturing with metals. As such, the defects that occur through both the planning of fiber paths and during manufacturing as a result of processing parameters should be reincorporated into the design and appropriate revisions made to the design and manufacturing plans of the structure. The following sections provide insight into the formation and propagation of these defects, and how they effect the resulting structure, along with the methods currently used to simulate and reincorporate back into the modern design tools.

2.2.1 Defect Stacking

Through thickness fiber defect interactions are highly complex and their effects largely depend on a number of factors including type of defects stacked, number of intermediate plies, process parameters, tool surface geometry, hard vs soft tooling, etc. Li et al. created 3D meshing tools to automatically generate plies with gaps and overlaps, combined to model full laminates with stacked defects. These models showed the effect of stacked overlaps and gaps on out-of-plane waviness and ply thickness and were used to predict overall strength knockdowns as a function of size and type of defect [13]. Lan et al. studied the impact of hard and soft tooling on thickness variation and mechanical performance for laminates with stacked gaps and overlaps. They found that severely stacked laminates have large variations in overall thickness, specifically when cured without caul plates, and that the use of caul plates mitigates many of the negative impacts of stacked defects on mechanical performance [14]. Croft et al. investigated the impact of gap, overlap, gap/overlap, and twisted tow defects on ultimate strength at the lamina and laminate level. It was discovered that defects have a much larger effect on ultimate strength on the laminate level (up to 13%) than on the lamina level ($\tilde{5}$%) [2]. These works highlight the importance and complexity of studying defect interactions through the thickness of a laminate.

Furthermore, literature has thoroughly investigated the effects of gaps and overlaps on structural properties within composite laminates. Fayazbakhsh et al. created a finite element (FE) defect layer model to investigate the effect of gaps and overlaps on elastic properties. They found that in variable stiffness laminates, gaps reduced buckling load by 15% while a complete overlap strategy increased buckling load by up to 71% [4]. Blom et al. investigated the impact of tow-drop areas (gaps) on strength and stiffness in variable stiffness laminates. They determined that staggering plies, shifting them by a factor of the course width based on number of like plies, resulted in an increase in strength varying from 3–29% based on tow width and fiber angle distribution [15]. This allows for significantly lower structural allowable in preliminary design and a delay in virtual testing until the detailed design phase.

2.3 Layup Strategies

This section covers the various concepts regarding the geometry of fiber paths that can be utilized to generate surface coverage. These geometrical concepts define the interaction of the thin and stiff material of the fiber tows being placed on a potentially complex geometrical tool surface.

2.3.1 Direction of The Fiber

The different courses laid up by the AFP process need to be placed in a way that the fibers orientations meet the required design specifications. Often, plies are manufactured with fibers having well-defined angles such as 0°, 90°, 45°, -45° as they provide a quasi-isotropic behavior for the structure [12]. Typically, the 0° angle direction follows the longest dimensions of the surface as in figure 2.1. It is straight-forward to lay up plies with these angles on a flat panel (figure 2.1) however on complex surfaces, it is more difficult as the fiber angles in the tow can change due to the geometry of the surface. Therefore, each layup strategy will produce its own uniquely oriented laminates as the tooling surface changes. This chapter details all the layup strategies found in the literature on the AFP process. This will allow the right strategy to be chosen for the tooling to obtain a proper structure.

2.3.2 Minimum Turning Radius

Another condition to check before finalizing the path design is the turning radius or the curvature of the path. Since the tows used in the AFP process have a finite width, the edges of the tow will be either under tension or compression while trying to adhere a rectangular shaped tow to a curved path. This mismatch in length between

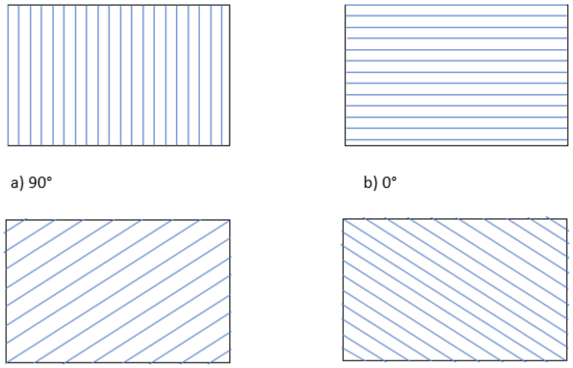

a) 90°

b) 0°

c) 45°

d) -45°

Figure 2.15 Flat panel with different layup fiber angles

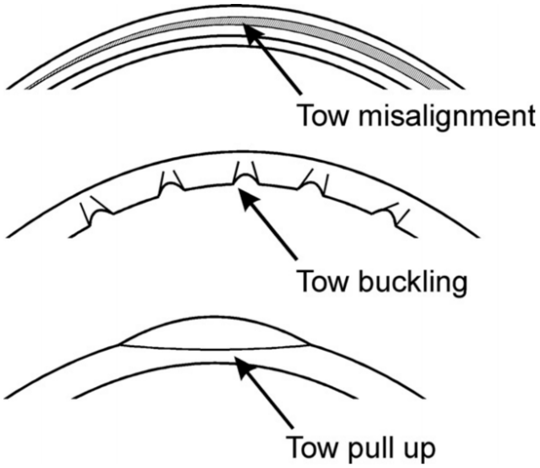

Figure 2.16 Most common tow steering defect

the tow and the actual path on the surface will push the excess material to buckle out-of-plane to form a pucker or wrinkle (figure 2.16) on the compressive edge of the tow. As for the tensile side, the shortage of material will push the fibers to move closer to the center line leading to tow straightening, or in the severe cases to move out-of-plane and fold over.

To avoid these defects (defined in chapter 2), a minimum steering radius must be set beforehand, depending on the material used. The minimum steering radius can be determined experimentally by trying different radii of curvature with different combination of process parameters (speed, temperature, roller pressure).

2.3.3 Reference Curves

In order to propagate fiber paths across the tool surface, an initial (or reference) curve is needed. In this section, the different strategies to determine the reference curve will be detailed. The literature describes both parametric approaches and the use of a meshes. A mesh provides useful information, such as the different areas of the facets and their normal, which are important to generate the toolpath along the course. Nevertheless, a mesh approximates the surface, so the precision obtained depends on the accuracy of the mesh. However, a more refined mesh increases the computation time. Using a parametric approach, the surface would be known more precisely. In this section and the following ones, the different strategies to find reference curves are detailed.

2.3.4 Constant Curvature

For a flat plate, a constant curvature path is an arc of circle, with a possible parametrization as defined by equation 2.1, where, (x_0, y_0) are the coordinates of the center, and $1/\kappa$ is the radius of curvature. Constant curvature paths are frequently used as trials to determine the critical radius at which wrinkling will occur for a given set of process parameters.

$$\begin{aligned} x(t) &= x_0 + \frac{1}{\kappa} * \cos t \\ y(t) &= y_0 + \frac{1}{\kappa} * \sin t \end{aligned} \tag{2.1}$$

$$\sin\varphi(x) = \frac{r_0 \sin T_0}{r(x)} + \frac{\kappa}{\sin\alpha}\left(\frac{r(x)^2 - r_0^2}{2r(x)}\right) \tag{2.2}$$

$$\kappa = \left(\frac{r_1}{r}\sin T_1 - \frac{r_0}{r}\sin T_0\right)\frac{1}{L}, \left[\bar{r} = \frac{r_0 + r_1}{2}\right] \tag{2.3}$$

For the special case of the cone (figure 2.17) presented in [16, 15, 17], it is possible to obtain a closed form solution for a reference curve with a constant curvature. The

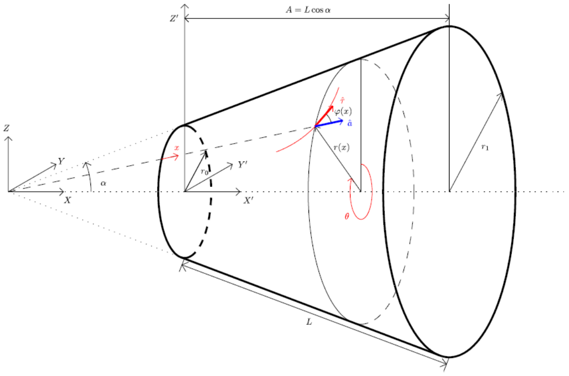

Figure 2.17 Cone geometry [16, 15, 17]

equation of the curvature κ and the local fiber orientation ϕ as a function of the position on the surface is therefore given by equation 2.2 and 2.3.

Where: r_0, r_1 and α are the small, the larger radii and the cone angle; $r(x)$ represents the perpendicular distance from the revolution axis to a point on the shell and varies linearly for this shell configuration: $r(x) = r_0 + x\sin(\alpha)$; L is the length along the surface; T_0 and T_1 are respectively the fiber orientation at the small and the big radius of the cone. Then the curvature κ is kept constant along the surface to obtain the reference curve (figure 2.20).

$$\begin{aligned} u'' + \Gamma^1_{11}u'^2 + 2 * \Gamma^1_{12}u'v' + \Gamma^1_{22}v'^2 &= \frac{k_g\left(Fu' + Gv'\right)\sqrt{Eu'^2 + 2Fu'v' + Gv'^2}}{\sqrt{EG - F^2}} \\ v'' + \Gamma^2_{11}u'^2 + 2 * \Gamma^2_{12}u'v' + \Gamma^2_{22}v'^2 &= \frac{-k_g\left(Eu' + Fv'\right)\sqrt{Eu'^2 + 2Fu'v' + Gv'^2}}{\sqrt{EG - F^2}} \end{aligned} \tag{2.4}$$

The case of a beam and a cylinder is studied respectively in [18] and [19] using the same method. The case of a planar surface is developed in [15] and [8] where the fiber angles follow a constant curvature path from a boundary to the center of the surface.

For a general surface, the following system of 2nd order differential equations in terms of the surface parameters u and v must be solved numerically with a prescribed geodesic curvature k_g, to obtain a constant curvature path:

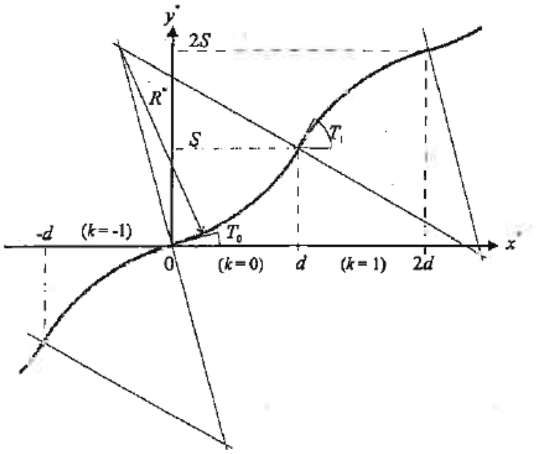

Figure 2.18 Reference curve based on circular arcs [20]

In equation 2.4, E, F and G represent the first fundamental coefficients of the surface and Γ^i_{jk} are the Christoffel symbols given in equation 2.4. The inconvenience of this strategy is that the fiber directions are not always respected.

$$\theta(x,y) = \begin{cases} \arctan -\frac{a_1+a_3y+2a_4x}{a_2+a_3x+2a_4y}, & \text{given } a_2+a_3x+2a_4y \neq 0 \\ \frac{\pi}{2}, & \text{else } a_2+a_3x+2a_4y = 0 \end{cases} \tag{2.5}$$

Another strategy which specifies a reference curve with a constant curvature on a flat panel is presented by [20]. This strategy uses the variation of the fiber angle between two points, each one having a different fiber angle T_0 and T_1 separated by a distance d. T_0 defines the starting point of this path. Between T_0 and T_1, a constant curvature arc with radius R^* is defined (figure 2.18).

A polynomial approach can be taken to find the reference curve, using a mesh description [21]. The method requires that the surface equation in the $x-y$ system (or a polar system) is known. Assuming that the path function is $z = f(x,y)$, one can deduce the fiber angle θ in each finite element center.

In this method, the fiber angle is constant in a finite element so that the reference curve can then be defined. Having $a_1, a_2,$ and a_3 equal to zero, a constant curvature path can be defined as in figure 2.19.

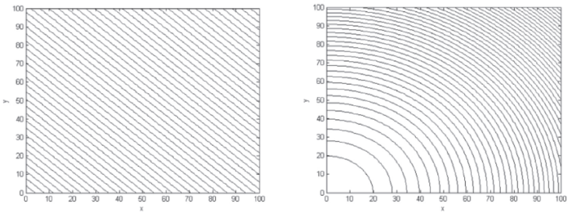

$z = x + y$ $z = x^2 + y^2$

Figure 2.19 Constant curvature reference curve using polynomial equation [21]

2.3.5 Geodesic Guide Curves

The geodesic path can also be known as the natural path. A geodesic is the shortest path between two points along a three-dimensional surface in Cartesian space [22]. This is why the geodesic path is a straight line on a flat panel [20].

Also, a geodesic path can be obtained by specifying a starting point and a direction of travel. For a general parametric surface, a geodesic path must satisfy the following system of differential equations:

$$\begin{cases} u'' + \Gamma^1_{11} u'^2 + 2 * \Gamma^1_{12} u'v' + \Gamma^1_{22} v'^2 = 0 \\ v'' + \Gamma^2_{11} u'^2 + 2 * \Gamma^2_{12} u'v' + \Gamma^2_{22} v'^2 = 0 \end{cases} \tag{2.6}$$

which can be obtained from equation 2.4 by setting the geodesic curvature to zero. In order to solve this system of equations, four initial conditions have to be set: $u(0) = u_0, v(0) = v_0, u(1) = u_1, v(1) = v_1$ for the geodesic path between two points $P_0 = S(u_0, v_0)$ and $P_1 = S(u_1, v_1)$, or $u(0) = u_0, v(0) = v_0, u'(0) = u'_0, v'(0) = v'_0$ for the geodesic path starting at $P_0 = S(u_0, v_0)$ with a direction (u', v').

For the case of a flat surface, the system of equations 2.6 can be simplified to obtain the parametric equation of a straight line which is the shortest path between two points.

For example, [16, 15, 17] define a geodesic path on a cone. It can be done from the equations of the conical surface as the geodesic path has a curvature κ equal to zero in the equation 2.1 and 2.3 (figure 2.20).

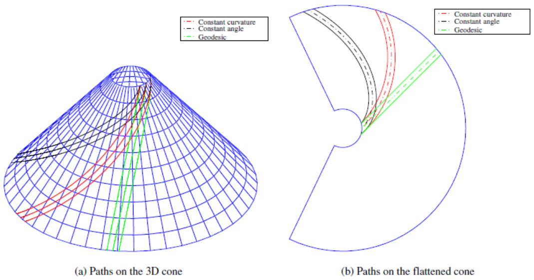

(a) Paths on the 3D cone (b) Paths on the flattened cone

Figure 2.20 Constant curvature, geodesic and constant angle path on a cone (with fiber orientation of the small and the big radius equal to 45°) [16, 15, 17]

In [23], a layup strategy algorithm is developed to fit a Y shape. Starting from one branch of the Y surface, and given an initial fiber angle, a geodesic path is defined. However, once at the junction of the Y, the geodesic path might change or will not be able to propagate on the surface. The different given solutions to continue the path are to go in the direction of the minimum curvature, to try to reach a geodesic path on the other branch of the Y (figure 2.21), or to create a straight path on the other branch respecting the steering conditions for the courses.

2.3.6 Fixed Angle Reference Curve

For a fixed angle strategy, the fiber angle in the reference curve is constant all along the surface. First, a constant angle reference curve is calculated using a mesh approach is given., Then the process of finding the reference curve using a parametric approach will be developed.

Using a mesh

The method presented in [24] uses the mesh information contained in a STL file. After a preliminary computation to perform initial topology reconstruction a functional model including the vectors/edges, the nodes, the facets, and the normal vectors of the facets is generated. If one uses another mesh file type, this information needs to be first generated to use this method. For instance, to find the normal vectors from

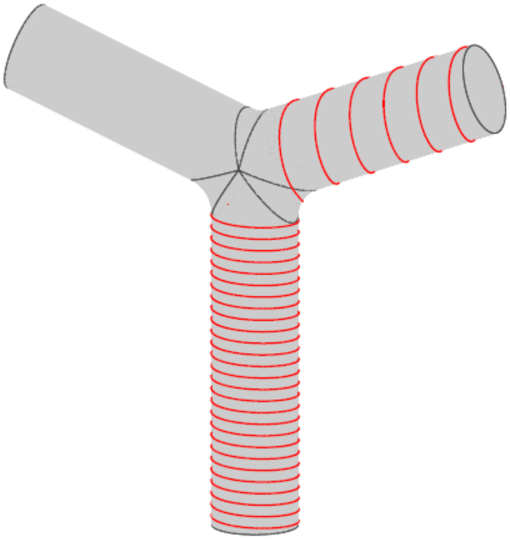

Figure 2.21 Reference curve on a Y surface [23]

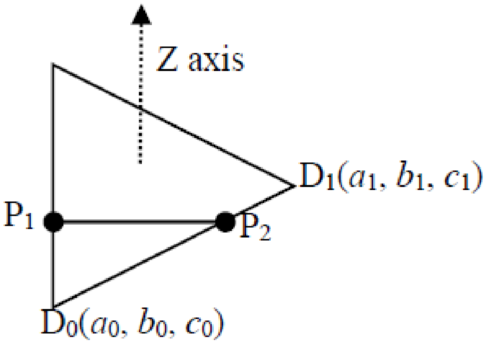

Figure 2.22 Fix angle reference curve using a mesh [24]

the vertices of a triangular mesh a method is provided in [25].

Using this information, a first slicing algorithm creates the reference curve. Basically, a tangent plane in one direction is used to find all the points on the mesh which intersect this plane (figure 2.23). To do so, a first point, P_1, of a triangle which intersects the plane and the edge, is found. Then, using the structure reconstruction, the mesh triangle in which this point belongs is already known. Finally, the second point, P_2, of the triangle mesh intersecting the plane is found and one can move forward to the next triangle that this last point belongs to. This loop continues until the tangent plane no longer intersects the surface anymore. The fact that the direction of the tangent plane used is constant results in the fiber angle constant along the surface.

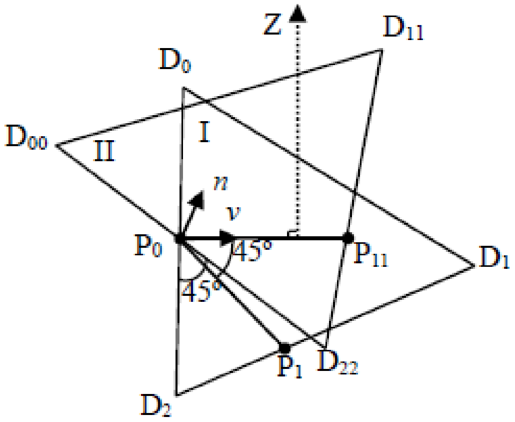

Figure 2.23 Constant angle method [24]

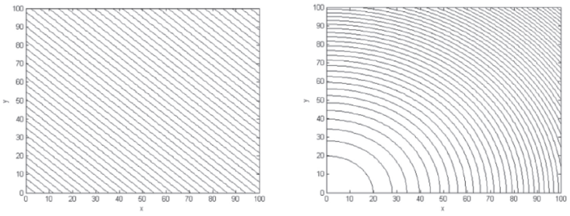

$z = x + y$ $z = x^2 + y^2$

Figure 2.24 Constant angle reference curve using polynomial equation [21]

To find another fix angle path, the meshed plane is rotated by a constant angle from the previous path defined before. In figure 2.23, the rotation around the z-axis of the triangle $D_0D_1D_2$ by an angle of 45° results in a new triangle $D_{00}D_{11}D_{22}$. In this diagram, the reference curve is v and P_0P_1 is the offset of this reference curve at a fixed angle of 45°.

PARAMETRIC APPROACH

As previously stated, the parametric approach is more dominant in the literature. The method in [21] explained in the previous section can also be used to determine a fixed angle reference curve on a flat panel. With $a_1 = a_2 = 1$ and $a_3 = a_4 = a_5 = 0$ in figure 2.23 the reference curve presented in figure 2.24 is obtained.

In [26, 27, 28, 29, 30, 31] a major axis is projected on the surface $S(u, v) = [x(u, v), y(u, v), z(u, v)]$. This projection gives an intersection line on the surface. The major axis plane equation is $P(x, y, z) = ax + by + cz + d = 0$. Hence, the surface

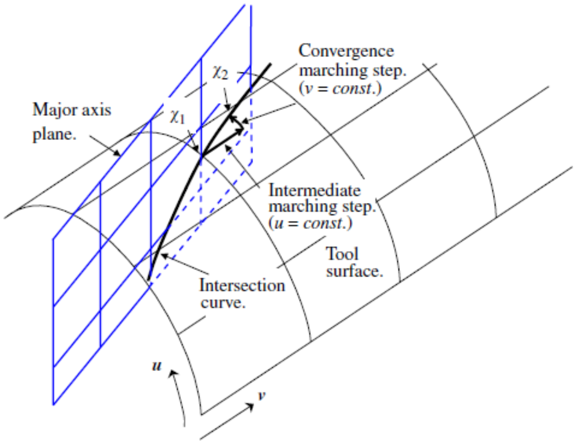

Figure 2.25 Projection of a major axis on the surface [28]

plane intersection equation is:

$$f(u,v) = ax(u,v) + by(u,v) + cz(u,v) + d = 0 \tag{2.7}$$

Discrete points are needed to find the offset curves to cover the surface, therefore points on this intersection line need to be determined. A starting point is needed from which the reference curve will be propagated. This starting point is found on a boundary using a bracket method followed by a Newton-Range method (NRM) on equation 2.7 to find the intersection point between the boundary and the projection of the major axis. To find the next point of the reference curve, one step is done in one direction (length of the step is defined) then the other step uses the NRM to converge to the surface-plane intersection line. The propagation is done until the major axis does not intersect with the surface anymore (figure 2.25). [30] uses the same method to find the reference curve but the compaction roller position is also considered. On every point of the reference curve, a tangent plane to the surface is inserted. The center of the roller is then placed on the normal to the surface calculated at each of the points (figure 2.26), thus, determining the roller path location following the reference curve allows, on very complex surfaces, to avoid defects therefore increasing the layup efficiency.

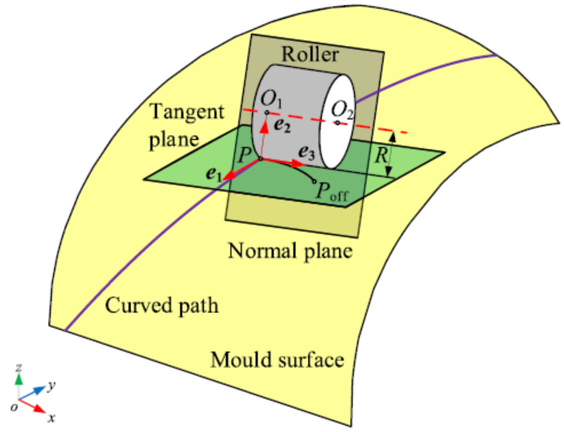

Figure 2.26 Reference curve with roller position [30]

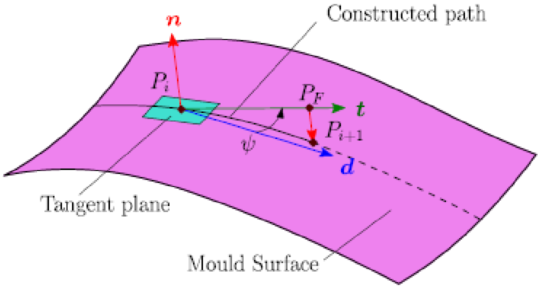

Figure 2.27 Reference curve using an iterative algorithm [23]

In [23, 32], an iterative algorithm is developed using a defined reference direction. Beginning from a point P_i, a tangent vector d of the surface is created, that follows the direction of the reference curve. Another vector t is created by rotating d around the normal vector by a defined placement angle ϕ. Finally, a point P_f is defined on this vector t at a certain distance from P_i and is projected on the surface which gives a point P_{i+1} on the surface (figure 2.27). The process is iterated until the path reaches a boundary.

Finally, [16, 15, 17] determined a reference curve for a conical shape (figure 2.17). It is a good example where the parametric approach is faster and more efficient than using a mesh due to the simplicity of the conical parametric surface. A resolution of equations 2.2 and 2.3 that keep the fiber angle constant gives the reference curve on the cone surface with a fixed angle. However, as these methods only focused on the fiber angle, it is possible to result in tow-steering too severe too severe at some points of the reference curve, which makes the manufacturing process difficult if not impossible. This is one of the main reasons why layup strategies need to include manufacturing configurations to generate optimal toolpaths.

2.3.7 VARIABLE ANGLE GUIDE CURVES

The fiber orientation can vary along the reference curve. This is in contradiction with the statements in Section 2.3.4, as the fiber directions are not constant anymore. This variation of the fiber direction leads to a variable-stiffness [33]. The higher degree of freedom for the reference curve allows the creation of structures which account for non-unidirectional constraints. Therefore, the calculations and the optimization are harder. In this section, different strategies to define the reference curve with variable angle fibers will be explained.

LINEAR VARIATION

A variable fiber angle layup strategy is based on the linear variation of the fiber directions in the path. This method has been used extensively in the literature, including: [15, 17, 18, 20, 21, 34, 35, 36, 37, 5, 38, 39, 40, 41, 42]. This strategy lies in the linear variation of the fiber angle between two points, each one having a different fiber angle T_0 and T_1 separated by a distance d. T_0 defines the starting point of this path. The axis system of fiber orientation is defined by rotating the rosette by an angle φ. This new axis defines a new fiber orientation called r. The fiber path is then defined by $\varphi(T_0, T_1)$ and varies linearly along r from T_0 to T_1 (figure 2.28).

According to figure 2.28, one can calculate $\theta(r)$ the fiber angle as a function of r in the polar coordinate of equation 2.8.

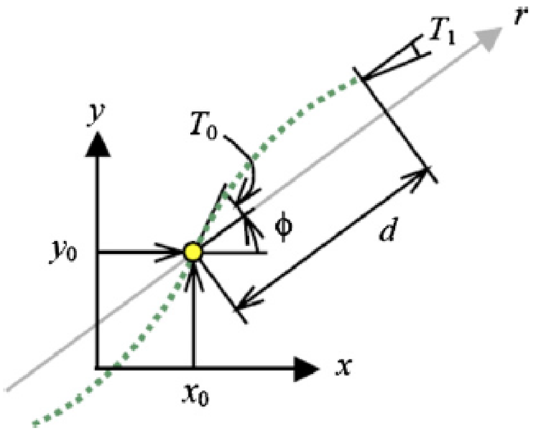

Figure 2.28 Reference curve with a linear variation [37, 43]

$$\theta(r) = \begin{cases} \phi + (T_0 - T_1)\frac{r}{d} + T_0, & \text{where } -d \leq r \leq 0 \\ \phi + (T_1 - T_0)\frac{r}{d} + T_0, & \text{where } 0 \leq r \leq d \end{cases} \tag{2.8}$$

The reference curve repeats indefinitely with a 2d period until it reaches a boundary.

NONLINEAR VARIATION

Non-linear angle variations have been employed to obtain higher structural performance [44]. Different methods have been used to define the layup trajectories with this non-linear variation and are explained in this section.

FREE FORM

First, B-spline curves have been used to define a parametric equation for reference curves. However, this method has its limits as larger amounts of control points reduce its effectiveness. This results in low-resolution path with bad connectivity between the control points [45].

A Bezier curve, frequently used in computer graphics to model a smooth curve, is another way to define the reference curve with a parametric equation of the path on the surface using a set of control points [46]. In [47], the Bezier curve is represented

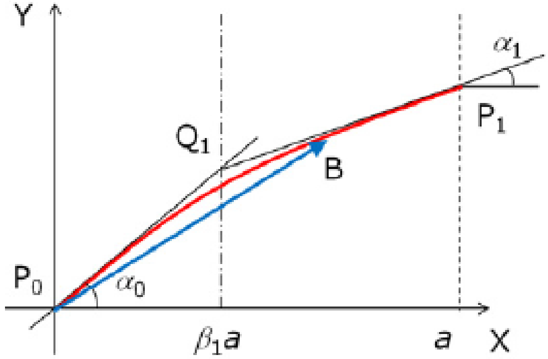

Figure 2.29 Tow path represented by piecewise quadratic Bezier curves with two control points [47]

with a vector equation including the control points and the junction angles between each point. An example of this equation for a Bezier curve between two control points is given bellow:

$$\overrightarrow{B}(t) = (1-t)^2\overrightarrow{P_0} + 2(1-t)t\overrightarrow{Q_1} + t^2\overrightarrow{P_2} \text{ for } t \in [0,1] \tag{2.9}$$

$$\overrightarrow{P_0} = (0,0), \overrightarrow{Q_1} = (\beta_1\alpha, \beta_1 \tan\alpha_0), \overrightarrow{P_1} = (\alpha, \beta_1\alpha\tan\alpha_0 + (1-\beta_1)\alpha\tan\alpha_1) \tag{2.10}$$

Where P_0 is the starting point, P_1 is the end point and Q_1 is the junction between the two of them; The angles a_0 and a_1 are defined as in figure 2.29 and β_1 is the angle variation coefficient which defines the location of the junction point Q_1.

One can then deduce the coordinates of any point on the curve:

$$x = (1-2\beta_1)t^2 + 2\beta_1 t \text{ for } 0 \leq x, t \leq 1 \tag{2.11}$$

$$y = ((1-\beta_1)\tan\alpha_1 - \beta_1\tan\alpha_0)t^2 + 2\beta_1\tan\alpha_0 t \tag{2.12}$$

It is also possible to add other segments to increase the freedom of the tow path. To do so, a new parameter needs to be introduced which makes the link between the

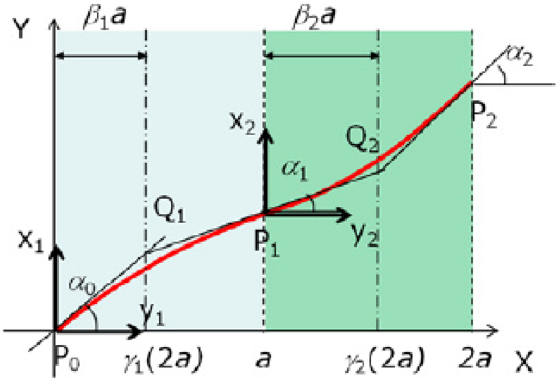

Figure 2.30 Tow path represented by piecewise quadratic Bezier curves [47]

different junction points: $\gamma = (i - 1 + \beta_i)/N$, where i and N are respectively the current segment number and the total number of segments. An example of a tow path between two segments is given in figure 2.30.

In [33], the surface is considered as a bicubic Bezier surface with 16 control points as design perimeters. The control points are forming a mesh and the fiber angle can be written in a cubic polynomial form:

$$sr = ar^3 + br^2 + cr + d \text{ and } r = x\cos\alpha + y\sin\alpha \tag{2.13}$$

As the fiber angle is constant in a finite element and considering the point $M(x_m, y_m)$ the center of the finite element, the fiber angle within a finite element is:

$$\theta = \arctan\Big(3\alpha(x_m\cos\alpha + y_m\sin\alpha)^2 + 2b(x_m\cos\alpha + y_m\sin\alpha + c)\Big) + \alpha \tag{2.14}$$

In [48], the reference curve trajectory is optimized following different control points. Indeed, control points are defined on the surface and the fiber angle varies until the compliance is minimized (figure 2.31). The optimization problems are resolved due to finite difference sensitivities. The curvature of the surface can also be considered in the optimization to decrease the compliance.

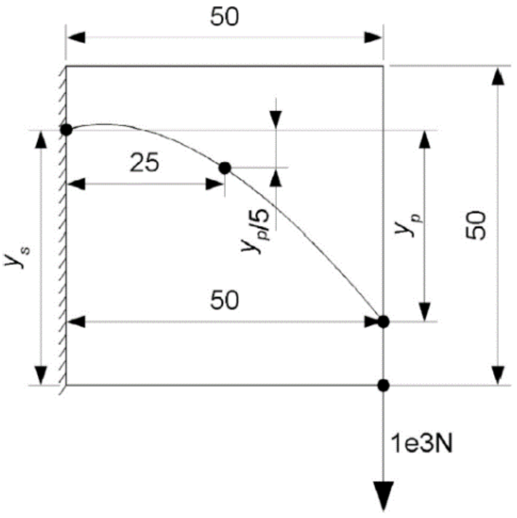

Figure 2.31 Reference curve optimizing the compliance constraints [48]

POLYNOMIAL

Multiple research groups, including [49, 50, 51, 44], utilize a mesh and a cubic polynomial function to determine the fiber angle along the surface.

$$f(x,y) = c_{00}+c_{10}x+c_{01}y+c_{20}x^2+c_{11}xy+c_{02}y^2+c_{30}x^3+c_{21}x^2y+c_{12}xy^2+c_{03}y^3 \quad (2.15)$$

The different coefficient of the polynomial function can vary with the surface as they determine the surface shape. The fiber angle θ is constant within a finite element (but can vary from one finite element to another) so it is calculated in the center of the finite element (x_C, y_C):

$$\theta(x_c, y_c) = \arctan\left(\frac{\partial f/\partial x}{\partial f/\partial y}\right), \text{ when } \partial f/\partial y = 0, \theta = 90^\circ \quad (2.16)$$

The method used is more efficient than the ones using spline functions [45]. The fiber shape is defined in the polynomial functions while, using spline functions, simultaneous equations need to be solved for the same task. The path is then optimized by the genetic algorithm defined in the following section.

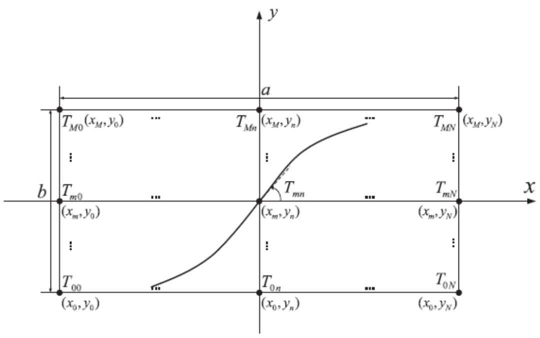

Figure 2.32 Non-linear path using Lagrangian polynomial function [52]

In [52], Lagrangian polynomial functions are used to determine the reference curve. The following equation gives the expression of the fiber angle on the surface:

$$\theta(x, y) = \sum_{m=0}^{M-1} \sum_{n=0}^{N-1} T_{mn} \cdot \prod_{m \neq 1} \left(\frac{x - x_i}{x_m x_i} \right) \cdot \prod_{n \neq j} \left(\frac{y - y_j}{y_n - y_j} \right) \tag{2.17}$$

Where (xi, yj), (xm, yn) are the x-y coordinates of reference points. The reference curve is then obtained by resolving the equation at different reference points (figure 2.32).

2.4 COVERAGE STRATEGIES

In this section, the different coverage strategies are detailed. Indeed, three strategies can be used to cover the entire surface. The first one computes the different curves independently and the two others compute all the other course paths from a reference curve.

2.4.1 OFFSET CURVES

The offset curves, or parallel curves strategy, is the most common for path planning. Adjacent curves on the surface are computed from the reference curve to achieve total coverage. Towpaths within a course must be determined using this method due to the roller mechanism that ensures all tows within a course are parallel. To explain this coverage strategy, the distinction between the parametric approach and the usage of a mesh are investigated.

Parametric approach

To compute the parallel curves parametrically, a closed form solution for continuous planar curves exists by taking equidistant points following the normal vector along the curve. This can be expressed as:

$$\mathbf{C}(t) : \begin{cases} x(t) = u_c(t) \\ y(t) = v_c(t) \\ z(t) = 0 \end{cases} \quad \mathbf{C}_p(t) : \begin{cases} x_p(t) = u_c(t) - d\frac{v'_c(t)}{\left({u'}^2_c(t)+{v'}^2_c(t)\right)^{1/2}} \\ y_p(t) = v_c(t) + d\frac{u'_c(t)}{\left({u'}^2_c(t)+{v'}^2_c(t)\right)^{1/2}} \\ z_p(t) = 0 \end{cases} \tag{2.18}$$

where $\mathbf{C}(t)$ is the reference curve and $\mathbf{C}_p(t)$ is a parallel curve at a distance d from the original, and d is either a positive or a negative number.

For a general surface, a closed form solution for the parallel curves does not exist in most cases. Hence several algorithms [27, 29, 30] have been developed to compute offset/parallel curves numerically.

For instance, a similar approach is used in [27] for the planar case to find parallel curves by following the vector normal to the reference curve. This vector designated $\mathbf{O}$ (figure 2.33) can be found by taking the cross product between the tangent vector to the curve and the normal vector to the surface. Then at a distance d along the vector $\mathbf{O}$, a point $\mathbf{P}'$ is projected to the surface following the normal vector using a Global Closest Technique. This process is repeated at every point-step along the curve to obtain the new parallel curve. The resulting error from using this technique from figure 2.33 is reported to be [27]:

$$Error = d\left(1 - \frac{\psi}{\tan\psi}\right) \tag{2.19}$$

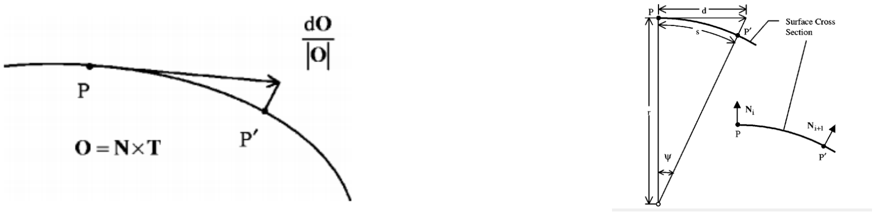

(a) (b)

Figure 2.33 (a) Cross Section showing calculation of offset point; (b) Error associated with placing a point on a surface with circular arc cross section [27]

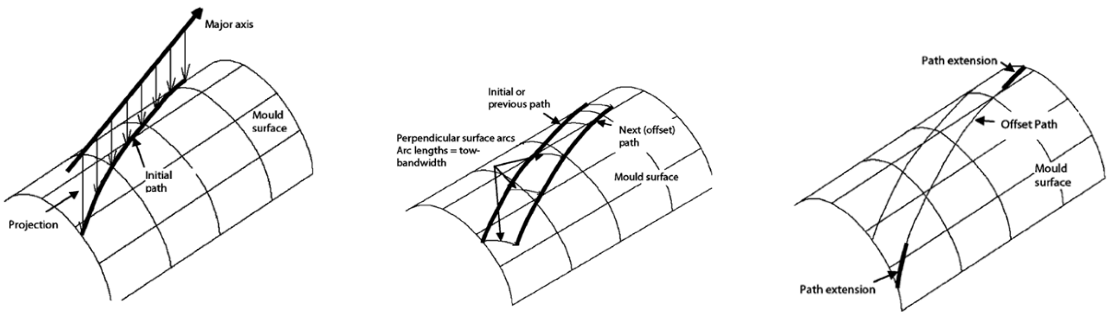

(a) Initial Path Generation (b) Curve Offset (c) Path Extension [29]

Figure 2.34 Path offset techniques

Therefore, the error increases by taking a further offset curve (in the case of wider courses), and in the case of highly curved surface.

A more accurate method is presented in [27, 29, 30, 31] by taking the intersection between the plane perpendicular to the curve and the mold surface. To do so, a numerical approach presented in [53] is used to determine the resulting curve. Then, the offset point can be found by taking the required distance along the perpendicular arc. If the reference path is shorter than the offset path which does not reach a boundary, a last step is needed to obtain a complete offset path. In this case, the offset curve is completed by interpolating the last point from the calculated ones until it reaches the boundary.

Three other methods are presented in [54] to compute parallel curves on a NURBS surface. The first method commonly referred to as “section curves” is similar to those presented in [27, 29, 30, 31]. The other two methods consist of generating orthogonal curves to the reference by either taking vector-field curves or geodesic curves. Once the orthogonal curve is defined in either of these methods, the offset points can be calculated at the required distance from the reference curve. The new parallel curve is then obtained by interpolating these points.

The advantage of computing parallel curves is that the offset curves are equidistant so there are no gaps or overlaps between the paths or the courses during the layup process. However, considering a complex surface, the fibers directions in the offset curve can change.

To optimize the fiber direction and to avoid significant deviation of these angles, [55] considers an interval of direction and tests the deviation of the offset fibers while the fiber direction in the reference path varies. The reference curve which conserves the most fiber directions in the offset path constant is then selected.

Mesh: Fast Marching Method

This method has been introduced by [48, 56] and is based on the Eikonal equation, with a depiction of the results in figure 2.35. This equation is mostly used in optics and is used to calculate the propagation of a wave with a particular speed. Hence one can calculate the different position of this wave at every time once it starts propagating.

The fast-marching methods starts from a random reference curve on the surface. First, the reference curve needs to be discretized. The intersection points between the mesh and the reference curve form the discretized reference path. For initialization, all these points have a time value of 0.

Then, the reference curve is propagated at a defined speed so every node of the mesh will hit the propagated curve at a certain time. Moreover, knowing the time value of two nodes of one mesh triangle, it is possible to calculate the time value of the last node. On an accurate triangular mesh figure 2.36, knowing the time values

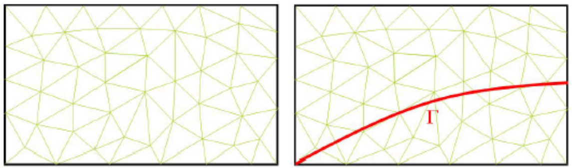

a) Define the mesh of the structure b) Trace the reference curve

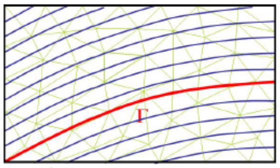

c) Solve the Eikonal Equation

Figure 2.35 Steps of the Fast Marching Method to offset a reference curve [56]

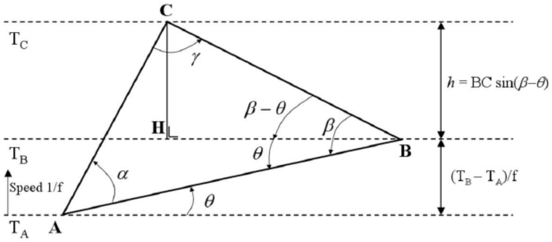

Figure 2.36 Finding T_C knowing T_A and T_B [56]

of the points A and B respectively T_A and T_B, one can find the time value of T_C.

Using the following equations and with $1/f$ the propagation speed of the reference curve:

$$\theta = \arcsin\left(\frac{T_B - T_A}{f \cdot AB}\right) \tag{2.20}$$

$$h = BC \sin\beta - \theta \tag{2.21}$$

One can calculate T_C:

$$T_C = h \cdot f + T_B \tag{2.22}$$

To propagate this calculation, the Fast Marching Method explained in [57] is used. This method looks for the neighbor nodes of the one with the lowest time value. Then, all the nodes around this one are updated. The initial node won't be considered anymore, and the update is done from the next node with the lowest value. It is important to notice that the time value of each node is updated only if the calculated value is smaller than the previous one.

(a) Tow path Definition: (a) Parallel method; (b) Shifting method [58]

(b) Gap and Overlap resulted in the shifting method [58]

Figure 2.37 Tow path definitions and defects resulting from shifting methods

Once all the nodes' time values are known, for each time value an offset curve of the reference curve is drawn. Knowing the speed and time, an offset curve with the proper distance from the reference curve can be found. The offset curve joins the different iso-value points.

However, to obtain a real parallel curve, the reference curve must be considered as infinite (meaning that it goes through the boundaries) when propagated with the Fast Marching Method. Indeed, if the reference path is not extended, the offset curves won't necessarily be parallel to it at every point.

2.4.2 Shifted Curves

In many methods, reference curve is simply shifted along its perpendicular direction on the surface by applying a translation. The advantage of this method is its simplicity, however, on a complex surface, the fiber directions of the offset path are not guaranteed, and the presence of gaps and overlaps is possible.

2.4.3 Independent Curves

Another approach to cover the entire surface is to draw the different curves independently. Regarding complex surfaces, independent curves can be a solution to limit extreme steering. To cover the surface, it is possible to draw the courses staggered one to another with a constant length and with a different direction [27]. If the surface is

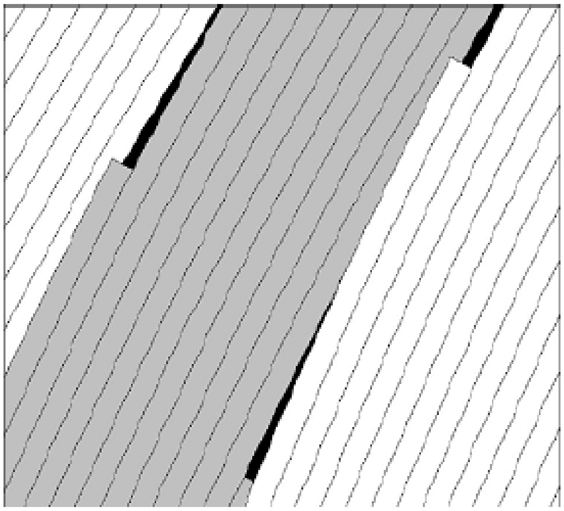

Figure 2.38 Gaps and overlaps induced by independent direction curves [27]

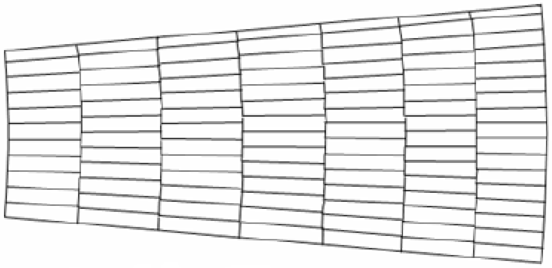

Figure 2.39 Succession of short independent courses to cover a conical surface [28]

complex, the different courses are not necessarily parallel to each other if the required direction is maintained. This will induce gaps and overlaps as seen in figure 2.38.

Another strategy based on the principle of independent fibers creates many short courses, where the short courses help control the presence of gaps and overlaps. This strategy has been studied by [28] for a conical surface figure 2.39. The drawback of this method is that the short independent courses reduce the resulting laminate's strength due to the many discontinuous fibers throughout the structure.

2.5 SUMMARY

This chapter has set forth a comprehensive list of AFP defects that occur during laminate manufacturing. These defects had several sources, including tool geometry, material and machine imperfections, and chance-based defects. The results of the defect identity cards were published in SAMPE 2017 [59]. Additionally, the concept of defects have been expanded to through thickness, with investigation into the formation and consequences of ply-ply defect interactions.

This chapter has also provided a literature review of the of the various layup strategies as they exist in literature to provide additional context on the formation of geometry based fiber defects, as well as the fundamental algorithms driving the generation of fiber paths. Important concepts that were covered include initiation and propagation of surface coverage. Initiation was commonly performed through the use of a single starting point combined with a desired fiber orientation, or with the use of a specified guide curve. The propagation methods had several variations, and would either strictly follow previous fiber paths, loosely follow previous paths, or be completely independent and strictly based on surface geometry. Additionally, strategies would either require complete surface definitions in the form of parametric surface data or could be computed on meshed surface representations. With these three concepts of initiation, propagation and surface representation, combined with varying complexity levels of the surface itself, a huge variety of coverage strategies can be defined, each with its own strengths and weaknesses in terms of total coverage, potential fiber defects, and structural properties of the overall resulting laminate. These results were published in CADA 2019 [60].

CHAPTER 3

PLY LEVEL EVALUATION

In the context of computer aided process planning, ply optimization targets the minimization of fiber defects resulting from interactions between the tool and tow geometry. To perform this optimization, it is necessary to quantify and score the layup. The chosen inputs to the optimization function are the starting point and layup strategy selection, which have the most direct control over the resulting ply. Each ply is initially defined by the ply boundary, fiber angle, and position in the laminate stack. Herein, several ply scenarios were generated for each ply, where the ply scenario would utilize the ply boundary and fiber angle of the given ply and specify a unique starting point and layup strategy combination. Thus, each ply scenario contained the information necessary to generate the fiber paths of that ply and could be measured for defects to identify the *"best"* ply scenario to represent that ply from the laminate.

The fiber defects were chosen as they directly resulted from the geometrical relationship between the tool surface and fiber paths, such that they could be detected and measured in a simulated ply. The defects measured in this study were gaps and overlaps, angle deviation, and fiber steering. As previously defined in Section 3.1, the magnitude of fiber steering is an indication of where certain defects are more likely to occur, namely puckers, wrinkles, folds, and twists.

The following section defines the techniques used for measuring the fiber defects and how they are combined to form a final score for each ply scenario. Following this, the iterative method used to identify the optimal ply is described.

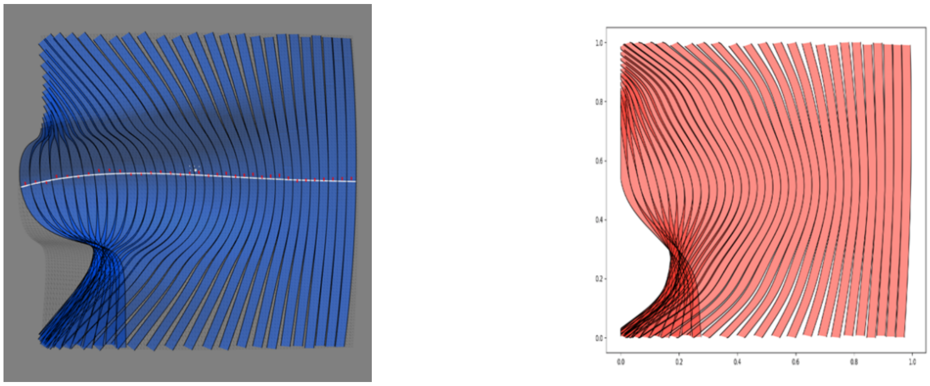

(a) Fiber paths on 3D tool surface

(b) Fiber paths dropped to parametric reprsentation

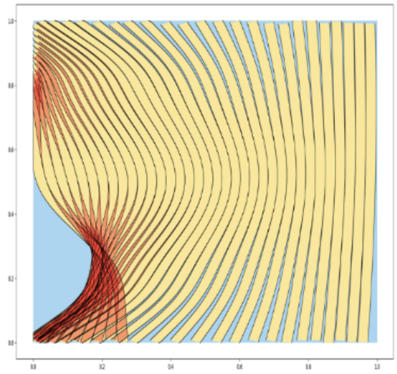

(c) Evaluated Gaps (blue) and Overlaps (red)

Figure 3.1 Gap and Overlap evaluation with parametric tool surface

3.1 IDENTIFYING AND MEASURING

3.1.1 GAPS AND OVERLAPS

Fiber gaps and overlaps (figure 3.1) are coupled defects that occur when adjacent tows are not perfectly parallel. The deviation of alignment results in a fiber path that will converge or diverge from neighboring paths, developing the course-to-course gaps and overlaps. These features are coupled since deviation resulting in an overlap with one neighbor will often result in a gap forming with the other adjacent neighbor.

The most common cause of gaps and overlaps during the process planning and simulation phase is the use of excessive steering for curved paths, and surfaces with high levels of double curvature, those which are non–developable. Often for these scenarios, it is impossible to completely remove the presence of gaps and overlaps. Gaps and overlaps may be a site for failure initiation under loads, where gaps create resin rich regions for crack growth, while overlaps create undulation in the fiber that can lead to compressive failures. For these reasons it is important to reduce the presence of gaps and overlaps to improve the final properties of the laminate.

When working with parametric tool surface's (e.g., NURBS), gaps and overlaps can be measured with the use of the surfaces parametric representation. Once fiber paths have been generated, their 3–dimensional forms can be dropped into the tool surface's parametric space in order to obtain 2-dimensional representations of the fiber paths. With the newly obtained 2-dimensional representation of the ply, gaps and overlaps are detected through basic boolean operations between each set of regions. Overlaps are found as the intersection of any combinations of courses, where gaps are developed from the total tool surface area minus the union of the courses.

3.1.2 Fiber Angle Deviation

For rosette angles to be applicable to non-planar surfaces, it is necessary to describe a referential coordinate system over the domain of our surface to serve as the basis for the angle deviation measurements. In this context, the referential coordinate system of each quad was used to generate the base vector.

The current method generates an angle deviation value for each relevant mesh element. A mesh element is relevant when it contains a portion of the course and can thus be assigned an angle deviation value.

$$\cos\theta = \frac{\overrightarrow{u} \cdot \overrightarrow{u}}{\|\overrightarrow{u}\| \cdot \|\overrightarrow{v}\|} \tag{3.1}$$

$$\theta_{Deviaton} = \theta_{Specified} - \theta_{Manufactured} \tag{3.2}$$

The directions of the courses are developed from their normalized tangential vectors along the path. The manufacturing angle along each path can be found relative to the relevant referential coordinate systems that were previously mapped. The vector dot product relation (3.1) allows for the calculation of the angles. The value of angle deviation was finally evaluated by comparing the measured manufacturing angle to the design angle as defined by equation 3.2.

3.1.3 Fiber Steering

The use of fiber steering allows for optimization of laminate loading properties in addition to altering laminates to avoid defects due to the presence of certain tool geometries. Fiber steering achieves these effects by changing the in-plane curvature of the fiber path from the classic linear orthogonal laminates.

However, due to the high modulus of elasticity of carbon fiber, the curvature from fiber steering results in tensioning of the outer edge of the fiber tow and compression of the inner portion of the fiber tow. These conditions may result in several defects such as gaps and overlaps, puckers, wrinkles, and etc. Therefore, steering constraints are necessary during the process planning stage to limit the magnitude of fiber steering and thus reduce the occurrence of defects generated by steering of the tows. A process planner will choose the limit based on his knowledge of the machine's steering abilities and the steering characteristics of the particular fiber-matrix combination to be used.

Fiber steering is defined as the difference between the curvature of a fiber path and the geodesic curvature of the tool surface. The closed form of curvature for spline curves presented by equation 3.3.

$$
\begin{aligned}
k_g = & \left[\left(u''_c + \Gamma^1_{11} u'^2_c + 2\Gamma^1_{12} u'_c v'_c + \Gamma^1_{22} v'^2_c \right) v'_c \right. \\
& \left. - \left(v''_c + \Gamma^2_{11} u'^2_c + 2\Gamma^2_{12} u'_c v'_c + \Gamma^2_{22} v'^2_c \right) u'_c \right] \\
& \times \frac{\sqrt{EG - F^2}}{\left(E u'^2_c + 2F u'_c v'_c + G v'^2_c \right)^{3/2}}
\end{aligned}
\tag{3.3}
$$

3.2 Fiber Defect Summary

Effective use of process planning works to minimize defects and unwanted features that will develop based on the chosen process planning parameters. Currently, there are techniques in place that can measure these defects in a case-by-case basis but lack the ability to efficiently summarize the defects on a ply-wide scale. Additionally, there is no system to compare the presence of defects on a common scale where they may be used to generate a logical, overall ranking for a generated scenario depending on the requirements set forth by the process planner.

To summarize these features, two aspects of their presence must be considered. Many manufacturing and design processes set a maximum instance threshold for each feature. The instance measurement represents the total amount of defects above a certain threshold. These limitations are imposed to reduce the propagation of more defects and to improve the manufacturability of the laminate.

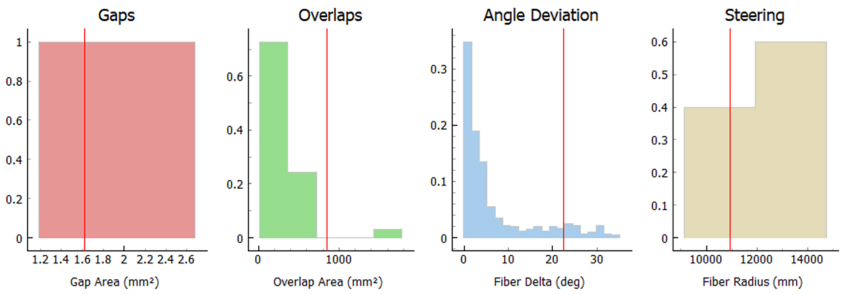

Figure 3.2 Defect distribution Histograms

The other measurement used to describe the defect is severity. The severity represents the amount that the defects above the threshold contribute to the total amount of defective regions. This measures how significantly certain defects would affect the overall laminate and will demonstrate if there are many small defects or several large defects. While the instance measurement functions as an indicator of commonality of the features for the given ply, the severity of the feature uses the threshold to find the sum of the instances as they occur in the ply. Figure 3.2 presents distributions of relevant defect types and the associated threshold depicted by the vertical red lines.

3.2.1 COMPARISONS AND RANKING

The Analytical Hierarchy Process (AHP) provides a method for creating an overall ranking of many features through a series of pair-wise comparisons. These comparisons are then used to develop a relative weight for each of the fiber defect variations.

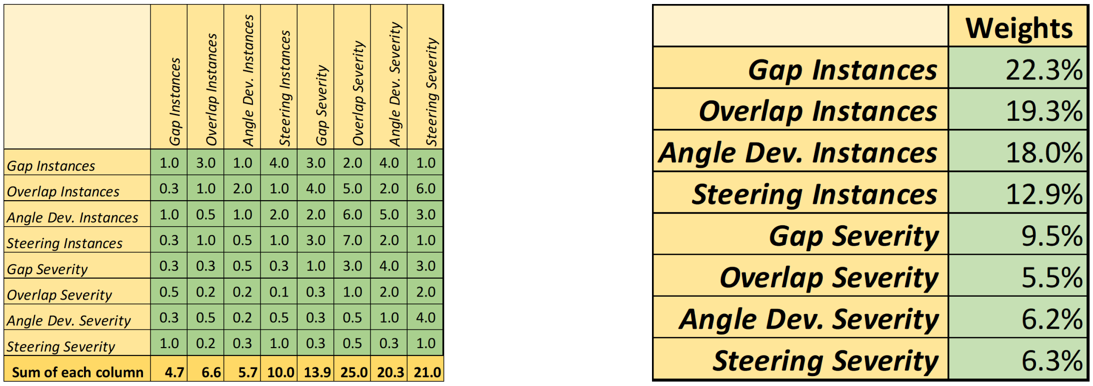

	Gap Instances	*Overlap Instances*	*Angle Dev. Instances*	*Steering Instances*	*Gap Severity*	*Overlap Severity*	*Angle Dev. Severity*	*Steering Severity*
Gap Instances	1.0	3.0	1.0	4.0	3.0	2.0	4.0	1.0
Overlap Instances	0.3	1.0	2.0	1.0	4.0	5.0	2.0	6.0
Angle Dev. Instances	1.0	0.5	1.0	2.0	2.0	6.0	5.0	3.0
Steering Instances	0.3	1.0	0.5	1.0	3.0	7.0	2.0	1.0
Gap Severity	0.3	0.3	0.5	0.3	1.0	3.0	4.0	3.0
Overlap Severity	0.5	0.2	0.2	0.1	0.3	1.0	2.0	2.0
Angle Dev. Severity	0.3	0.5	0.2	0.5	0.3	0.5	1.0	4.0
Steering Severity	1.0	0.2	0.3	1.0	0.3	0.5	0.3	1.0
Sum of each column	**4.7**	**6.6**	**5.7**	**10.0**	**13.9**	**25.0**	**20.3**	**21.0**

(a) AHP matrix with inputs

	Weights
Gap Instances	22.3%
Overlap Instances	19.3%
Angle Dev. Instances	18.0%
Steering Instances	12.9%
Gap Severity	9.5%
Overlap Severity	5.5%
Angle Dev. Severity	6.2%
Steering Severity	6.3%

(b) Resulting defect weights

Figure 3.3 Development of individual rankings through AHP pair-wise comparisons

The value of relative importance between each pair of defects are entered into the upper half of the matrix and signifies how much the column is preferred over the row criteria. By doing this, the bottom half of the matrix is automatically computed as the inverse values of the upper half as seen in figure 3.3a. From there, the sum of each column is computed and divides the value in each column to achieve figure 3.3b. The final weights are achieved by averaging the values of each column in figure 3.3a. These final weights represent the relative importance of each type of defect and are utilized in the objective function.

3.3 Demonstration of Ply Scores

The following section presents a study of the scoring system over the domain of a tool surface. The study examines the resulting distribution of ply scores as a function of ply starting point. The ply scores represent the weighted aggregate scores computed for the instance and severity score of each defect type. Multiple weighting strategies are utilized to examine the effect of each defect's impact on the final ply score. The selected tool surface represents shape of the root portion of a wind tunnel blade (figure 3.4a) with a moderate amount of surface curvature, providing a non-trivial layup for investigation.

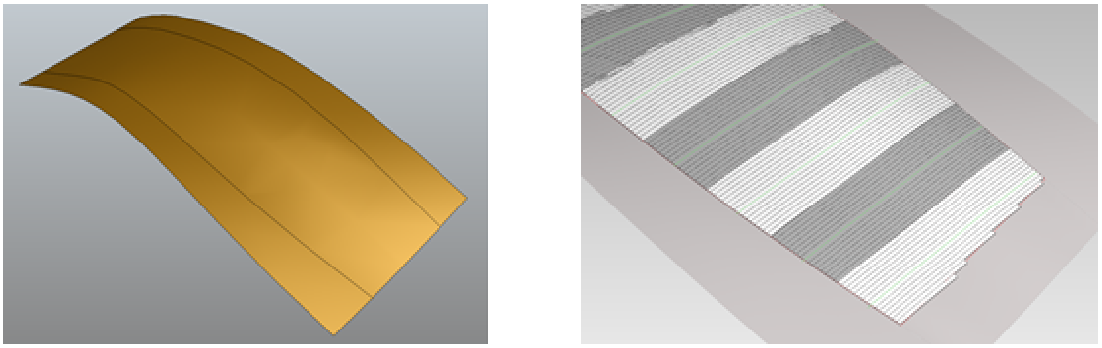

(a) Tool surface

(b) Sample of generated fiber paths

Figure 3.4 AMES blade

A layup was generated using 6.35mm wide fiber tows, with 16-tow courses (figure 3.4b) to reduce processing time, which is primarily influenced by the number of individual courses. Courses consisting of more tows increase course width, therefore reducing the total number of required courses for a given tool surface. For this scenario, a 0° fiber angle was chosen, which was perpendicular to the long axis of the tool surface. A large ply boundary was selected which maximized the layup region.

In order to investigate the values and distributions of ply scores, the following shows the results for a highly sampled tool surface. These results provide insight into the distribution of ply scores over the tool surface as a function of the layup generation starting point. The layup strategy was set to Natural path, and held

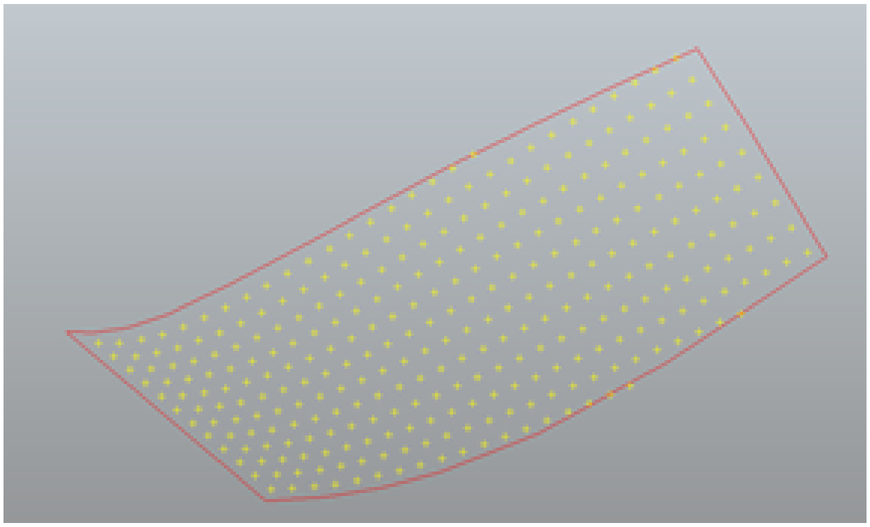

Figure 3.5 Starting point distribution

constant for all the ply scenarios. The scenarios were initialized within the region of the tool surface as defined by the ply boundary (figure 3.5) and was roughly 14 x 30 starting points, of which 309 starting points were valid for layup generation. Finally, the scenarios were exported to be generated and analyzed by VCP.

A total of 309 scenarios were generated and analyzed to obtain the results presented in figures 3.6. The total processing time for those scenarios through VCP was 50 minutes, or 10 seconds per scenario. A primary observation from the two data sets obtained is the range of scores obtained in each heatmap.

The first set of results (figure 3.6) were generated with a $650mm2$ threshold for fiber gaps and overlaps, $>2^\circ$ fiber angle deviation threshold, and $<2500mm$ threshold for radius of curvature.

An additional set or tighter defect thresholds were supplied to control the scoring, to demonstrate AHP defect prioritization. The second set of results (figure 3.7) were generated with a $400mm^2$ threshold for fiber gaps and overlaps, $> 1.5^\circ$ fiber angle deviation threshold, and $< 1500mm$ threshold for radius of curvature.

The first set utilized larger thresholds, thus tolerating more of the defects that were present. As a result, the observed scores range from 0.65-0.87, with 1 being the

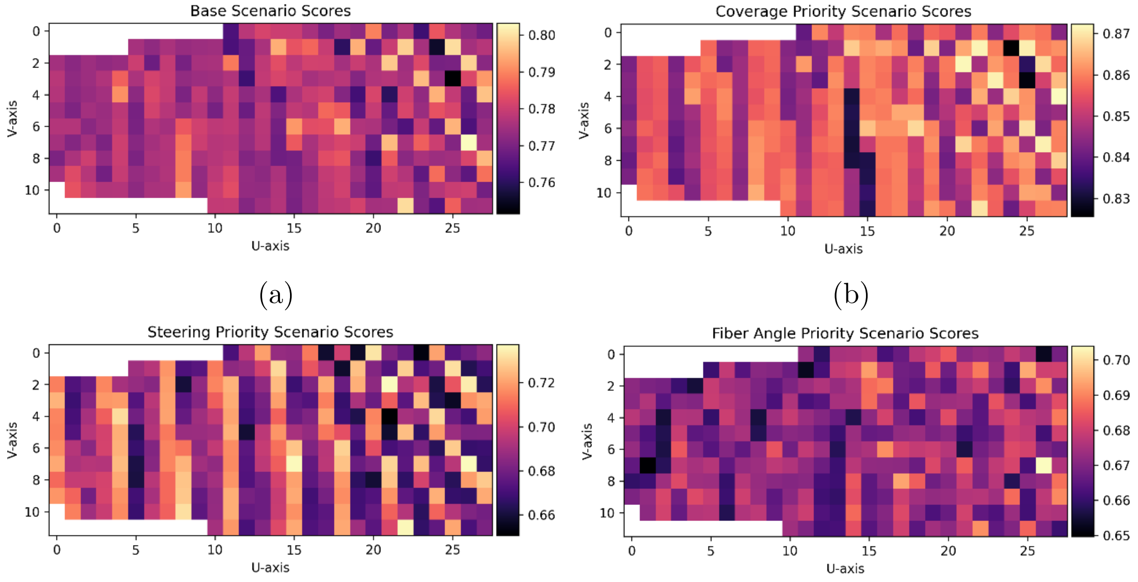

(a) (b)

(c) (d)

Figure 3.6 Various ply scoring priorities

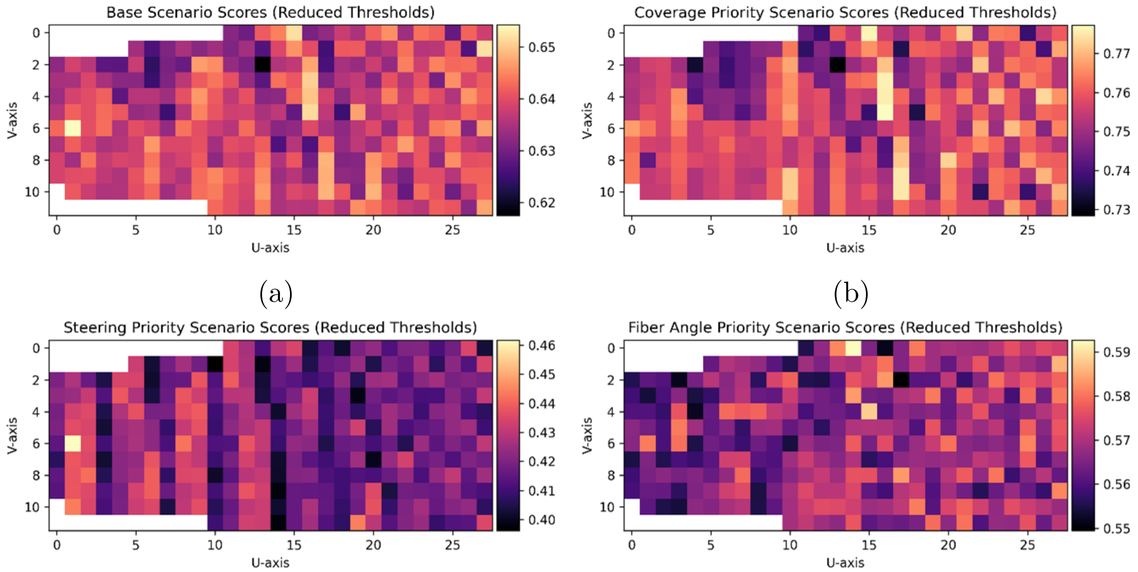

(a) (b)

(c) (d)

Figure 3.7 Various ply scoring priorities with tighter thresholds

best. However, for the second set of thresholds, fewer of the defects were tolerated, thus impacting the overall scenario scores, resulting in a range of scores from 0.4-0.78. The reduction in scores observed as more restrictive thresholds are implemented supports the primary ply scoring system for the instance and severity scores.

However, an interesting phenomenon does present itself through the relative distribution of scores which is only minimally impacted by the thresholds applied. Particularly for the coverage and steering priority-based scores, the scenario scores are periodic along the length of the tool surface. These distributions roughly match the gap and overlap distribution observed over the part (figure 3.8a) that lie parallel to the fiber directions generated for the plies. Regarding the coverage score periodicity, the likely source is the course efficiency, or how many full and partial courses have been utilized to populate the ply.

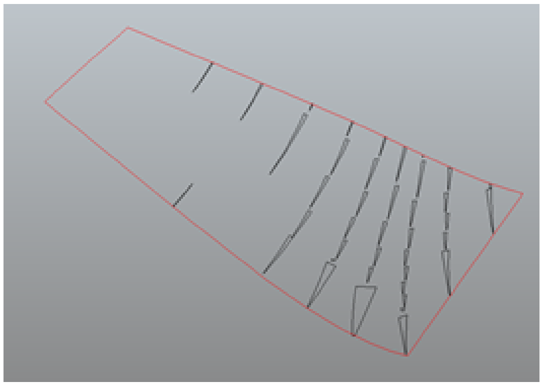

(a) Overlap distribution

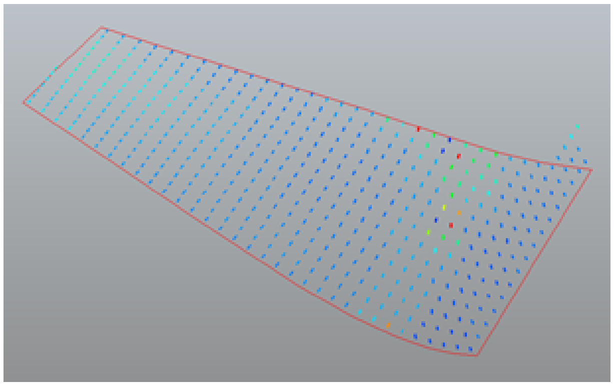

(b) Fiber steering distribution

Figure 3.8 AMES blade defects

The steering coverage periodicity has developed due to the region of high surface curvature (figure 3.8b). Depending on the offset of the course centerline from the starting point, the course will interact differently with the high curvature region. The course can potentially follow the trough, minimizing fiber steering, or may be forced to traverse it, such that fiber steering is necessary to ensure coverage through the highly curved region.

3.4 Summary

The methods set forth in this chapter enable the identification of fiber defects and quantification of ply scenarios. This quantification was a function of both the resultant geometrical defects from the layup process and the rankings set by the process planner. The geometrical defects were measured as functions of their instances and severity, where the combinations of both these measures were meant to summarize the extent of the defects. These measurements were combined with the one-to-one ranking process enabled by the AHP and resulted in single normalized scores for each ply scenario. The starting point optimization was performed by considering the distribution scores from the previous iteration.

Additionally, an investigation into the distribution of ply scores over the domain of the tool surface was performed via a high degree of starting point sampling. Understanding the distribution enables selection of an appropriate optimization method to maximize the quality of generated plies while reducing the number of necessary ply scenarios to process.

Chapter 4

Computer Aided Process Planning Software

The goal of the Computer Aided Processes Planning (CAPP) software is to implement and appropriately automate the process planning functions identified in the down selection process presented in [61]. The following chapter discusses the creation of the CAPP software and how it aids in the rapid prototyping design phase of composite laminates along with the ply level optimization to reduce geometry related fiber defects. The methods laid out will ultimately help find the ideal starting points and layup strategies to reduce the fiber defects.

The CAPP software is broken down into three major functions. First, the software helps to create several ply scenarios by locating starting points with potential layup strategies and presents the resulting geometrical fiber defect instance and severity measurements. The second portion allows the process planner to define the relative importance of defect types in order to create an overall ranking of the defect set that is used for the ply level optimization. The final function presents final scores for each ply scenario and organizes them by starting point and the chosen layup strategy. These scores can be used to decide if a satisfactory solution has been reached or if additional iterations should be performed. Minimizing the ply's overall score, or objective function, indicates that a solution has been reached which adequately minimizes the prioritized defect types.

Before continuing into the description of the CAPP itself, it is important to discuss how the CAPP module has been integrated into a higher-level workflow for the reduction of fiber defects and their impact on a laminate's structural properties. The following section describes the inter-software communication that occurs to achieve this overall laminate optimization of which the CAPP is a part of.

4.1 Inter-Software Communication

The purpose of inter—software communication is to leverage well developed functionality that is contained within pre-existing tools. Utilizing these other tools enables abstraction and new functionality of their methods. The CAPP software takes a similar approach, utilizing several other software solutions, namely Collier Research's Central Optimizer (CO) and CGTech's Vericut Composite Programming (VCP). The flow of communication is presented in figure 4.1.

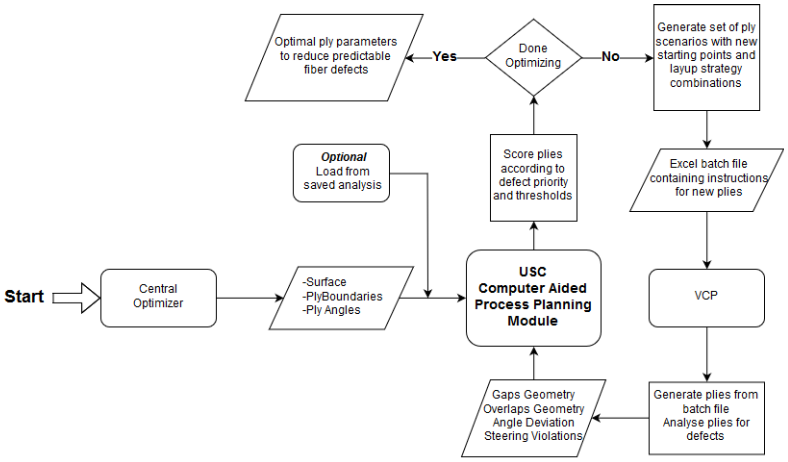

Figure 4.1 Software flow diagram

The flow diagram presents the CAPP's relationship with the other software and which types of data are shared during each step to achieve the laminate optimization. The process begins with the CO, which passes the basic laminate definitions to the CAPP. These laminate definitions contain the tool surface on which the laminate will be constructed as well as the ply boundary and ply angles that define each individual ply in that laminate. The CAPP takes this laminate definition and constructs and enters the ply level optimization loop with VCP. Here, different laminates are iterated upon to minimize the prioritized defects. VCP enables this iteration by building the geometry of the ply scenarios supplied by the CAPP and identifying the resulting geometric defects. After a sufficiently optimized laminate has been generated, the process planning results can be used to continue the laminate design phase.

The remaining sections of this present the software interface and explain the CAPP's own software workflow. The goal is to gain a better understanding of the CAPP module, and how it can incorporate the optimization previously definer optimization schemes in order to benefit the laminate design process.

4.2 Software Interface Overview

The CAPP software is a standalone package that can opened to the following interface presented in figure 4.2. The individual portions of the software are presented and described in the following sections in the order that typical user would interact with them.

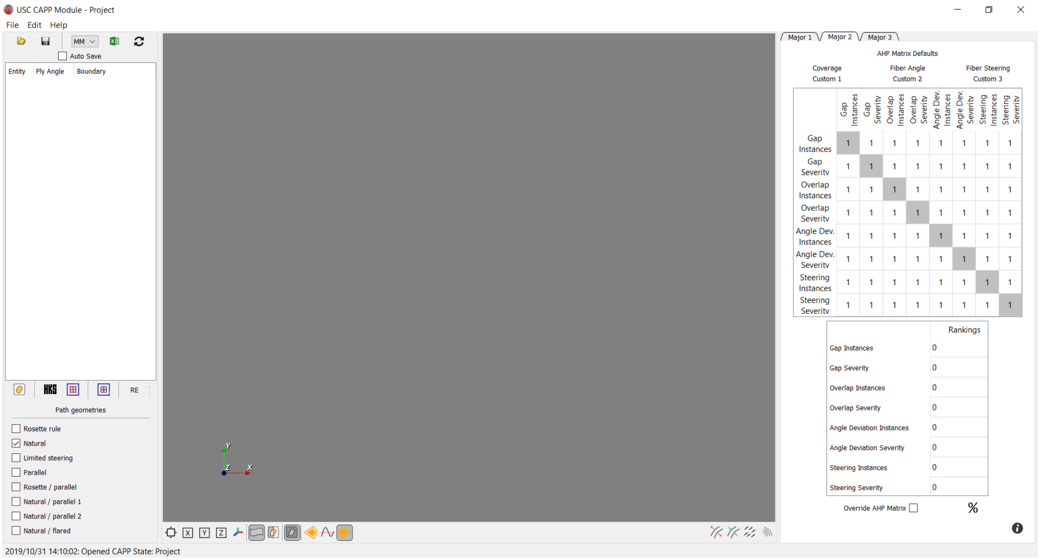

☐ Auto Save

AHP Matrix Defaults

Coverage Custom 1 | Fiber Angle Custom 2 | Fiber Steering Custom 3

	Gap Instances	Gap Severity	Overlap Instances	Overlap Severity	Angle Dev. Instances	Angle Dev. Severity	Steering Instances	Steering Severity
Gap Instances	1	1	1	1	1	1	1	1
Gap Severitv	1	1	1	1	1	1	1	1
Overlap Instances	1	1	1	1	1	1	1	1
Overlap Severitv	1	1	1	1	1	1	1	1
Angle Dev. Instances	1	1	1	1	1	1	1	1
Angle Dev. Severitv	1	1	1	1	1	1	1	1
Steering Instances	1	1	1	1	1	1	1	1
Steering Severitv	1	1	1	1	1	1	1	1

	Rankings
Gap Instances	0
Gap Severity	0
Overlap Instances	0
Overlap Severity	0
Angle Deviation Instances	0
Angle Deviation Severity	0
Steering Instances	0
Steering Severity	0

Override AHP Matrix ☐ %

Path geometries

☐ Rosette rule
☑ Natural
☐ Limited steering
☐ Parallel
☐ Rosette / parallel
☐ Natural / parallel 1
☐ Natural / parallel 2
☐ Natural / flared

2019/10/31 14:10:02: Opened CAPP State: Project

Figure 4.2 CAPP Opening Screen Snapshot

As stated previously, the CAPP module begins by opening a laminate definition and a surface path that have been defined by the CO. The interface looks like the one presented in figure 4.3a. The structure of the laminate can be observed in figure 4.3b, where each ply, its ply angle, boundary name, and its various ply scenarios are organized.

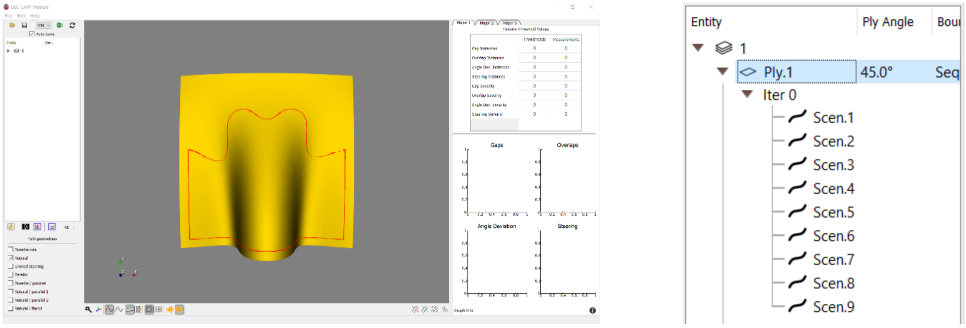

(a) Populated CAPP interface

(b) CAPP laminate tree

Figure 4.3 CAPP interface and laminate tree

The initial state for optimization is created through the interface featured in figure 4.4. This set of functionality performs the surface splitting, HKS computation, and surface center point discovery for each ply contained in the laminate. In the same toolbar, there is also the option to create the next iteration and refresh the viewer. This process can also be done individually by right-clicking any of the plies.

These buttons create the data necessary for the generation of the initial VCP batch file for layup simulation and defect identification. The tool bar in figure 4.5 contains the functionality for generation of the VCP file creation and allows the use of batch templates. This also features the button for importing the output of the VCP analysis.

4.3 CREATION AND PROCESSING OF PLY SCENARIOS

The CAPP's initial function is to find the starting points for different tools and boundaries and then export these to the Vericut Composites Program (VCP) software. Finding the correct starting point is a critical function of process planning. Finding the correct starting point can be a tedious and challenging task that benefits greatly from automation. To help reduce the time for this task the CAPP module

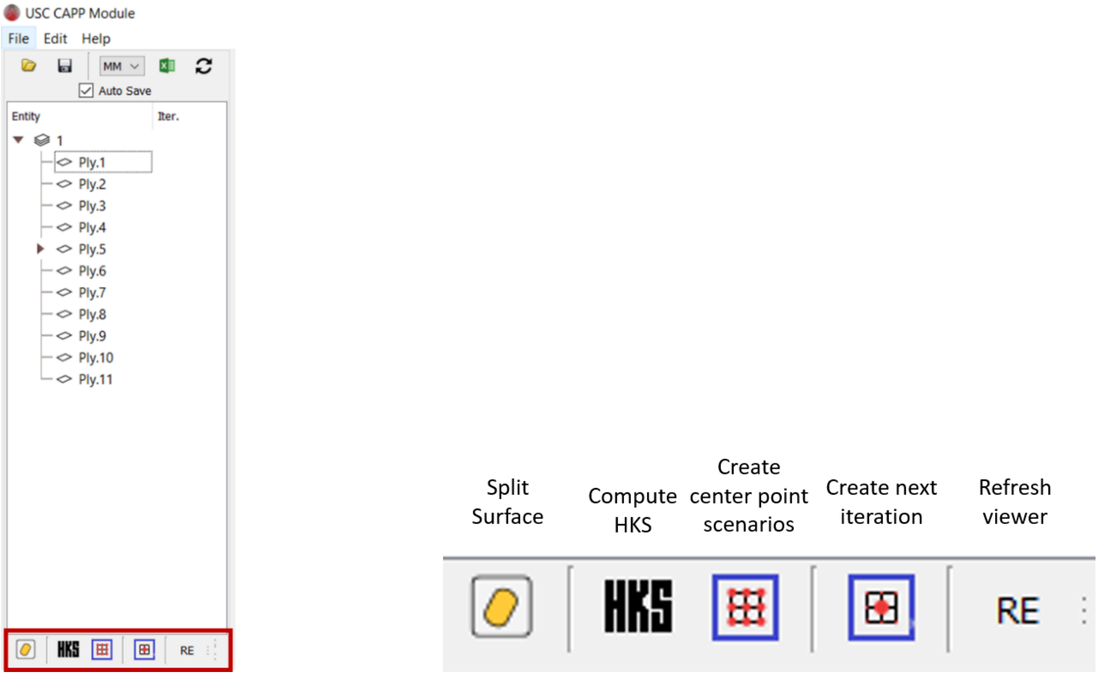

(a) Laminate tree overview

(b) Laminate tree processing operations

Figure 4.4 CAPP laminate tree

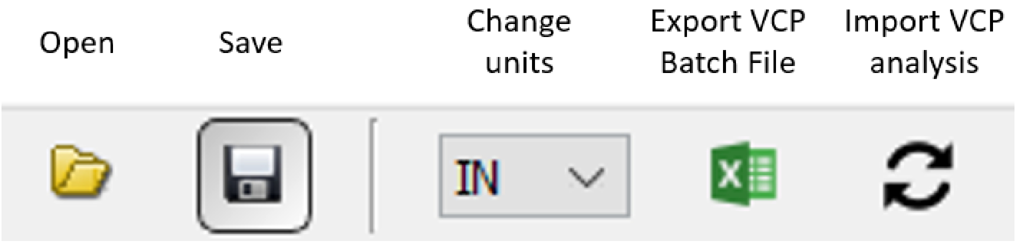

Figure 4.5 File options toolbar

finds an array of starting points for each ply. The following section discusses how the starting points are located. The CAPP module takes in a Catia Laminate consisting of a laminate definition and surface path. This sets up the ply boundaries and tool surface as seen below in figure 4.6.

The starting points can now be identified for all the plies that create the laminate. The CAPP module performs the following three steps in order to identify the starting points: Splits the surface at the ply boundary so only the area inside the surface is worked on; finds the Heat Kernel Signature (HKS) on the area inside the ply

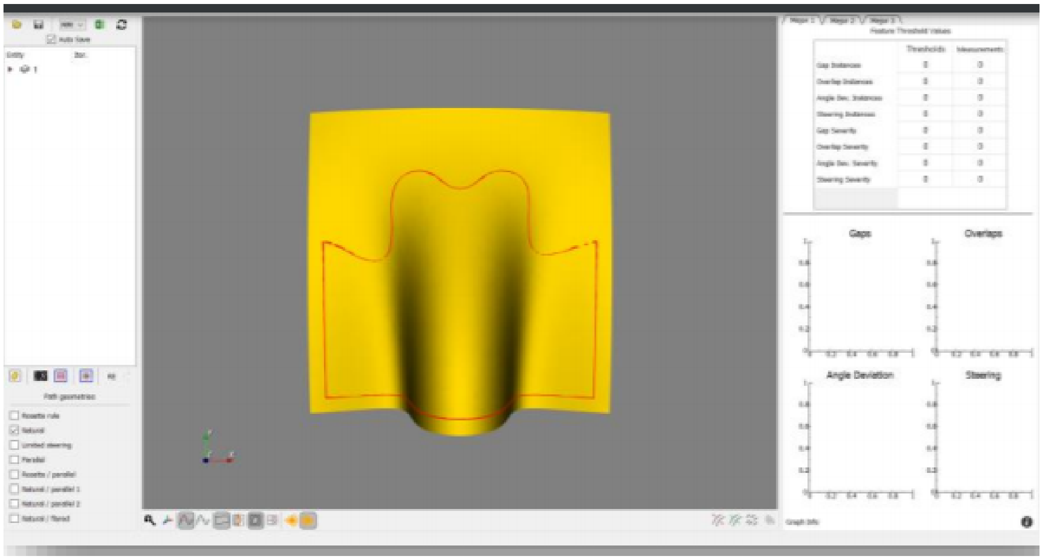

Figure 4.6 CAPP module import; surface and ply boundary (red)

boundary; create an array of starting points where the HKS is the “hottest”. The HKS simulates the application of heat to a part, and observes which regions dissipate the least amount of the applied energy [62]. Typically, these least conductive regions will correspond to central areas of the tool surface, where effective starting points can be generated.

The process is simple but greatly reduces the time it takes for process planners to find starting points. With three clicks, the starting points for all the plies can be generated. The following contains a detailed explanation of each of these steps.

In step 1, the software locates the ply boundary and isolates the surface inside as in figure 4.7a. This is important so that HKS calculations occur in the correct area and the starting points for the specific ply being worked on are found.

In step 2, the software performs an HKS calculation on the part. The results of an HKS calculation can be seen in figure 4.7b.

The final step creates an array of starting points at the “hottest” part of the tool as indicated by the HKS results, figure 4.8. An array of 9 potential starting points is placed on the part. Having an array of starting points will help create iterations later to find the best possible starting point.

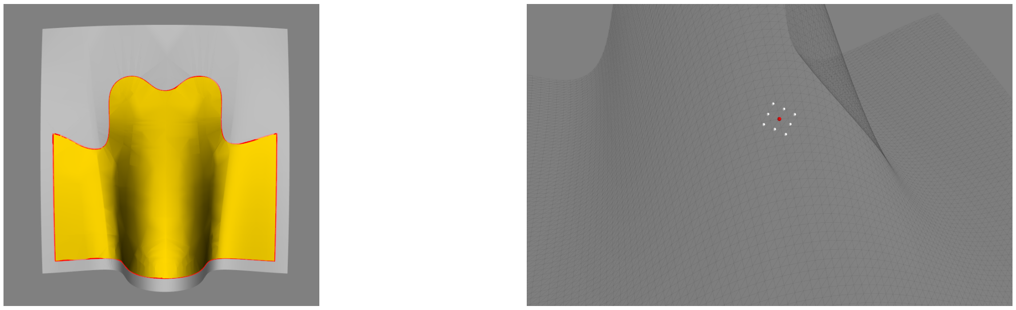
(a) Split Surface (b) Heat Kernel Signature Result

Figure 4.7 Surface preparation

Each starting point will have a specific layup strategy associated with it. These layup strategies are created in VCP and use the principles set out in Chapter 2. The process planner will have the option of choosing which layup strategy they want each time they create a starting point array.

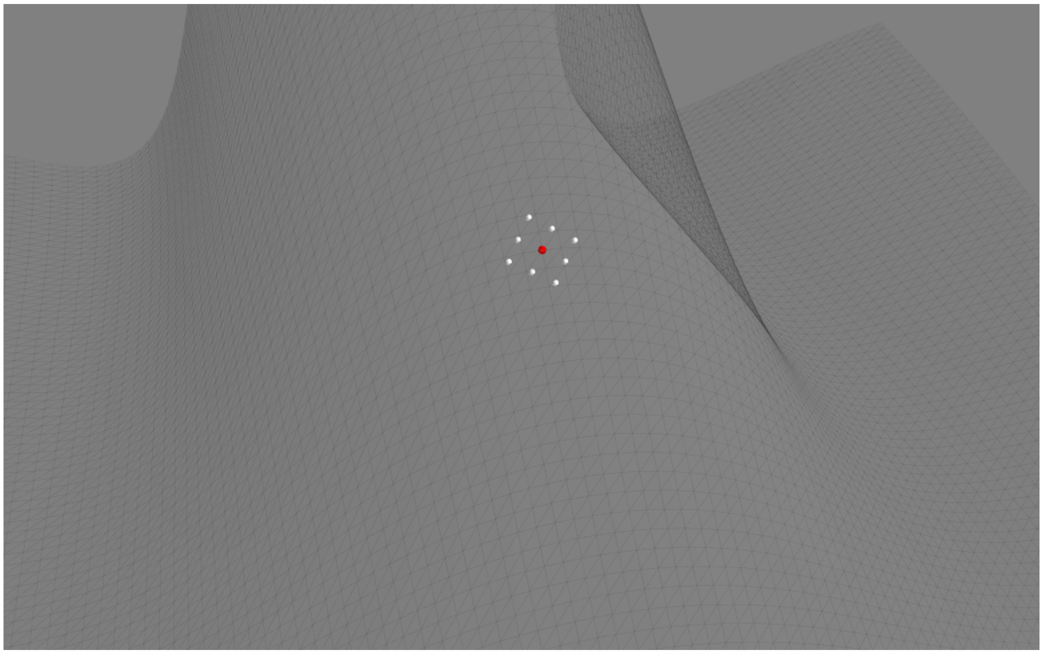
Figure 4.8 Central Starting point and resulting grid

Once these ply scenarios have been generated through this portion of the interface, VCP batch processing can be utilized to generate the appropriate ply and defect data.

4.4 SUMMARY

The CAPP Software integrates many of the previously discussed defects and layup strategies to allow the process planner to seamlessly find the best starting points and layup strategies. After the initial setup in the CAPP software, the process planner can save hours of time that would be spent guessing and checking to find the best starting point. The defects are easily laid out before them, and the graphs and charts intuitively display the information and rankings. By using multiple iterations, the process planner can pinpoint the best starting point on the layup.

Additionally, the CAPP software has been developed with the intention of developing new modules to handle additional defect and optimization strategies. The remaining chapters present the recent work that has been performed within the CAPP environment and present the flexibility of CAPP as a general process planning platform.

Chapter 5

Experimental Validation of Defect Predictions

Due to the increased performance and reliability of the AFP process, it has been rapidly advancing towards use on increasingly complex structures. However, these complex structures bring about their own issues, the resulting unavoidable defects that originate from both the fundamental interaction of fiber paths with these complex parts, and increased complexity of selecting process parameters. These consequences can have adverse effects on the local and global laminate properties through the formation of fiber defects presented through the literature review. Recent research has included predictions on the occurrence of these defects. The predictions on the occurrence of these defects allows for optimization of the fiber path generation and manufacturing processes in order to minimize defects. Although the predictions are considered to be adequate, it is rare that they are validated with the actual manufacturing results.

This chapter presents a comparison between the predictions and simulations to real-world manufacturing results to examine their accuracy and validity leading to more integrated predictive capabilities. This is accomplished with the Computer Aided Process Planning (CAPP) software. The software is used to perform process planning on a doubly curved tool to create tool paths and extract the predicted defects. Inspection results of the manufactured plies are then imported for comparison between predicted and actual defects.

The benefits of such integrated predictive capabilities will arise after multiple manufacturing trials, where virtual optimization of defects provides an initial "best" ply structure. Any defects remaining after the initial optimization can be correlated to those during the real-world manufacturing. The presence of additional defects relating to process parameters can be highlighted by filtering out those predicted through the model. Through repeated trials, a better understanding of the direct effects of process parameters on ply quality for a given setup can be developed. Eventually, a virtual model of process parameters could be developed using such empirical data to further speed the development of future optimized composite parts.

5.1 Tool Surface Selection

A sufficiently complex tool surface (figure 5.1) with a region of double curvature was selected to ensure the generation of defects for further analysis. Path planning was performed to generate a manufacturing program which consisted of 8-tow courses of 6.35mm pre-impregnated thermoset composite material. From the path planning, predictions were made for the existence and location of the primary defects, gaps, and overlaps. The fiber paths were then post-processed to include the necessary processing parameters to transition to manufacturing. The automated inspection was performed upon the completion of each ply, before continuing manufacturing.

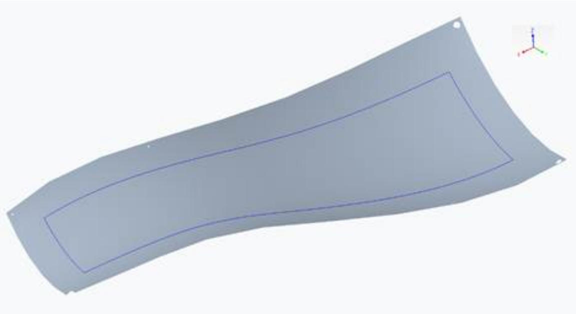

Figure 5.1 Complex tool surface

These steps are not novel on their own, however they have been combined into a rapid toolchain that is contained within a single environment. This allows for data gathering throughout the AFP process (design, process planning, manufacturing, inspection). Each step comes with its own information which is then combined into a dataset that is usable across multiple process domains. This data accumulation methodology has resulted in the ability to directly compare predicted and as-manufactured defects.

5.2 Defect Predictions

The prediction of tow gaps, overlaps, angle deviations, and steering was performed with CGTech's Vercicut Composite Programming (VCP) tool, which indicated the existence and location of the defects within the individual plies [63]. VCP is initially provided with the general laminate specifications to begin computing the fiber coverage. The laminate specifications indicated the extent of material coverage and primary fiber orientation for each ply. During the fiber coverage computation within each of the designated plies, the specific course paths were defined which were consistent with the fiber orientation and layup strategy.

Layup strategies are key to planning fiber placement for complex surfaces, as they control individual fiber paths according to specific relationships between the surface geometry and previous fiber paths. A variety of layup strategies exist for different use cases, such as ensuring consistent fiber angle (rosette), managing fiber curvature (natural), or ensuring consistent alignment between neighboring courses (parallel) [60]. The course paths were the primary result of process planning, which are used along with machine processing parameters to create the final manufacturing program. However, the computed paths can be used to virtually reproduce the fiber placement and resulting geometry of the individual tows.

The calculation of defects directly follows the virtual reproduction of tow paths. The geometry of tows was utilized to compute the area of defects; gaps and overlaps (figure 5.2). It is important to note that gaps and overlaps were only computed between neighboring courses and not between tows within each course. The placement

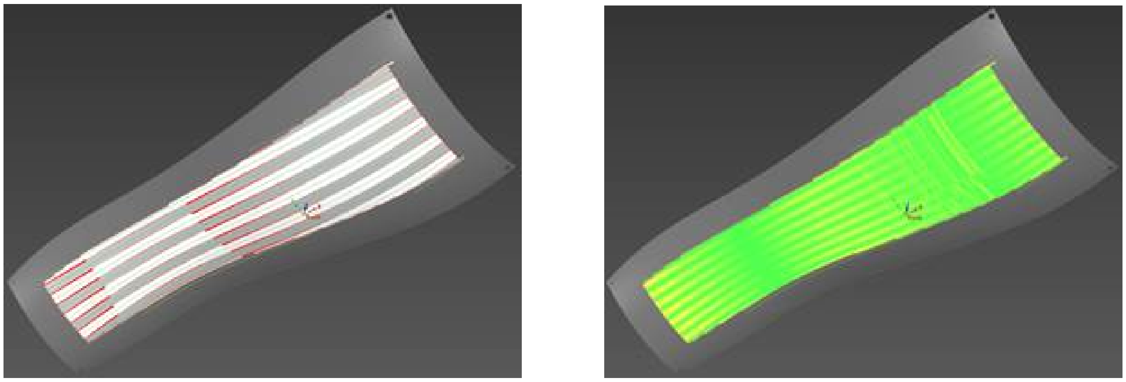

(a) Overlaps (red)

(b) Angle Deviation (Green (0°) -> Yellow (3°))

Figure 5.2 Results of VCP defect analysis

simulation did not include any draping or deformation of the tows that would occur during actual fiber placement, which would be necessary for the prediction of tow-to-tow interactions within courses. The resulting course to course overlaps were exported from VCP as a STEP files defining each gap and overlap instance as a unique closed surface.

5.3 Inspection: Defect Identification and Classification

Inspection of the AFP manufactured structure was accomplished through the interfacing of custom defect identification tools with the IMT developed Advanced Composite Structures Inspection System (ACSIS) [64]. ACSIS performs a ply-by-ply inspection system consisting of a Kuka KR120 robotic arm actuating 4 laser profilometers. Through the profilometry data, height profiles of the scanned surface can be created, compressing height data to create a greyscale image that can be further processed by automated detection software. After layup, the mandrel rotates the ply so that it is exposed to the ACSIS scanners. ACSIS then scans the part and processes the data as the mandrel rotates back into position for the deposition of a new ply.

ACSIS is provided with a complete software suite of defect identification tools, with the current automated detection tools for ACSIS providing patches of image that are classified as a defect or no defect. To provide more accurate defect representations, allowing for exact size and shape data to be extracted from layup scans, a custom data analysis tool was developed to aid in the inspection process. This computer vision tool is constructed from a convolutional neural network performing a semantic image segmentation task. The predicted defect pixels are then extracted and enveloped by a bounding polygon generated by the marching squares algorithm. This polygon and its respective vertices become the basis for defect representation throughout the rest of the inspection process. This tool was built on previous defect detection software developed at the McNair Center. The software has the capability to automatically label individual pixels in an image as a given defect class, allowing for significantly more refined representation.

In addition to a more refined defect representation, the inspection software also has the capability to intake ACSIS toolpath data and reconstruct the trajectory of the scanners during inspection. Incorporating this data with the defect representations and tool geometry allow for mapping of the defects in scan images back to their original locations on the tool. The final mapping reconstructs an almost exact match to the size, shape, and location of the original defect within the tool coordinate system (figure 5.3).

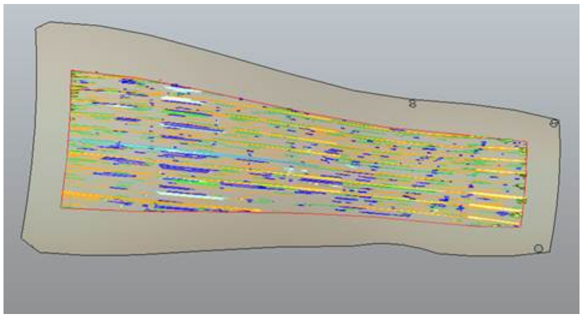

Figure 5.3 Defects identified through ACSIS inspection

This detection and classification method has the ability to separate defects into 16 categories. Table 5.1 below list each of these types with an associated ID and red,

Table 5.1 List of defect types, IDs, and colors

Type	**ID**	**R**	**G**	**B**	**Color**
No Defect	0	0	0	0	⬛
Twist	1	136	0	27	🟥
Fold	2	247	249	165	🟨
Missing Tow	3	0	168	243	🟦
Gap	4	14	209	69	🟩
Overlap	5	255	157	0	🟧
Wrinkle	6	4	0	255	🟦
FOD	7	255	0	255	🟪
Surface Separation	8	153	153	102	🟫
Loose Tow End	9	51	102	0	🟩
Pucker	10	13	255	0	🟩
Bridging	11	140	255	251	🟦
Shredders	12	142	137	143	▨
Position Error	13	204	153	0	🟨
Boundary Coverage	14	221	162	234	🟪
Splice	15	236	28	36	🟥

green, blue (RGB) color. These IDs and colors combined with the defect shapes are used to communicate the as-manufactured defect data for visualization and comparisons.

5.4 Incoporating Inspection Results

Both the defect predictions and inspection results are returned as boundaries and faces along the tool surface. In this format, comparison is difficult to accomplish programmatically due to the small size or high aspect ratio of some of the defects. This is remedied through a coordinate transformation from cartesian space to parametric u/v space (pixels system) as shown in figure 5.4. This transformation is done with the following steps:

1. An empty high-resolution array of pixels is created with the array's size being dependent on the maximum u and v parameters of the tool surface.

2. The boundary of individual defects are projected onto the surface to be represented in u/v space.

3. The projected boundaries are discretized into high fidelity polygons and filled with its associated color (table 5.1) to produce the defect area in the pixel array.

4. Step 2 is repeated for each defect present in the current ply.

5. The final array of color pixels is then saved as a PNG file for later use.

6. Steps 1–5 are repeated for each defect type for predicted and as-manufactured defects.

The representation of the defects through the pixel system facilitates faster and more accurate computation of boolean operations between different defect sources and surface areas resulting from those operations.

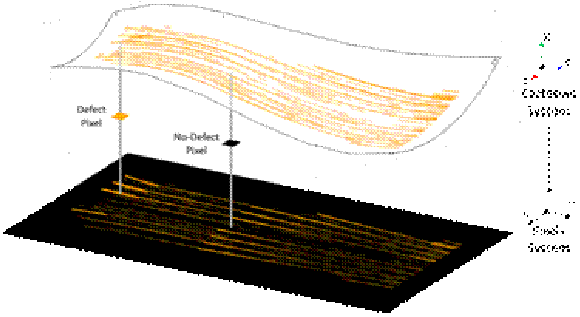

Figure 5.4 Mapping of tool surface defects

5.5 LAYUP AND DATA COLLECTION

For experimentation, a zero-degree ply angle was used with the ply boundary and starting point shown in figure 5.5a, combined with a Rosette Rule layup strategy. This information was then used to manufacture the zero-degree ply figure 5.5b. The following sections details the data collected from both the defect predictions and the inspection results.

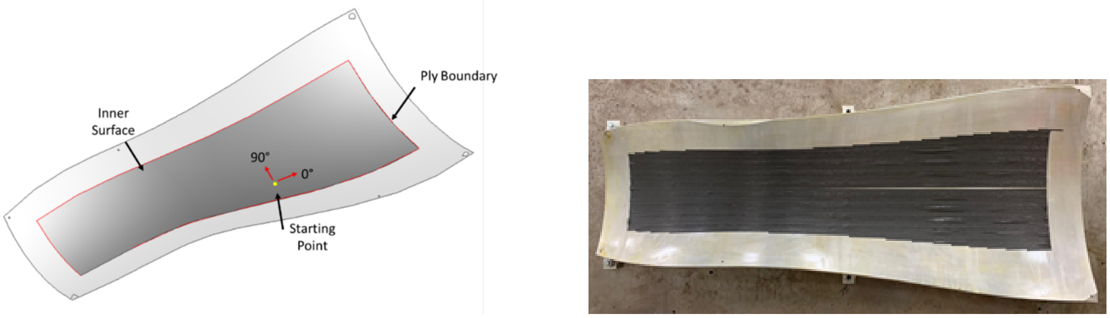

(a) Description of process planning information

(b) Resulting manufactured 0° ply

Figure 5.5 Tool surface fiber definitions

5.5.1 Defect Predictions

The zero-degree ply was processed through VCP to generate the defect predictions. A total of 8 tows were utilized for each course to match the manufacturing capabilities. The maximum course to course gap was set to 0mm and a maximum overlap of 6.35mm (one tow width). These settings ensured the presence of material overlap while preventing gaps. Those settings enabled the comparison of predictions and inspection for overlaps, while ensuring the present of any gaps would occur as a result of manufacturing processes and would only be detected by the inspection. Following generation of the course paths and individual tow geometry, the defect analysis was performed for gaps, overlaps, and angle deviation.

No tow gaps were detected during the defect analysis. However, tow overlaps and angle deviation were detected extensively through the divergent regions of the tool surface. The overlaps (figure 5.2a) depicted in red, exist between the neighboring courses, alternatingly depicted in white and gray. Fiber angle deviations (figure 5.2b) are depicted on a continuous spectrum, where green represents little to no deviation, while yellow represents 3–4° of fiber angle deviation. The defects were then converted to the discretized pixel representation for further investigation (figure 5.4).

5.5.2 Inspection

Following the placement of the zero-degree ply, the ACSIS profilometry inspection was performed. Through the inspection process a total of 8 defect types were extracted (missing tow, gap, overlap, pucker, wrinkle, surface separation, loose tow, and bridging).

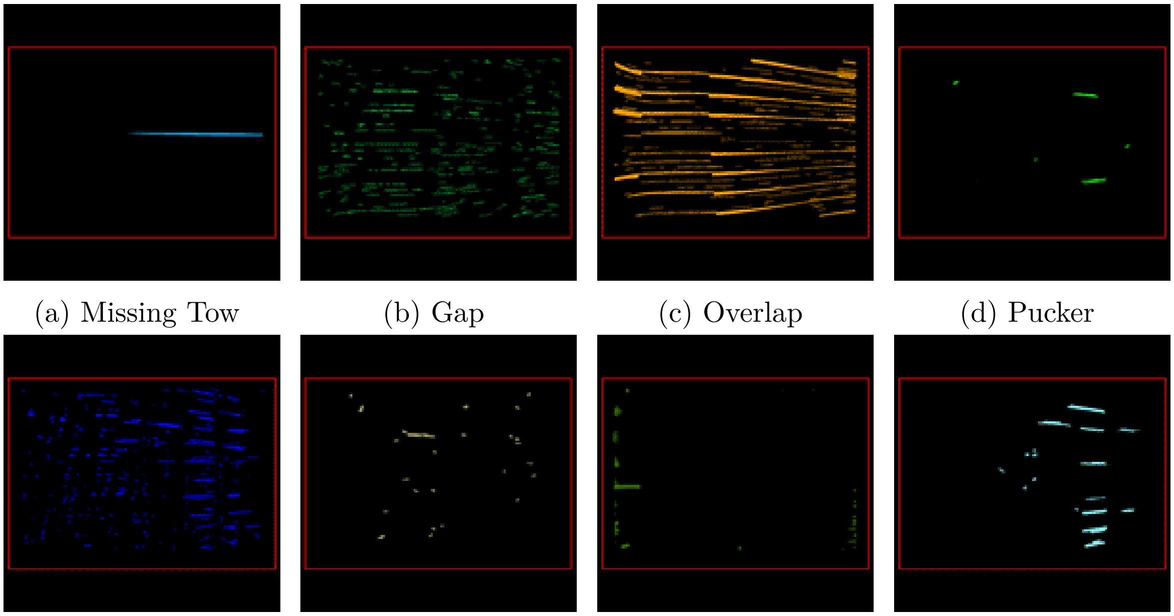
(a) Missing Tow (b) Gap (c) Overlap (d) Pucker

(e) Wrinkle (f) Surface Separation (g) Loose Tow (h) Bridging

Figure 5.6 Images of the pixelated defects of each type found during processing of inspection data

The inspection was programmed to replicate the manufacturing motion in order to scan the individual courses. The profilometry data was then stitched together to generate a unified scan of the ply to finally generate the labeled defect data. These defects were referenced back to the tool surface and then pixelated, using the previously defined method, resulting in the images in figure 5.6.

5.6 Defect Comparison and Validation

The comparison of the predicted and detected defects were performed using the pixelated data generated through the methods outlined previously. The projections

Table 5.2 Comparisons of overlap defect areas

	Predicted	**Actual**	**Error**
Area	55001.6 mm^2	67717.9 mm^2	18.8%

mapped the defects back to the individual faces of the CAD model, since the tool surface utilized only had a single face, only a single discretization was necessary.

The comparison of the predicted and actual overlaps is presented in figure 5.7. The predicted overlaps (red) correspond to the edge of neighboring courses, whereas the actual overlaps (blue) were measured over the entire ply and thus detected overlaps between tows within individual courses as well as the overlaps between courses. It is important to note that the prediction of gaps and overlaps were limited to simple geometric models, whereas prediction of tow-tow interactions may require more detailed models to account for tow deformation over the tool surface during placement.

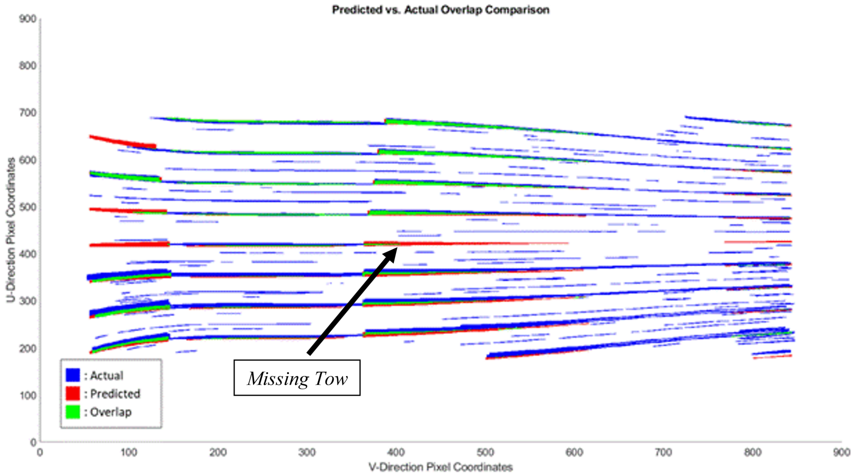

Figure 5.7 Comparisons of predicted and actual overlaps

Another plausible reason for mismatch between the predicted and measured overlaps is the development of other types of defects in that region during manufacturing and their capture and labeling under another type of defect during inspection. For instance, the occurrence of a missing tow where a gap was predicted to occur can result in such discrepancy. The same applies to out-of-plane defects such as puckers, wrinkles, surface separation, and bridging, where a "designed" overlap could possibly act as an instigator for such defects. As a result of this difference in capabilities between prediction and actual inspection, the actual overlap area was approximately 23% greater than the predicted area (Table 5.2).

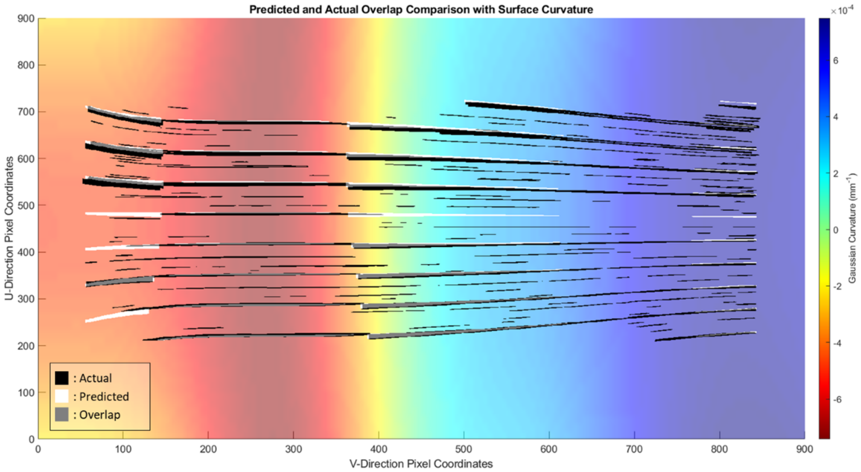

Figure 5.8 Comparisons of predicted and actual overlaps combined with surface curvature

Additionally, the results of the predicted and actual defects were overlaid onto the curvature of the surface (figure 5.8). The extent of the defects closely matches the curvature of the surface, where sets of defects are delineated at the changes of curvature. These results reflect on the modification of tow count and course direction in order to meet the gap and overlap settings that were utilized.

5.7 SUMMARY

This chapter has presented a functional toolchain for the comparison of fiber defects from various sources, focusing on digital predictions and inspection data. The approach relies heavily on the accurate CAD representation of the tool surface, and the ability to digitally capture and predict defects and map them back to the tool surface. The digitized defects can then be discretized according to the tool surface geometry, allowing for further evaluation of the defect capture sources. The experiment focused on the prediction and inspection results for the overlap defect but can be expanded to other defect types relating back to tow geometry which be utilized to predict defects. The ply geometry and overlap predictions were performed with VCP and CAPP, and the subsequently manufactured plies were inspected with ACSIS.

The ability to accurately map and compare defect instances and severity back to the digital tool surface can greatly benefit the overall understanding of fiber defects during manufacturing and process planning. Through the understanding of the fiber defects and their origins, designers can accurately design composite structures around manufacturing capabilities. This can significantly enhance the application of AFP to larger and more complex composite structures and reduce the time from design to manufacturing.

The comparison of defects provides a two-fold benefit, where each defect detection method can be used to augment the other. Simple geometric defect detection provides the ability to identify many problematic defects before any manufacturing occurs and enables modification of ply coverage to correct for those defects. Whereas post manufacturing inspection techniques can identify and classify defects regardless of source but requires an iterative design and manufacturing cycle to eliminate defects induced by the originally planned laminate design. The combination of these two systems could be used to more accurately predict and model defects before they appear during manufacturing trials, and the prediction of defects can be used during the training of defect inspection systems. Additionally, the comparison of defects should expand into more complex defect classes, particularly those which derive from fiber steering [65], which is a necessary process to manufacture the increasing complex structures required by industry.

CHAPTER 6

THROUGH THICKNESS DEFECT STACK-UP

CAPP's existing ply optimization is based on the measurement and scoring of geometry-based defects such as gaps, overlaps, angle deviation, and steering on a per ply-level. This chapters presents laminate level process planning optimization that focuses on mitigating defect stacking through the thickness of the laminate. This is achieved by generating laminate scenarios from combinations of the best ply scenarios and comparing the defects of each ply through the thickness to identify regions where defects are stacking on top of each other. The frequency and severity of stacked defects are then described using a novel scoring system, allowing process planners to craft fiber paths that mitigate the number of geometry-based defects and the compounding effect they have throughout a laminate. The chapter also presents a case study of the laminate optimization technique performed with a doubly curved tool surface to demonstrate the novel scoring system and the resulting minimization of through thickness defect interactions.

6.1 LAMINATE SCENARIO AND DEFECT INTERACTIONS

The initial development of CAPP has been focused on ply-based optimization. However, the interaction of defects between individual plies through the thickness of the laminate presents an additional optimization domain which can further reduce the impact of fiber defects and improve the quality of AFP manufactured structures, the importance of which has been highlighted in the previous section. The remainder of this section presents the terminology which will be used throughout the chapter, the development and functionality of the CAPP's laminate optimization module, and a virtual case study utilizing the new module for the optimization of fiber defects through the thickness of a composite structure.

CAPP optimization begins with a laminate skeleton, which defines ply boundaries and associated fiber angles. These represent the most basic parameters which may be generated through a structural design software for composite structures. Ply scenarios represent different combinations of process planning variables which relate to the generation of individual fiber paths, namely layup strategy and seed point. Evaluation of these ply scenarios is determined by the resulting geometrically predicted fiber defects during the calculation of fiber paths.

Similarly, laminate scenarios are used for the extension of CAPP to full laminate-based defect interaction optimizations. A laminate scenario is a collection of ply scenarios. The ply scenarios carry over starting point location, path geometry, and the subsequent predicted defect geometry. Additionally, the individual ply scores calculated during the ply optimization process can be utilized to create a ply summary score, describing the average quality of the collection of ply scenarios forming the laminate scenario.

The next step is the evaluation of the laminate scenarios as a function of defect interactions from the individual plies. In order to evaluate the quality of a given laminate scenario, the fundamentals of ply scoring are extended to the ply scenario combinations. To quantify the extent of defect interaction, or more plainly defect stacking, the concept of levels are introduced. Level 0 corresponds to the area(s) of the tool surface that sees only one defect through the depth of the laminate. Level 1 corresponds to the area(s) of the surface that have two defects stacked upon each other through the thickness of the laminate. Level 2 is three defects and so on and so forth. Currently, this work looks at the defects for all plies globally and projects them onto the same tool surface. Defects are also compared independently, meaning gaps are compared to gaps and overlaps to overlaps.

6.2 Laminate Scenario Creation

Once the best ply scenarios have been identified, the process planner must combine these to form a full laminate scenario. This is done first by comparing the ply scenarios of the first two plies and choosing the two scenarios with the lowest cumulative stacked gap and overlap area. Then the scenarios from the next ply are compared to the first two chosen ply scenarios. The defects of all three plies are compared through the thickness of the laminate and scored using the metrics described below in section 6.4. The ply scenario from the next ply that contributes to the best overall laminate score is chosen and this process is repeated until a ply scenario has been selected for all plies in the laminate. The creation of the laminate scenario focuses specifically on defect stacking rather than total defect area. This is because it is assumed that total defect area has been optimized in the previous ply optimization step. The final laminate score is a combination of two sub-scores and attempts to describe the overall frequency and severity of defect stacking within the laminate

6.3 Discretization and Identification of Defect Stacking

During the ply optimization process, the course-to-course gap and overlap defects are represented as sets of bounding contours with cartesian coordinates with their locations relative to the 3-dimensional tool surface. In order to detect any interactions between the individual defects in two neighboring plies, even before the actual interaction is computed, each defect must check the nearness of every other defect in the other ply. Therefore, naively for n plies having m defects each, mn comparisons must be performed to even determine which ply defects will interact before the interaction is computed. The problem becomes even more complex with the defects represented in 3-dimensions, where tolerances with the actual representation of the

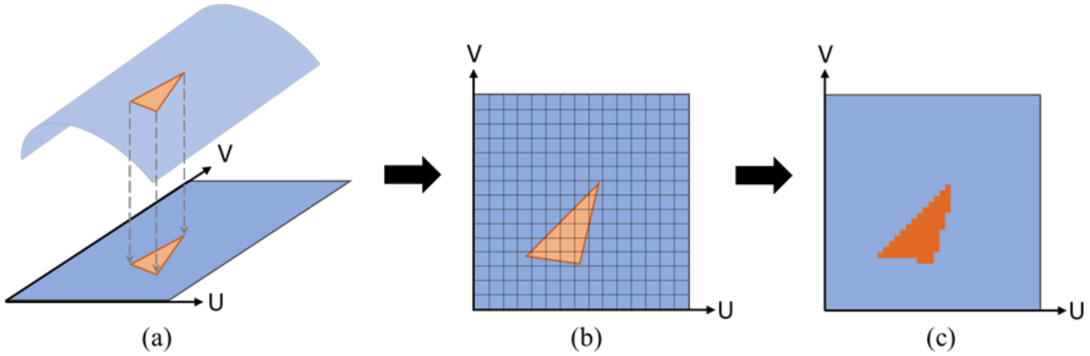

Figure 6.1 Gap and Overlap evaluation with parametric tool surface

defects complicate the interaction calculation. The number of comparisons may be reduced through such algorithms as spatial hashing, but we propose an alternative method which discretizes defects into a common 2-dimensional domain between each ply, so that the comparisons can be performed in parallel for each element in the discretized domain.

The basis for the defect discretization relies on the parametric domain of the tool surface models. The tool surfaces are represented through non-uniform rational b-splines (NURBS), which is a standard mathematical model for representing curves, surfaces, and solids among many computer aided design (CAD) softwares. For these representations, NURBS utilizes a net of control points along with its standard piece-wise polynomial function to evaluate the entity with varying degrees of geometric continuity. For creating 3-dimensional surfaces, it utilizes a 2-to-3dimensional mapping, $S(u, v) \to P_{xyz}$. Additionally, the NURBS mapping can be inverted in order to project 3-dimensional entities back to the 2-dimensional parametrized domain of the surface.

The projection of 3-dimensional entities relative to a NURBS surface, to its parametric domain serves as the foundation for the defect discretization (figure 6.1). The process begins with the cartesian contour representation of the defects, through the use of NURBS curves, creating a closed loop. These are then projected onto the tool

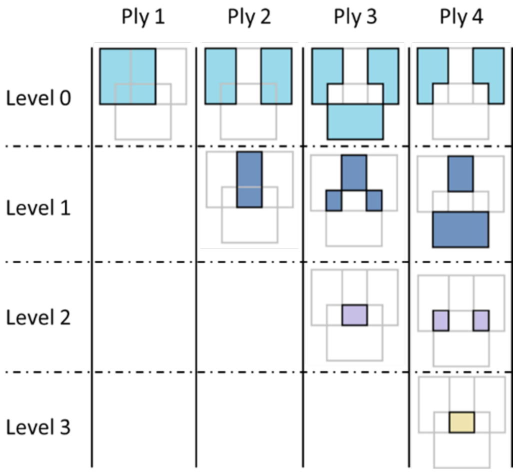

Figure 6.2 Evolution of defect level with increasing ply count

surface obtaining their 2-dimensional representations in the tool surface's parametric domain. The parametric domain is then subdivided into a regular rectangular grid for the discretization step. The area enclosed within the projected defect polygon is then mapped to this rectangular grid. The final discretized defects are represented through the value of individual cells within the grid. With the newly parametrically discretized defects, the evaluation of stacked defects can be performed efficiently for laminate scenarios of varying size.

6.4 Evaluating Defect Stacking

The stacking of defects is considered throughout the entire thickness of the laminate. Such that defects from the any given ply can interact with any another overlapping defects regardless of the through-thickness distance between plies. The computation of defect interactions begins from the base ply and updates the levels of defect interaction as additional plies are considered.

Consider figure 6.2, which describes the evolution of these levels. The colored shapes denote "defect" regions, where each row defines the level of interaction of those defects, and the grayed boundaries identify the next defect region to consider. Each subsequent column introduces the new defect regions and updates the level of interaction appropriately.

All defects of the initial ply are placed into level 0. When incorporating subsequent plies, the common region of defects are elevated by a single level and checked for updated common regions, where they may again be elevated. The defects will be propagated upward through the interaction levels until no more common regions are detected. At which point another set of defects from the next ply can be incorporated, and the levels updated similarly. The result when all defects from the n plies is a set of at most n-1 levels of defect interaction.

The measurement and scoring of stacked defects rely principally on the defect levels. These levels describe the area of each defect type at each degree of stacking, starting at level zero which denotes one defect through the thickness with no stacking and continuing until the highest level of stacking. The max number of levels possible for any given laminate is one minus the total number of plies, this means every ply had a defect stacked through the thickness. The scores include a threshold, which corresponds to the level at which the process planner is concerned about defect stacking. Choosing a threshold requires some judgement, if the part requires tight geometrical constraints a lower threshold may be chosen.

6.4.1 Frequency Score

A metric was created, called the frequency score, to describe the total stacked defect area above the chosen threshold in comparison to the total defect area. Starting at the threshold level, defect level area is summed and then divided by the total levels area. The frequency score, equation 6.1, is shown below.

$$Frequency = 1 - \frac{\sum_{threshold}^{n_{levels}} A_{level}}{\sum_{0}^{n_{levels}} A_{level}} \tag{6.1}$$

The symbol n_{levels} is the total number of defect levels in the laminate and A_{level} is the area of the level. The fraction is subtracted from one so that as the defect area stacked beyond the threshold decreases to zero, the frequency score increases to one. A frequency score of zero denotes the case where all defects are stacked to a level beyond the chosen threshold. If the number of defect levels falls below the threshold, a frequency score of 1 is defaulted.

6.4.2 Severity Score

The severity score is similar to the frequency score in that it compares defect levels above the threshold to total defect level area. However, with this metric laminates with more area further above the threshold are scored lower than those with more area closer to the threshold. The severity score, equation 6.2, is shown below.

$$Severity = 1 - \frac{\sum_{threshold}^{n_{levels}} (Level - Threshold + 1)^2 \cdot A_{level}}{\sum_{0}^{n_{levels}} (Level + 1) \cdot A_{level}} \tag{6.2}$$

The main addition here is the squared term in the numerator which attempts to weight the score by how far it is from the threshold. This is balanced similarly in the denominator of the fraction. The purpose of the severity score is to describe the distribution of the stacked defect area beyond the threshold. Two laminate scenarios could have the same frequency score if they have the same amount of stacked area above the threshold regardless of if that area exists in the level immediately above the threshold or in the highest possible level. This metric helps process planners identify laminate scenarios that have particularly high levels of stacking, even if the area is lesser.

6.5 Laminate Scenario Demonstration

The demonstration tool surface provides a non-trivial geometry for the development of fiber defects. The surface (figure 6.3) measures approximately 1.75m in length and 0.8m at the widest section. It features regions with double curvature which forces the generation of many of the geometrically based fiber defects. The depicted ply

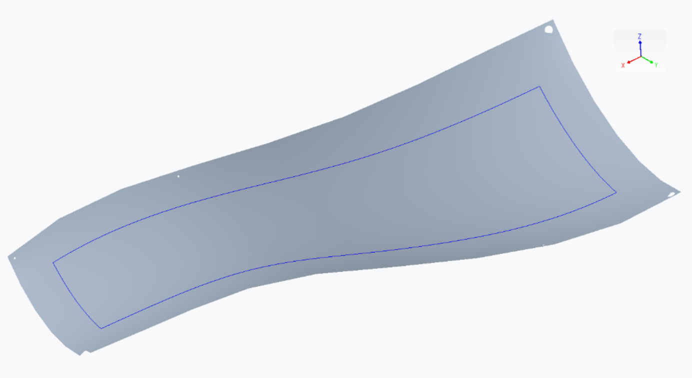

Figure 6.3 Complex tool surface with boundary (blue) and fiber angle rosette

boundary was used for each ply in the laminate, each ply was assigned a random ply angle from [0, ±45, 90], relative x-axis on the depicted rosette, and the layup strategy was chosen from the selection provided by VCP, including Rosette Rule, Natural, Limited Steering, Parallel, Rosette-Parallel, Natural-Parallel 1 & 2, and Natural Flared. Finally, a random seed point was chosen within the ply boundary set on the tool surface.

Utilizing the random ply scenario generation technique laid out, 20 plies were generated, each with an associated fiber angle. From these fiber angle-ply boundary definitions, 5 ply scenarios were generated for each ply with a random layup strategy and seed point. These processes resulting in a total of 100 ply scenarios which were then processed through VCP to generate the fiber paths and to compute the geometrical fiber defects. The courses were generated according to the ply scenario parameters, with 8 individual ¼” (6.35mm) tows. The results of the fiber path generation and ply defect identification were imported to CAPP for further analysis.

With the processed set of plies, multiple laminate scenarios were then generated. Additionally, one set of scenarios only utilized the results from the first 10 plies, whereas the second used all 20 plies for its analysis. The following sections present the results of the defect level calculations on the tool surface and the resulting frequency and severity scores that occur at varying level scoring thresholds. The results focus solely on the formation of through thickness overlap defects.

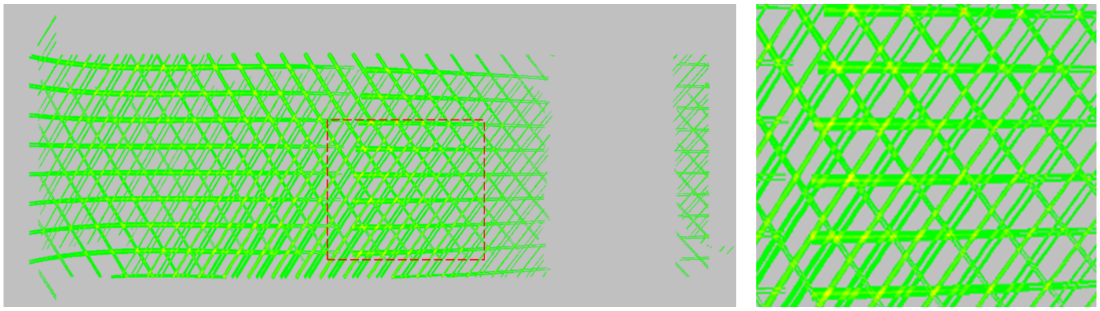
(a) Overlap levels (b) Zoomed in overlap levels

Figure 6.4 Overlap stacking of 10-ply laminate scenario

An example of the level scenarios for a 10-ply laminate scenario are presented in figure 6.4a. Additionally, figure 6.4b presents a focused patch to highlight the stacking of defects that occur between plies. The color map presents independent defects as green, and additional levels of stacking transitions through shades of yellow and finally red. Figure 6.5 presents the mapping of the discretized levels back to the original tool surface and allows for an undistorted view of the defects which occurred during the mapping to the parametric domain.

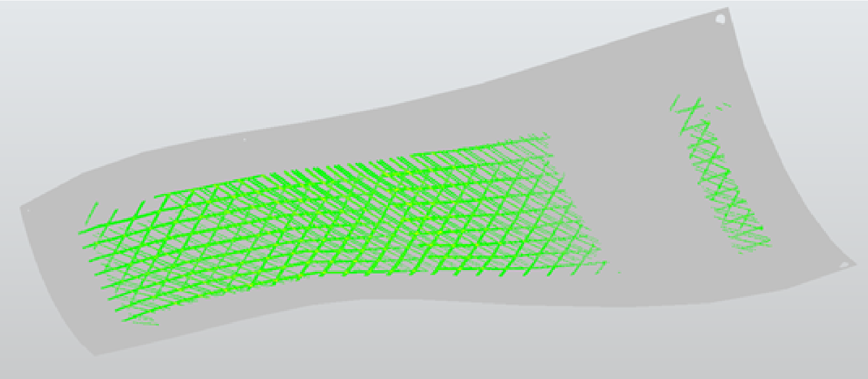
Figure 6.5 Discretized overlap levels mapped back to the tool surface

6.5.1 10 Ply Laminate Scenario Scoring

The following section presents the results from the set of 5 laminate scenarios which contained 10 plies each. Figure 6.6 presents the level value trends for each of the laminate scenarios groups, beginning from level 0, reach at most level 5, such that a total of 6 defects have been stacked at some regions within the laminate.

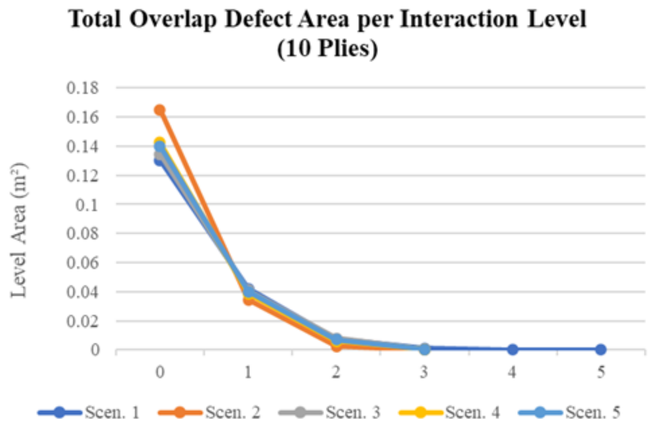

Figure 6.6 10 ply laminate scenario overlap defect level scores

The resulting scores were obtained utilizing the methods outlined in section previously, where various thresholds including level 1, 2 and 3 were applied. The use of increasing thresholds demonstrates the effect of relaxing defect interaction constraints. The scoring results are presented in table 6.1.

Table 6.1 Comparisons of overlap defect areas

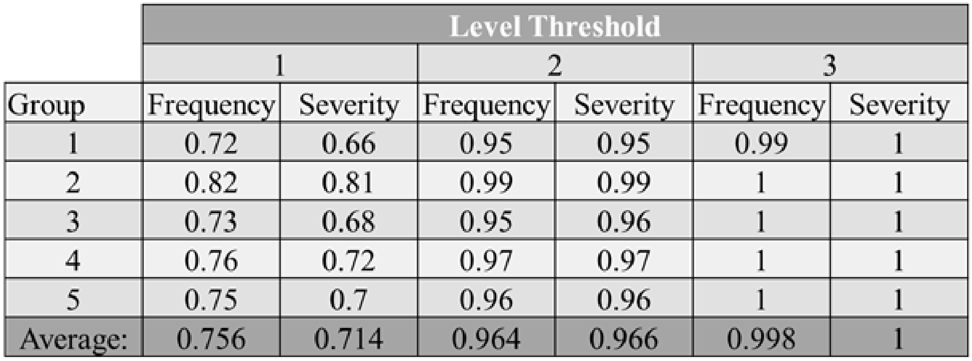

	Level Threshold					
	1		2		3	
Group	Frequency	Severity	Frequency	Severity	Frequency	Severity
1	0.72	0.66	0.95	0.95	0.99	1
2	0.82	0.81	0.99	0.99	1	1
3	0.73	0.68	0.95	0.96	1	1
4	0.76	0.72	0.97	0.97	1	1
5	0.75	0.7	0.96	0.96	1	1
Average:	0.756	0.714	0.964	0.966	0.998	1

Finally, the results of the scoring methods were used to determine the relative best and worst laminate scenario combinations from the group, depicted in figure 6.7.

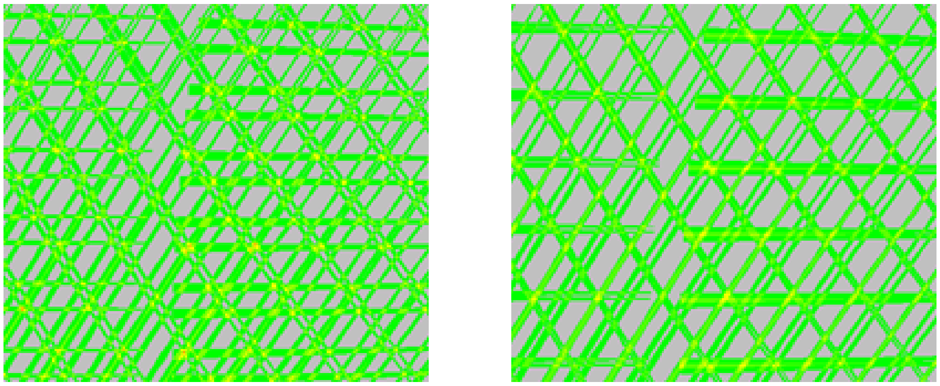

(a) Best average scores (group 2)

(b) Lowest average scores (group 1)

Figure 6.7 Overlap defect levels sample from randomized laminate scenario set

6.5.2 20 Ply Laminate Scenario Scoring

The following section presents the results from the set of 5 laminate scenarios which contained 20 plies each. Figure 6.8 presents the level value trends for each of the laminate scenarios groups, beginning from level 0, reach at most level 5, such that a total of 6 defects have been stacked at some regions within the laminate.

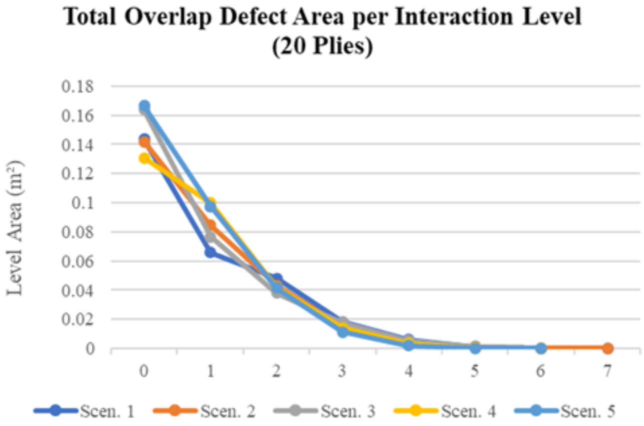

Figure 6.8 20 ply laminate scenario overlap defect level scores

The resulting scores were obtained utilizing the methods outlined previously, where various thresholds including levels 1–5 were applied. The use of increasing thresholds demonstrates the effect of relaxing defect interaction constraints. The scoring results are presented in table 6.2.

Table 6.2 Comparisons of overlap defect areas

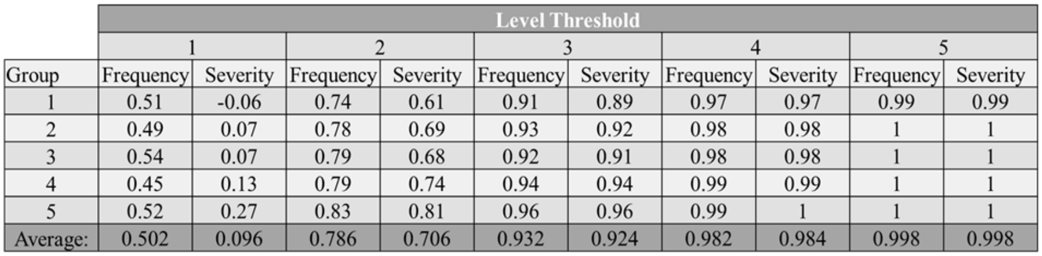

	Level Threshold									
	1		2		3		4		5	
Group	Frequency	Severity	Frequency	Severity	Frequency	Severity	Frequency	Severity	Frequency	Severity
1	0.51	-0.06	0.74	0.61	0.91	0.89	0.97	0.97	0.99	0.99
2	0.49	0.07	0.78	0.69	0.93	0.92	0.98	0.98	1	1
3	0.54	0.07	0.79	0.68	0.92	0.91	0.98	0.98	1	1
4	0.45	0.13	0.79	0.74	0.94	0.94	0.99	0.99	1	1
5	0.52	0.27	0.83	0.81	0.96	0.96	0.99	1	1	1
Average:	0.502	0.096	0.786	0.706	0.932	0.924	0.982	0.984	0.998	0.998

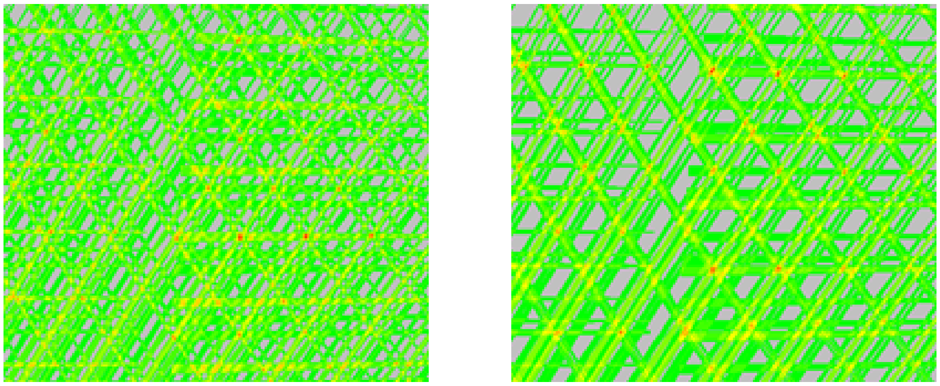

(a) Best average scores (group 4)

(b) Lowest average scores (group 1)

Figure 6.9 Overlap defect levels sample from randomized laminate scenario set

6.6 Summary

This chapter has presented methods for identifying and evaluating defect stacking through the thickness of a laminate. The demonstrations provide insight into the methodologies set forth. These demonstrations focused on the generation of overlap defects and their interactions throughout laminates of varying sizes, namely 10 and 20 plies each. A common ply boundary was held constant for each ply, and a random fiber angle was then assigned. The final set of parameters required for the generation of fiber path generation were randomly assigned to the various ply scenarios. The laminate scenarios utilized for the demonstration were randomly chosen from that set of ply scenarios.

The figures showing the graph of overlap defect level distribution (figure 6.6 & figure 6.8) present an interesting relationship to the final distributions of scores presented through the tables (Table 6.1 & Table 6.2). The groups which exhibit the best (highest) frequency and severity scores exhibit the highest amount of spatial defect spreading, compared to their lowest average scoring scenario of their respective laminate scenario groups. These groups also exhibited lower overall number of levels, indicating reduced defect interaction overlap defects between the plies throughout the laminate.

The spatial defect spreading would account for the reduce levels of interaction, as plies with partially shifted defects had been correctly identified by the frequency and severity scores as having reduce interactions. Ideally, more variation might be observed in the overall distributions of defect areas between the different levels, however, such a scenario would likely be realized once the current scoring techniques become implemented into a proper laminate optimization routine within the CAPP software.

Chapter 7

Defect Data Mapping

The use of various automated inspection technologies during the manufacturing of large scale composite structures provides a great deal of insight to the existence and development of detrimental features. Additionally, many techniques exist for the numerical analysis of processing parameters prior to physical layup of composite materials. In combination, prediction and inspection enable informed iteration on design and processing parameters. However, it is necessary to understand the relationship between these various conditions, and the positioning on the tool surface is a significant driving factor.

The following chapter defines a mapping technique which enables the evaluation of spatial data from many different sources. Through these mapping techniques, a simplified 2d representation of the data relative to the tool surface is created. With the uniform format of the data, further steps can be made to the improvement of fiber paths and processing parameters.

7.1 Tool Surface Meshing

In order to simplify the process of data mapping, the first step involves the generation of a discrete triangular mesh from the tool surface representation. For the case where the tool surface is a continuous spline representation made from multiple patches, particular care must be taken to ensure that that the resuling mesh is correctly associated with the individual patch regions.

GMSH [66] was chosen for this application, due to its superior support for spline

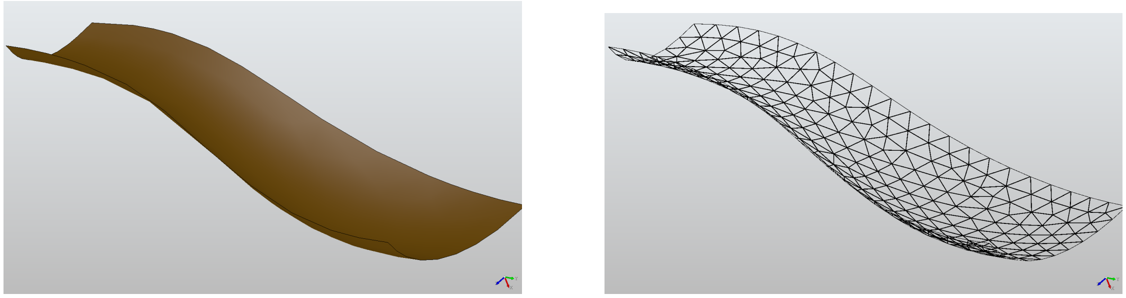

(a) Tool Surface (b) Resulting Mesh

Figure 7.1 GMSH Results for tool surface

entities imported through *.step* and *.iges* file formats. Additionally, GMSH provides a great deal of control through the meshing process, over quality and density of the resulting meshes. Information about the mesh vertices with relation to the original spline representation can also be output during the meshing process. From this, the uv-parameters of the mesh point on the associated spline patch enable connectivity between both the discrete and continuous representations of the tool surface.

7.2 GLOBAL MESH PARAMETERIZATION

In 3-dimensional spline surfaces such as B-Spline and NURBS, a mapping is performed from from a parameterized space (uv) to a 3d form using a set of weightings between given control points. Through this representation, a spline surface of arbitrary complexity can be constructed, while any point on that surface can be dropped into the uniform parameterized space. Conversely, entities can be represented in the parameterized space and evaluated on the surface to obtain their 3-dimensional forms. Thus, the parameter space of splines provide a useful tool for representing the relationship between a complex surface and other associated entities

However, a complication arises when multiple spline patches are utilized for representing objects. For these multiple patch surfaces, the splines will be adjacent and geometrically continuous in their 3d forms, but the individual parameter spaces are not guaranteed to align. As a result, it is no longer a trivial task to drop a 3d entity into the parameter space of a multi-patch surface.

In order to mitigate this issue, global parameterization techniques originating from graphics texturing process can be implemented. These methods rely on a discrete mesh of the tool surface, which will be generated through [66]. Additionally, the association of the mesh points with the individual spline patches are retained, so that points from the global parameterization can be remapped to the individual spline parameterization as necessary.

7.2.1 Least Squares Conformal Mapping

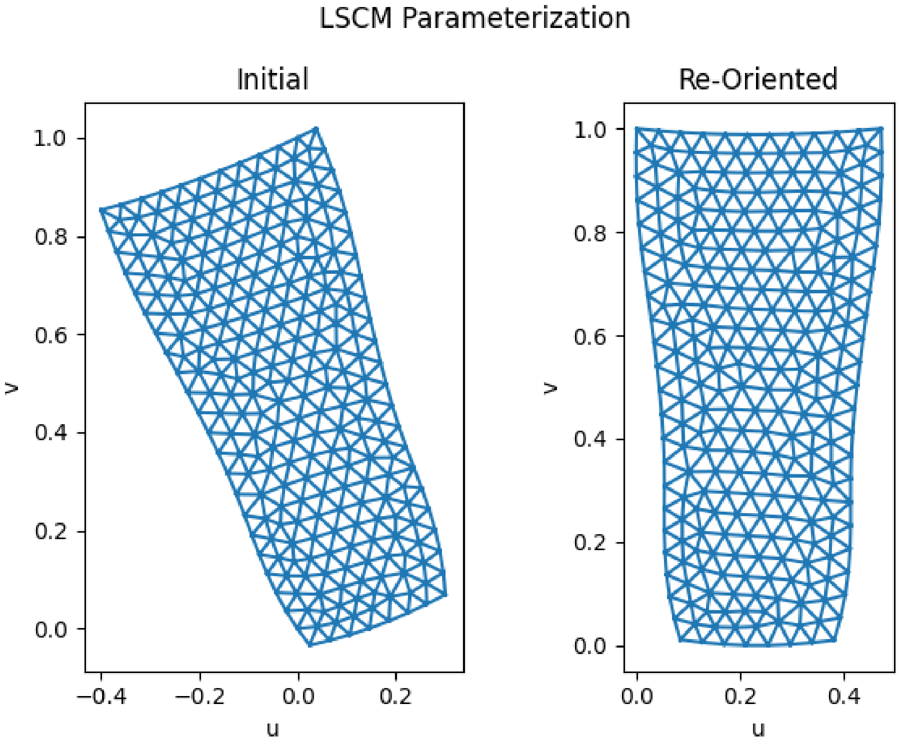

Figure 7.2 LSCM parameterization of tool surface

Lease squares conformal mapping (LSCM) provides a robust method for the generation of 2d parameterizations for 3d meshes. The minimization of angle deformations and non-uniform scaling are the primary criterion for the generation of the 2d representation As such, the facets of the 2d mesh should closely match those from the original 3d mesh. Additionally, a unique minimum should always exist for a given input, therefore any mesh can be processed with this method. Finally, this method ensures that the handedness of all triangles remains constant to the 2d representation such that traversal of both forms provides similar results.

$$C\left(T\right) = \left|\frac{\partial \mathcal{U}}{\partial x} + i\frac{\partial \mathcal{U}}{\partial y}\right|^2 A_T \tag{7.1}$$

Equation 7.1 defines criterion of the mesh to be minimized for the generation of the 2d representation. The criterion $C(T)$ is computed over each triangle in the mesh. Terms x and y are the components representing each triangle's local orthonormal basis, with A_T representing the triangles area. The $\mathcal{U}$ provides the inverse mapping that relates to triangles to the final parameterization. Finally, summing over the entire mesh ($C\left(\mathcal{T}\right) = \sum_{T \in \mathcal{T}} C\left(T\right)$) provides the minimization criterion [67].

7.2.2 As Rigid as Possible Parametrization

As rigid as possible (ARAP) parameterization applies additional constraints onto the generation of the 2d mesh representation which benefit its use for data mapping. The additional constraints assist in the creation of a mesh which further reduces the distortion of the 2d mesh in relation to the 3d form. ARAP utilizes the initial results from other parameterization techniques in order to further enhance the properties of the 2d mapping.

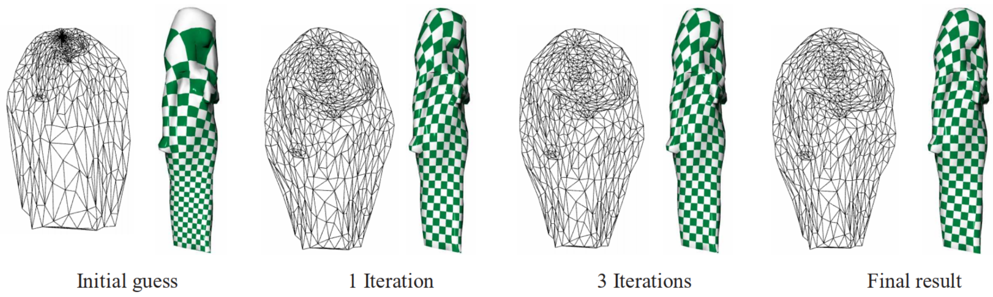

Figure 7.3 Evolution of ARAP parameterization from initial LSCM parameterization [68]

The shape-preserving results (figure 7.3) create a bijective mapping exhibiting reduced deformation of textures. Therefore, mappings utilizing ARAP parameterization will have similar density of samples across the entire mesh. An implementation of both LSCM and ARAP were utilized from the libigl [69] geometry process library.

7.3 Data Mapping

Following the preparation of the tool surfaces mesh representation and parameterization, the data mapping can be considered. Many sources of data can be candidates for the data mapping process, in which a set of data can be spatially represented against the tool surface. The data types can vary from simple grid of points with associated values, up to complex images that were scanned along the tool surface. With a connected mesh of spatially defined data points, an interpolation can be performed which evaluates the data to the desired level of detail. The result from this process is a discretized dataset which has been simplified into the 2d parameterization of tool surface. Thus, the data mapping process can accumulate and normalize the spatial representation from many data sources into a common format. The following sections describe in detail the steps performed to bring in a data surface, and the internal tools used to transfer the data into the normalized format.

7.3.1 Data Surface Alignment and Projection

The data surface alignment step represents an important step in the projection process. In order to generate valid and accurate results for the parameterization of the data surface, it must be correctly associate with the tool surface. At this point, a detailed mesh has been developed from the tool surface (section 7.1), which facilitates the data surface corrections. The data surface corrections borrow from several classic mesh handling techniques.

The first step involves the association of points from the data surface, with the individual triangular facets from the tool surface mesh. For large meshes, it becomes very time consuming to test each point from the data surface against the large set of facets. An efficient search method must be implemented in order to build the association, as the very large meshes are necessary for high fidelity data mapping. For this application, the k-dimensional tree (kd-tree) was implemented.

The kd-tree provides an efficient method for nearest neighboring searching for a given set of n-dimensional data points [70]. The kd-tree method involves a pre-processing step of the initial data set, such that subsequent searches through the kd-tree utilize the pre-processed data to expediently find the set of nearest neighbors. The primary efficiency of the kd-tree methods arises from the use of hierarchical spatial decomposition, utilizing a binary tree based on the hierarchical subdivisions of the search space, which enables rapid binary searches through the data set.

The SciPy implementation of the kd-tree was selected for this application [71]. Since the objective was the association of points with individual facets from the tool surface mesh, the facets' centroids were used to initialize the kd-tree. As a result, the centroids function as a proxy for the mesh facets, and additional checks must be performed to determine the actual facet to associate with a given point.

The primary hurdles from the kd-tree using centroids involves the miss-attribution of points to the incorrect facets. Miss-attribution can occur when the centroid from an alternate facet is nearer to a point, even though the point should be associated with an alternative facet (figure 7.4a). Querying the kd-tree to obtain multiple neighbors increases the chances of including the correct facet's centroid in the results. However, the querying can be further disrupted in the case where extremely long triangles are including in the mesh (figure 7.4b). In order to minimize the chances of obtaining incorrect triangles in the query, the meshing of the tool surface should ideally create a mesh with primarily equilateral triangles. Such a mesh with equilateral triangles, and using a query which obtains several neighbors, a final processing step can be used to obtain the true facet in which the points lie.

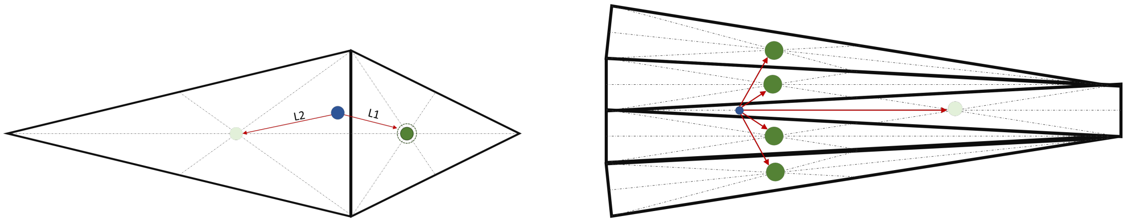

(a) Basic nearest centroid error *(L1 < L2)*　　(b) Unresolved error with many neighbors

Figure 7.4　Incorrect facet association using nearest centroid kd-tree

By querying the kd-tree for the n nearest neighbors from the tool surface mesh, the approximate location of the sample point has been identified. The final step to determine the correct facet from the set of neighbors involves the use of a fast ray-triangle intersection technique [72]. In order to use this technique, a normal vector must be associated with each point from the data surface. However, the generation of normal vectors can be performed automatically when the connectivity of the data points have been provided.

The ray-triangle intersection technique arises from the need for very fast and efficient computations for applications in ray-tracing and computer graphics. In these applications, vast numbers of light rays must be considered in order to create realistic scenes. Similar to the kd-tree structure, this technique also precomputes an additional data set from the given mesh in order to efficiently perform the intersection for given rays. The technique generally relies upon the normalization of individual triangular facets from the tool surface mesh, and an inverse barycentric mapping step in order to compute intersections.

$$T = \begin{bmatrix} \overrightarrow{E}_{1x} & \overrightarrow{E}_{2x} & a & \overrightarrow{v_1}_x \\ \overrightarrow{E}_{1y} & \overrightarrow{E}_{2y} & b & \overrightarrow{v_1}_y \\ \overrightarrow{E}_{1z} & \overrightarrow{E}_{2z} & c & \overrightarrow{v_1}_z \\ 0 & 0 & 0 & 1 \end{bmatrix} \tag{7.2}$$

The precomputed transformation utilizes the the representation of the mesh facets as canonical triangles in the xy plane with sides of unit length. Equation 7.2 describes the transformation, using the edge vectors; $\overrightarrow{E_1} = \overrightarrow{v_2} - \overrightarrow{v_1}$ and $\overrightarrow{E_1} = \overrightarrow{v_2} - \overrightarrow{v_1}$. T must be invertible in order to later utilizes the transformation, so *a, b and c* must be manipulated to ensure T has a non-zero determinant. In order to ensure that $|T| \neq 0$, either *a, b or c* are exclusively set to 1. Specifically, the assignment is performed according to which component from the normal ($\overrightarrow{n} = \overrightarrow{E_1} \times \overrightarrow{E_2}$) has the largest magnitude.

$$T^{-1} = \begin{cases} a = 1; b = c = 0, & \begin{bmatrix} 0 & \frac{\overrightarrow{E_{2z}}}{\overrightarrow{n}_x} & -\frac{\overrightarrow{E_{2y}}}{\overrightarrow{n}_x} & \frac{\left(\overrightarrow{v_3} \times \overrightarrow{v_1}\right)_x}{\overrightarrow{n}_x} \\ 0 & -\frac{\overrightarrow{E_{1z}}}{\overrightarrow{n}_x} & \frac{\overrightarrow{E_{1y}}}{\overrightarrow{n}_x} & -\frac{\left(\overrightarrow{v_2} \times \overrightarrow{v_1}\right)_x}{\overrightarrow{n}_x} \\ 1 & \frac{\overrightarrow{n}_y}{\overrightarrow{n}_x} & \frac{\overrightarrow{n}_z}{\overrightarrow{n}_x} & -\frac{\left(\overrightarrow{n} \cdot \overrightarrow{v_1}\right)}{\overrightarrow{n}_x} \\ 0 & 0 & 0 & 1 \end{bmatrix} \\ b = 1; a = c = 0, & \begin{bmatrix} -\frac{\overrightarrow{E_{2z}}}{\overrightarrow{n}_y} & 0 & \frac{\overrightarrow{E_{2x}}}{\overrightarrow{n}_y} & \frac{\left(\overrightarrow{v_3} \times \overrightarrow{v_1}\right)_y}{\overrightarrow{n}_x} \\ \frac{\overrightarrow{E_{1z}}}{\overrightarrow{n}_y} & 0 & -\frac{\overrightarrow{E_{1x}}}{\overrightarrow{n}_y} & -\frac{\left(\overrightarrow{v_2} \times \overrightarrow{v_1}\right)_y}{\overrightarrow{n}_y} \\ \frac{\overrightarrow{n}_x}{\overrightarrow{n}_y} & 1 & \frac{\overrightarrow{n}_z}{\overrightarrow{n}_y} & -\frac{\left(\overrightarrow{n} \cdot \overrightarrow{v_1}\right)}{\overrightarrow{n}_y} \\ 0 & 0 & 0 & 1 \end{bmatrix} \\ c = 1; a = b = 0, & \begin{bmatrix} \frac{\overrightarrow{E_{2y}}}{\overrightarrow{n}_z} & -\frac{\overrightarrow{E_{2x}}}{\overrightarrow{n}_z} & 0 & \frac{\left(\overrightarrow{v_3} \times \overrightarrow{v_1}\right)_z}{\overrightarrow{n}_z} \\ -\frac{\overrightarrow{E_{1y}}}{\overrightarrow{n}_z} & \frac{\overrightarrow{E_{1x}}}{\overrightarrow{n}_z} & 0 & -\frac{\left(\overrightarrow{v_2} \times \overrightarrow{v_1}\right)_z}{\overrightarrow{n}_z} \\ \frac{\overrightarrow{n}_x}{\overrightarrow{n}_z} & \frac{\overrightarrow{n}_y}{\overrightarrow{n}_z} & 1 & -\frac{\left(\overrightarrow{n} \cdot \overrightarrow{v_1}\right)}{\overrightarrow{n}_z} \\ 0 & 0 & 0 & 1 \end{bmatrix} \end{cases} \tag{7.3}$$

The cases for either *a, b or c = 1* are outlined in equation 7.3, which were derived from the general equation of T described in equation 7.2. These cases can be applied to every facet from the given tool surface mesh inorder to define the individual transformations of each facet.

$$t = -\frac{\overrightarrow{o}_z}{\overrightarrow{d}_z} \tag{7.4}$$

$$b_1 = \overrightarrow{o}_x + t\,\overrightarrow{d}_x,\;\; b_2 = \overrightarrow{o}_y + t\,\overrightarrow{d}_y \tag{7.5}$$

Thus, the actual intersecting facet from the given set of neighbors provided by the kd-tree can be computed accordingly. The origin and direction from the given ray are transformed using the T_{-1} for each facet order to compute the ray according to the simplified representation. Subsequently, the barycentric coordinates of the rays intersection with the facet are computed with the transformed origin $\overrightarrow{o}$ and direction $\overrightarrow{d}$ according to equations 7.4 and 7.5. The barycentric coordinates for the correct interesting facet will obey the conditions: $0 \leq b_1 \leq 1$ and $0 \leq b_2 \leq 1$ and $b_1 + b_2 \leq 1$.

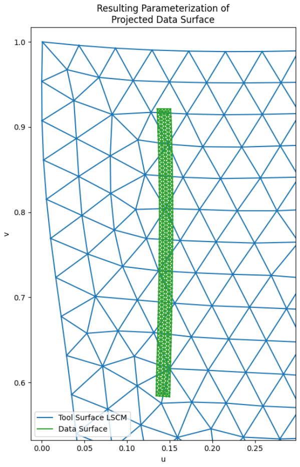

Figure 7.5 Resulting of data surface projection

Finally, the data surface can be properly aligned with the tool surface. The kd-tree and ray intersection techniques have provided the correcting intersecting facet and associated barycentric coordinates for each point from the data surface. The 3d representation of the data surface can via interpolation with the barycentric coordinates 7.6. Additionally, the data surface can be dropped into the 2d tool surface

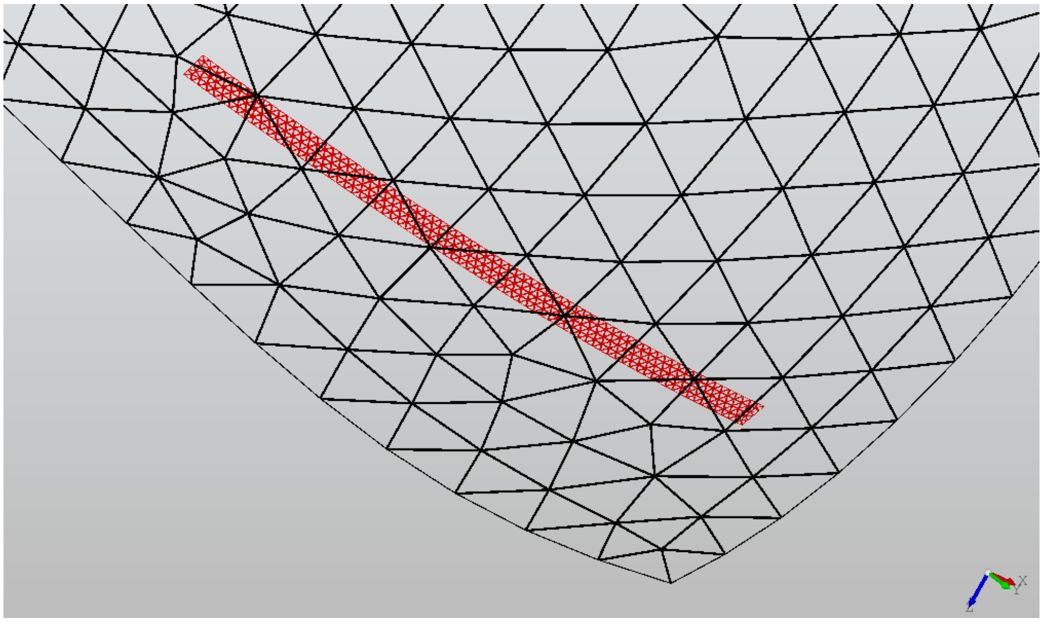

Figure 7.6 Mesh of the generated data surface

representation, utilizing a similar interpolation of each mesh points associated 2d values. Figure 7.5 demonstrates this operation by dropping the data surface into the 2d representation from figure 7.2

7.3.2 Evaluation of Data Surface

The evaluation of the data surface utilizes the projection of the data surface points and the tool surface mesh parameterization to generate a uniform representation. Such a uniform representation enables multiple data surfaces to be directly converted into a global form, simplifying further comparisons. Additionally, the evaluation step implements interpolation of the data surface, enabling continuous evaluation of values within the data surface's region. The result of this evaluation is a discretized global form of the data surface referenced against the tool surface mesh.

The global mesh parameterization from section 7.2 has generated a mapping from the *uv* to 3d representation of the tool surface. Therefore, region of the *uv* space occupied by the projected data surface can be evaluated with corresponding data point values. Additionally, the discretized form of this evaluation can be mapped back to the 3d representation of the tool surface as a "texture", enabling an integrated visualization of the data surface.

Efficient generation of the discretized, global form of the data surface relies on the capabilities of OpenGL [73]. OpenGL leverages the graphics hardware to speedup the interpolation and discretization of the data surface, and enables several types of data surfaces to be evaluated, including single values at data points, up to entire images. The capabilities of OpenGL primary benefit the evaluation of large data surfaces representing images, where the images are of a very high resolution.

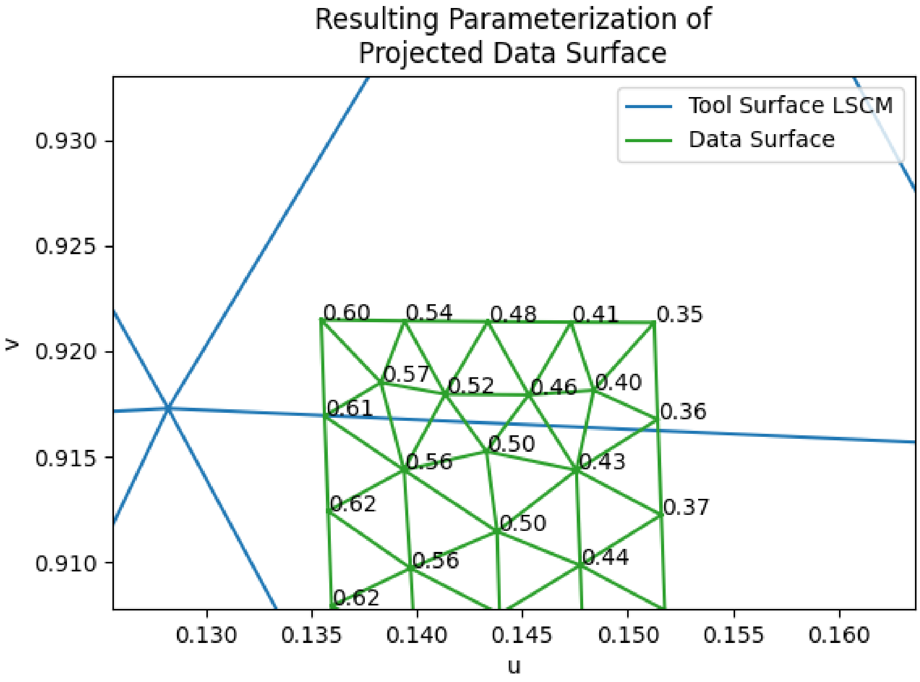

Figure 7.7 Single value data points

The OpenGL process first begins with defining the type of value represented by the data surface. Valid types include either singular values (figure 7.7) or vectors encoded as integer or floating point numbers. In the case that the data surface maps to another source, such as an image, the provided data points should be the parameters that define the mapping. For the case of a mapping data surface, the type of value will match that of the source representation.

Finally, the data surface and associated values can be bound to OpenGL to perform the interpolation. In the context of OpenGL, binding exposes the formatted data to the graphics hardware for processing. Each vertex from the data surface is associated with the associated value or mapping parameter. The vertices are the 2d form obtained from the projection of the data surface projection to the tool surfaces global parameterization. In the case of a mapping data surface, the mapped source will also be bound. Finally, the connectivity of the discretized data surface is bound, which defines the individual facets which make up the triangular mesh.

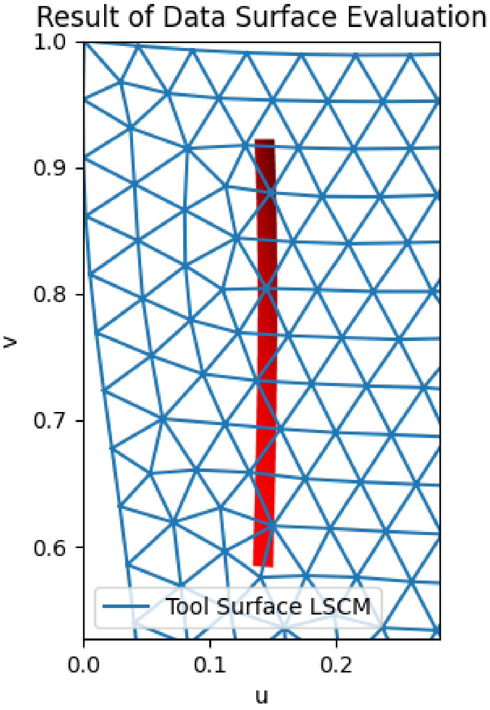

Figure 7.8 Evaluated data surface in global parameterization

The bound information defining the data surface is then processed with the use of a shader program. Shader programs define the interpolation of the values within each facet of the mesh. The specific type of shader program will be determined by the type of information represented by the data surface. OpenGL will apply the shader program to each facet of the data surface mesh, providing the final discretized uniform representation of the data surface in the global parameterization of the tool surface (figure 7.8).

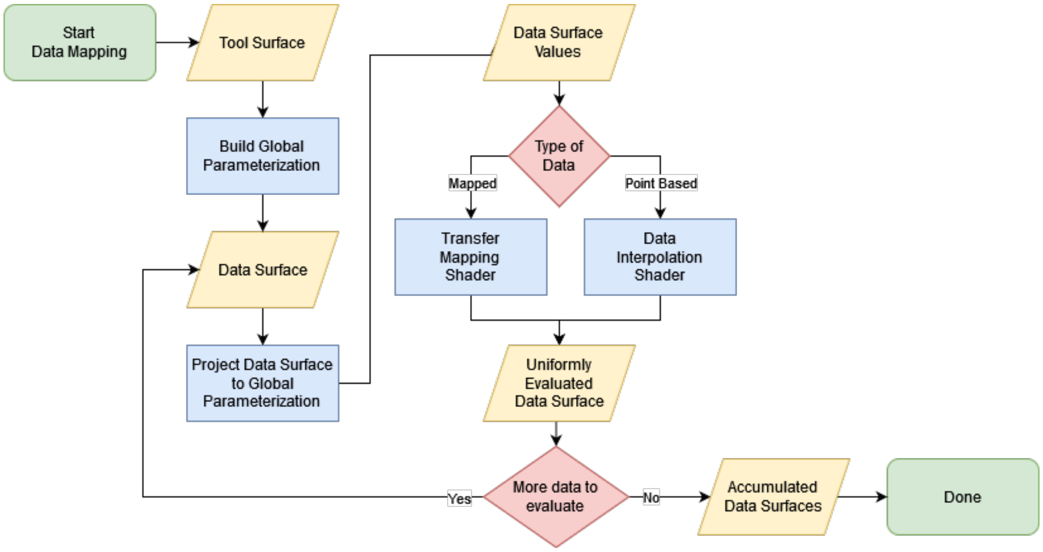

Figure 7.9 Overview of data mapping process

7.4 Applications for Data Mapping

The data mapping tool presented in the previous sections enables the incorporation of data from multiple sources. Fundamentally, the mapping tool only requires a cloud of points that either directly encode for some specific value or map to another data source. In this form, the data points may encode for singular values such as compaction pressure or temperature, or define the position of a point in a map of the tool surface. The following section sets out to present the implementation of the data mapping tool to various sources of data, and additionally describes the methods for generating the associated cloud of points.

7.4.1 Profilometry Scanning

First, the evaluation of data from a profilometry data source will be discussed. The profilometry system which provided the following results was previously covered in

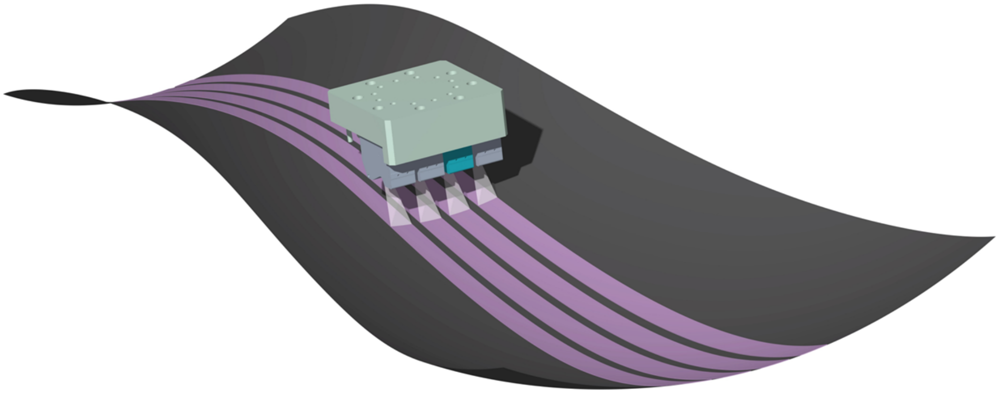

Figure 7.10 ACSIS Profilometry Scan Regions

section 5.3. To highlight the capabilities of this system, it features a set of 4 independent laser profilometers mounted to a Kuka KR120 robotic arm. The profilometers collect height data from the scanned surface, which are then post processed into gray scale images. The resulting gray scale images describe the height profile along the entire scan path of the profilometers. Each scan path is processed independently, therefore a single scan pass results in 4 individual processed images. Figure 7.10 depicts the regions captured from the individual profilometers.

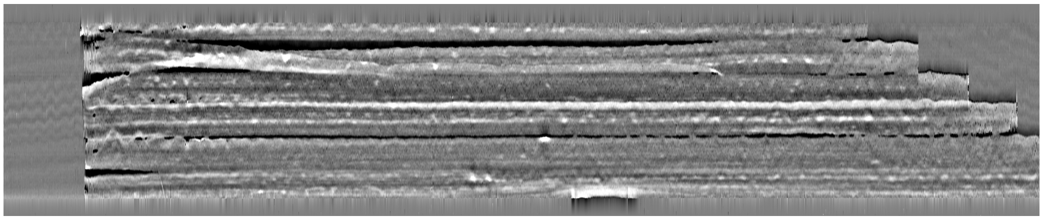

Figure 7.11 Post processed ACSIS scan

The gray scale images (figure 7.11) generated from the scan post processing are the data to be mapped back to the uniform tool surface representation. The post processing step generates a linear image, regardless of the shape of the scan path. Warping from rotations of the profilometers are additionally eliminated during post processing, such that scanned fiber paths are straightened.

The incorporation of inspection data from such a profilometry system represents a mapped data source. As such, the initial data source is present, but the data surface which contains the data must be defined. In order to utilize the data generated from a robotic system, it is essential to understand the motions performed during scanning relative to the tool surface. Fortunately, the programming of such a system involves the definition of tool center points (TCP), which can be transformed to a coordinate system relative to the tool surface. Additionally, the profilometers are precisely mounted relative to the TCP which was utilized to understand the portions of the tool surface captured by the individual profilometers.

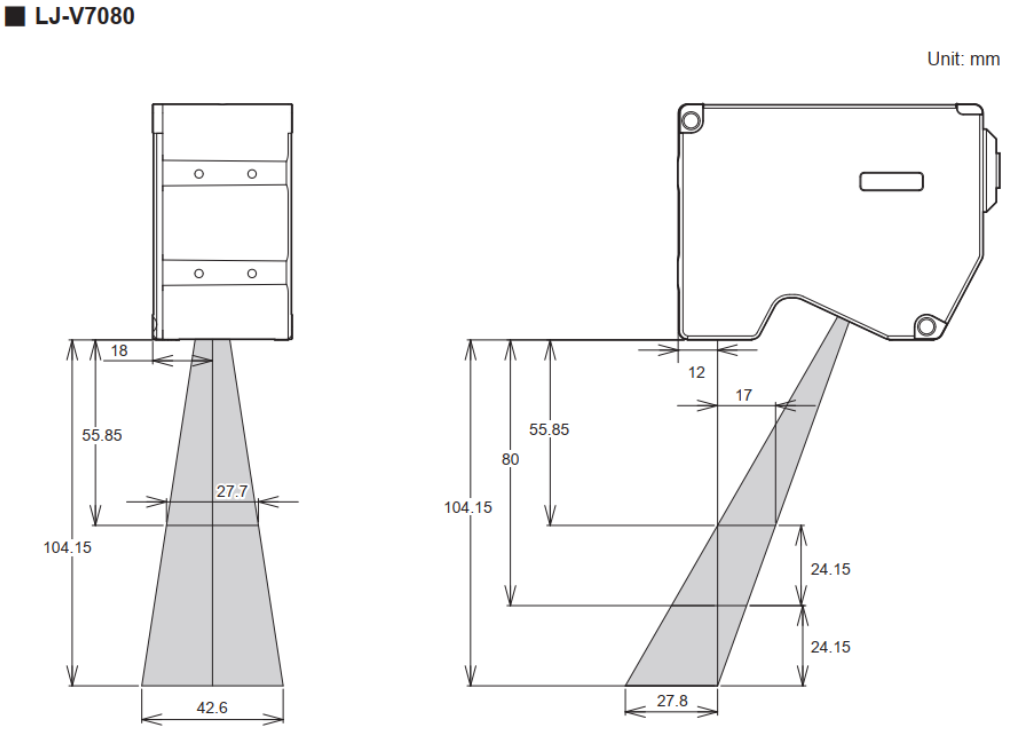

Figure 7.12 Profilometer mutual interference area [74]

By combining the motion path of the TCP during the scanning process, and the scan region (figure 7.12), the resulting data surface can be defined. An iterative process utilizes the TCPs defining the programmed scanning motion and correctly positions the expected field of view (FOV) from the profilometer. By determining the intersection of the FOV with the tool surface model at these instantaneous points, the data surface can be reconstructed. The data surface travels along the tool surface and its bounds are defined by the intersection between the scanners FOV and tool surface. An example of the resulting data surfaces are depicted in figured 7.10 by the purple regions.

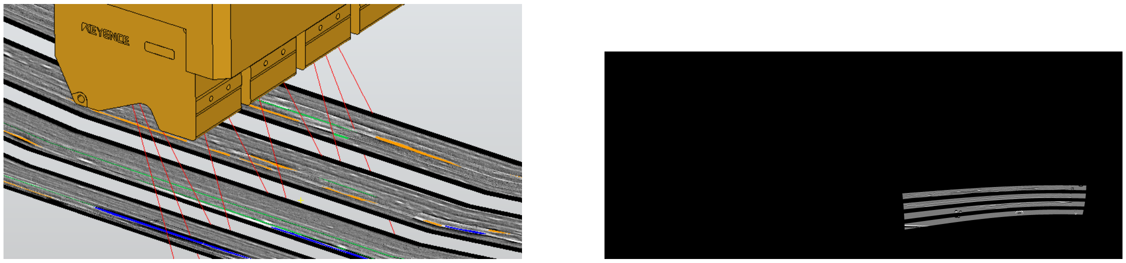

(a) Mapped scan images

(b) Evaluated scan images

Figure 7.13 Individual scan paths

The last step required to evaluate the scan data is the determination of the mapping between the post processed gray scale images and the data surface from the previous step. A mapping is predicted which aligns each of the edge from the scans with images, resulting in figure 7.13a). An even sampling of the image along the length of the scan path is assumed, and that the FOV method for the data surface reconstruction should restore the linear images.

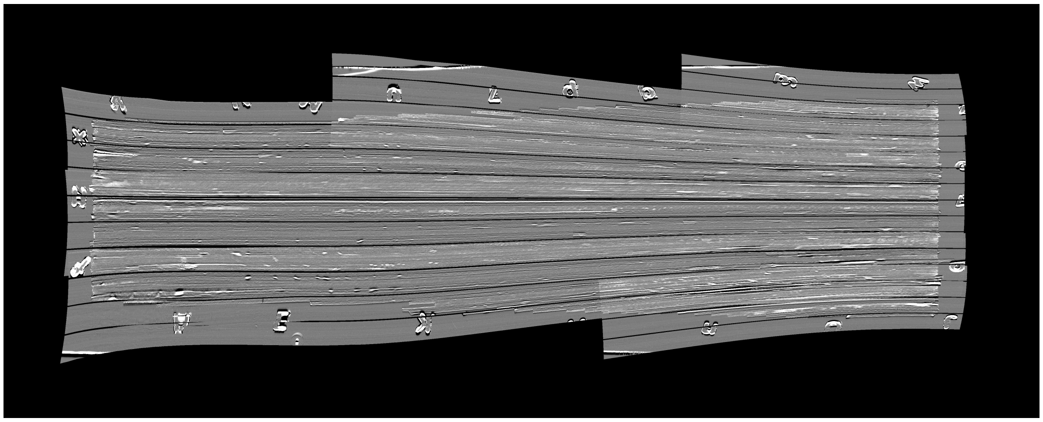

Figure 7.14 Aggregate of scan data

Now that the data surface and associated mapping for each of the profilometers has been determined, the images can be evaluated to the uniform representation (figure 7.13b), utilizing the mapping shader described in section 7.3. The primary benefit for the application of the mapping technique is the ability to evaluate data from multiple scans in the uniform representation. Ordinarily, the scans would be processed individually, and since these scans depict only specific regions of the tool surface, context would be lost for the contents of the scans. By collecting each of the scans into the global representation, a comprehensive understanding of the data collected during the scanning process can be better understood (figure 7.14). Additionally, the development of the mapping from the scan region to the tool surfaces global parameterization can be utilized for processing data within the scan images.

7.4.2 Numerical Compaction Predictions

In addition to the evaluation of results for normalizing data generated from digitization processes, it can also be applied during the numerical evaluations performed for AFP process planning. For these applications, information about the process planning parameters and processing conditions can be numerically computed according to the conditions expected to layup. Through the analysis of these conditions, careful adjustments can be performed in order to improve the properties of the manufactured laminate structures. The development of such capabilities could enable the future incorporation of process parameters and conditions into the ply optimization loop of CAPP. Such that, with the understanding of how various process parameters, such as compaction, lead to processing related defects, an ideal set of process parameters could be determined to minimize those resulting defects.

Such an application of this numerical analysis is the compaction pressures experienced during fiber placement. During the layup of thermoset based carbon fiber composites, roller compaction and heating are the driving factors behind the adhesion of the newly place fibers to previous plies. Inadequate heating and compaction parameters will lead to a host of fiber defects (section 2.1), due to poor adhesion. Specifically, low levels of compaction increase the likelihood of fiber wrinkling, puckers and bridging during fiber steering and in regions of high curvature [59].

The numerical model described in [75] performs efficient compaction analysis utilizing a simplified roller model. Fundamentally, the model relies on Hertzian contact theory, describing the frictionless contact between two curved elastic bodies [76]. While the theory describes the contact of an elastic sphere, it has been adopted here to describe the contact between an elastic cylinder contacting a tool surface with general geometry.

For the numerical application described in [75], an effect modulus was defined for the compaction roller. The compaction roller was constructed from a steel shaft with an outer layer of silicone polymer. With a simplified understanding of the roller's deformation, the modified form of the Hertzian contact theory was applied.

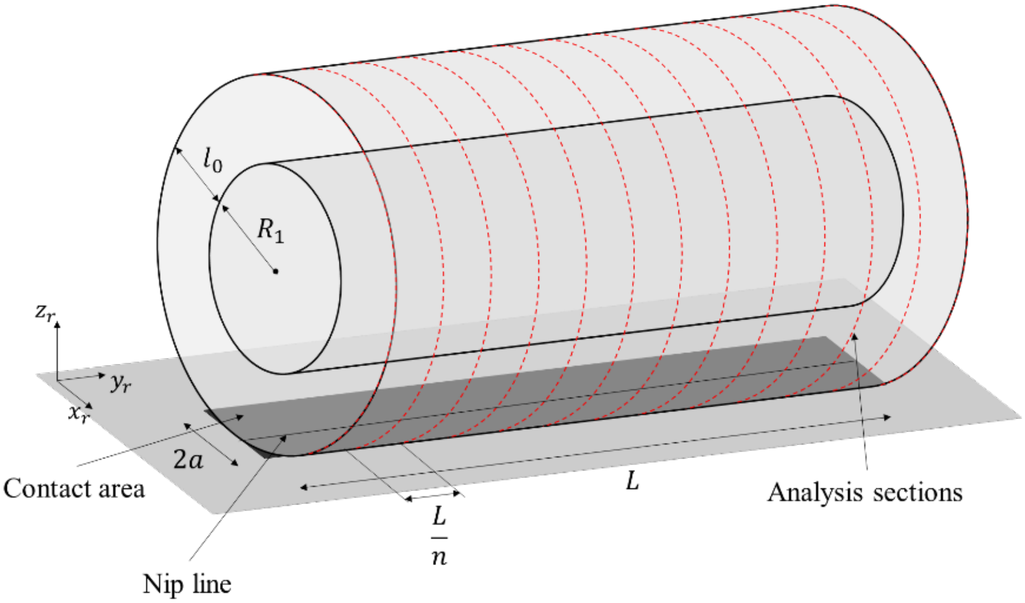

Figure 7.15 Discretized compaction roller model

$$F_{total} = \frac{L}{n}\sum_{i=1}^{n} F_i \tag{7.6}$$

In order to utilize the numerical compaction model for complex tool surface, the cylindrical roller was discretized along its length 7.15. With the discretized section, the individual deformation and compaction forces could be computed. The numerical compaction model varies the deformation of the roller in order to understand the variation of the compaction force throughout the roller's contact region. The total compaction force from the individual contact forces would be computed with equation 7.6.

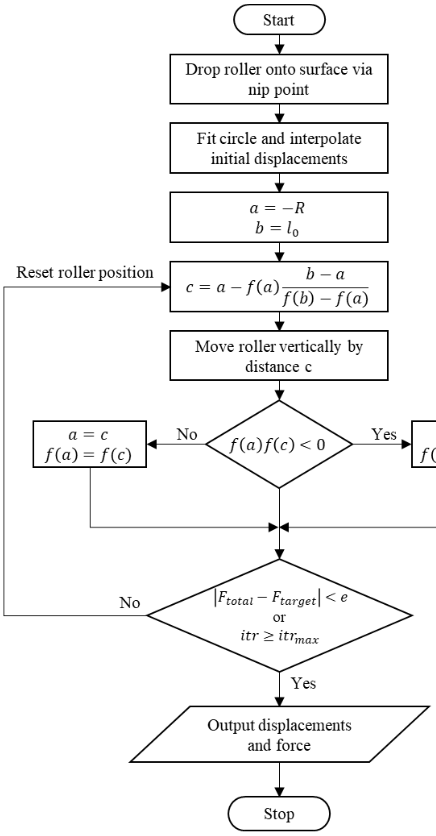

Figure 7.16 Secant method for roller displacements [75]

The actual displacement along the normal to the contact plane was converged on that would satisfy the total numerical force between the discretized regions and the programed compaction force programmed for the layup 7.16. An understanding of the varied compaction force can be computed anywhere along the fiber path utilizing the numerical compaction model 7.17.

The maximum compaction pressure experienced by an individual point during the placement motion will most significantly affect the final adhesion of the placed

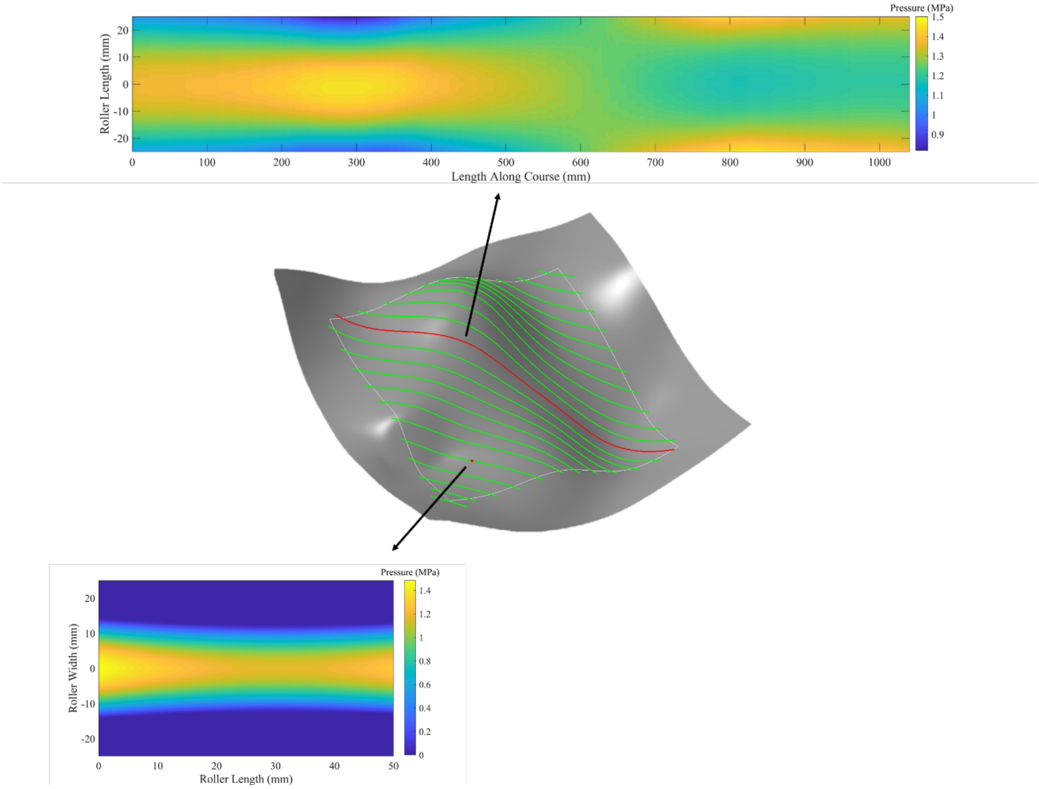

Figure 7.17 Individual compaction patch and aggregated path

tows. Therefore, by running the compaction analysis along the entire fiber path and extracting the maximum compaction pressures from each path, an aggregated definition of compaction pressures can be obtained 7.17.

Most significantly, the compaction pressures are obtained with reference to the frame of the compaction roller. In this form, it can be difficult to understand the spatial distribution of the resulting compaction pressure and understanding its relationship to the underlying geometry of the tool surface. Thus, the data mapping techniques provide an efficient means for normalizing the compaction data and generation global understanding of pressures experienced during the layup of entire plies.

In a similar fashion to the evaluation of profilometry scans from section 7.4.1, data regarding the compaction pressure has been obtained, but the spatial relationship needs to be further defined with reference to the tool surface to obtain the global form. Since the compaction analysis utilizes the predefined fiber paths, these can be utilized to understand the spatial relationship of the compaction roller to the tool surface. Along with the geometrical dimensions of the compaction roller, length and radius, the model of the roller can be well understood. By simulating the motion of the roller model and understanding the position of the edges against the tool surface, the nip-line of the roller is defined 7.15.

Accumulating the contact regions between the roller and the tool surface along the entire fiber path defines the final roller contact surface which defines the overall expected path of the roller. Along with the maximum compaction pressures experience along the fiber path (figure 7.17), the position and values have been prepared for data mapping.

As previously defined, the data points will be converted to the global parameterization of the tool surface in order to obtain the regularized 2d form. In this form of data evaluation, the compaction pressure is explicitly defined and each point, such that a direct interpolation of the data values can be performed. This is in contrast to the application of data mapping where large images are utilized as in 7.4.1.

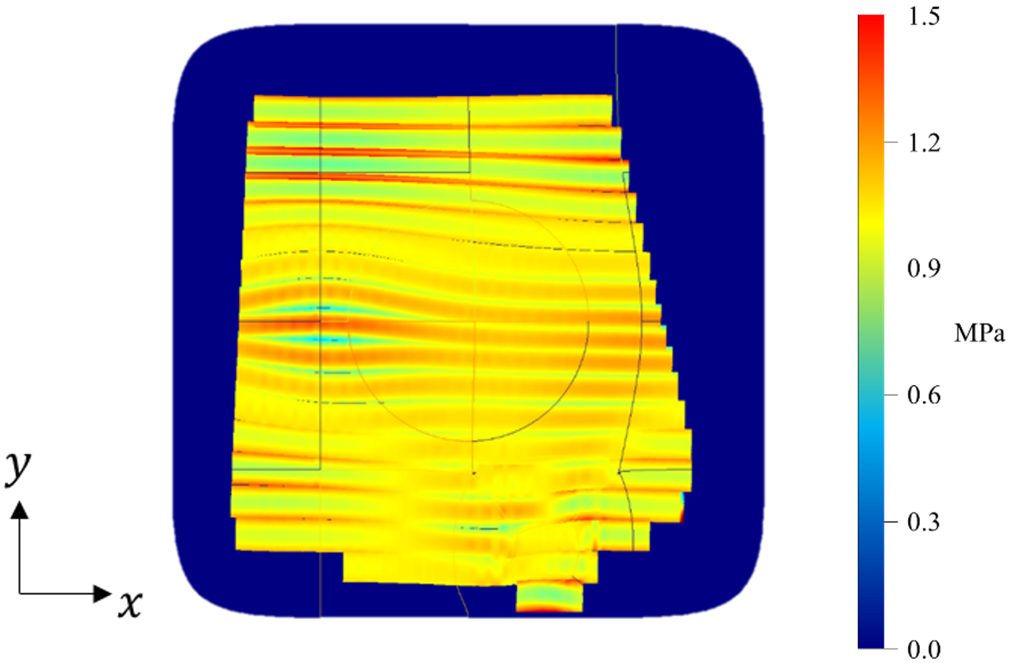

Figure 7.18 Aggregate of compaction data

Through the application of data evaluation and mapping to the numerical compaction analysis, a global form of the compaction pressures can be obtained 7.18.

7.5 Conclusion

This chapter has presented a generalized ata mapping techniques which enables the utilization of data from multiple disparate sources. The techniques begin with a discretization of the tool surface using the GMSH tool set. The discretization enables the subsequent global parameterization of the tool surface. The global parameterization relying on either LSCM or ARAP methods builds a global 2d parametrization of the tool surface which provides an essential mapping back to the original 3d representation.

Following the preparation of data concerning the tool surface, actual numerical and process data can be considered. The data must be mapping to a spatial representation which can be referenced against the 3d tool surface. Furthermore, the data associated with that spatial form can be a simple values or map to more complex data. Finally, the appropriate mapping strategy is applied to the data in order to obtain the final global representation. Applications of the technique were demonstrated for both profilometry scans collected post-layup, in addition to data collected regarding the numerical analysis of compaction data. A flowchart summary of the entire mapping process is depicted in figure 7.9

CHAPTER 8

SCORING CASE STUDY

The following chapter presents an extensive exploration of the ply quantification methods discussed in chapter 3. The study provides insight into the relationship of the starting point and layup strategies along with the geometry of the tool surface. The complexity of the selected tool surfaces ensures that non-trivial fiber paths will be generated, and thus measurable fiber defects will occur.

8.1 DESIGN OF EXPERIMENT

In order to sufficiently explore the input space for the generation of plies, a series of experimental conditions were set forth for the case study. The following sections describe the overarching conditions that were considered and provide insight into the expected influence on the overall case study results.

8.1.1 TOOL SURFACE VARIATIONS

The tool surface selected for the placement of tow paths will be the driving factor behind the generation of fiber defects. Non-developable and high surface curvature lead to situations in which general path planning strategies begin diverging in their effectiveness. In other words, the increased creation of fiber defects should begin to provide insight into the benefits and drawbacks of the various layup strategies. Additionally, each tool surface had multiple variations in order to further inspect the variation of ply scores.

Two tool surfaces were selected for this case-study, featuring different distributions of curvature and symmetry. Each tool surface was $750mm$ square and featured a single ply boundary which was $250mm$ in radius.

$$z(x,y) = A_1 * \cos(\omega_1 * x) + A_2 * \sin(\omega_2 * y) \tag{8.1}$$

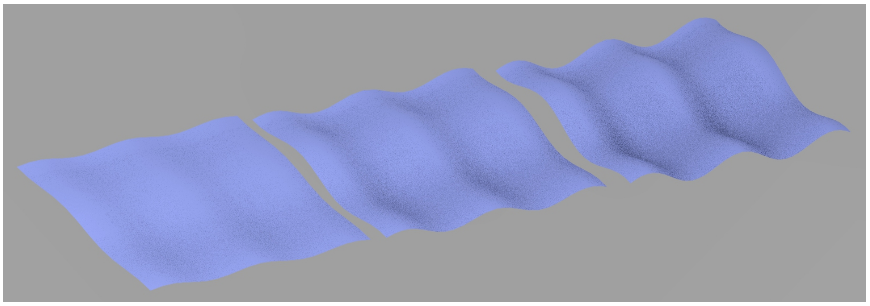

Figure 8.1 Variations of the periodic surface

The first tool surface (figure 8.1) featured periodicity due to the *sine* and *cosine* components of equation 8.1. The A_1 and A_2 components controlled the amplitude of the tool surface, with values ranging from 10 to $30mm$. The frequencies were held constant, with $\omega_1 = 1/50$ and $\omega_2 = 1/75$, such that they varied in each direction of the tool surface.

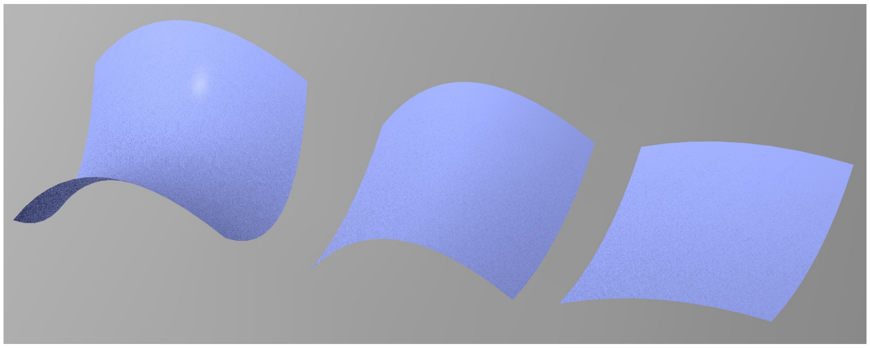

Figure 8.2 Variations of the hyperbolic-paraboloid surface

The second tool surface (figure 8.2) has features derived from a hyperbolic-paraboloid, equation 8.2. The denominators, A_1 and A_2, were used to control the magnitude of curvature. An important aspect of hyperbolic-paraboloids is the "saddle-point", where the derivatives of the function in orthogonal directions are zero. This will form a region of convergence or divergence for fiber paths depending on the orientation the path traverses through the saddle-point.

$$z(x, y) = \left(\frac{x}{A_1}\right)^2 - \left(\frac{y}{A_2}\right)^2 \tag{8.2}$$

The Gaussian curvature of each variation was measured in figure 8.3.

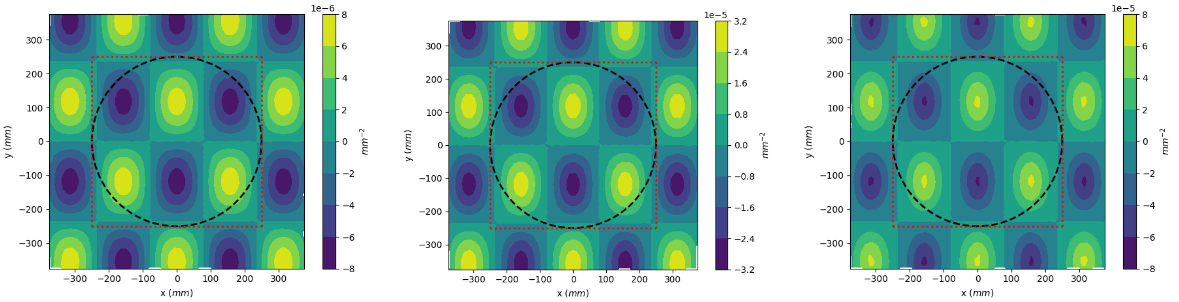

(a) Variation 1: $A_1 = A_2 = 10$ (b) Variation 2: $A_1 = A_2 = 20$ (c) Variation 3: $A_1 = A_2 = 30$

Figure 8.3 Gaussian Curvature of Periodic Sine-Surface Variations (eq 8.1)

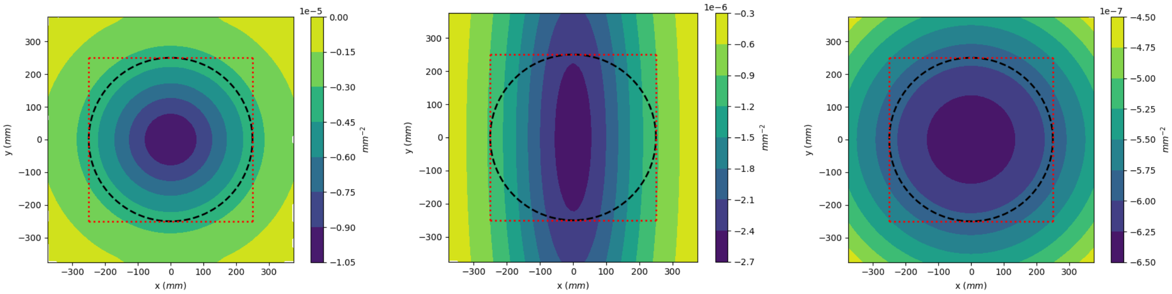

(a) $A_1 = A_2 = 10$ (b) $A_1 = 25$; $A_2 = 50$ (c) $A_1 = A_2 = 50$

Figure 8.4 Gaussian Curvature of Hyperbolic-Paraboloid Variations (eq 8.2)

Gaussian curvature represents the product of the principal curvatures at a given spot. The Gaussian curvature is relevant to the formation of fiber paths, as a curvature of 0 defines a developable surface. Such a surface would enable efficient placement of constant curvature paths with no coverage defects (section 3.1.1). The follow chapter will demonstrate the interactions of fiber paths with tool surfaces exhibiting complex Gaussian curvature distributions.

8.1.2 Layup Strategies

The layup strategies were selected to demonstrate their various impact on defect formation. The primary strategies selected were rosette and natural path strategies. Rosette would primarily modify the outcome of fiber paths in terms of the observed fiber angle deviation. Alternatively, natural path would primarily relate to the overall fiber steering observed. Additionally, these two methods would be expected to result in a relative increase in other defect types as the primary defect is reduced.

In order to investigate the impact on total coverage, the parallel strategy form of the rosette and natural path were additionally generated. The parallel strategy would function to generate the trade-off the strategies' primary objective and the formation of gaps and overlaps. The gaps and overlaps would be prioritized until the magnitude of angle deviation or steering become excessive.

8.1.3 Fiber Angles

The selected fiber angles were chosen to investigate the interaction of fiber paths along various curvature paths of the underlying surface geometry. Fiber angles of 0°, 45° and 90° were selected. These fiber angles are traditionally used in quasi-isotropic layups, and thus should sufficiently describe the commonly utilized path orientations.

8.1.4 Miscellaneous Fiber Path Parameters

The fiber paths in the following chapter were generated with 8 tow courses, where individual tows were $6.35mm$. Excessive angle deviation was set at 3° for scoring. The minimum steering radius was set at $1750mm$ for scoring. Gaps and overlaps both had the same limit set for scoring at $300mm^2$. For fiber path generation, the gap and overlap settings were set at half a tow width, to avoid excessive gap or overlap instances.

8.2 Results

The following section describes the results of the case study utilizing the combination of parameters from section 8.1. The results are grouped between the two different layup surfaces. Additionally, the results are further grouped between the fiber angle and the variation of the layup surface. By grouping between the variations of each layup surface, the distribution and magnitude of defects can be presented.

Furthermore, several types of plots will be presented to demonstrate the various results. Score distribution plots function to map the result of the ply generated from that seed point for fiber coverage generation. In other words, given a seed point and the associated parameters including fiber angle and layup strategy, the fiber coverage was generated. Utilizing the scoring techniques from chapter 3, the resulting fiber coverage and defects were evaluated. Finally, that single ply score was associated with the seed point, to provide spatial association for the ply scores. Thus, when all the seed points from the upper quadrant within the ply boundary have been evaluated, a complete heatmap can be generated. With the heatmap, relationships between the underlying surface geometry and fiber path parameters can be evaluated.

Beyond the score distribution plots, scoring histograms are also generated which enable a deeper look into the individual defects and their distribution which make up the overall ply score. These histograms are generated according to groupings between tool surface variation and given fiber angle.

Finally, aggregate plots generate an overlay of the actual defect instances from all the generated fiber path geometry. The aggregate plots consider the distribution and magnitude of defect instances. However, a distinction is made between the "discrete" and "continuous" defect types. Discrete defects include gaps and overlaps, as no distinction is made about the magnitude of gaps or overlaps at a given point, they will either exist or be absent. Alternatively, angle deviation and steering radius constitute the continuous defect types. Both defects have a measurable component at a given location, and thus their magnitude needs to be considered.

Aggregate plots for discrete data therefore consider the spatial distribution of gaps and overlaps through simple accumulation between plies. For each, the discrete defects from every ply sharing the same layup strategy and fiber angle are overlaid to generate the aggregate plot. Thus, the heatmap format of the aggregate plots demonstrate the spatial distribution of defects within the ply boundary. The hotter region of these aggregate plots indicate regions where many of the discrete defects occurred, and the value represents the number of ply scnearios in which a defect occured in that location.

Alternatively, aggregate plots accumulate the discrete value throughout the ply scenarios and generate an average value distribution throughout the ply boundary. Thus, the values presented through the heatmap plots indicate the average value of the defect at a given location as measured from each ply scenario. The hot regions of these plots indicate regions where more severe defects occurred, and would thus be regions of consideration when attempting to reduce defect instances.

Through the combination of these plots evaluation ply scores and defect distributions, along with the underlying tool surface geometry, interactions between fiber paths and topology are investigated. The follow section will present the results for the periodic tool surface.

8.2.1 Surface 1: Periodic

The periodic tool surface utilized *sine* functions to generate the underlying periodic surface topology. Due to this periodicity, some similarity was predicted with the distribution of scores and defects.

The scores are organized by layup strategy and scoring priorities. High scores indicate fewer instances of the defects occurring with the associated seed point. Each of the scoring priorities demonstrates the impact of the individual instance and severity score of that defect type. Coverage includes both gap and overlap defects, to provide insight into the overall relative placement of individual courses. The combined score shows the result when each of the defect specific scores is equally weighted. From the combined score, the most impactful defect component should be evident.

Variation 1 Scoring

The first set of data begins with figure 8.5. The rosette strategy variations demonstrate horizontal banding of scores. These bands follow the fiber direction. Hotspots are correlated between coverage and excessive steering defects, but inverse to the angle deviation defects. Coverage focused score makes up the majority of the combined score. There was no significant difference between the rosette and rosette-parallel strategy scores.

The natural strategy variations present very different score distributions, with more prominent vertical banding. However, a similar correlation is observed between the coverage and steering, with an inverse correlation to the angle deviation. This correlation does not extend to the natural-parallel strategy. In this instance, the hotspots between the 3 defect types occur in the same regions. Additionally, for natural-parallel the steering does exhibit some small instances of horizontal banding as well. Finally, the majority of the combined scores results from the high coverage scores.

Figure 8.6 presents the scores for layups with 45° fiber angles. Similarly to the 0° fiber angles, the score distributions correlate to the fiber direction. The rosette strategy variations indicate a strong banding of the scores in the direction of the fiber paths. The distributions for the natural strategy variations are less well defined, but some banding can be seen to correlate to the fiber direction. However, the fiber angle deviation for the natural strategy presents banding which is orthogonal to the fiber direction.

Rosette Strategy

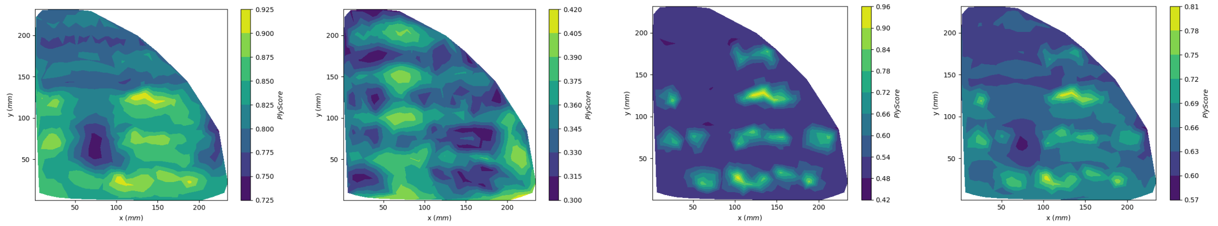

(a) Coverage (b) Angle Deviation (c) Excess Steering (d) Combined

Natural Strategy

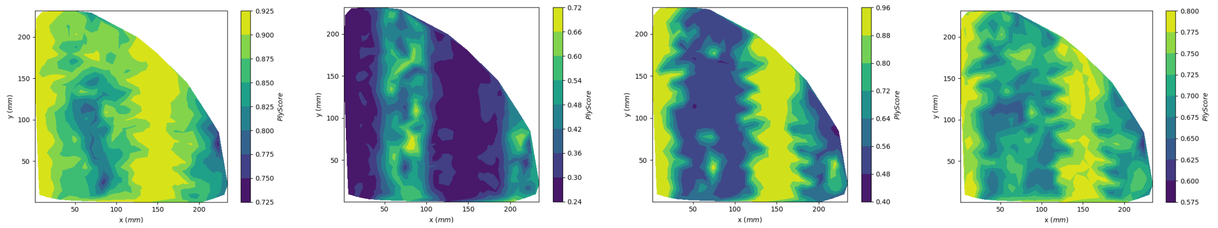

(e) Coverage (f) Angle Deviation (g) Excess Steering (h) Combined

Rosette-Parallel Strategy

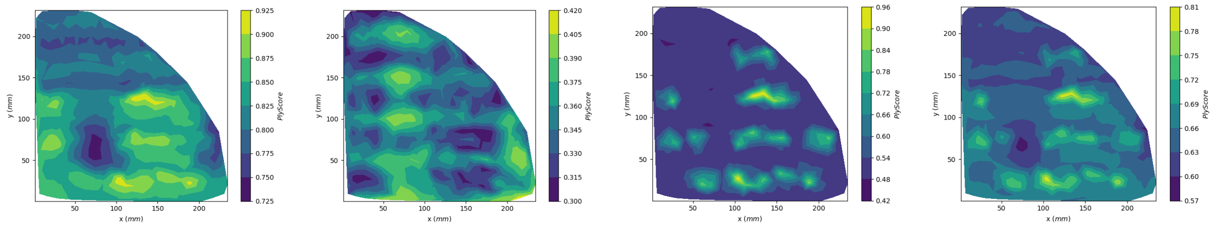

(i) Coverage (j) Angle Deviation (k) Excess Steering (l) Combined

Natural-Parallel Strategy

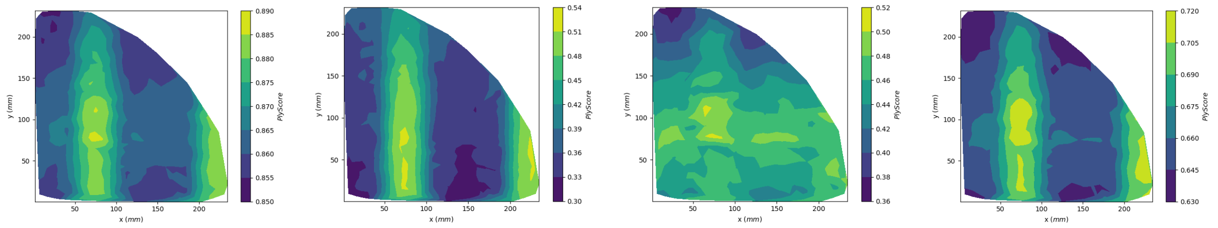

(m) Coverage (n) Angle Deviation (o) Excess Steering (p) Combined

Figure 8.5 Score distributions of periodic surface (variation 1 - $\theta = 0°$)

Hotspots between the various defects largely correlate, in contrast to the previous 0° plies where coverage and excess steering were inversely correlated to the angle deviation. It is also important to note the approximate distance between the banding as well. The courses consist of 8 6.35mm tows, such that full courses are $\tilde{5}$0.8mm,

Rosette Strategy

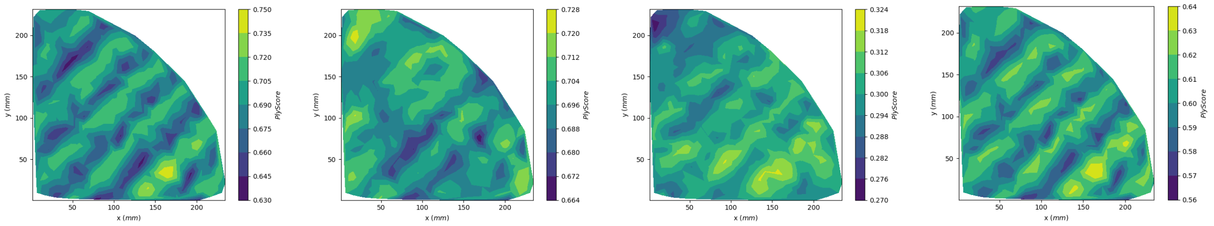

(a) Coverage (b) Angle Deviation (c) Excess Steering (d) Combined

Natural Strategy

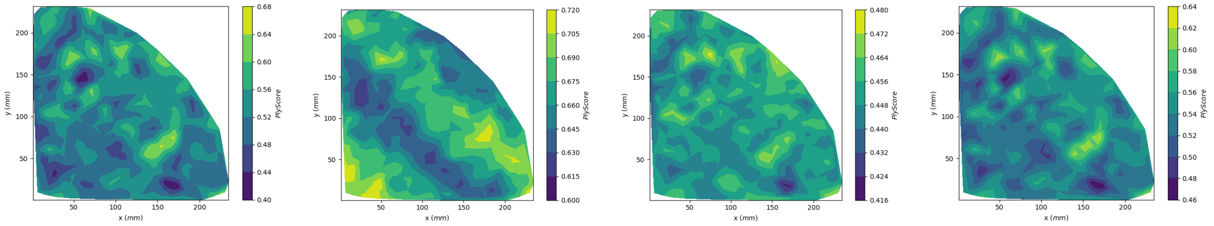

(e) Coverage (f) Angle Deviation (g) Excess Steering (h) Combined

Rosette-Parallel Strategy

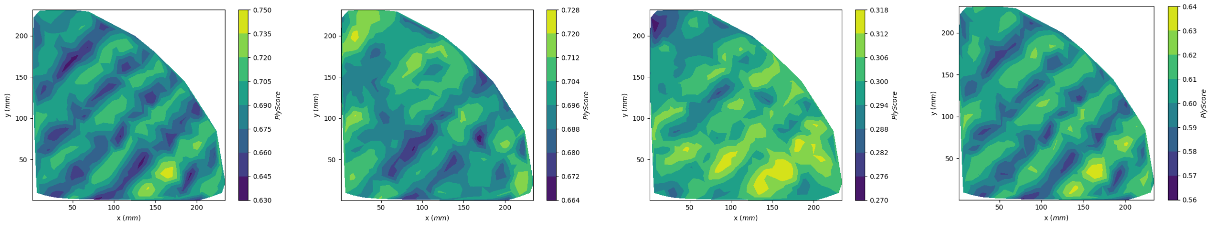

(i) Coverage (j) Angle Deviation (k) Excess Steering (l) Combined

Natural-Parallel Strategy

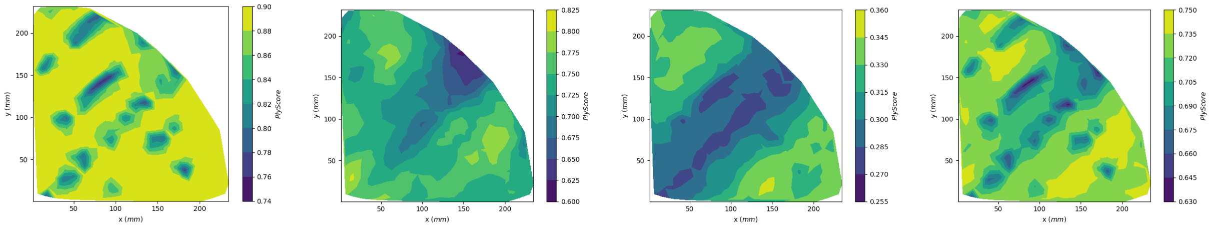

(m) Coverage (n) Angle Deviation (o) Excess Steering (p) Combined

Figure 8.6 Score distributions of periodic surface (variation 1 - $\theta = 45°$)

which closely compares to the peak to peak distance of the banding.

Figure 8.7 present the 90° plies, where the fiber directions follows the tool surface direction with a lower frequency of deflection. Thus, the peak to peak distances of the tool surface are longer than those experienced in the 0° plies. The lower frequency of

Rosette Strategy

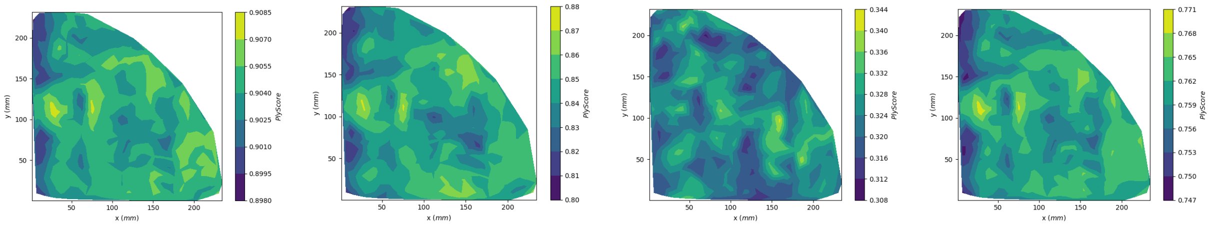

(a) Coverage (b) Angle Deviation (c) Excess Steering (d) Combined

Natural Strategy

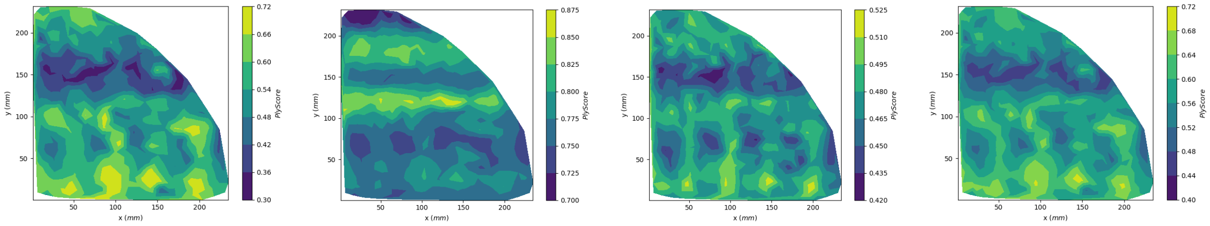

(e) Coverage (f) Angle Deviation (g) Excess Steering (h) Combined

Rosette-Parallel Strategy

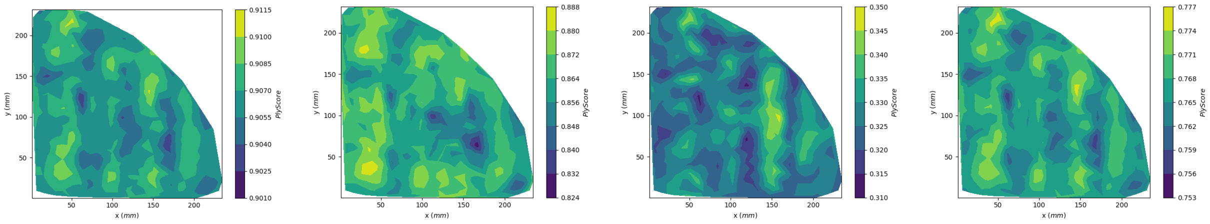

(i) Coverage (j) Angle Deviation (k) Excess Steering (l) Combined

Natural-Parallel Strategy

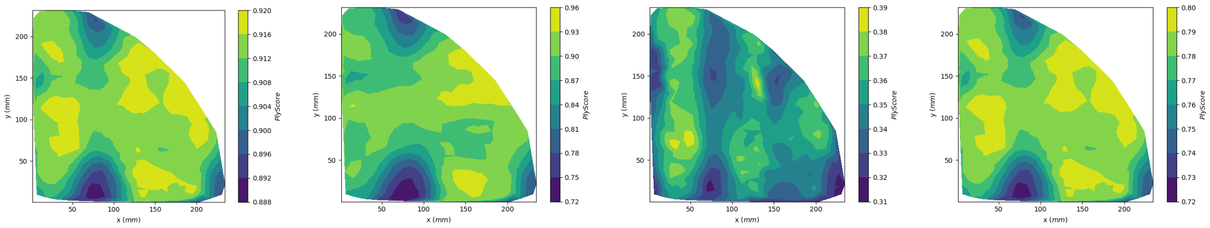

(m) Coverage (n) Angle Deviation (o) Excess Steering (p) Combined

Figure 8.7 Score distributions of periodic surface (variation 1 - $\theta = 90°$)

deflection effectively lowers the overall curvature experienced by a fiber path follow this orientation.

Formation of banding for the rosette strategy is significantly less defined than from the previous orientations. Both rosette strategies exhibit some banding which similarly follows the fiber angle, however, it is much more pronounced with the rosette-parallel strategy. Correlation of hotspots between all types of scores is again observed, with no significant variation in location between coverage and steering when compared to the angle deviation scores.

The natural strategy variations show primarily orthogonal banding compared to the fiber path direction, with some evident of vertical banding. However, the natural-parallel strategy shows significant deviation from previous scoring patterns for both the coverage and angle deviation scores. In these ply scenarios, the majority of the samples region exhibits higher scores, while two regions of lower scores are present near the inflection point of the tool surface, presented in figure 8.3.

Variation 2 Scoring

The previous section covered the initial variation of the tool surface The next variation has increased the amplitude of the *sine* and *cosine* components of the surface geometry. From figure 8.3, it can be observed that the amplitude of the Gaussian curvature has been roughly quadrupled, from peak to peak.

Figure 8.8 presents the score distributions for the 0° fiber orientation ply scenarios. The general distribution of fiber defect scoring resembles that of figure 8.5, where the rosette strategies exhibit banding which aligns with the fiber orientation, while natural and natural-parallel exhibit banding orthogonal to the fiber direction. However, the magnitude of the scores have dropped significantly from the lowest curvature variation of the tool surface. Additionally, the coverage scores for the natural-parallel strategy do not exhibit strong patterns regarding the hotspots in accordance to the fiber orientation as previously observed.

Figure 8.9 presents scores distributions for the 45° fiber orientation ply scenarios. The rosette and rosette-parallel strategies exhibit banding of the score distributions, where the banding is oriented along the fiber direction. The natural and natural-

Rosette Strategy

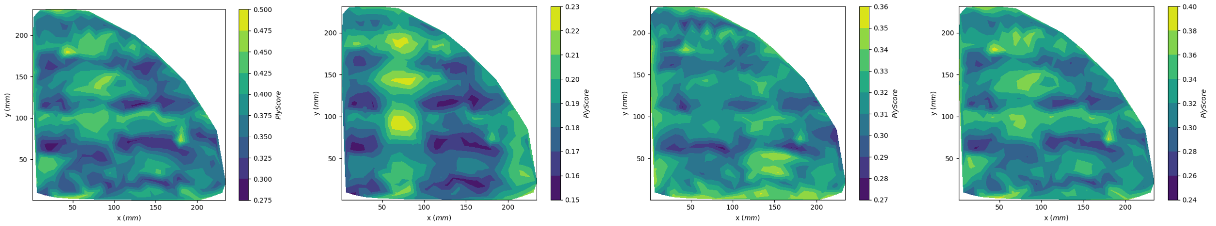

(a) Coverage (b) Angle Deviation (c) Excess Steering (d) Combined

Natural Strategy

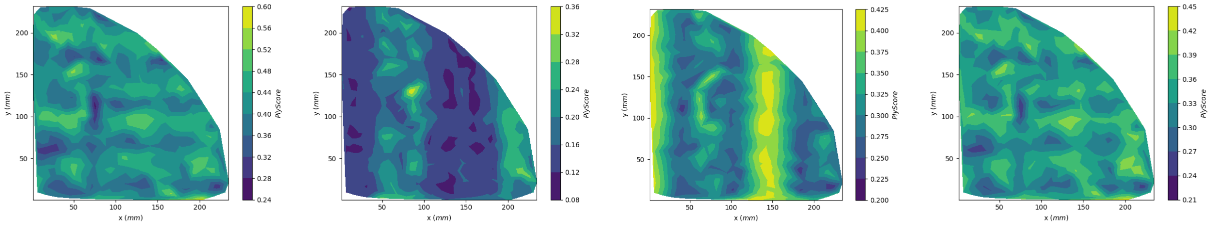

(e) Coverage (f) Angle Deviation (g) Excess Steering (h) Combined

Rosette-Parallel Strategy

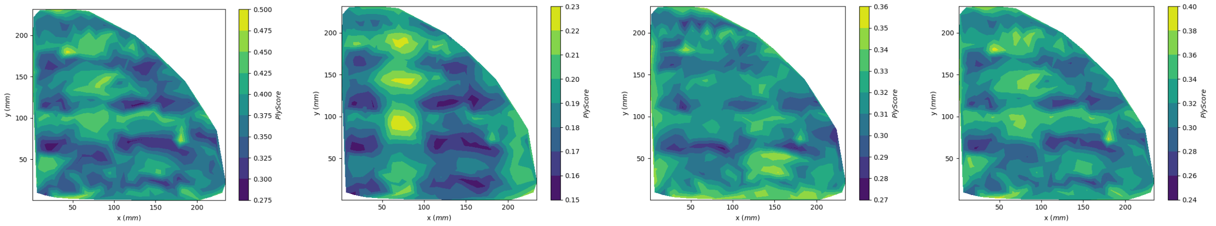

(i) Coverage (j) Angle Deviation (k) Excess Steering (l) Combined

Natural-Parallel Strategy

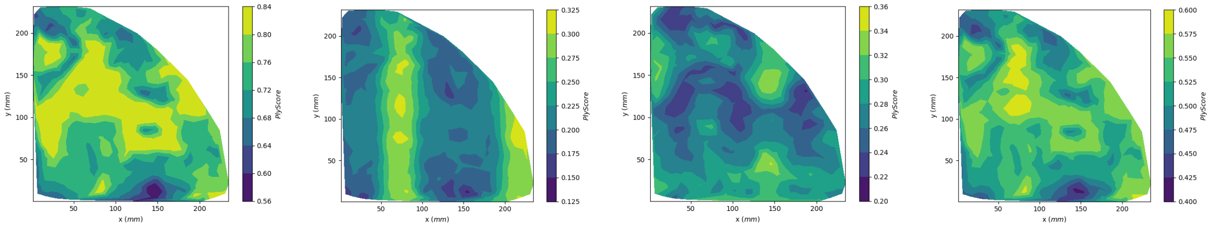

(m) Coverage (n) Angle Deviation (o) Excess Steering (p) Combined

Figure 8.8 Score distributions of periodic surface (variation 2 - $\theta = 0°$)

parallel strategies continue to exhibit some banding which is orthogonal to the fiber orientation, but is significantly less pronounced than the distributions from figure 8.6.

Figure 8.10 presents scores distributions for the 90° fiber orientation ply scenarios. The banding exhibited in the 90° fiber orientations maintain the same banding trends

Rosette Strategy

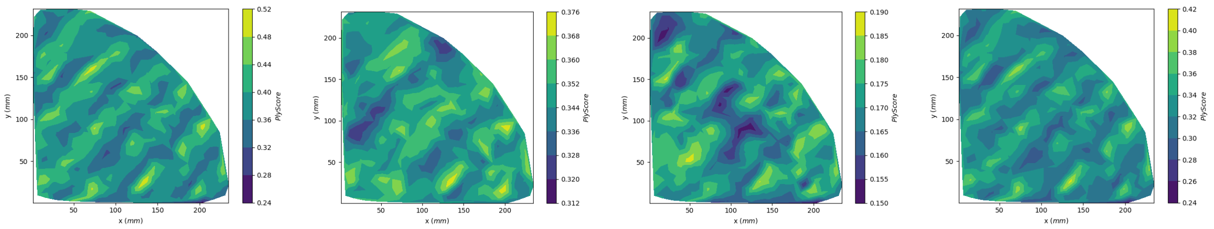

(a) Coverage (b) Angle Deviation (c) Excess Steering (d) Combined

Natural Strategy

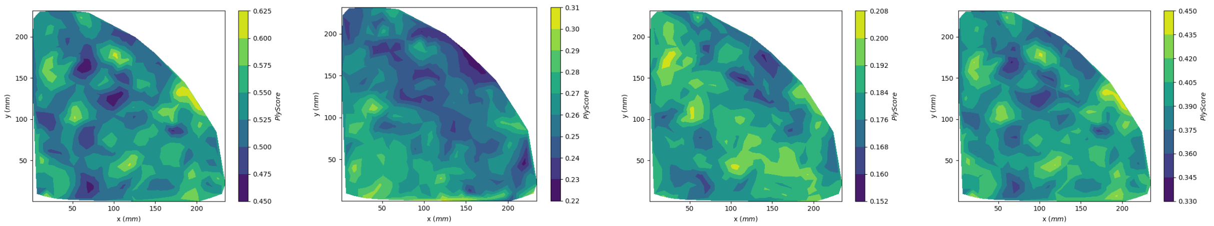

(e) Coverage (f) Angle Deviation (g) Excess Steering (h) Combined

Rosette-Parallel Strategy

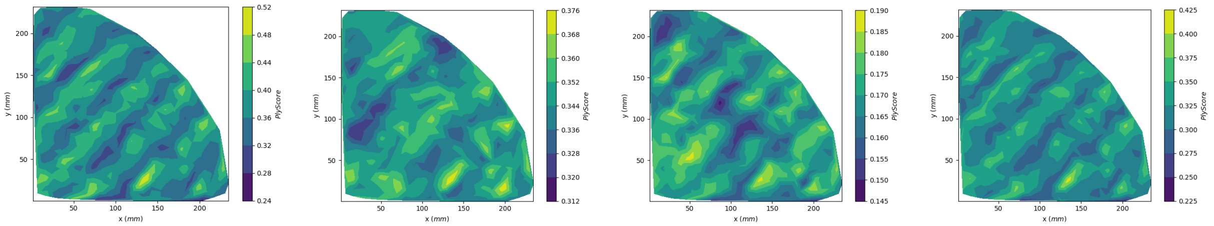

(i) Coverage (j) Angle Deviation (k) Excess Steering (l) Combined

Natural-Parallel Strategy

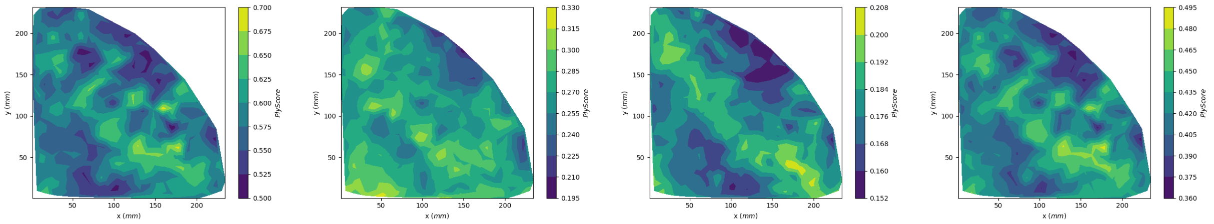

(m) Coverage (n) Angle Deviation (o) Excess Steering (p) Combined

Figure 8.9 Score distributions of periodic surface (variation 2 - $\theta = 45°$)

for both rosette and natural path strategies. However, more contrast can be observed for the scoring distributions as opposed to the lower curvature variation of the tool surface. The contrast develops from well defined regions of lower and higher scores, with shorter gradients between the two. This differs from the previous set, where more

Rosette Strategy

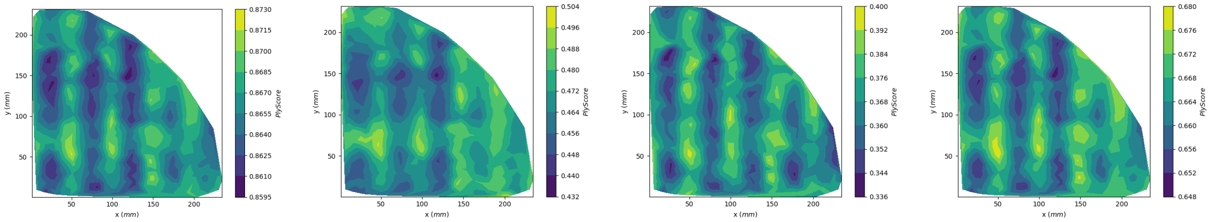

(a) Coverage (b) Angle Deviation (c) Excess Steering (d) Combined

Natural Strategy

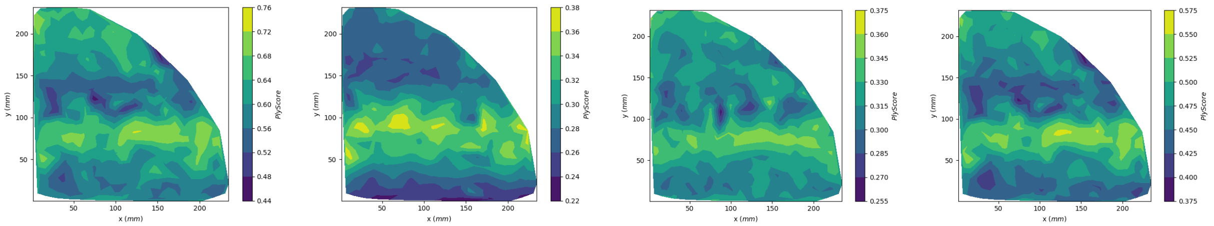

(e) Coverage (f) Angle Deviation (g) Excess Steering (h) Combined

Rosette-Parallel Strategy

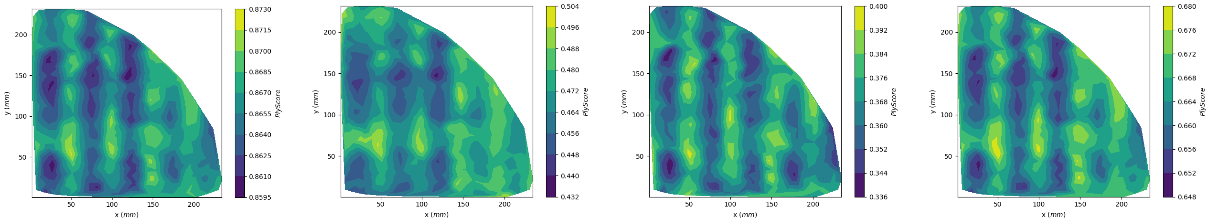

(i) Coverage (j) Angle Deviation (k) Excess Steering (l) Combined

Natural-Parallel Strategy

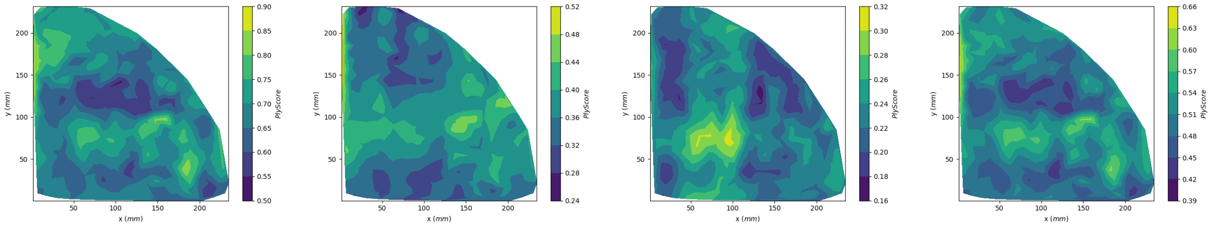

(m) Coverage (n) Angle Deviation (o) Excess Steering (p) Combined

Figure 8.10 Score distributions of periodic surface (variation 2 - $\theta = 90°$)

extensive gradients were observed between the scoring extremes. Additionally, fewer bands were observed for the natural and natural-parallel strategies, with a primary band occurring along the $y = 75mm$ regions of the ply boundary.

VARIATION 3 SCORING

The final variation of the periodic tool surface additionally increased the overall amplitude of the curvature exhibited by the tool surface. The amount of Gaussian curvature is roughly double from the previous tool surface variation. The frequency of the underlying *sine* functions was left unchanged.

Figure 8.11 presents scores distributions for the 0° fiber orientation ply scenarios. First an observation towards the banding which was very prominent from the previous tool surface variations. For this instance, the banding has been significantly reduced for the rosette and rosette-parallel strategies. Some banding along the fiber orientation can be detected for the angle deviation defect, but does not appear as clearly as previously observed. However, a vertical component of banding has begun to appear for the rosette and rosette-parallel strategy along the $x = 75mm$ region. This was observed in previously instances, but has begun to dominate as the horizontal banding component diminishes.

The scoring distribution remains largely unchanged for the natural and natural-parallel strategies. However, significant a reduction in the extent of high scoring regions have begun to recede.

Figure 8.12 presents scores distributions for the 45° fiber orientation ply scenarios. The general spatial score distribution between all layup strategies was largely unchanged from the previous tool surface variations. The largest changes in the overall magnitude of scores occured in the rosette and rosette-parallel strategies for the excessvie steering defects. Thus, the existence of excees steering deviation for those ply scenarios result in roughly a halving of the excess steering scores. Overall scores for the rest of the ply scenario combinations were largely unchanged.

Figure 8.13 presents scores distributions for the 90° fiber orientation ply scenarios. The distributions for the rosette and rosette-parallel strategy have continued to lose the spatial organization of the scores observed from the previous tool surface

Rosette Strategy

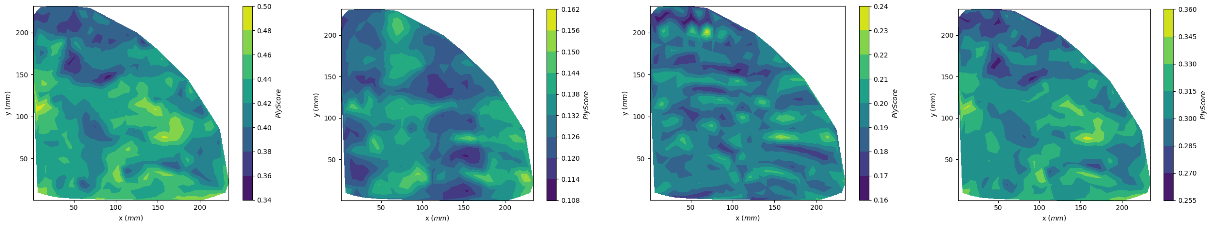

(a) Coverage (b) Angle Deviation (c) Excess Steering (d) Combined

Natural Strategy

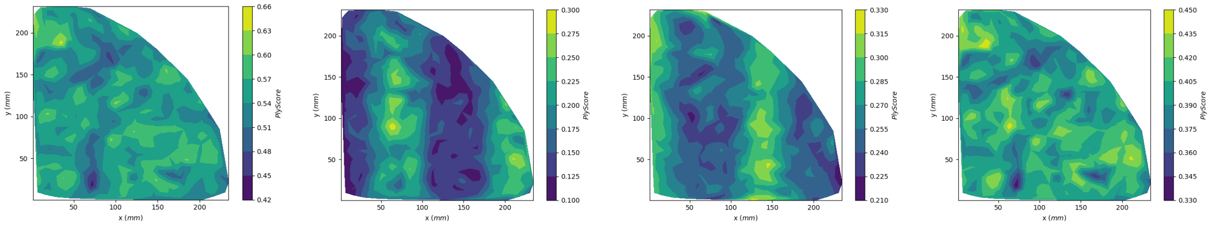

(e) Coverage (f) Angle Deviation (g) Excess Steering (h) Combined

Rosette-Parallel Strategy

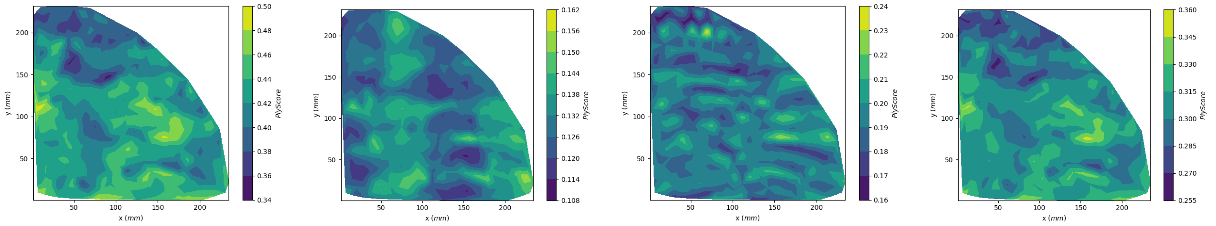

(i) Coverage (j) Angle Deviation (k) Excess Steering (l) Combined

Natural-Parallel Strategy

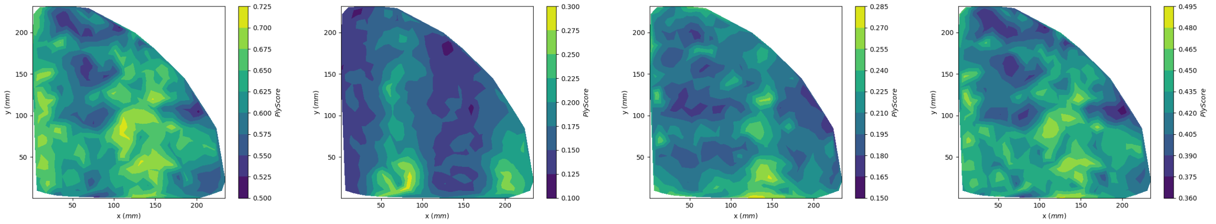

(m) Coverage (n) Angle Deviation (o) Excess Steering (p) Combined

Figure 8.11 Score distributions of periodic surface (variation 3 - $\theta = 0°$)

variations. The distribution can still be observed for the angle deviation defect, but can not be clearly observed for the coverage and excess steering defects.

However, the distribution of scoring for hte natural and natural-parallel strategies have persisted. Again, the banding follows the direction orthogonal to the fiber

Rosette Strategy

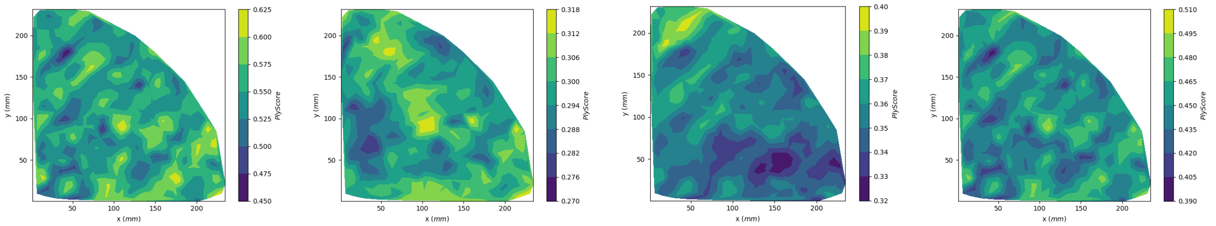

(a) Coverage (b) Angle Deviation (c) Excess Steering (d) Combined

Natural Strategy

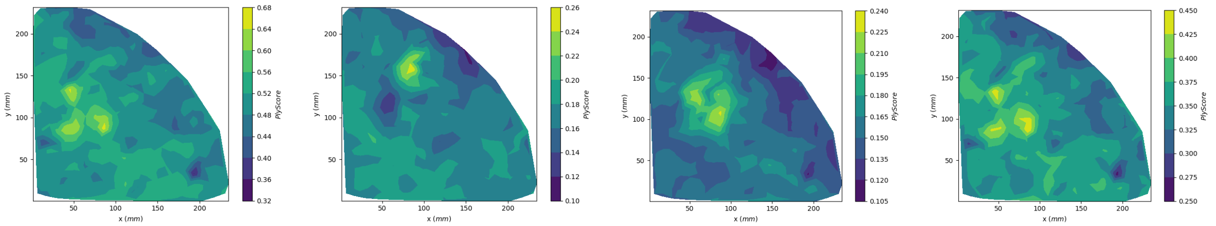

(e) Coverage (f) Angle Deviation (g) Excess Steering (h) Combined

Rosette-Parallel Strategy

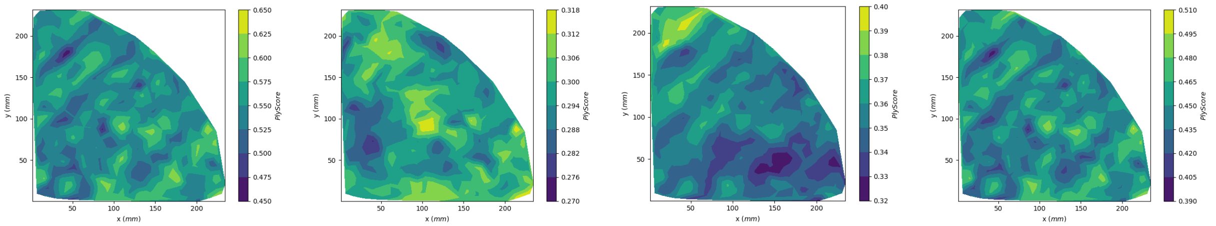

(i) Coverage (j) Angle Deviation (k) Excess Steering (l) Combined

Natural-Parallel Strategy

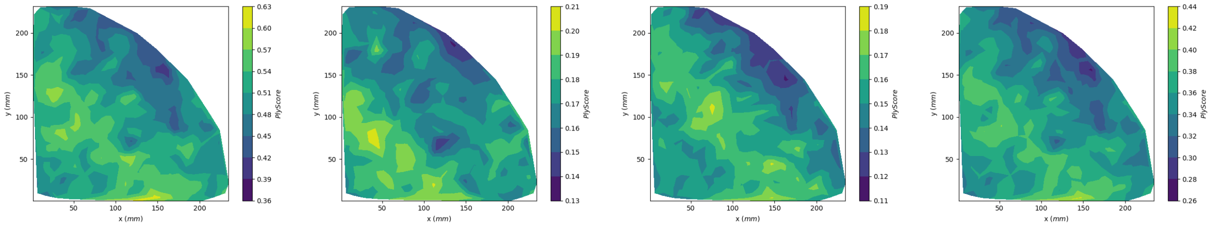

(m) Coverage (n) Angle Deviation (o) Excess Steering (p) Combined

Figure 8.12 Score distributions of periodic surface (variation 3 - $\theta = 45°$)

orientation, and the band of the highest scoring region follows the $y = 75mm$ path.

Some drop in the overall magnitude of scores was observed for each of the layup strategy and defect type. However, no significant drops in the magnitude were observed from the previous variation with lower Gaussian curvature.

Rosette Strategy

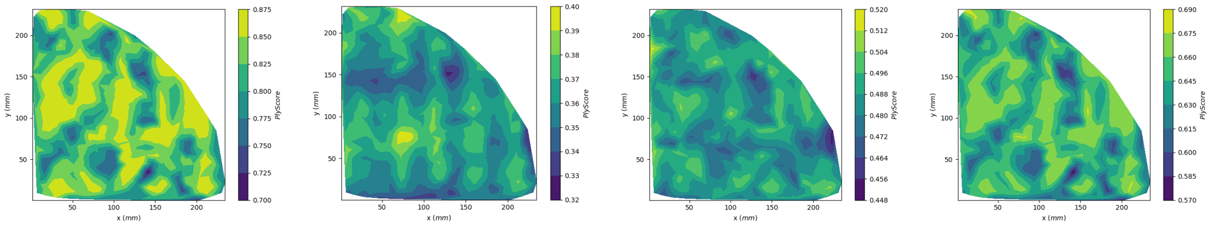

(a) Coverage (b) Angle Deviation (c) Excess Steering (d) Combined

Natural Strategy

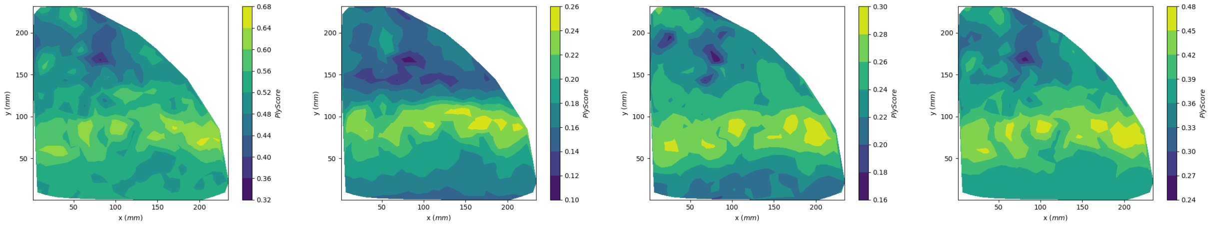

(e) Coverage (f) Angle Deviation (g) Excess Steering (h) Combined

Rosette-Parallel Strategy

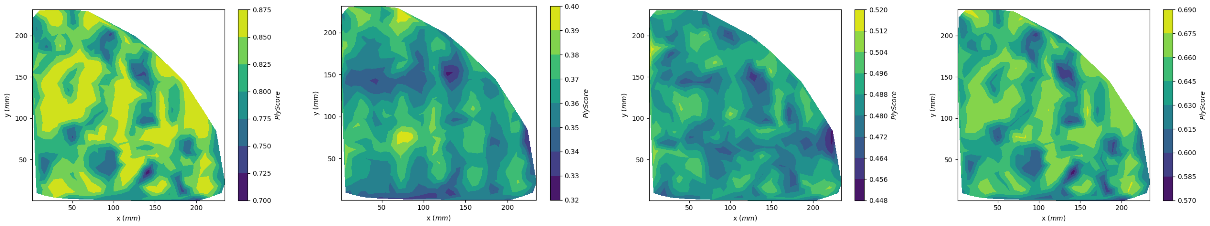

(i) Coverage (j) Angle Deviation (k) Excess Steering (l) Combined

Natural-Parallel Strategy

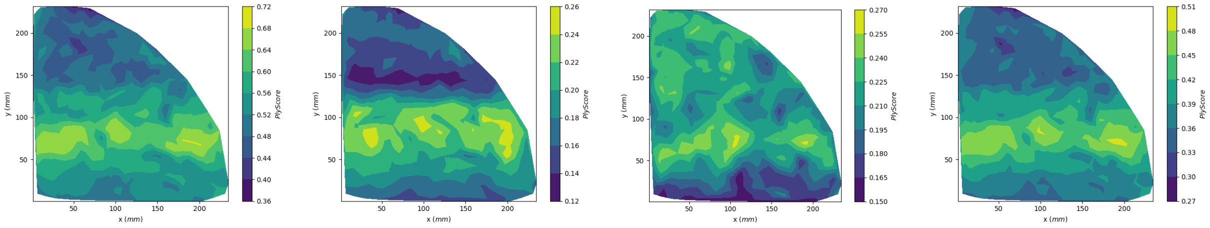

(m) Coverage (n) Angle Deviation (o) Excess Steering (p) Combined

Figure 8.13 Score distributions of periodic surface (variation 3 - $\theta = 90°$)

Histogram Distributions

The follow section covers the scoring histogram distributions for the rosette strategy. The histograms present a summarized view of the data from the previous sections covering the spatial distribution of scoring within the single quadrant of the ply boundary.

Each row represents the different variations of the tool surface geometry, working from the surface with the least curvature to the surface with the most Gaussian curvature. Each column represents the different fiber angles used to generate the fiber paths. Finally, each histogram has a plot of the individual defect scores, including coverage, steering and angle deviation, additionally including the combined scoring metric consisting of all defects.

The $x-axis$ indicates the scores of the scenarios, with the $y-axis$ describing the number of ply scenarios which fell into that scoring range. The plot legend indicates the average score and the associate standard deviation.

Beginning with variation 1, a significant shift in the scoring distributions was observed between the 0° plies and 45°/90° plies. The primary component which shifted was the angle deviation scoring distribution. The 0° plies seemingly exhibited excessive angle deviation resulting in the lower scores. However, for the other fiber orientations, excessive steering was primarily observed.

Moving to the second variation, a significant drop in the average scores can be directly observed. However, the drop in scores for the 90° plies was much less significant for the coverage defect. Such that the coverage score significantly affects the average, maintaining a much higher after score than the other ply angles. Additionally, coverage comprises the high scoring priority for each of the fiber angles, as was observed for the first tool surface variation.

The final surface variation exhibits a much higher variation in scoring mean than the previous variations. The coverage prioritization has remained as the highest scoring component.

Variation 1

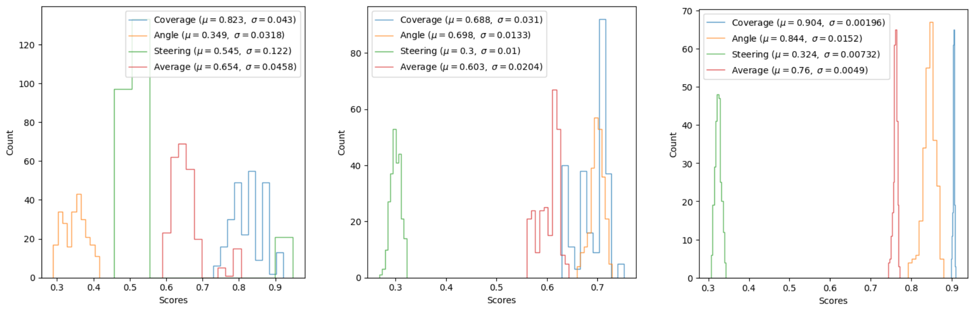

(a) $\theta = 0°$ (b) $\theta = 45°$ (c) $\theta = 90°$

Variation 2

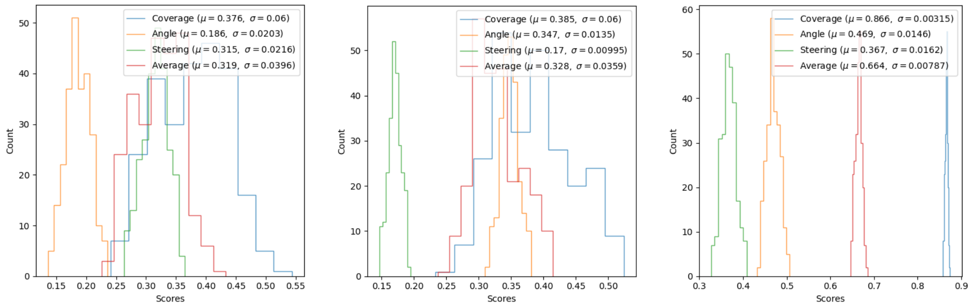

(d) $\theta = 0°$ (e) $\theta = 45°$ (f) $\theta = 90°$

Variation 3

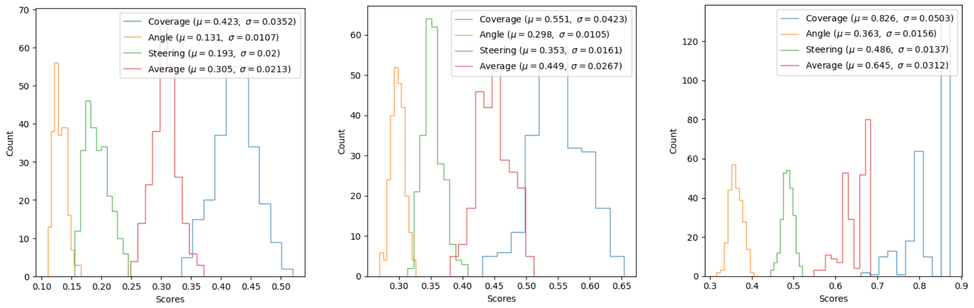

(g) $\theta = 0°$ (h) $\theta = 45°$ (i) $\theta = 90°$

Figure 8.14 Score distributions of periodic surface

Angle Deviation Distribution

The follow figures demonstrate the aggregate average scoring for excess angle deviation. The individual groups of figures are organized by fiber angle, then surface variation and finally the layup strategy used to generate the fiber coverage.

Figure 8.15 presents the plots for fiber angle deviation for the 0° plies. Similarly

Variation 1

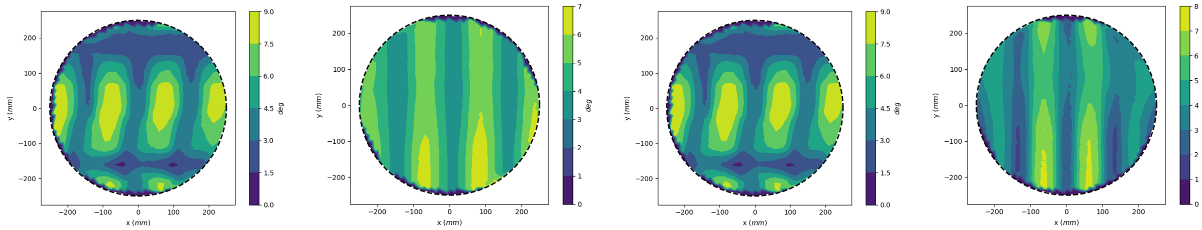

(a) Rosette (b) Natural (c) Rosette Parallel (d) Natural Parallel

Variation 2

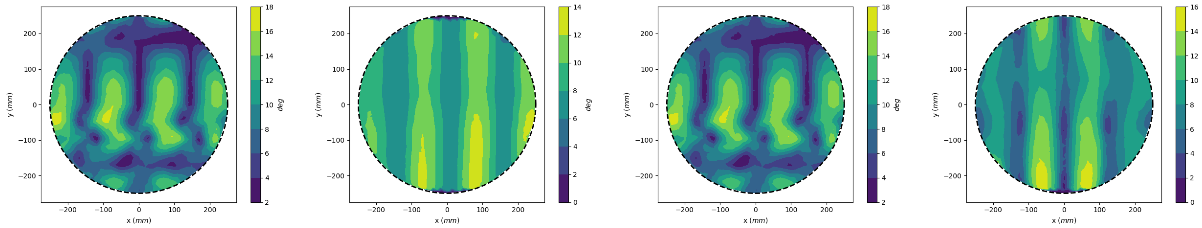

(e) Rosette (f) Natural (g) Rosette Parallel (h) Natural Parallel

Variation 3

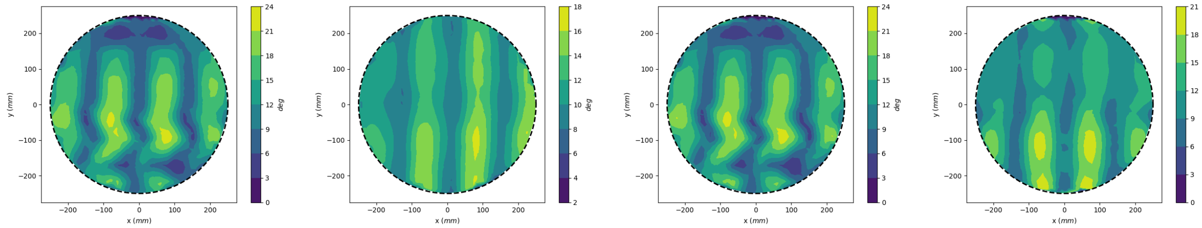

(i) Rosette (j) Natural (k) Rosette Parallel (l) Natural Parallel

Figure 8.15 Aggregate average of excess angle deviation for periodic surfaces ($\theta = 0°$)

to the score distributions from section 8.2.1, periodic banding is present, with very regular intervals. It is important to notice the variation in distributions between the rosette and natural layup strategy variations. The rosette and rosette-parallel strategy have a localized hotspot, which was not extend to the ends of the ply boundary. However, the natural and natural-parallel strategies exhibit excessive angle deviation much closer to the ply boundaries.

Additionally, the localization fo the defects corresponds to specific features within the Gaussian curvature distribution. For the rosette strategies, the most angle deviations occurs around the saddle points of defection, (figure 8.3). The angle deviation for the natural and natural-parallel strategies are less locally restricted to the saddle points, but to follow the inflection point of the Gaussian curvature in the orientation orthogonal to the fiber paths.

Finally, the overall magnitude of the fiber angle does increase with increase in the underlying Gaussian curvature. Such a trend exist for each strategy type. Additionally, the increase in magnitude from variation 1 to variation 2 has the largest change, where the difference between variation 2 and variation 3 is less drastic. Interestingly, this does correlate to the general trend in the overall increase in the magnitude of Gaussian curvature between the variations.

Variation 1

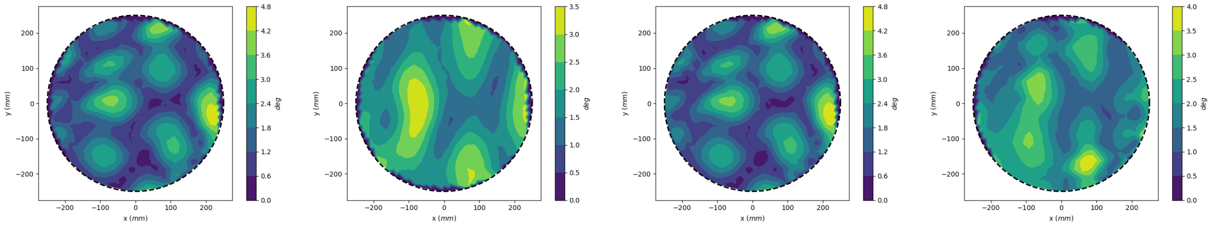

(a) Rosette (b) Natural (c) Rosette Parallel (d) Natural Parallel

Variation 2

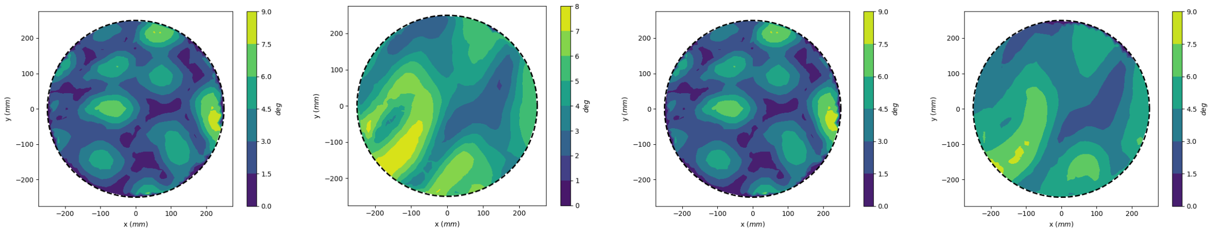

(e) Rosette (f) Natural (g) Rosette Parallel (h) Natural Parallel

Variation 3

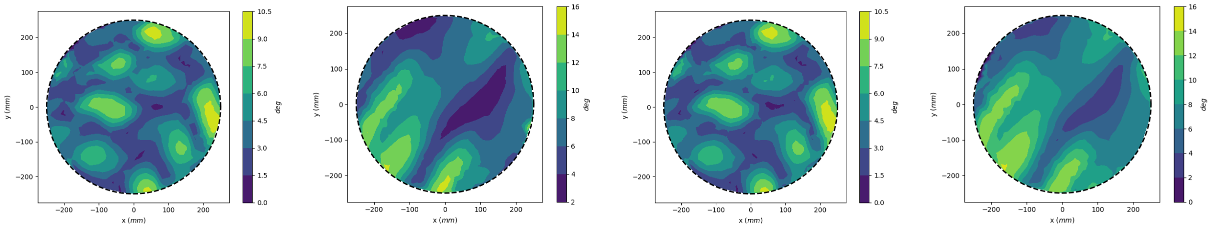

(i) Rosette (j) Natural (k) Rosette Parallel (l) Natural Parallel

Figure 8.16 Aggregate average of excess angle deviation for periodic surfaces ($\theta = 45°$)

Figure 8.16 presents the plots for fiber angle deviation for the 45° plies. Trends in the distribution of excess angle deviation again differ between the rosette and natural strategy families. However, the trends are less well defined than the previous 0° plies, where the rosette strategy has distributed and mostly local hotspots. Whereas the natural and natural-parallel strategies have more broadly distributed hotspots.

However, the trends for all layup strategies still trend with the locations of inflection in the Gaussian curvature. The most significant angle deviation occurs around the saddle points, with the majority occurring around regions of singular inflection.

Variation 1

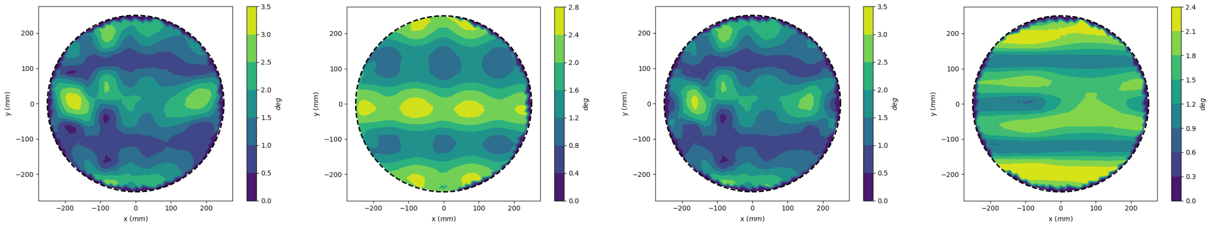

(a) Rosette (b) Natural (c) Rosette Parallel (d) Natural Parallel

Variation 2

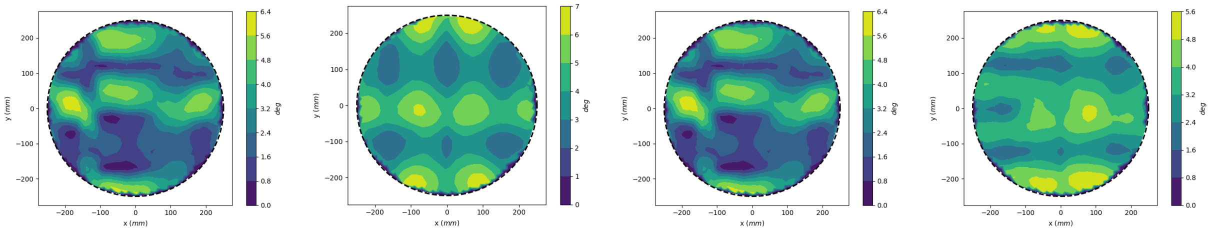

(e) Rosette (f) Natural (g) Rosette Parallel (h) Natural Parallel

Variation 3

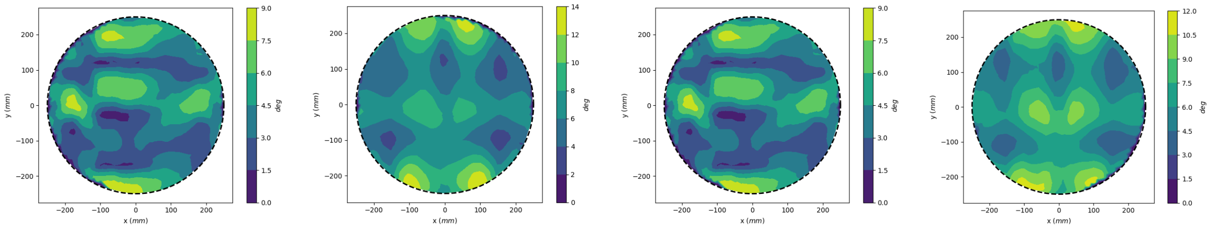

(i) Rosette (j) Natural (k) Rosette Parallel (l) Natural Parallel

Figure 8.17 Aggregate average of excess angle deviation for periodic surfaces ($\theta = 90°$)

Figure 8.17 presents the plots for fiber angle deviation for the 90° plies. The spatial distribute of the excess angle deviation is again more strongly defined in the 90° oriented fiber paths. The majority of the banding occurs orthogonally to the fiber direction, for both the rosette and natural based path strategies. Interestingly, the excess angle deviation is better defined for the natural and natural-parallel strategies. The majority of the angle deviation occurs near the inflection regions for the Gaussian curvature.

Excessive Steering Distribution

The follow figures demonstrate the aggregate average scoring for excessive fiber path steering. The individual groups of figures are organized by fiber angle, then surface variation and finally the layup strategy used to generate the fiber coverage. Blank regions of the plots indication areas where the steering radius was unable to measured accurately, and thus the data points have been discarded to avoid skewing data for the remainder of the ply boundary

Figure 8.18 presents the plots for excessive steering for the 0° plies. All the ply scenarios for the lowest curvature tool surface exhibit very low levels of fiber steering. As such, the minimal radius experienced here is several meters. Therefore, little to no fiber steering has occurred, even for the natural and natural-parallel strategies.

However, subsequent variations with the increase in curvature, do begin to present regions of the tool surface where fiber steering becomes necessary for fiber placement. The spatial distribution of the excessive steering follow the fiber orientation. For both the rosette and natural path strategy families, the majority of steering occurs in bands at approximately $y = \pm 100mm$. These horizontal bands corresponds to the y level where the minimal and maximal Gaussian curvature is experienced. The minimum steering for each set of ply scenarios follows the inflection points along the y direction.

Figure 8.19 presents the plots for excessive steering for the 45° plies. The steering

Variation 1

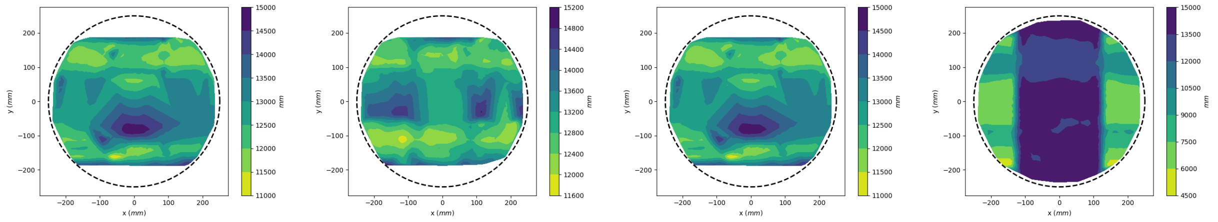

(a) Rosette (b) Natural (c) Rosette Parallel (d) Natural Parallel

Variation 2

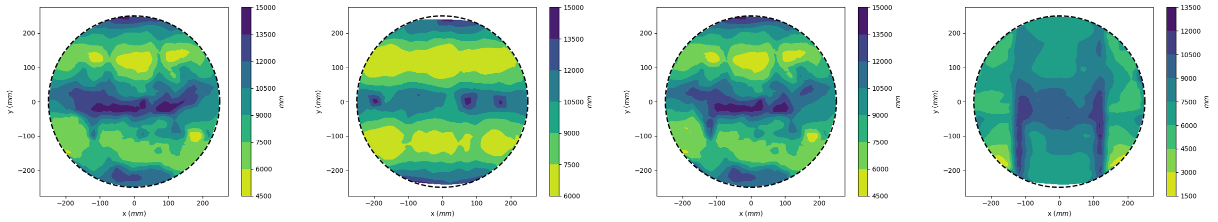

(e) Rosette (f) Natural (g) Rosette Parallel (h) Natural Parallel

Variation 3

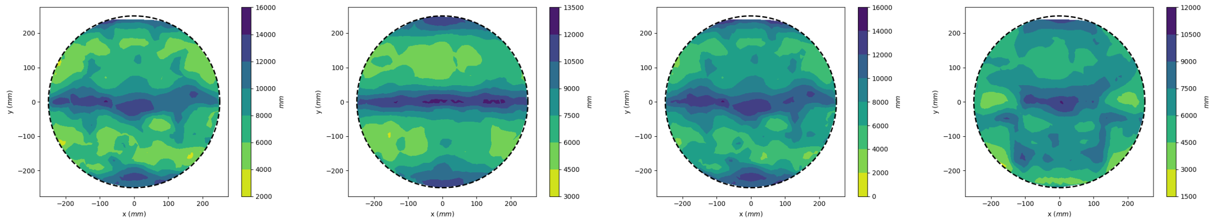

(i) Rosette (j) Natural (k) Rosette Parallel (l) Natural Parallel

Figure 8.18 Aggregate average of excess steering radius for periodic surfaces ($\theta = 0°$)

presented here varies greatly from the previous plot, and even a moderate amount of steering is required for the lowest curvature tool surface variation.

The majority of excessive steering occurs within the rosette and rosette parallel strategies for each tool surface variation. Continuous bands are no observed here, but instead localized regions where steering occurs between the ply scenarios.

Additionally, and inverse correlation in the spatial distribution of the excess steering is observed between the rosette and natural strategy families. Maximum steering for the rosette strategies occurs between the peaks and troughs of curvature, and indeed along the inflection points. Alternatively, the majority of steering for the natural and natural-parallel strategies occurs at the maximal and minimal regions of

Variation 1

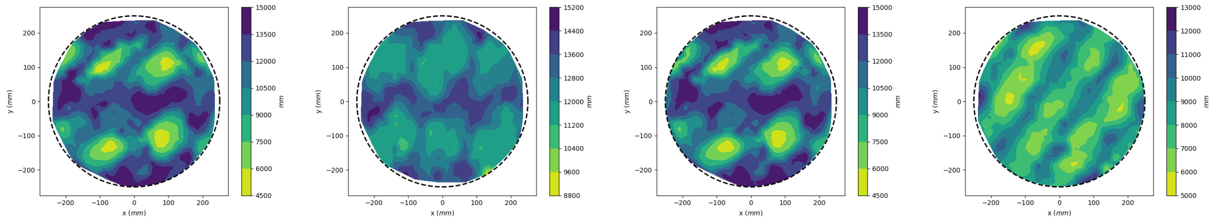

(a) Rosette (b) Natural (c) Rosette Parallel (d) Natural Parallel

Variation 2

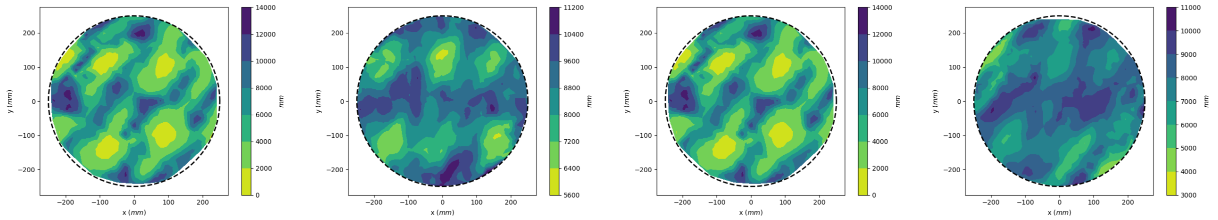

(e) Rosette (f) Natural (g) Rosette Parallel (h) Natural Parallel

Variation 3

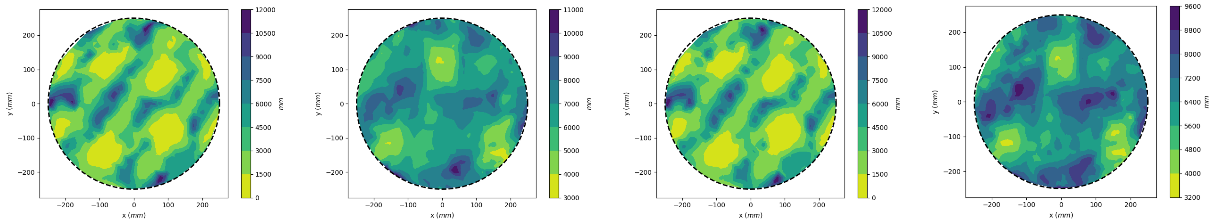

(i) Rosette (j) Natural (k) Rosette Parallel (l) Natural Parallel

Figure 8.19 Aggregate average of excess steering radius for periodic surfaces ($\theta = 45^\circ$)

Gaussian curvature. Interestingly the natural-parallel strategy tends to exhibit more steering than the base natural strategy.

Figure 8.20 presents the plots for excessive steering for the 90° plies. The spatial steering radius distributions again exhibit a pattern corresponding to the fiber orientation. Specifically in this case, the bands follow the fiber orientation.

The rosette and rosette-natural strategies exhibit very similar steer radius and do no differ significantly as the tool surface curvature is increased. However, the natural and natural-parallel strategies to differ moderately. The natural path strategy exhibits the majority of steering in vertical bands at each of the minimal and maximal

Variation 1

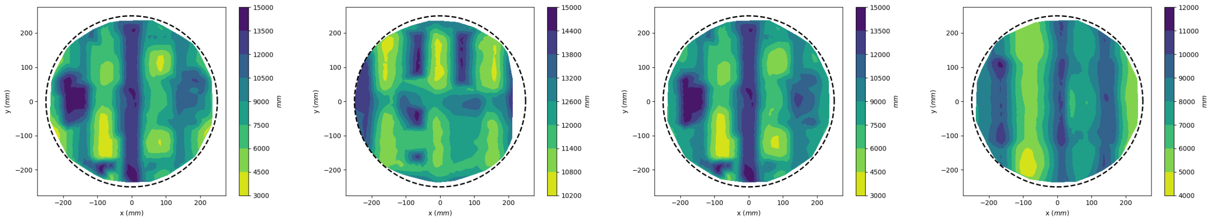

(a) Rosette (b) Natural (c) Rosette Parallel (d) Natural Parallel

Variation 2

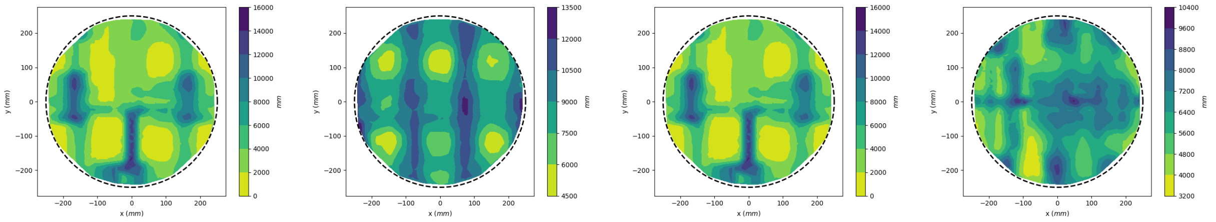

(e) Rosette (f) Natural (g) Rosette Parallel (h) Natural Parallel

Variation 3

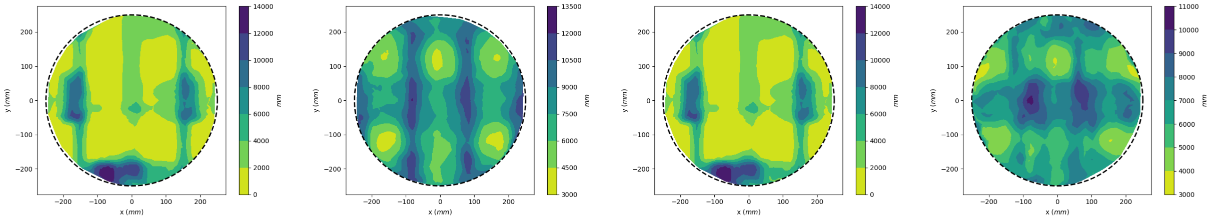

(i) Rosette (j) Natural (k) Rosette Parallel (l) Natural Parallel

Figure 8.20 Aggregate average of excess steering radius for periodic surfaces ($\theta = 90°$)

Gaussian curvature. Instead, the rosette, rosette-parallel, and natural-parallel produce the majority of steering along the vertical bands of inflection of the Gaussian curvature. Initially the natural-parallel strategy exhibits much high magnitude of steering than the base natural strategy, however as the surface curvature increases, their magnitude of steering begins to converge.

COURSE GAP DISTRIBUTION

The follow figures demonstrate the aggregate average scoring for course-to-course gaps. Points within these plots that exhibit high values indicate regions where gap defects were particularly common among the ply scenarios. The individual groups of figures are organized by fiber angle, then surface variation and finally the layup strategy used to generate the fiber coverage.

Variation 1

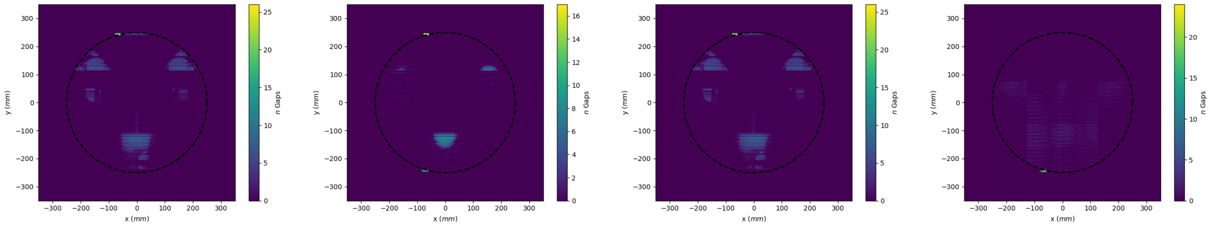

(a) Rosette (b) Natural (c) Rosette Parallel (d) Natural Parallel

Variation 2

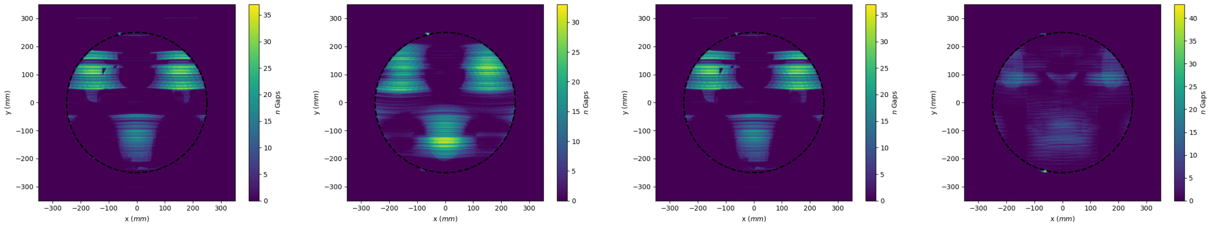

(e) Rosette (f) Natural (g) Rosette Parallel (h) Natural Parallel

Variation 3

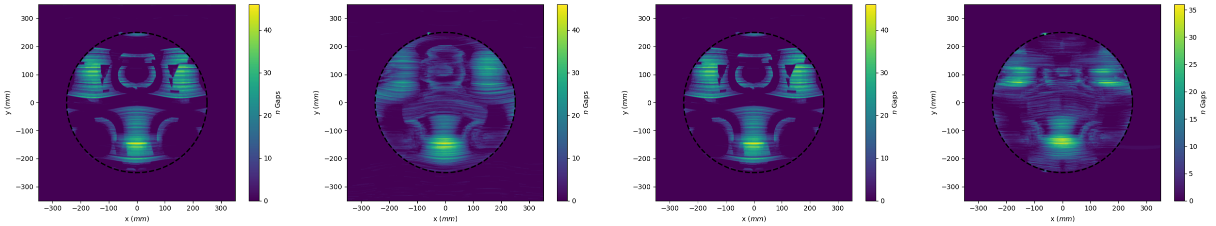

(i) Rosette (j) Natural (k) Rosette Parallel (l) Natural Parallel

Figure 8.21 Aggregate of excess course-course gaps for periodic surfaces ($\theta = 0°$)

Figure 8.21 presents the plots for gap distribution for the 0° plies. Minimal presence of gaps were observed for the lowest curvature tool surface variation. However, as the curvature is increased, the presence of course gaps is similarly increased. Interestingly, the course gaps are primarily occurring near the regions of maximum negative Gaussian curvature. Most notably, the natural-parallel strategy tends to introduce the lease amount of course-to-course gaps when compared to the other layup strategies.

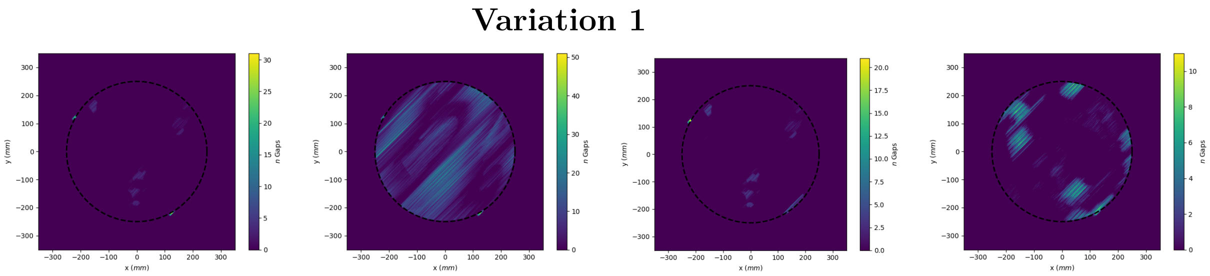

(a) Rosette (b) Natural (c) Rosette Parallel (d) Natural Parallel

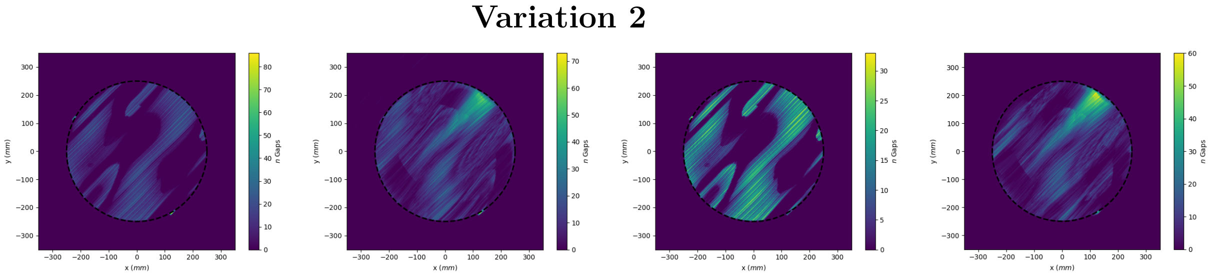

(e) Rosette (f) Natural (g) Rosette Parallel (h) Natural Parallel

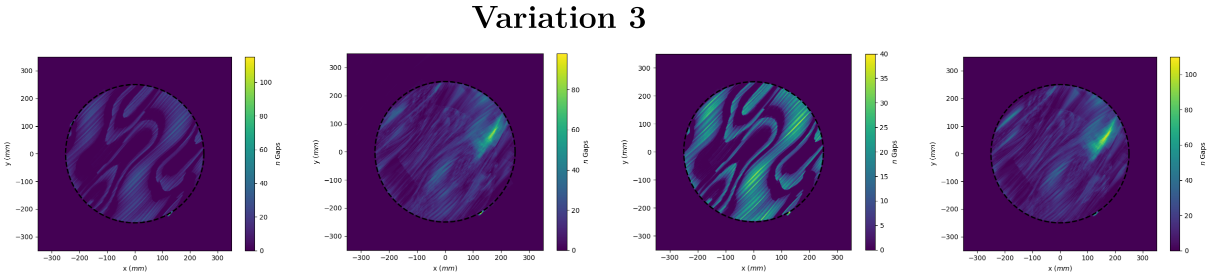

(i) Rosette (j) Natural (k) Rosette Parallel (l) Natural Parallel

Figure 8.22 Aggregate of excess course-course gaps for periodic surfaces ($\theta = 45°$)

Figure 8.22 presents the plots for gap distribution for the 45° plies. Some correlation can be observed with the banding of the course-to-course gaps along the fiber orientation. The overall amount of gaps increases as the tool surface Gaussian curvature is increased. In this instance, the rosette-parallel strategy generally produces the lesser amount of course-to-course gaps, but instead they have been broadly distribute through the ply boundary. This is in contrast to teh other strategies where the gaps typically occurred around the same locations. In this case, no clear correlation was observed between the gap distribution and the underlying tool surface curvature.

Figure 8.23 presents the plots for gap distribution for the 90° plies. The presence of gaps for the 90° plies present a very different situation from the 0° plies. For

Variation 1

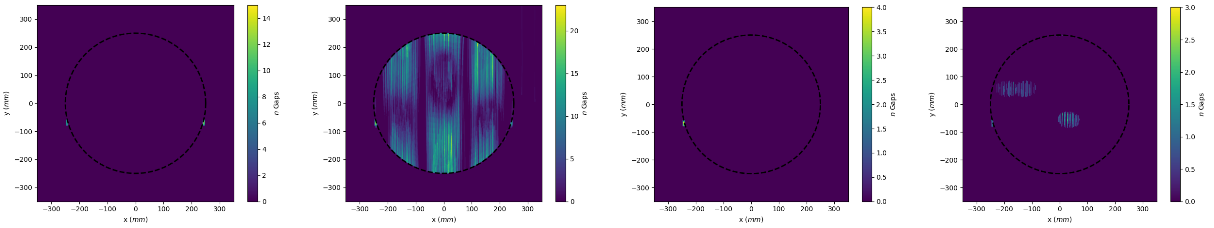

(a) Rosette (b) Natural (c) Rosette Parallel (d) Natural Parallel

Variation 2

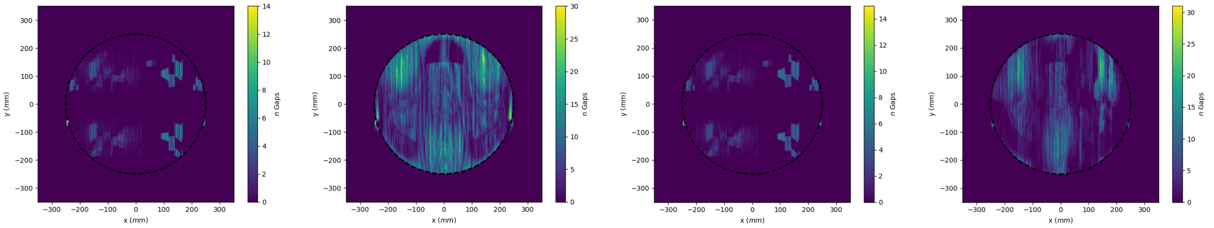

(e) Rosette (f) Natural (g) Rosette Parallel (h) Natural Parallel

Variation 3

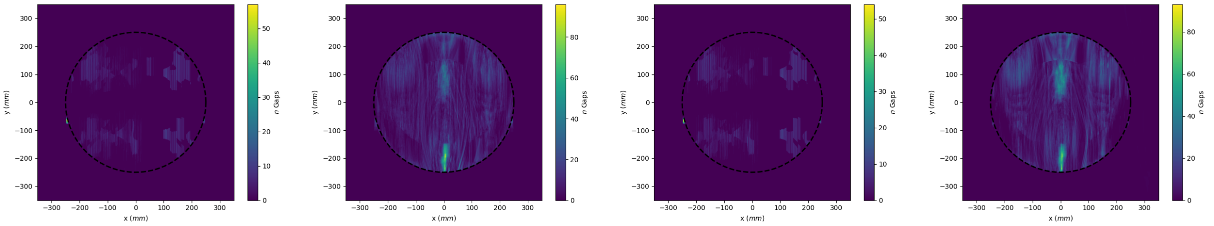

(i) Rosette (j) Natural (k) Rosette Parallel (l) Natural Parallel

Figure 8.23 Aggregate of excess course-course gap for periodic surfaces ($\theta = 90°$)

these ply scenarios, natural strategy produces significantly more gaps, whereas the rosette and rosette parallel strategy produce a very minimal amount. Natural-parallel follows closely behind the base natural strategy in terms of gap presence. From the gap distributions that can be observed, the majority of gaps occur around the regions of negative Gaussian curvature, with some additionally occurring around the positive Gaussian curvature as well. It is important to note that the effective period of curvature is nearly twice as long as experienced by paths in 0° orientation.

Course Overlap Distribution

The follow figures demonstrate the aggregate average scoring for course-to-course overlaps. Points within these plots that exhibit high values indicate regions where overlap defects were particularly common among the ply scenarios. The individual groups of figures are organized by fiber angle, then surface variation and finally the layup strategy used to generate the fiber coverage.

Variation 1

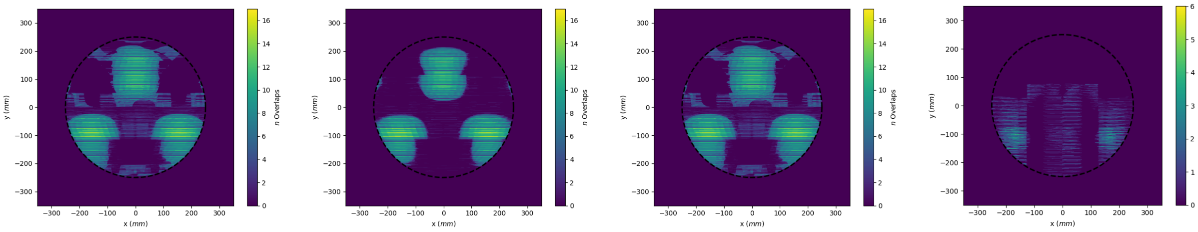

(a) Rosette (b) Natural (c) Rosette Parallel (d) Natural Parallel

Variation 2

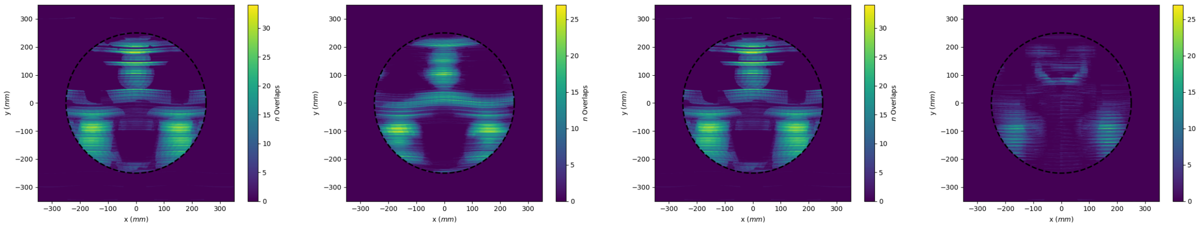

(e) Rosette (f) Natural (g) Rosette Parallel (h) Natural Parallel

Variation 3

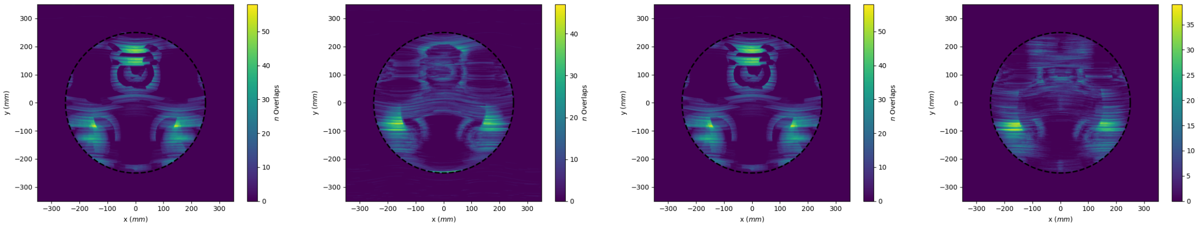

(i) Rosette (j) Natural (k) Rosette Parallel (l) Natural Parallel

Figure 8.24 Aggregate of excess course-course overlaps for periodic surfaces ($\theta = 0°$)

Figure 8.24 presents the plots for overlap distribution for the 0° plies. The general trend in the distribution of overlap defects is very similar for rosette, rosette-parallel and natural path strategies. However, the natural-parallel strategy exhibits significantly lower levels of defects while still sharing the same general distribution. The overlap distribution occurs inversely to the gap distributions, with overlaps occurring near the regions of maximal Gaussian curvature. Additionally, increasing the magnitude of the curvature also results in an increase of the presence of overlap defects.

Variation 1

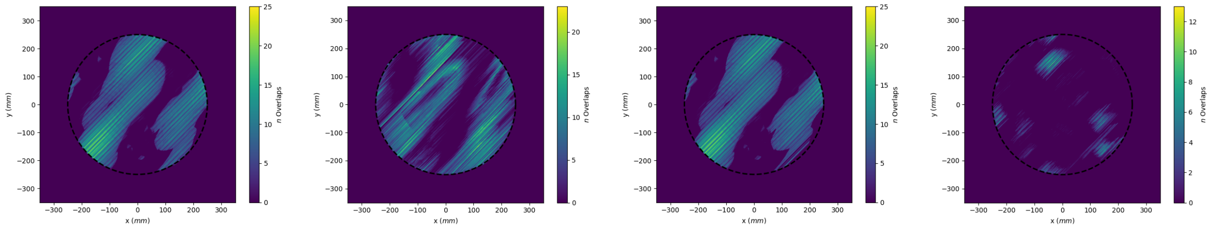

(a) Rosette (b) Natural (c) Rosette Parallel (d) Natural Parallel

Variation 2

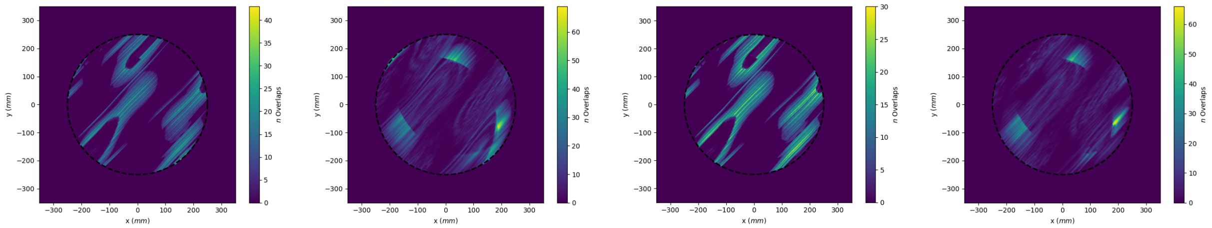

(e) Rosette (f) Natural (g) Rosette Parallel (h) Natural Parallel

Variation 3

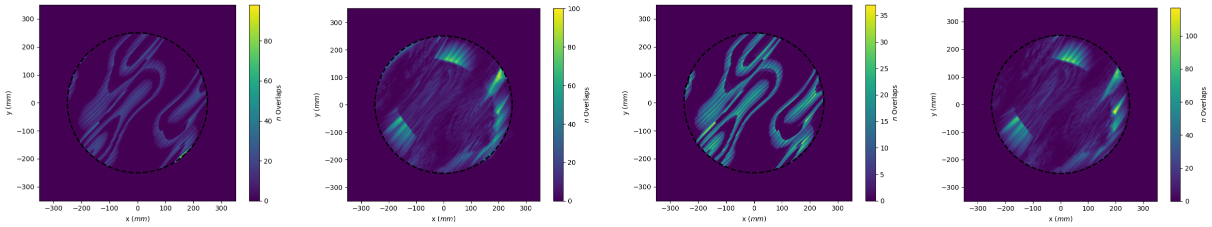

(i) Rosette (j) Natural (k) Rosette Parallel (l) Natural Parallel

Figure 8.25 Aggregate of excess course-course overlaps for periodic surfaces ($\theta = 45°$)

Figure 8.25 presents the plots for overlap distribution for the 45° plies. The presence of overlaps was more prominent among the lower Gaussian curvature surfaces, but still does not show stress correlation to the location of the Gaussian curvature, similarly to the gap distribution for the 45° plies. However, the gap and overlaps do have a strong inverse correlation, with gaps and overlaps main occurring mutually exclusive throughout the ply boundary.

Variation 1

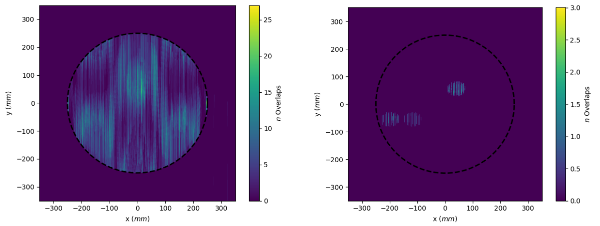

(a) Natural (b) Natural Parallel

Variation 2

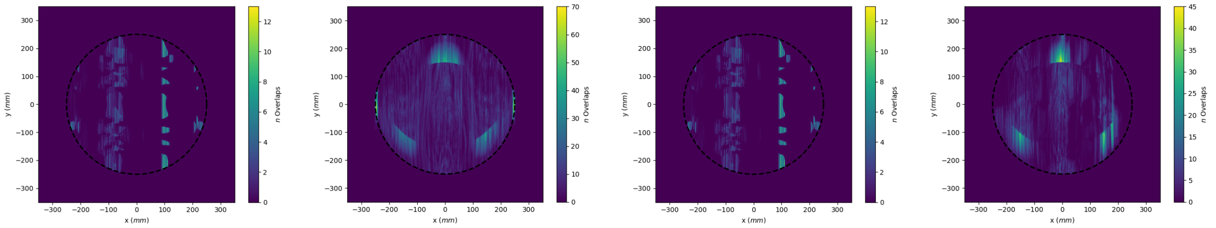

(c) Rosette (d) Natural (e) Rosette Parallel (f) Natural Parallel

Variation 3

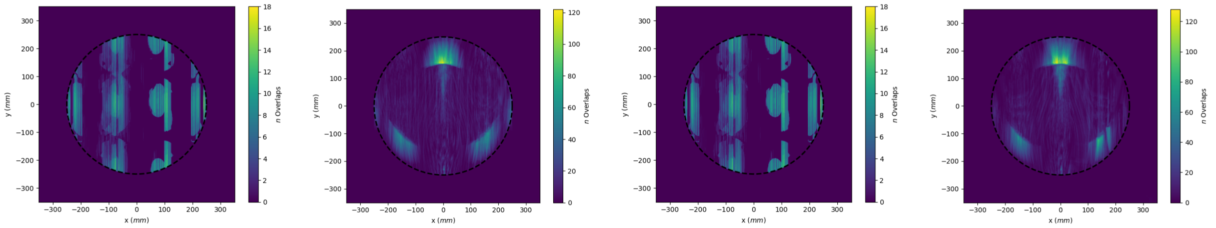

(g) Rosette (h) Natural (i) Rosette Parallel (j) Natural Parallel

Figure 8.26 Aggregate of excess course-course overlaps for periodic surfaces ($\theta = 90°$)

Figure 8.26 presents the plots for overlap distribution for the 90° plies. The rosette and rosette-parallel plots were excluded from variation 1 due to no presence of overlap defects. Similarly to the gap distributions for the 90° plies, distribution of overlaps is more poorly defined for this orientation. Some regions high in overlaps can be observed near the maximum Gaussian curvature again. The severity of overlaps additionally increases as the Gaussian curvature of the tool surface is increased.

8.3 CONCLUSIONS

This chapter presented an extensive exploration of the ply quantification methods discussed in chapter 3. Accordingly, this study provides insight into the relationship of the starting point and layup strategies along with the geometry of the tool surface. The complexity of the selected tool surfaces ensured that non-trivial fiber paths were generated and thus measurable fiber defects were produced.

The tool surfaces selection provided insight into the interaction of fiber paths with both periodic and saddle shaped tools. Additionally, the magnitude of the tool surface curvature was increased through several steps in order to additionally observe changes in defect presence as surface curvature was modified. Fiber paths were generated using the standard fiber angles: 0°, 45°, and 90°. The geometry of the fiber paths were generated utilizing the standard fiber layup strategies, including rosette, rosette parallel, natural, and natural-parallel.

The first set of results generated, present the generate distribution of ply scenario scores through the upper quadrant of the ply boundary using the quantification methods from chapter 3. These plots strong banding of the scores would occur, in which the distance between peaks would typically match the course width. Interestingly, the bands would typically follow the fiber orientation for the rosette and rosette-parallel strategy, but would occur orthogonal to the fiber orientation for natural and natural-parallel strategies. The scores were largely independent of the underlying surface curvature, and were primarily driven by the general fiber definitions.

The following sections looked more closely into the formation and distribution of the actual defects which constituted these scores. Typically, defect magnitude was closely correlated to the underlying surface curvature, such that high Gaussian curvature would typically experience more severe and broadly distributed defects. Additionally, the defects were largely driven by the existence and relative location of inflection points of the tool surfaces Gaussian curvature.

Angle deviation occurred most significantly in regions of double inflection points. The angle deviation was even more focused at these locations for rosette and rosette-parallel strategies, while natural and natural-parallel resulted in broader distributions.

Steering radius mostly occurred along the Gaussian inflection regions. Excessive steering would typically follow the fiber path orientation.

Finally, gap and overlap defects were closely correlated and generally existed in opposite regions of the tool surface. Course-to-course gaps occurred in regions of negative Gaussian curvature, and overlaps in regions of positive Gaussian curvature. Also it is important to note that the natural-parallel strategy typically results in the least amount of gap and overlap occurrences.

With the summary of these results, some conclusions can be made about the general trends of defects during fiber path generation and potentially help to better inform process planners. Since overall ply scores typically occur in bands, once a handful of points can be evaluated, it should be possible to predict the lower performing areas across the remainder of the tool surface. In other words, for the rosette and rosette-parallel strategies, the high scoring regions following the fiber direction and are approximately a coursed width apart. Alternatively natural and natural-parallel presented primarily orthogonal to the fiber direction. These trends can be established with a few sample ply scenarios and predicted across the remained of the tool surface in order to select appropriate seed points for fiber path generation.

Furthermore, the underlying defects which were averaged and quantified to generate the summary ply score show strong trends with the underlying surface curvature. Gaps and overlaps occur in regions of minimal and maximal curvature. In other words, these are regions where the tool surface would force neighboring courses to either diverge or converge to account for the peaks and valleys. The gap and overlaps were less severe when the fiber paths did not directly align with the inflection points of the tool surface. The natural-parallel strategy often had the most flexibility to create subsequent parallel courses and minimize the presence of gaps and overlaps.

Angle deviation and steering were also closely related to the underlying surface curvature. Angle deviation was best minimized by the rosette strategy, except in saddle points where the paths could not be sufficiently oriented. However, it had less broadly distributed regions of angle deviation when compared to the natural path. So it is important to note that even using the rosette strategy, high angle deviation will likely occur near regions of Gaussian curvature double inflection.

CHAPTER 9

DYNAMIC LAYUP STRATEGY

Layup strategies provide the fundamental functionality to create series of fiber paths which place material within the specified ply boundaries. The algorithms driving these layup strategies are limited to the material properties of composite tows, and design constraints.

The primary considerations towards material properties center around the stiffness of the carbon fibers within the tows. Due to the high level of stiffness, in-plane steering of the tows must be minimized where possible. The differential radii across the tow lead to a multitude of defects related to slipping and out of plane warping which arise as natural mechanisms of strain relief. Additionally, limitations within the steering of the tows will necessarily lead to the gaps and/or overlaps of material. These are generated where the generated of a perfectly parallel course would begin to exceed the minimum steering radius.

As for design considerations, the most significant feature of fiber paths is the level of angle deviation encountered. Simple CLT models rely on known fiber directions in order to model the expected performance of the composite structure. Fiber angle deviation induced by steering to accommodate the underlying curvature of the tool surface will cause the as manufactured structural performance to deviate from the modeled behavior of the structure. However, the effects of this can be mitigated through the connection between modeling and fiber path planning. Through this form of integration, the manufacturable fiber paths developed through the various layup strategies can be fed back to the structural model. With the manufacturable fiber paths, the structural analysis can be augmented and more accurate predictions of structural performance can be predicted. In the case that structural performance has been too severely degraded by the planned fiber paths, the fiber paths would be appropriately redefined. Naturally, an optimization strategy develops from the modeling and fiber path planning relationship.

Thus, the existence of fiber defects can be handled as a series of tradeoffs, where steering may improve coverage and the presence of gaps and overlaps, while increasing the amount of fiber angle deviation. Alternatively, parallel propagation strategies may be implemented, but may lead to excess steering or angle deviation violations.

The following chapter presents the development of the dynamic layup strategy. The dynamic layup strategy intends to abstract away the decision-making present with layup strategy selection. As previously discussed, fiber coverage methods and fiber defects are closely coupled, and present a series of tradeoffs. Furthermore, the selection of a given layup strategy will provide the specified benefits when some aspects of a different layup strategy may also be desired. Thus, the current paradigm with layup strategy selection is a very discrete one. The dynamic layup strategy presents a continuous integration of multiple layup strategies, where each may be partially implemented to gain a tailored blend of performance. Additionally, performance can vary over the tool surface, such that specified layup properties can be targeted for differet regions of the structure.

The chapter will begin with describing the basic tools and structure for the dynamic layup strategy. This includes the tools developed for working with continuous spline surfaces representing the tool surface. Additionally, the basic anatomy for the representing of the course structure are defined.

Following the fundamental implementation of a layup strategy, the specific algorithms defining the dynamic layup strategy are described. An evaluation of the dynamic layup strategy is subsequently provided, demonstrating its unique features

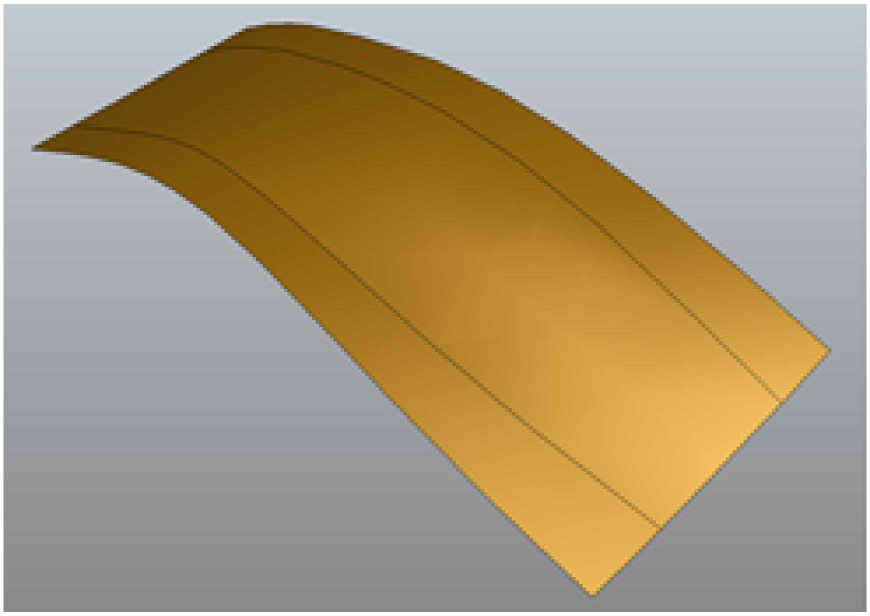

Figure 9.1 Tool surface consisting of 3 individual spline patches

in comparison to the traditional layup strategies as presented in chapter 8.

9.1 Layup strategy Utilities

In order to begin the implementation of additional layup strategies, it is necessary to understand the existing layup strategies. A comprehensive analysis of previously defined layup strategies is provided in section 2.3. The strategies primarily covered in this section rely on the geometry of the tool surface in addition to limitations placed on the propagation of additional fiber paths.

Additionally, it is necessary to implement the proper utilities for the generation of fiber paths on the continuous tool surfaces utilized in the CAPP software. CAPP retains the B-spline and NURBS representation of the tool surfaces, so that no level of detail is sacrificed during operations on the tool surface geometry. However, many tool surfaces are constructed from many continuous spline surfaces which are combined to make the shell (figure 9.1).

Depending on the level of continuity, expansions of fiber paths along the tool surface can encounter difficultly when transitioning between individual patches. In order to abstract away the difficulties of multi-patch tool surfaces, the shell adaptor was implemented.

9.1.1 Shell Adaptor & Point Wrapper

The shell adaptor is a custom abstraction of simple spline surfaces implemented in the CAPP software. It is provided with a surface consisting of one or more individual patches. However, it enables simple queries of the parametric and cartesian space as though it were a single patch. Such abstraction greatly simplifies interrogation of complex tool surfaces for the generation of paths spanning multiple unique patches.

The "point wrapper" of the shell adaptor enables the simplified used of complex tool surfaces. The pointer wrapper assists in the evaluate of 2d and 3d points of the complex tool surfaces. When a 3d point is evaluated, it will be tested against the current patch which is active in the shell adaptor. If the 3d point belongs on the current patch, the corresponding 2d parametric values of that point on the patch will be evaluated. However, if the 3d point does not belong on the patch, or it extends beyond the valid parametric boundaries of the patch, the point wrapper will attempt to choose the correct patch. The *BRepExtrema* functionality from OpenCascade provides the minimum distance between the point and patches belonging to the shell adaptor. If another patch exist with a minimum distance below a specified tolerance, it will be loaded as the new active patch within the shell adaptor. After the correct, further operations will continue as normal. Such operation fits neatly with the development of continuous curves along the tool surface, as they will be developed though the incremental offset of many points along the surface. Thus, as the construction of points nears the end of the current patch, the new patch will be automatically selected and the curve development can continue uninterrupted.

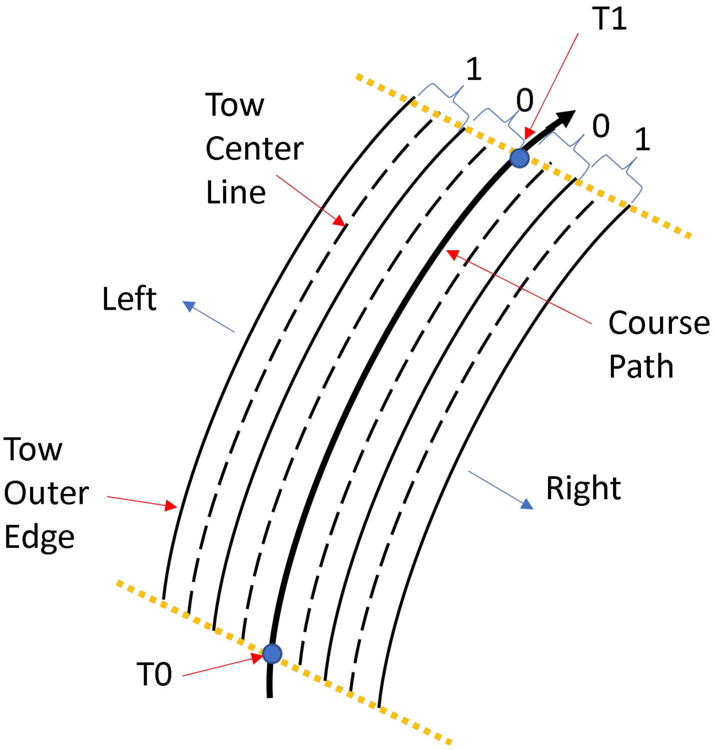

Figure 9.2 Anatomy of course and tows

9.1.2 Course and Tow Paths

Tow packets are the fundamental units which define the geometry of fiber paths on the tool surface. In order to translate the courses generated with dynamic layup strategy to VCP for further analysis and processing, it is first important to understand how the tow packets are internally represented.

Geometry with the tow packets is represented with discretized polylines. Course centerlines are the leading entity within tow packet definitions (figure 9.2). The course centerline defines *extents*, which define where the course is actually valid along the polyline definition. The use of extents enables course definitions to span the entire tool surface, but only regions near the actual ply boundary would be valid according to the extents.

Tows within the course are similarly defined with polylines, but one must be provided for both the centerline and outer edge of the tow. Typically, tow definitions

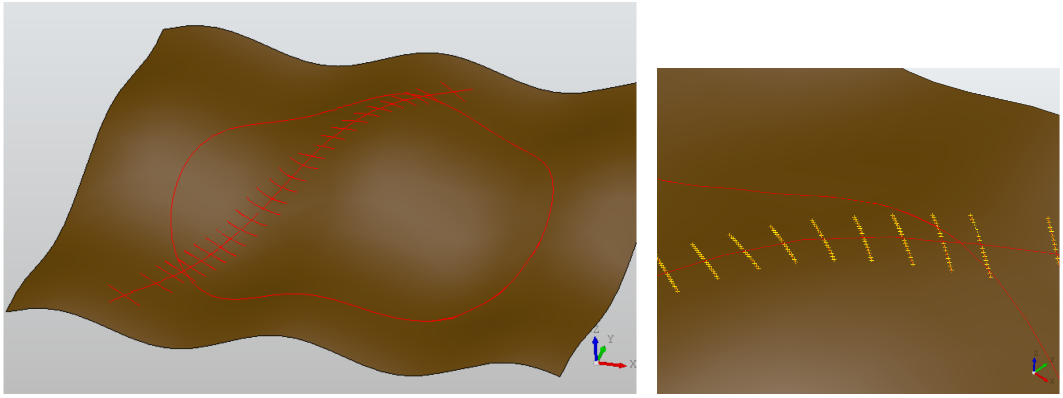

(a) Perpendicular Paths (b) Sampled Points

Figure 9.3 Course centerline and perpendicular paths for point sampling and tow creation

will extend out from either side of the course centerline.

Both courses and tows are indexed within the packets, including references to their relative orientations. The initially generated course is defined with index zero, where subsequent courses will have their index increment going outwards. The relative *sides* (left or right) from the initial course are additionally included in subsequent courses. Similarly, tows are indexed outwards from their respective course, also including the left and right terms. Finally, the extent of tows along the course are defined along with the tow centerline. The methods utilized for computing the extent of tows are defined in the following subsections.

9.1.3 Path Trimming

In order to generate the tow paths defining centerline and outer edges, a series of parallel curves are generated from the centerline. The parallel curves are created with the assistance of a series of curves which lay perpendicular from the course centerline on the tool surface (figure 9.3a). The perpendicular paths are created along the length of the centerline according to its deflection. Thus, increased centerline complexity will result in a higher sampling of perpendicular paths to improve the accuracy of generated tows.

The tow paths are subsequently generated by sampling at half and full tow widths along the perpendicular paths (figure 9.3b). Additionally, the directionality of the fiber path at these points is generated with the cross product of tool surface normal and tangent of the perpendicular path. With the points and associate tangency generated for the tow paths, a curve fitting routine is utilized to generate a spline curve representing the continuous tow paths.

The initial tow paths generated parallel to the course centerline will also have the same extension as the centerline. However, the tow paths should not extend past the ply boundaries, as these define the regions which should contain fiber paths. In order to reduce the tow paths to the valid region, a trimming routine is needed. Such a routine should consider the intersection of the tow path with the ply boundaries (figure 9.4). However, it is not initially clear when the tow should be *active*, particularly when more than two intersections with the boundary occur, or when a cutout is utilized.

In order to track the intersections with the boundary, a right-hand rule is applied to the direction of the boundary loop. Thus, the tangency of the loop at intersection points should be considered, in addition to the local normal of the tool surface. Through the combination of boundary tangent and normal, *entering* and *exiting* directions can be established. When the tangent of the path at the intersection point is to the left of the boundary tangent, the point has just entered the ply boundary, and alternatively when to the right, it has exited the ply boundary.

Furthermore, trimming of the tow paths should also be computed against other tow paths to minimize the overlap in regions where the paths have converged. However, it additionally becomes important to track which side of the previous tows the tow being trimmed exist on figure 9.5a. The intersection of tow paths can be combined with the information of tow and boundary intersections to better track the valid extents of the tow along the paths.

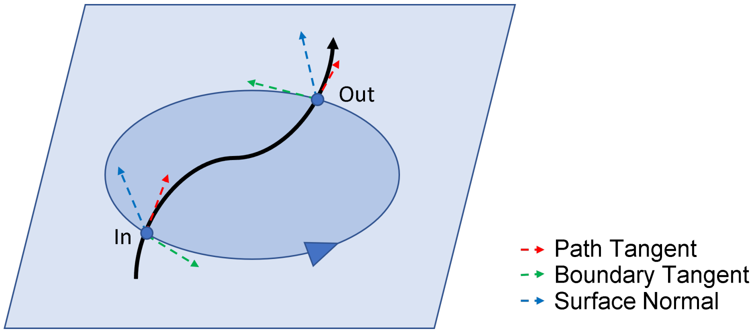

Figure 9.4 Trimming of path against closed loop boundary

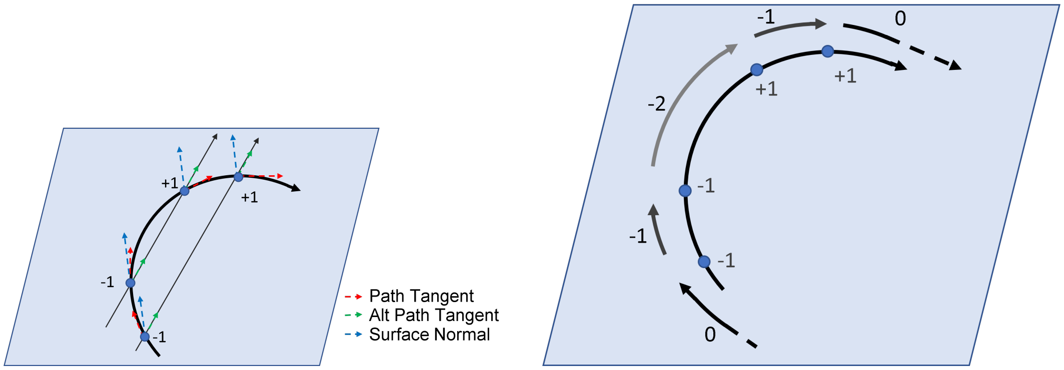

(a) Tow-Tow Intersections (b) Tracking Intersctions

Figure 9.5 Trimming of path against oriented curves

Each tow tracks the number of intersections it encounters, and state of tow intersections is initialized to -1, which means no intersections have yet occurred. Whenever a tow is *entering* a ply boundary or returning from a tow-tow overlap, the number of intersections is incremented. Alternatively, when the tow is *exiting* a ply boundary, or beginning to overlap another tow, the number of intersections is decremented. With this set of operations, and assuming the tow path initially extends beyond the ply boundary, the tow will be valid when the number of intersections is 0 (figure 9.5b).

The final valid extends of the tow are determined by sorting the calculated intersections along the length of the tows path. Using the valid regions of the tow path to define the actual extent of material, a compatible tow packet has been generated for VCP. The process of coverage propagation along tow generation and trimming is repeated across the tool surface and the final results are exported to VCP for evaluation of the relevant fiber defects.

9.1.4 Path Propagation & Coverage

Propagation strategies are utilized following the creation of an initial seed curve. They utilize positioning of previous courses to generate additional courses, and will continue until the specified ply region has been satisfactorily populated with courses. Propagation strategies can be independent, parallel, or conditional parallel. For independent coverage strategies, new courses will be generated with an offset from the previous courses using the specified layup strategy, with minimal consideration to the previous courses. Parallel strategies will ignore the layup strategy, and instead build a parallel offset curve from the previous course to define the new course, as a result, course-to-course gaps and overlaps should be non-existent. Conditional parallel strategies will propagate until a condition of a newly generated course exceeds a set limit. Once the propagation condition has been triggered, a new independent course using the basic layup strategy will be generated, which will serve as the seed for further course generation until a condition is once again triggered. For conditional parallel strategies, rosette-parallel, the measured fiber angle deviation within parallel courses is considered. When excessive fiber angle deviation is measured, a new, fiber angle aligned course will be generated with the rosette strategy.

9.2 Functionality of Dynamic Layup Strategy

The dynamic layup strategy provides a continuous integration of the fundamental layup strategies. Each layup and coverage strategy provides different sets of benefits to the development of geometrically defined fiber defects. These defects include course-to-course gaps and overlaps, in addition to fiber angle deviation and excessive fiber steering.

Fiber angle deviation and fiber steering are best mitigated through basic layup strategy selection. The rosette rule determines fiber paths through the use of the defined fiber angle. Fiber paths are created such that each new step is adjusted to align with the fiber angle. As a result, the rosette strategy generates fiber paths which generally minimized the overall fiber angle deviation.

Similarly, the use of the natural path strategy provides significant benefits to the existence of fiber steering. The natural path will adjust the newly generated path segments to closely align with the general curvature of the underlying tool surface. Through the alignment with the tool surface, the natural path will follow the contours of the tool surface and minimize the paths in-plane steering.

Following the generation of a seed curve with one of the previously defined layup strategies, subsequent courses must be generated with a coverage strategy. A strictly parallel coverage strategy would induce the least amount of coverage defects, namely the course-to-course gaps and overlaps. In order to generate a parallel course on a complex tool surface, it is important to consider the actual traversed distance along the tool surface. As such, strictly parallel courses provide the basis for minimizing coverage defects.

Each of these layup and coverage strategies individually provide the general ability to minimize a respective family of fiber defects.

9.2.1 Layup Strategy Implementations

The dynamic layup strategy utilizes the fundamental logic from each of these layup and coverage algorithms, enabling the ability to continuously target the minimization of various fiber defect types. In order to implement the dynamic layup strategy, it was necessary to first develop the infrastructure to construct arbitrary path planning algorithms. Through this infrastructure, the traditional layup and coverage strategies were implemented to be utilized within the dynamic layup strategy. The implementation begins with the *pointer-stepper*.

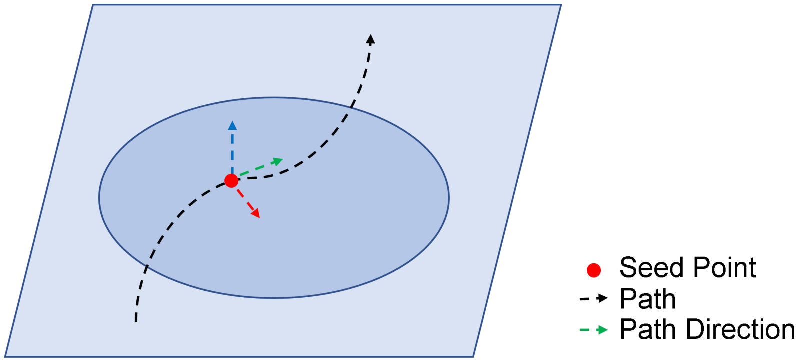

Figure 9.6 Point-stepper seed and direction generation

As described through section 2.3, fiber coverage begins with the definition of a seed point, fiber angle and ply boundaries. The seed point and fiber angle, along with the surface normal, provide the initial reference frame which is utilized for the path generation. The point-stepper begins at that seed point and provides the logic which is utilized to discretely update the fiber path which is currently under construction. From that seed point, the point-stepper logic is extended outwards until the ply boundaries are reached. Fundamentally, the point-stepper provides the local tangent of the path, where the tangent is utilized to generated the subsequent point of the path in addition to re-evaluating the local path's tangent.

The following sections provide insight into the specific implementation of the point steppers for the fundamental layup and coverage strategy techniques. In order to build a final course centerline with the following strategies, the individual iterations of the point stepper generation discrete pairs of points and path tangents. A spline curve fitting is performed with this data to generate a final continuous form of the course centerline for further processing.

COVERAGE POINT STEPPER

The coverage strategy utilizes the fundamental properties of the parallel propagation to minimize the presence of course-to-course gaps and overlaps. A new path should be parallel to the previous course in order to minimizes gaps and overlaps. Therefore, any deviation from that parallel path can be understood as the generation of gaps and overlaps. Thus, the coverage based point stepper is primarily concerned with minimizing deviation of the constructed path from the idealized parallel offset from the previous course.

When initializing the coverage point stepper for the generation of a new course centerline, it begins when generating the idealized parallel offset from the previous course. As a result, the coverage point stepper is only applicable once the seed course has been generated.

During each update with the coverage point stepper, the current leading point of the path is projected to the parallel reference curve. In order to minimizing gap and overlap presence, the step direction is set towards the parallel reference curve. The total change of direction is limited, however, to avoid the creation of excess angle deviation or steering radii. Therefore, the step direction is rotated to point towards the reference curve, and the maximum amount of rotation is the allowable maximum angle deviation. The use of the maximum angle deviation for redirecting the step direction acts to minimize the amount of induced angle deviation encounter when attempting to maintain the trajectory along the parallel reference curve.

The factor of course correction for the coverage point stepper additionally considers the deviation that as occurred from the parallel reference curve. Small deviations correspond to smaller changes in redirection of the step direction. The amount of coverage deviation is correlated to the ratio of the current step point's distance from the reference edge, and the total half-width of the current course configuration (total number of tows / 2 * tow width).

Additionally, considerations can be made which lower the amount of change of the step direction, and alternately rely on the trimming of tows within the course under construction. When the path has deviated from the reference course by integer ratios of the tow width. In this scenario that this deviation has developed, towards the

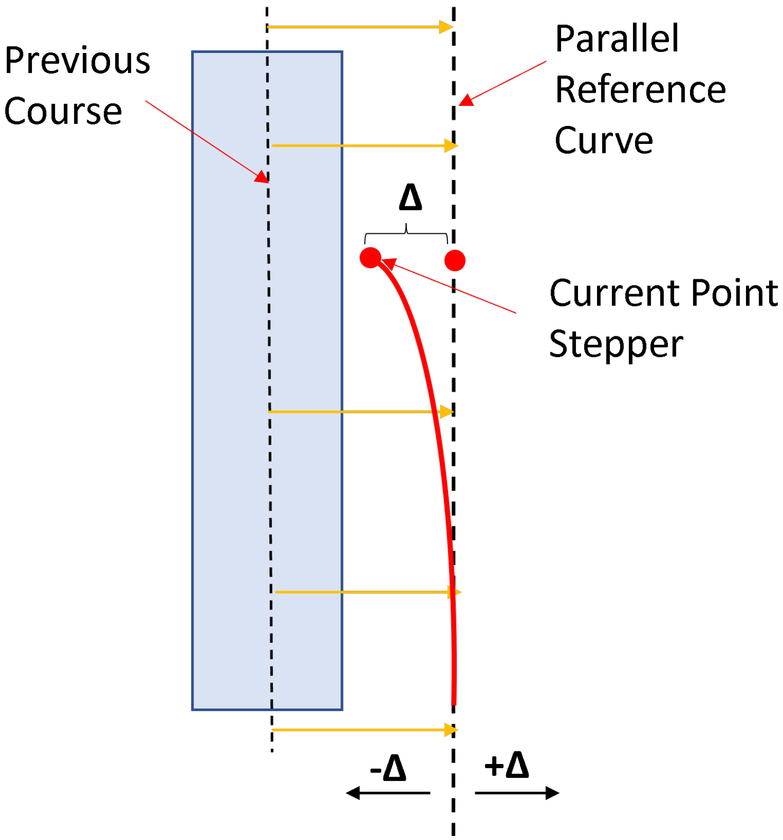

Figure 9.7 Parallel reference curve and offset convention for coverage based point stepper

previous course, the entire tow could be trimmed, resulting in local adjacent courses that exhibit no gaps or overlaps. Thus, gaps and overlaps within coverage point stepper are handled with some nuance.

Course-to-course gaps occur when the distance from the previous course has exceeded the course half-width, or when the current distance has a remainder of less than a half tow-width. Similarly, overlaps only occur when the distance is less than a half course-width, and the remainder of greater than a half tow-width. Distances away from the previous course centerline are considered positive, while distances towards the previous course are negative. The convention is utilized for both the left and right sided propagations from the central course, but the relative directions of positive and negative would be flipped.

Rosette Point Stepper

The rosette point stepper primarily relies on the rosette and programmed fiber angle to generate the fiber paths. At each iteration of the point stepper, an axis system will be constructed relative to the tool surface and the reference rosette system. At the given point, the surface normal will be computed. The surface normal and point defined the tangent plane to the tool surface at the leading edge of the path under construction. The direction of the point stepper will then be re-oriented in this tangent plane to satisfy the rosette layup strategy conditions.

In order to obtain the updated point stepper direction, the relevant axis from the rosette axis is rotated by the ply angle. For all the fiber paths generated in the following sections, the ply angle was measured from the rosettes $X-axis$ and rotated in the rosette's $XY-plane$, around the positive $Z-axis$. With the reference axis adjusted to represent the ply's fiber angle, it will then be used to update the local axis system at the paths leading point. The reference axis is projected into the local systems plane, forming the direction of the local axis system. The projected reference axis now represents the direction for the next iteration of the point stepper. A new point will then be computed utilizing the rosette direction, and subsequently a new stepper direction will be computed.

Natural Point Stepper

The natural point stepper relies on the local natural curvature of the tool surface at the leading point of the path under construction. The natural curvature represents a combination of the local curvature of the tool surface and the curvature of the path. Thus, in order to do generate the curvature values along the path, a numerical method is necessary. The method described in [77] represents the idea method for the generation of new points along the course's path.

$$(u_1, v_1) = (u_0 + u'(q_0)\Delta s, v_0 + v'(q_0)\Delta s) \tag{9.1}$$

Initially consider the path on the parametric surface as the paraemters; $u = u(s)$, $v = v(s)$. Here, $u(s)$ and $v(s)$ represent the equation that defines the path over through the evaluation of the parametric coordinates, and s reprsents the parametric value along the curves length. In order to prepare the curve for the numerical method, consider equation 9.1, where subsequent points can be approximated as the curve's local tangent offset by the length increment Δs. Subsequently the tangent vector of the curvature can also be updated numerically, resutling in equation 9.2.

$$\mathbf{T}_1 = \mathbf{T}_0 + k_0\beta_0\Delta s = \mathbf{T}_0 + k_0\mathbf{n}_0\Delta s \tag{9.2}$$

However, the β_0 is the principal normal vector of the curve at the leading point. Through the assumption that the path under construction represents a natural path, β_0 can be substituted with $\mathbf{n}_0$, the unit normal vector as the current location on the tool surface.

Finally, the local curvature of the curve must be evaluated to provide the last term for the numerical step. Equation 9.3 provides the paths curvature as a function of the current tangent direction and normal vector at the next iteration point on the tool surface. The level of curvture is finally modulated by the step length increment, Δs.

$$k_0 = \lim_{\Delta s \to 0} \left| \frac{a}{\Delta s} \right| = \frac{|\mathbf{n}_1 \cdot \mathbf{T}_0|}{\Delta s} \tag{9.3}$$

Utilizing these numerical methods presented by [77], the step direction can directly be computed, such that it takes into account the local curvature of the path under construction.

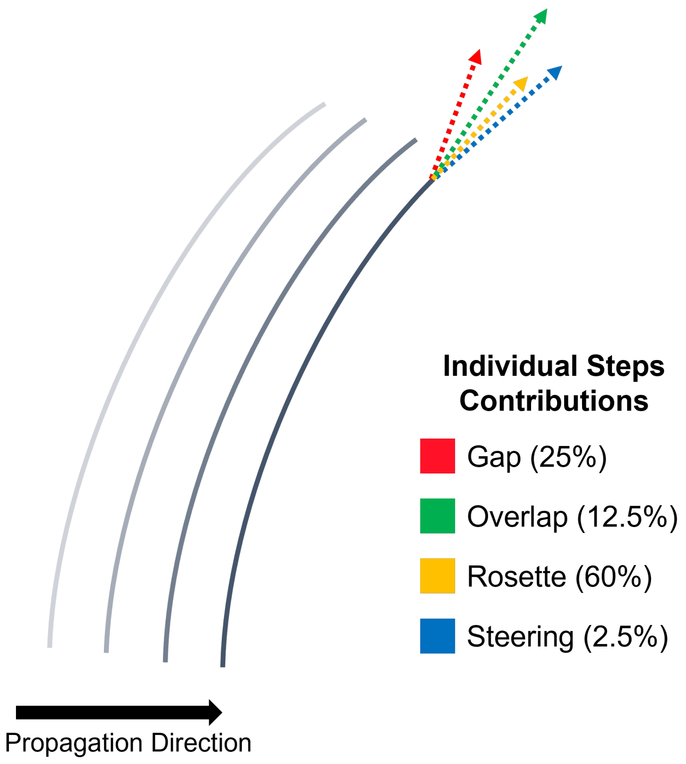

Figure 9.8 Computation of various layup strategy propagation directions

9.2.2 Implementation and Evaluation of Dynamic Layup Strategy

The implementation of the dynamic layup strategy utilizes the traditional architecture necessary for the functionality of a layup strategy. The path generation must remain on teh tool surface and utilizes numerical methods and discrete steps to build the path through several iterations of the numerical method. The utilities implemented for the handling of parametric tool surfaces were described in section 1.1. These tool abstract the underlying topology of mutli-patch spline surfaces, and the evaluation of points from both parametric and 3d forms.

Additionally, the traditional layup strategies were implemented though the *point-stepper* structure, where the numerical portion of the path generation is performed. Given an initial point and tangent vector, subsequent points are generated by traversing across the tool surface in the direction of the tangent vector. Furthermore, the direction of the tangent vector is recomputed at the new point, taking into account

Layup Strategy	**Associated Defect**
Parallel Offset	Gap + Overlap
Rosette	Angle Deviation
Natural	Steering Radius

Table 9.1 Layup strategies and relevant defects

new conditions, such as changes in surface curvature and deviation from the expected fiber path angle.

The dynamic layup strategy has also been implemented as a point stepper, and takes in information about the current point, and previous direction vector that reached it. Next, each of the basic point steppers are polled to obtain their expected direction vector for the next step of propagation (figure 9.8). Each of these point steppers represent the direction that the traditional layup strategies would take in order to generate paths. Associated with each of these layup strategies are the geometric consequences, such that the various defects would be generated. These include the generation of gaps, overlaps, angle deviation and excess steering radius. However, due to the fact that each layup strategy will minimize a specific family of these defects, the chosen iteration direction will influence the generation of these defects.

Table 9.1 provides the general association between layup strategy and relevant defects. The relevant defects are typically minimized through the use of that layup strategy, and thus through the selection of that layup strategy, it is expected that the relevant defect would be minimized more than other layup strategies. Parallel offsets provide a unique case, as this is presented as a coverage based strategy, as opposed to the strict generation of fiber paths from rosette and natural path strategies. As such, the creation of the parallel reference curve provides the basis for implementing coverage defect minimization. Additionally, parallel offset strategies are handled slightly different from rosette and natural path strategies. The relative location of the leading edge of the path under construction will influence the amount of change in the propagation direction. Additionally, the relative emphasis on the minimization of gaps versus overlaps will be a driving factor.

Gaps will be consider when the constructed path has begun to propagate away from the parallel reference cure, such that the approximate distance between the previous and current course center lines have exceeded a single course width. Conversely, overlaps are considered with the constructed path begins to propagate towards the previous course center line, lowering the distances between a single course width. Overlaps can additionally be handled through the trimming of tows within a single course packet, therefore distances below the single course offset that are an integer multiples of the tow width are acceptable. In the case that tows can be trimmed to minimize the overlap, no change in direction would be create, such that the next propagation step would expect to be parallel to the reference curve, which minimizes the creation of gaps and overlaps further down the path.

Finally, with the expected direction from each fundamental layup strategy, the actual propagation step can take place within the dynamic layup strategy.

Weighting variations

The weighting variation of the dynamic layup strategy allows one to tailor the specific properties of the generated fiber paths. The primary inputs for the dynamic layup path generation include the seed point and the fiber orientation. The actual development of the path will rely upon the routine described in section 9.2.2. Through the specification of individual weights for the dynamic layup strategy, the fiber defect development can be controlled.

An ideal setup with the dynamic layup strategy would connect the individual weighting components to that of the AHP weighting strategy from chapter 3. The AHP method provided an intuitive method for developing the prioritization weights using the relative importance of the various fiber defect families. Subsequently, the AHP weights can be directly mapped to the individual components from table 9.1.

The connection relies upon the understanding that various layup strategies better minimizes specific types of defects, so that the defect most highly prioritized by the AHP weighting can be minimized through the most relevant layup strategy. Additionally, the weighting is a continuous system, so partial priority can be assigned to multiple defect types.

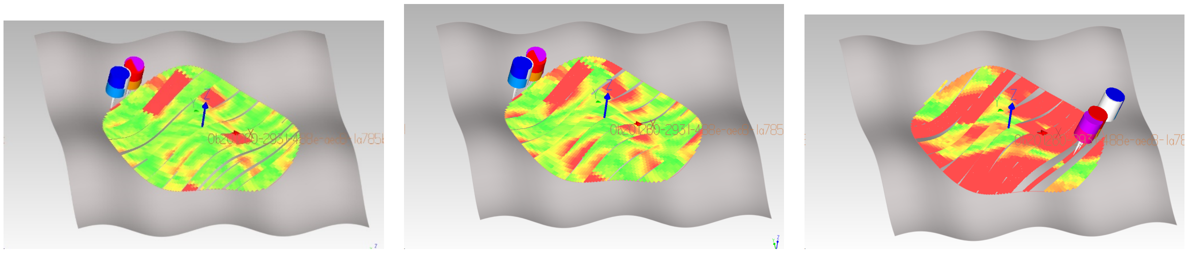

(a) Rosette: 1; Natural: 0 (b) Rosette: .5; Natural: .5 (c) Rosette: 0; Natural: 1

Figure 9.9 Presence of excessive angle deviation for various dynamic weightings

Figure 9.9 presents the weighting variation on the periodic tool surface. The weighting shows the transition from rosette strategy to parallel strategy, with an interpolation step in between. The current defect measured is the fiber angle deviation. The color scale shows no angle deviation from green, where red shows angle deviation above 3°. It is immediately apparent that the rosette strategy exhibits significantly lower angle deviation, whereas angle deviation predominates through the ply boundary for the natural path strategy. However, the interpolate step where the rosette and natural path strategy are equally considered, exhibits an average amount of angle deviation. From the angle deviation distribution at the interpolation step, the contribution of the rosette strategy can be observed as reducing the overall angle deviation, but moderate angle deviation is contributed from the natural strategy's contribution. Additionally, the contribution of each strategy's component to the overall angle deviation corroborates the information set for in table 9.1.

Figure 9.10 presents the steering radius induced in the fiber paths for different dynamic layup strategy weights. The color scale used indicates high radius (low curvature) areas as green, where low radius (high curvature) regions are red. The

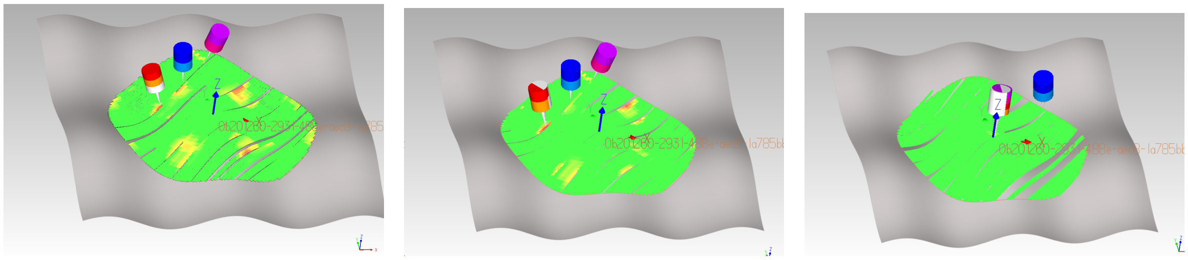

(a) Rosette: 1; Natural: 0 (b) Rosette: .5; Natural: .5 (c) Rosette: 0; Natural: 1

Figure 9.10 Presence of excessive steering radius for various dynamic weightings

figures transition from 100% rosette strategy to 100% natural path strategy. Figure 9.10a presents several regions of the ply boundary where steering is present. As the weighting transitions to the natural strategy, the total steering decreases. From these results, one can observe that rosette strategy will induce more steering than the natural path strategy, corroborating the relationship set forth in table 9.1.

9.3 Discussion

This chapter presented the development and evaluation of the dynamic layup strategy. Layup strategies provide the fundamental functionality to create series of fiber paths which place material within the specified ply boundaries. The algorithms driving these layup strategies are limited to the material properties of composite tows, and design constraints.

The dynamic layup strategy abstracts away the decision-making present with layup strategy selection. As previously discussed, fiber coverage methods and fiber defects are closely coupled, and present a series of tradeoffs. Furthermore, the selection of a given layup strategy will provide the specified benefits when some aspects of a different layup strategy may also be desired.

The dynamic layup strategy presents a continuous integration of multiple layup strategies, where each may be partially implemented to gain a tailored blend of performance. Additionally, performance can vary over the tool surface, such that specified layup properties can be targeted for different regions of the structure.

The development of such a layup strategy necessitated the implementation of relevant infrastructure, namely the shell adaptor for complex tool surfaces, point steppers to enable numerical methods of path creation, and the ability to define and trim tows for processing with VCP.

An evaluation of the dynamic layup strategy is subsequently provided, demonstrating its unique features in comparison to the traditional layup strategies.

Chapter 10

Conclusions and Future Work

In order to develop complex aerospace structures using composite materials, it is essential to understand the behavior and emergent aspects of the material system. The contents of this document have focused primarily on the geometric considerations of the automated placement of composite tows. Those primary considerations include the placement paths of the tows (section 2.3), which will largely be driven by structural design considerations. Additionally, from the geometric placement of fiber paths, several different families of placement defects may occur (section 2.1).

The different courses laid up during the AFP process need to be placed in a way that the fibers orientations meet the required design specifications. Often, plies are manufactured with fibers having well-defined angles such as 0°, 90°, 45°, -45° as they provide a quasi-isotropic behavior for the structure. On complex surfaces, however, the fiber orientation is no longer trivial as the fiber angles in the tow can change due to the geometry of the surface. Therefore, various layup strategies will produce their own uniquely oriented laminates as the tooling surface changes. The fundamental layup strategies target either the minimization of fiber angle deviation from the specified orientation, or the minimization of fiber path lengths, using Rosette or Natural paths respectively.

Due to limitations in the placement of tows, both from structural and material properties, fiber defects will be present in a structure. Several types of fiber defects can be predicted directly from the geometry of the fiber paths generated during process planning. Thus, an initial evaluation of a given set of fiber paths can be performed virtually to describe the performance of the resulting ply in terms of defect presence. The primary fiber defects considered throughout this document include, course-to-course gaps and overlaps, fiber angle deviation, and steering radius.

Course-to-course gaps and overlaps occur wherever neighboring courses are not placed perfectly in parallel. Such a condition is necessarily met when using various layup and coverage strategies, and will typically occur when paths converge on complex tool surfaces, and strictly parallel placement of courses needs to be abandoned due to other issues such as excessive fiber angle deviation. Gaps and overlaps are important design considerations as they can lead respectively to resin-richness or voids and out of plane fiber paths and unexpected thickness build. Fiber angle deviation occurs when the actual fiber angle is no longer aligned with the defined fiber angle. The presence of excessive angle deviation may have significant impacts on structural properties, as composite design methods strictly define fiber angles in order to estimate the expected properties of the manufactured structure. Finally, steering radius occurs when fiber paths are non-linear on the tool surface. Due to the high stiffness of composite materials, differential lengths of the inner and outer radius of the tows can result in several out of plane deformations. Similarly, these defects resulting from fiber steering may have unpredictable effects on structural properties, thus unconstrained fiber steering is undesirable.

Fiber path generation and the resulting fiber defects present a relationship which can be approached from the perspective of optimization. Thus, ply optimization (chapter 3) targets the minimization of fiber defects resulting from interactions between the tool and tow geometry. To perform this optimization, it is necessary to quantify and score the layup. The chosen inputs to the optimization function are the starting point and layup strategy selection, which have the most direct control over the resulting ply. Therefore, the objective function and input space for that objective function are well defined, and can thus be applied to the optimization of plies.

Chapter 8 presented the scoring case study, exploring the relationship between the various layup strategies and resulting fiber defects on different tool surface geometries. Such a study enables the high sampling of the input space to the ply optimization's objective function, by thoroughly sampling fiber angle, seed point and layup strategies. Through such broad sampling and characterization of the resulting plies, connections were made to the existence and distribution of the various defect types. Clear correlations were observed between the direction of fiber paths along the tool surface and the underlying curvature, exhibiting periodicity that matched course widths. One might leverage such information by evaluating a coarser sampling of the input parameters, in order to develop a general understanding for the development of fiber defects on a novel tool surface. Additionally, such information can also intelligently inform the internal ply level optimization within CAPP, enabling faster convergence on optimized ply by avoiding combinations of input parameters which are predicted to perform poorly.

In addition to the ply scoring case study on the traditional layup strategies, a novel layup strategy was proposed in chapter 9 which provides a more informed approach to fiber path generation. They dynamic layup strategy borrows concepts from rosette, natural and parallel path strategies to handle the different defects. Through the weighting mechanism, paths will adjust dynamic during generation to minimize the high priority defect type. The weighting can be directly tied to the scoring priority AHP (chapter 3), allowing close integration to CAPP optimization techniques. Such a layup strategy enables a continuous tradeoff between various defects, enabling greater control over the final fiber paths and resulting structural properties.

The defect characterization techniques discussed during the ply scoring case study, and the dynamic layup strategy are ideal techniques for full integration to the CAPP software. These techniques would help to accelerate the optimization loop and create better informed decisions when selecting seed points. An ideal workflow would begin with the coarse defect characterization on the desired tool surface. The defect study would identify seed points on the tool surface and their relationship to the development of the fiber defects. The coarse defect study would also indicate which defect families are most prevalent for the given tool surface and in which regions. With the newly acquired understanding and formation of defects, an ideal AHP defect weighting can be developed. The AHP could be tailored for the most prevalent defects, or the defect family which most impacts the structural properties. Finally, the dynamic layup strategy can be propagated over the tool surface to achieve the desired fiber path coverage. The ply scoring could then be applied to ensure that the given defect presence was optimized as desired, otherwise, the seed point for the dynamic layup strategy could be updated again utilizing the information obtained through the tool surface specific defect study.

Future work would involve the expansion of CAPP optimization to fully incorporate laminate level optimization and process parameter considerations. The laminate level optimization would expand on the techniques described in chapter 6, enabling the minimization of defect interactions through the thickness between nearby plies. Process parameter optimization would develop around the techniques from chapter 7 and 5. Such feature in CAPP would consider the impact of various process parameters on the formation of fiber defects. This analysis of fiber defects related to processing conditions would extend past the solely geometrical considerations that CAPP currently takes to the formation of fiber defects. The primary parameters would include compaction, speed, and temperature of the substrate during fiber placement. Through the mapping of these applied conditions to the tool surface, the relationship to defect formation could be developed. Effective use of these process parameters would likely rely on the use of numerical methods to approximate the process conditions experienced by the fibers during placement.

BIBLIOGRAPHY

[1] Dirk H.-J.A. Lukaszewicz, Carwyn Ward, and Kevin D. Potter. "The engineering aspects of automated prepreg layup: History, present and future". In: *Composites Part B: Engineering* 43.3 (Apr. 2012), pp. 997–1009. DOI: `10.1016/j.compositesb.2011.12.003`. URL: `https://doi.org/10.1016%2Fj.compositesb.2011.12.003`.

[2] Kaven Croft et al. "Experimental study of the effect of automated fiber placement induced defects on performance of composite laminates". In: *Composites Part A: Applied Science and Manufacturing* 42.5 (May 2011), pp. 484–491. DOI: `10.1016/j.compositesa.2011.01.007`.

[3] Pierre Debout, Hélène Chanal, and Emmanuel Duc. "Tool path smoothing of a redundant machine: Application to Automated Fiber Placement". In: *Computer-Aided Design* 43.2 (Feb. 2011), pp. 122–132. DOI: `10.1016/j.cad.2010.09.011`. URL: `https://doi.org/10.1016%2Fj.cad.2010.09.011`.

[4] Kazem Fayazbakhsh et al. "Defect layer method to capture effect of gaps and overlaps in variable stiffness laminates made by Automated Fiber Placement". In: *Composite Structures* 97 (Mar. 2013), pp. 245–251. DOI: `10.1016/j.compstruct.2012.10.031`.

[5] C.S. Lopes et al. "Progressive failure analysis of tow-placed, variable-stiffness composite panels". In: *International Journal of Solids and Structures* 44.25-26 (Dec. 2007), pp. 8493–8516. DOI: `10.1016/j.ijsolstr.2007.06.029`.

[6] A. Sawicki and P. Minguett. "The effect of intraply overlaps and gaps upon the compression strength of composite laminates". In: *39th AIAA/ASME/ASCE/AH-*

S/ASC Structures, Structural Dynamics, and Materials Conference and Exhibit. American Institute of Aeronautics and Astronautics, Apr. 1998. DOI: `10.2514/6.1998-1786`.

[7] Marine Lan et al. "Influence of embedded gap and overlap fiber placement defects on the microstructure and shear and compression properties of carbon–epoxy laminates". In: *Composites Part A: Applied Science and Manufacturing* 82 (Mar. 2016), pp. 198–207. DOI: `10.1016/j.compositesa.2015.12.007`. URL: `https://doi.org/10.1016%2Fj.compositesa.2015.12.007`.

[8] Mahdi Arian Nik et al. "Optimization of variable stiffness composites with embedded defects induced by Automated Fiber Placement". In: *Composite Structures* 107 (Jan. 2014), pp. 160–166. DOI: `10.1016/j.compstruct.2013.07.059`. URL: `https://doi.org/10.1016%2Fj.compstruct.2013.07.059`.

[9] Daniel O'Hare Adams and M.W. Hyer. "Effects of Layer Waviness on the Compression Strength of Thermoplastic Composite Laminates". In: 12.4 (Apr. 99), pp. 414–429. DOI: `10.1177/073168449301200404`. URL: `https://doi.org/10.1177%2F073168449301200404`.

[10] A. Beakou et al. "Modelling slit tape buckling during automated prepreg manufacturing: A local approach". In: 93.10 (Sept. 1), pp. 2628–2635. DOI: `10.1016/j.compstruct.2011.04.030`. URL: `https://doi.org/10.1016%2Fj.compstruct.2011.04.030`.

[11] A Caiazzo et al. "The Effects of Marcel Defects on Composite Structural Properties". In: *Composite Structures: Theory and Practice*. ASTM International, pp. 158–158–30. DOI: `10.1520/stp14509s`. URL: `https://doi.org/10.1520%2Fstp14509s`.

[12] Bijan Shirinzadeh et al. "Fabrication process of open surfaces by robotic fibre placement". In: *Robotics and Computer-Integrated Manufacturing* 20.1 (Feb. 2004), pp. 17–28. DOI: `10.1016/s0736-5845(03)00050-4`.

[13] Xiangqian Li, Stephen R. Hallett, and Michael R. Wisnom. "Modelling the effect of gaps and overlaps in automated fibre placement (AFP)-manufactured laminates". In: *Science and Engineering of Composite Materials* 22.2 (Mar. 2015), pp. 115–129. DOI: `10.1515/secm-2013-0322`.

[14] Marine Lan et al. "Microstructure and tensile properties of carbon–epoxy laminates produced by automated fibre placement: Influence of a caul plate on the effects of gap and overlap embedded defects". In: *Composites Part A: Applied Science and Manufacturing* 78 (Nov. 2015), pp. 124–134. DOI: `10.1016/j.compositesa.2015.07.023`.

[15] Adriana W. Blom et al. "Fiber path definitions for elastically tailored conical shells". In: *Composites Part B: Engineering* 40.1 (Jan. 2009), pp. 77–84. DOI: `10.1016/j.compositesb.2008.03.011`. URL: `https://doi.org/10.1016%2Fj.compositesb.2008.03.011`.

[16] Adriana W. Blom et al. "Design of variable-stiffness conical shells for maximum fundamental eigenfrequency". In: *Computers & Structures* 86.9 (May 2008), pp. 870–878. DOI: `10.1016/j.compstruc.2007.04.020`. URL: `https://doi.org/10.1016%2Fj.compstruc.2007.04.020`.

[17] A. W. Blom. "Structural Performance of Fiber-Placed, Variable-Stiffness Composite Conical and Cylindrical Shells". PhD thesis. TU Delft, 2010.

[18] Z. Zamani, H. Haddadpour, and M.R. Ghazavi. "Curvilinear fiber optimization tools for design thin walled beams". In: *Thin-Walled Structures* 49.3 (Mar. 2011), pp. 448–454. DOI: `10.1016/j.tws.2010.08.002`. URL: `https://doi.org/10.1016%2Fj.tws.2010.08.002`.

[19] Adriana W. Blom, Patrick B. Stickler, and Zafer Gürdal. “Optimization of a composite cylinder under bending by tailoring stiffness properties in circumferential direction”. In: *Composites Part B: Engineering* 41.2 (Mar. 2010), pp. 157–165. DOI: `10.1016/j.compositesb.2009.10.004`. URL: `https://doi.org/10.1016%2Fj.compositesb.2009.10.004`.

[20] Zafer Gurdal, Brian Tatting, and K. Wu. “Tow-Placement Technology and Fabrication Issues for Laminated Composite Structures”. In: *46th AIAA/ASME/ASCE/AHS/ASC Structures, Structural Dynamics and Materials Conference*. American Institute of Aeronautics and Astronautics, Apr. 2005. DOI: `10.2514/6.2005-2017`. URL: `https://doi.org/10.2514%2F6.2005-2017`.

[21] Guanxin Huang, Hu Wang, and Guangyao Li. “An efficient reanalysis assisted optimization for variable-stiffness composite design by using path functions”. In: *Composite Structures* 153 (Oct. 2016), pp. 409–420. DOI: `10.1016/j.compstruct.2016.06.043`. URL: `https://doi.org/10.1016%2Fj.compstruct.2016.06.043`.

[22] Nicholas M. Patrikalakis and Takashi Maekawa. “Geodesics”. In: *Shape Interrogation for Computer Aided Design and Manufacturing*. Springer Berlin Heidelberg, Oct. 2009, pp. 265–291. DOI: `10.1007/978-3-642-04074-0_10`. URL: `https://doi.org/10.1007%2F978-3-642-04074-0_10`.

[23] Clément Hély, Lionel Birglen, and Wen-Fang Xie. “Feasibility study of robotic fibre placement on intersecting multi-axial revolution surfaces”. In: *Robotics and Computer-Integrated Manufacturing* 48 (Dec. 2017), pp. 73–79. DOI: `10.1016/j.rcim.2017.02.005`. URL: `https://doi.org/10.1016%2Fj.rcim.2017.02.005`.

[24] Lina Li et al. “A Placement Path Planning Algorithm Based on Meshed Triangles for Carbon Fiber Reinforce Composite Component with Revolved Shape”. In: 2014.

[25] Vaclav Skala. “Gradient Vector Estimation and Vertex Normal Computation”. In: (Jan. 2003).

[26] Ian B. Land. “Design and manufacture of advanced composite aircraft structures using automated tow placement”. In: 1996.

[27] Kurt Schueler, James Miller, and Richard Hale. “Approximate Geometric Methods in Application to the Modeling of Fiber Placed Composite Structures”. In: *Journal of Computing and Information Science in Engineering* 4.3 (Sept. 2004), pp. 251–256. DOI: `10.1115/1.1736685`. URL: `https://doi.org/10.1115%2F1.1736685`.

[28] M. Favaloro and David Hauber. “Process and design considerations for the automated fiber placement process”. In: *International SAMPE Technical Conference* (Jan. 2007).

[29] Bijan Shirinzadeh et al. “Trajectory generation for open-contoured structures in robotic fibre placement”. In: *Robotics and Computer-Integrated Manufacturing* 23.4 (Aug. 2007), pp. 380–394. DOI: `10.1016/j.rcim.2006.04.006`. URL: `https://doi.org/10.1016%2Fj.rcim.2006.04.006`.

[30] Long Yan et al. “An accurate approach to roller path generation for robotic fibre placement of free-form surface composites”. In: 30.3 (June 1), pp. 277–286. DOI: `10.1016/j.rcim.2013.10.007`. URL: `https://doi.org/10.1016%2Fj.rcim.2013.10.007`.

[31] Xiaoping Wang, Weizhong Zhang, and Liyan Zhang. “Intersection of a ruled surface with a free-form surface”. In: *Numerical Algorithms* 46.1 (Aug. 2007),

pp. 85–100. DOI: `10.1007/s11075-007-9118-y`. URL: `https://doi.org/10.1007%2Fs11075-007-9118-y`.

[32] Zhenyu Han et al. "A Path Planning Algorithm of Closed Surface for Fiber Placement". In: *Proceedings of the 1st International Conference on Mechanical Engineering and Material Science*. Atlantis Press, 2012. DOI: `10.2991/mems.2012.100`. URL: `https://doi.org/10.2991%2Fmems.2012.100`.

[33] Levend Parnas, Süha Oral, and Ümit Ceyhan. "Optimum design of composite structures with curved fiber courses". In: *Composites Science and Technology* 63.7 (May 2003), pp. 1071–1082. DOI: `10.1016/s0266-3538(02)00312-3`. URL: `https://doi.org/10.1016%2Fs0266-3538%2802%2900312-3`.

[34] Dawn Jegley, Brian Tatting, and Zafer Gurdal. "Optimization of Elastically Tailored Tow-Placed Plates with Holes". In: *44th AIAA/ASME/ASCE/AHS/ASC Structures, Structural Dynamics, and Materials Conference*. American Institute of Aeronautics and Astronautics, Apr. 2003. DOI: `10.2514/6.2003-1420`. URL: `https://doi.org/10.2514%2F6.2003-1420`.

[35] Brain Tatting, Zafer Gurdal, and Dawn Jegley. "Design and Manufacture of Elastically Tailored Tow Placed Plates". In: (Sept. 2002).

[36] Chauncey Wu, Zafer Gurdal, and James Starnes. "Structural Response of Compression-Loaded, Tow-Placed, Variable Stiffness Panels". In: *43rd AIAA/ASME/ASCE/AHS/ASC Structures, Structural Dynamics, and Materials Conference*. American Institute of Aeronautics and Astronautics, Apr. 2002. DOI: `10.2514/6.2002-1512`.

[37] C.S. Lopes, Z. Gürdal, and P.P. Camanho. "Variable-stiffness composite panels: Buckling and first-ply failure improvements over straight-fibre laminates". In: *Computers & Structures* 86.9 (May 2008), pp. 897–907. DOI: `10.1016/j.`

compstruc.2007.04.016. URL: https://doi.org/10.1016%2Fj.compstruc.2007.04.016.

[38] K. Wu and Zafer Gurdal. “Thermal testing of tow-placed, variable stiffness panels”. In: *19th AIAA Applied Aerodynamics Conference*. American Institute of Aeronautics and Astronautics, June 2001. DOI: 10.2514/6.2001-1190.

[39] Bret K. Stanford, Christine V. Jutte, and K. Chauncey Wu. “Aeroelastic benefits of tow steering for composite plates”. In: *Composite Structures* 118 (Dec. 2014), pp. 416–422. DOI: 10.1016/j.compstruct.2014.08.007. URL: https://doi.org/10.1016%2Fj.compstruct.2014.08.007.

[40] H. Haddadpour and Z. Zamani. “Curvilinear fiber optimization tools for aeroelastic design of composite wings”. In: *Journal of Fluids and Structures* 33 (Aug. 2012), pp. 180–190. DOI: 10.1016/j.jfluidstructs.2012.05.008. URL: https://doi.org/10.1016%2Fj.jfluidstructs.2012.05.008.

[41] K. Wu et al. “Design and Manufacturing of Tow-Steered Composite Shells Using Fiber Placement”. In: *50th AIAA/ASME/ASCE/AHS/ASC Structures, Structural Dynamics, and Materials Conference*. American Institute of Aeronautics and Astronautics, May 2009. DOI: 10.2514/6.2009-2700. URL: https://doi.org/10.2514%2F6.2009-2700.

[42] Mahdi Arian Nik et al. “Surrogate-based multi-objective optimization of a composite laminate with curvilinear fibers”. In: *Composite Structures* 94.8 (July 2012), pp. 2306–2313. DOI: 10.1016/j.compstruct.2012.03.021.

[43] Z. Gürdal, B.F. Tatting, and C.K. Wu. “Variable stiffness composite panels: Effects of stiffness variation on the in-plane and buckling response”. In: *Composites Part A: Applied Science and Manufacturing* 39.5 (May 2008), pp. 911–922. DOI: 10.1016/j.compositesa.2007.11.015. URL: https://doi.org/10.1016%2Fj.compositesa.2007.11.015.

[44] Adriana W. Blom, Mostafa M. Abdalla, and Zafer Gürdal. “Optimization of course locations in fiber-placed panels for general fiber angle distributions”. In: *Composites Science and Technology* 70.4 (Apr. 2010), pp. 564–570. DOI: `10.1016/j.compscitech.2009.12.003`. URL: `https://doi.org/10.1016%2Fj.compscitech.2009.12.003`.

[45] Shinya HONDA, Yoshihiro NARITA, and Katsuhiko SASAKI. “Maximizing the Fundamental Frequency of Laminated Composite Plates with Optimally Shaped Curvilinear Fibers”. In: *Journal of System Design and Dynamics* 3.6 (2009), pp. 867–876. DOI: `10.1299/jsdd.3.867`. URL: `https://doi.org/10.1299%2Fjsdd.3.867`.

[46] Chanderjit Bajaj and Gerald Farin. “Curves and Surfaces for Computer Aided Geometric Design–A Practical Guide.” In: *Mathematics of Computation* 55.192 (Oct. 1990), p. 874. DOI: `10.2307/2008458`. URL: `https://doi.org/10.2307%2F2008458`.

[47] Byung Chul Kim, Kevin Potter, and Paul M. Weaver. “Continuous tow shearing for manufacturing variable angle tow composites”. In: *Composites Part A: Applied Science and Manufacturing* 43.8 (Aug. 2012), pp. 1347–1356. DOI: `10.1016/j.compositesa.2012.02.024`. URL: `https://doi.org/10.1016%2Fj.compositesa.2012.02.024`.

[48] Etienne Lemaire, Samih Zein, and Michael Bruyneel. “Optimization of composite structures with curved fiber trajectories”. In: *Composite Structures* 131 (Nov. 2015), pp. 895–904. DOI: `10.1016/j.compstruct.2015.06.040`. URL: `https://doi.org/10.1016%2Fj.compstruct.2015.06.040`.

[49] A. Alhajahmad, M. M. Abdalla, and Z. Gürdal. “Design Tailoring for Pressure Pillowing Using Tow-Placed Steered Fibers”. In: *Journal of Aircraft* 45.2 (Mar.

2008), pp. 630–640. DOI: `10.2514/1.32676`. URL: `https://doi.org/10.2514%2F1.32676`.

[50] Shinya Honda and Yoshihiro Narita. “Vibration design of laminated fibrous composite plates with local anisotropy induced by short fibers and curvilinear fibers”. In: *Composite Structures* 93.2 (Jan. 2011), pp. 902–910. DOI: `10.1016/j.compstruct.2010.07.003`. URL: `https://doi.org/10.1016%2Fj.compstruct.2010.07.003`.

[51] Shinya Honda, Teruki Igarashi, and Yoshihiro Narita. “Multi-objective optimization of curvilinear fiber shapes for laminated composite plates by using NSGA-II”. In: *Composites Part B: Engineering* 45.1 (Feb. 2013), pp. 1071–1078. DOI: `10.1016/j.compositesb.2012.07.056`. URL: `https://doi.org/10.1016%2Fj.compositesb.2012.07.056`.

[52] Zhangming Wu et al. “Buckling analysis and optimisation of variable angle tow composite plates”. In: *Thin-Walled Structures* 60 (Nov. 2012), pp. 163–172. DOI: `10.1016/j.tws.2012.07.008`. URL: `https://doi.org/10.1016%2Fj.tws.2012.07.008`.

[53] Anis Limaiem and François Trochu. “Geometric algorithms for the intersection of curves and surfaces”. In: *Computers & Graphics* 19.3 (May 1995), pp. 391–403. DOI: `10.1016/0097-8493(95)00009-2`. URL: `https://doi.org/10.1016%2F0097-8493%2895%2900009-2`.

[54] Akemi Gálvez, Andrés Iglesias, and Jaime Puig-Pey. “Computing parallel curves on parametric surfaces”. In: *Applied Mathematical Modelling* 38.9-10 (May 2014), pp. 2398–2413. DOI: `10.1016/j.apm.2013.10.042`. URL: `https://doi.org/10.1016%2Fj.apm.2013.10.042`.

[55] Pierre Debout. “Calcul de trajets de dépose dans le cadre de la fafrication de pièces aéronautiques”. Theses. Université Blaise Pascal - Clermont-Ferrand II, u 2010. URL: `https://tel.archives-ouvertes.fr/tel-00719111`.

[56] Michaël Bruyneel and Samih Zein. “A modified Fast Marching Method for defining fiber placement trajectories over meshes”. In: *Computers & Structures* 125 (Sept. 2013), pp. 45–52. DOI: `10.1016/j.compstruc.2013.04.015`. URL: `https://doi.org/10.1016%2Fj.compstruc.2013.04.015`.

[57] Christopher J. Brampton and H. Alicia Kim. “Optimization of Tow Steered Fibre Orientation Using the Level Set Method”. In: 2013.

[58] Byung Chul Kim et al. “Limitations of fibre placement techniques for variable angle tow composites and their process-induced defects”. In: Aug. 2011.

[59] Ramy Harik et al. “Automated fiber placement defect identity cards: cause, anticipation, existence, significance, and progression”. In: Jan. 2018.

[60] Guillaume Rousseau et al. “Automated Fiber Placement Path Planning: A state-of-the-art review”. In: *Computer-Aided Design and Applications* 16.2 (Aug. 2018), pp. 172–203. DOI: `10.14733/cadaps.2019.172-203`.

[61] Joshua Halbritter et al. “Automation of AFP Process Planning Functions: Importance and Ranking”. In: *SAMPE 2019 - Charlotte, NC*. SAMPE, Apr. 2019. DOI: `10.33599/nasampe/s.19.1592`. URL: `https://doi.org/10.33599%2Fnasampe%2Fs.19.1592`.

[62] Valentin Zobel, Jan Reininghaus, and Ingrid Hotz. “Generalized heat kernel signatures”. In: (2011).

[63] CGTech. *VERICUT Composite Programming*. 2022. URL: `https://www.cgtech.com/products/vcp.html`.

[64] Christopher Sacco et al. "Machine learning in composites manufacturing: A case study of Automated Fiber Placement inspection". In: *Composite Structures* 250 (Oct. 2020), p. 112514. DOI: `10.1016/j.compstruct.2020.112514`.

[65] Roudy Wehbe. "Modeling Of Tow Wrinkling In Automated Fiber Placement Based On Geometrical Considerations". In: 2017.

[66] Christophe Geuzaine and Jean-François Remacle. "Gmsh: A 3-D finite element mesh generator with built-in pre- and post-processing facilities". In: *International Journal for Numerical Methods in Engineering* 79.11 (May 2009), pp. 1309–1331. DOI: `10.1002/nme.2579`.

[67] Bruno Lévy et al. "Least squares conformal maps for automatic texture atlas generation". In: *ACM Transactions on Graphics* 21.3 (July 2002), pp. 362–371. DOI: `10.1145/566654.566590`.

[68] Ligang Liu et al. "A Local/Global Approach to Mesh Parameterization". In: *Proceedings of the Symposium on Geometry Processing*. SGP '08. Copenhagen, Denmark: Eurographics Association, 2008, pp. 1495–1504. DOI: `10.5555/1731309.1731336`.

[69] Alec Jacobson, Daniele Panozzo, et al. *libigl: A simple C++ geometry processing library*. https://libigl.github.io/. 2018.

[70] Songrit Maneewongvatana and David M. Mount. *Analysis of approximate nearest neighbor searching with clustered point sets*. 1999. DOI: `10.48550/ARXIV.CS/9901013`.

[71] Pauli Virtanen et al. "SciPy 1.0: Fundamental Algorithms for Scientific Computing in Python". In: *Nature Methods* 17 (2020), pp. 261–272. DOI: `10.1038/s41592-019-0686-2`.

[72] Doug Baldwin and Michael Weber. “Fast Ray-Triangle Intersections by Coordinate Transformation”. In: *Journal of Computer Graphics Techniques (JCGT)* 5.3 (Sept. 2016), pp. 39–49. ISSN: 2331-7418. URL: `http://jcgt.org/published/0005/03/03/`.

[73] Khronos Group Inc. *OpenGL*. URL: `https://www.opengl.org/`.

[74] *Ultra-High Speed In-line Profilometer*. English. Version LJ-V7000 Series. Keyence.

[75] Alex Brasington et al. “Development of a Numerical Model for Compaction Pressure Predictions in Automated Fiber Placement”. In: (2022).

[76] Hertz. “On the Contact of Elastic Solids”. In: *Crelle’s Journal* 92 (), pp. 156–171.

[77] Peng Zhang, Ronglei Sun, and Tao Huang. “A geometric method for computation of geodesic on parametric surfaces”. In: *Computer Aided Geometric Design* 38 (Oct. 2015), pp. 24–37. DOI: `10.1016/j.cagd.2015.08.001`.

APPENDIX A

SURFACE 2: HYPERBOLIC-PARABOLOID

The following section presents the scoring and defect data computed for the hyperbolic tool surface. The parameters for the generation fo the fiber paths were defined in chapter 8.

Rosette Strategy

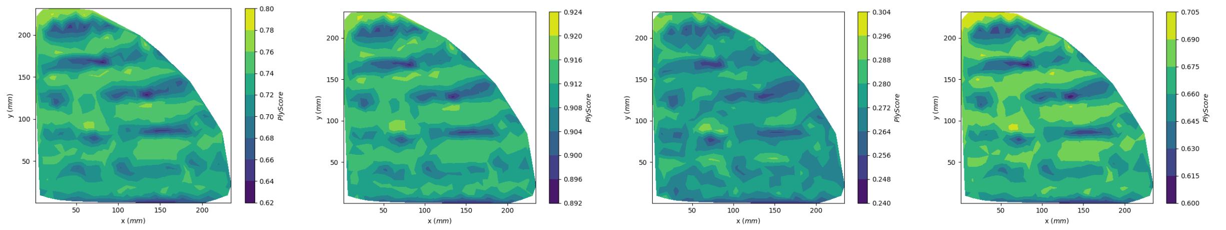

(a) Coverage (b) Angle Deviation (c) Excess Steering (d) Combined

Natural Strategy

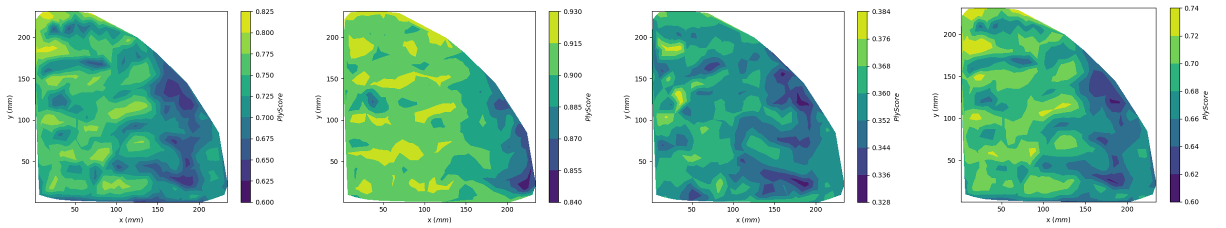

(e) Coverage (f) Angle Deviation (g) Excess Steering (h) Combined

Rosette-Parallel Strategy

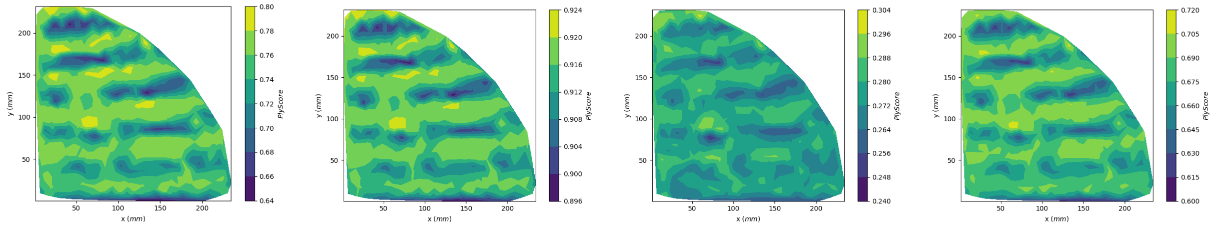

(i) Coverage (j) Angle Deviation (k) Excess Steering (l) Combined

Natural-Parallel Strategy

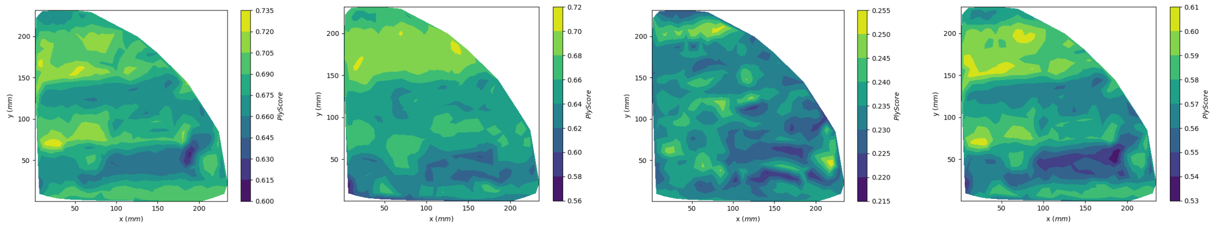

(m) Coverage (n) Angle Deviation (o) Excess Steering (p) Combined

Figure A.1 Score distributions of hyperbolic-paraboloid surface (variation 1 - $\theta = 0°$)

Rosette Strategy

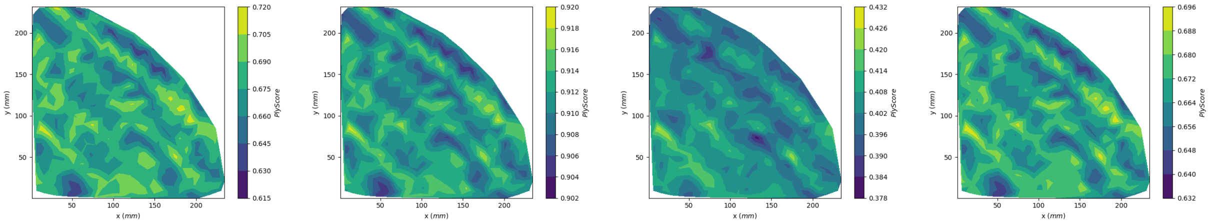

(a) Coverage (b) Angle Deviation (c) Excess Steering (d) Combined

Natural Strategy

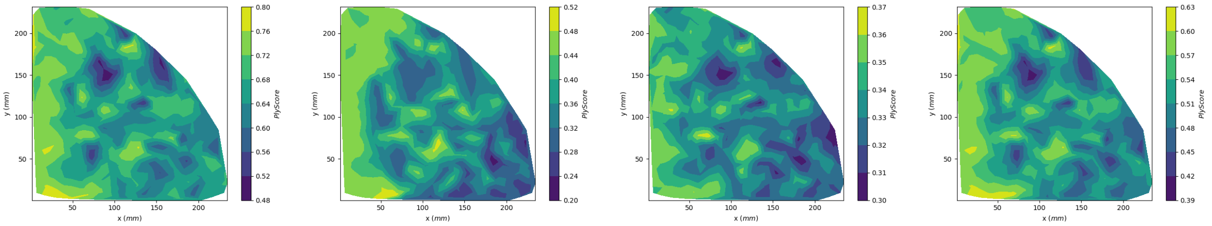

(e) Coverage (f) Angle Deviation (g) Excess Steering (h) Combined

Rosette-Parallel Strategy

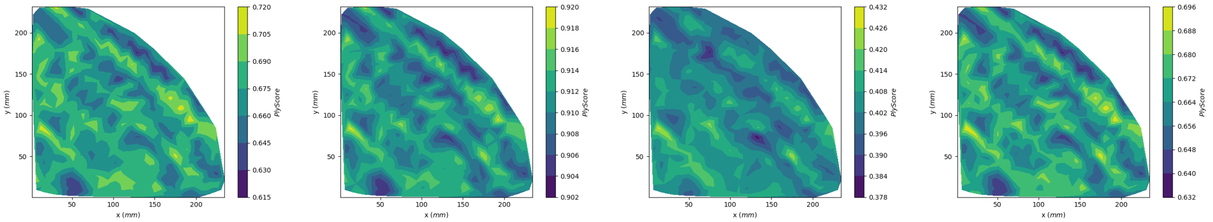

(i) Coverage (j) Angle Deviation (k) Excess Steering (l) Combined

Natural-Parallel Strategy

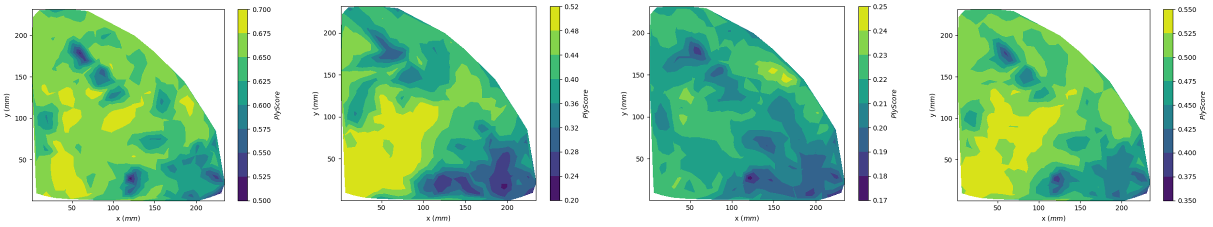

(m) Coverage (n) Angle Deviation (o) Excess Steering (p) Combined

Figure A.2 Score distributions of hyperbolic-paraboloid surface (variation 1 - $\theta = 45°$)

Rosette Strategy

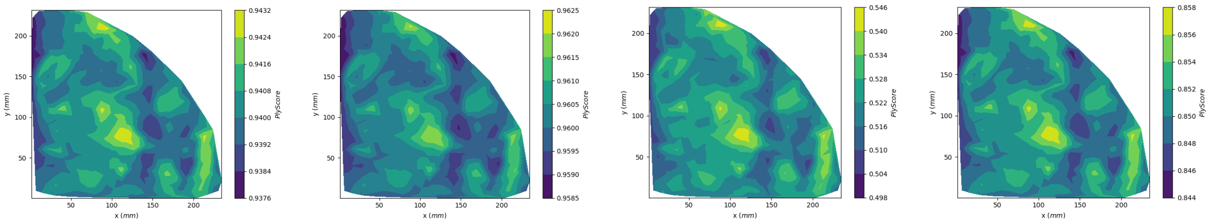

(a) Coverage (b) Angle Deviation (c) Excess Steering (d) Combined

Natural Strategy

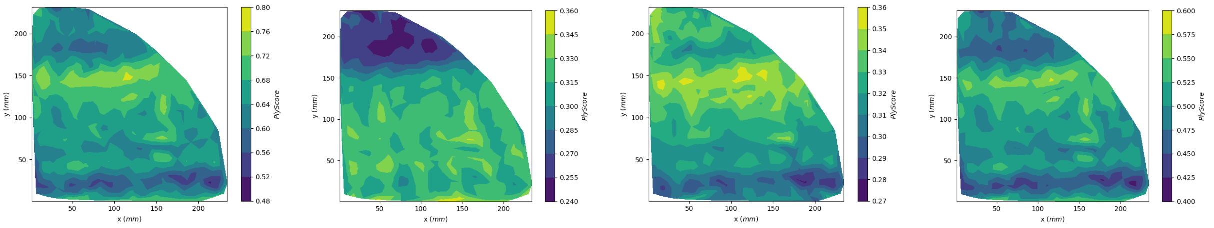

(e) Coverage (f) Angle Deviation (g) Excess Steering (h) Combined

Rosette-Parallel Strategy

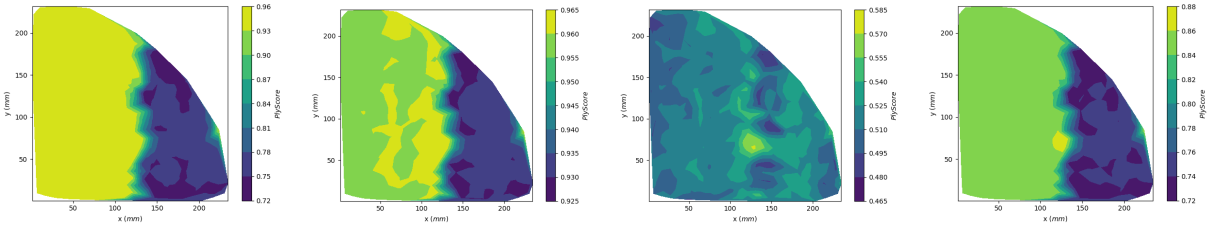

(i) Coverage (j) Angle Deviation (k) Excess Steering (l) Combined

Natural-Parallel Strategy

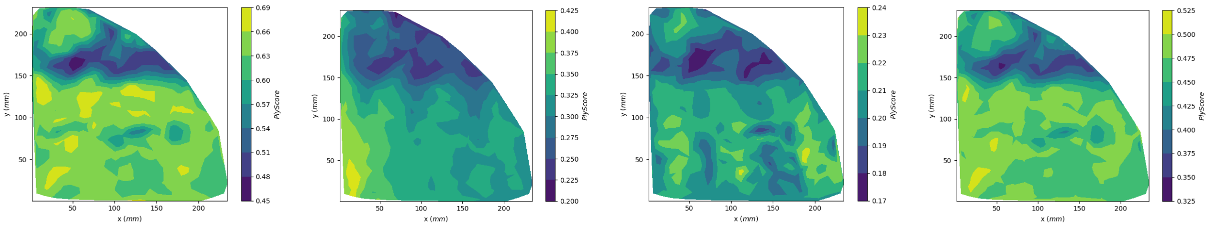

(m) Coverage (n) Angle Deviation (o) Excess Steering (p) Combined

Figure A.3 Score distributions of hyperbolic-paraboloid surface (variation 1 - $\theta = 90°$)

Rosette Strategy

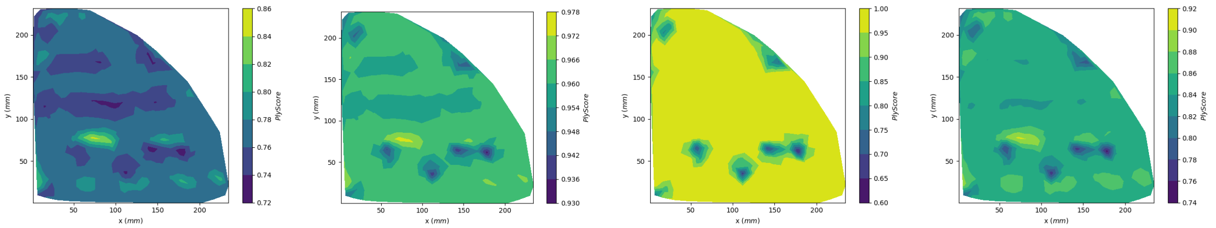

(a) Coverage (b) Angle Deviation (c) Excess Steering (d) Combined

Natural Strategy

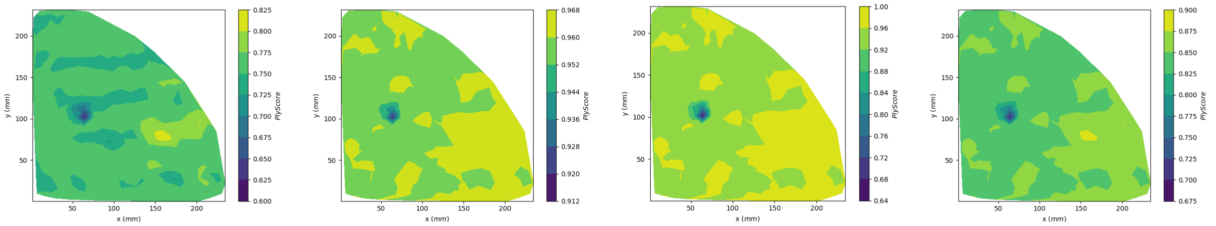

(e) Coverage (f) Angle Deviation (g) Excess Steering (h) Combined

Rosette-Parallel Strategy

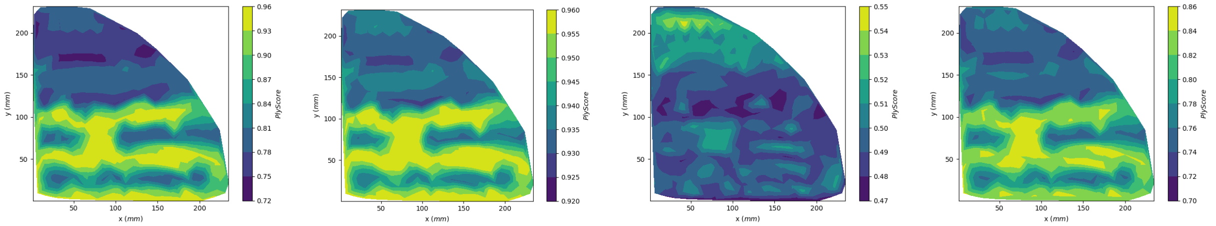

(i) Coverage (j) Angle Deviation (k) Excess Steering (l) Combined

Natural-Parallel Strategy

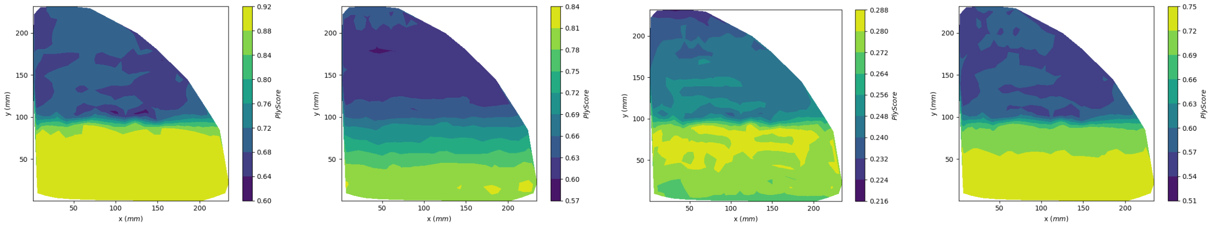

(m) Coverage (n) Angle Deviation (o) Excess Steering (p) Combined

Figure A.4 Score distributions of hyperbolic-paraboloid surface (variation 2 - $\theta = 0°$)

Rosette Strategy

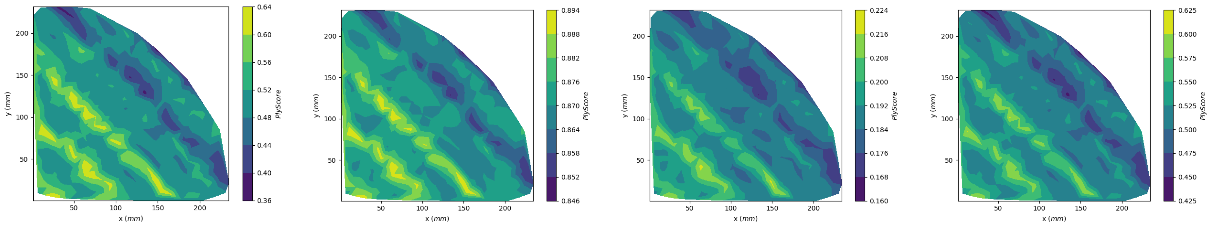

(a) Coverage (b) Angle Deviation (c) Excess Steering (d) Combined

Natural Strategy

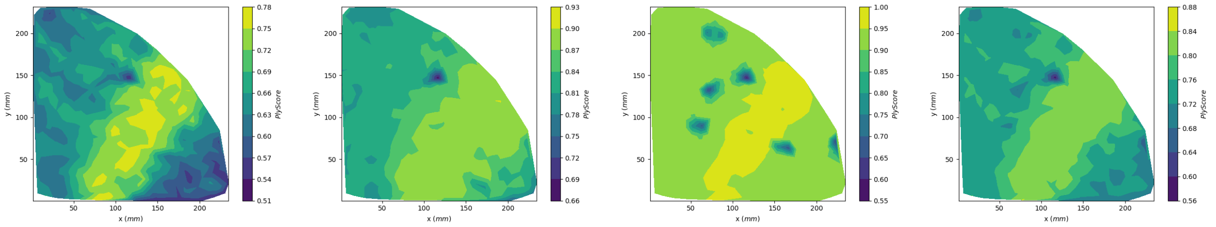

(e) Coverage (f) Angle Deviation (g) Excess Steering (h) Combined

Rosette-Parallel Strategy

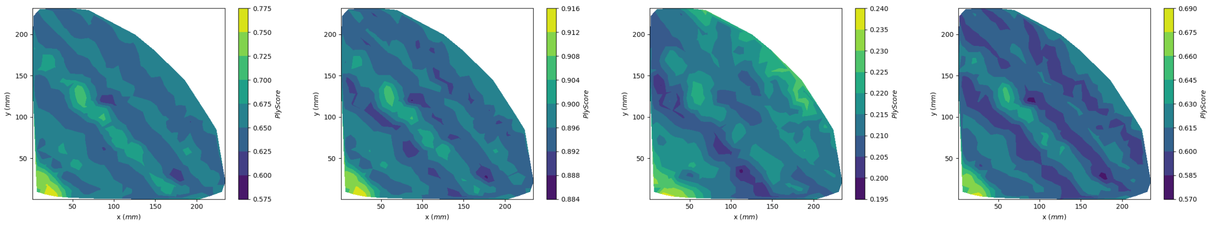

(i) Coverage (j) Angle Deviation (k) Excess Steering (l) Combined

Natural-Parallel Strategy

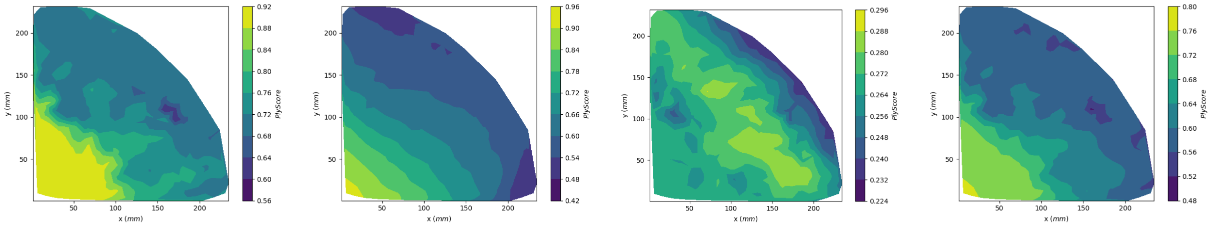

(m) Coverage (n) Angle Deviation (o) Excess Steering (p) Combined

Figure A.5 Score distributions of hyperbolic-paraboloid surface (variation 2 - $\theta = 45°$)

Rosette Strategy

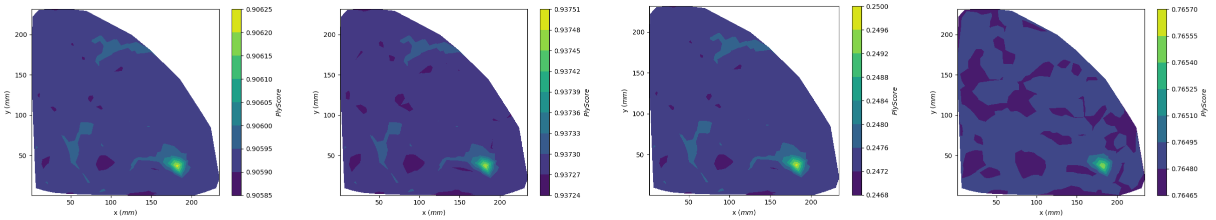

(a) Coverage (b) Angle Deviation (c) Excess Steering (d) Combined

Natural Strategy

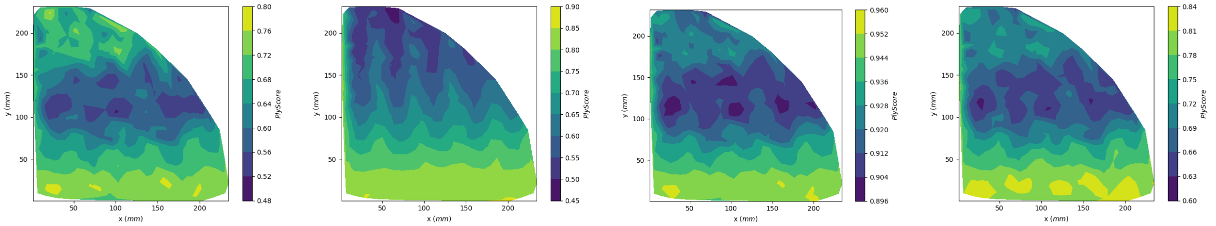

(e) Coverage (f) Angle Deviation (g) Excess Steering (h) Combined

Rosette-Parallel Strategy

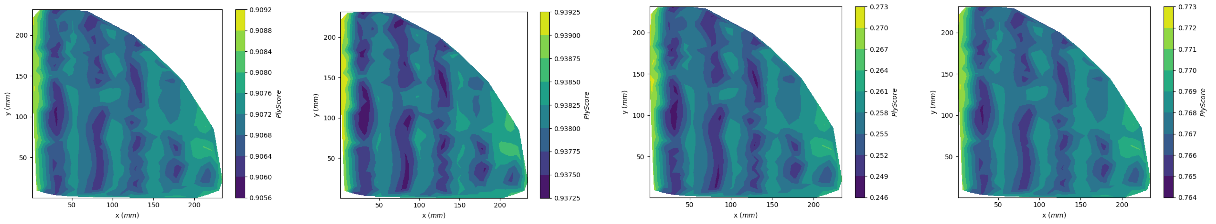

(i) Coverage (j) Angle Deviation (k) Excess Steering (l) Combined

Natural-Parallel Strategy

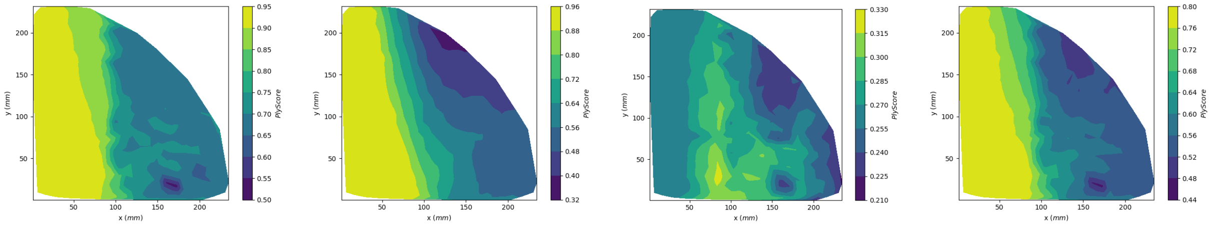

(m) Coverage (n) Angle Deviation (o) Excess Steering (p) Combined

Figure A.6 Score distributions of hyperbolic-paraboloid surface (variation 2 - $\theta = 90°$)

Rosette Strategy

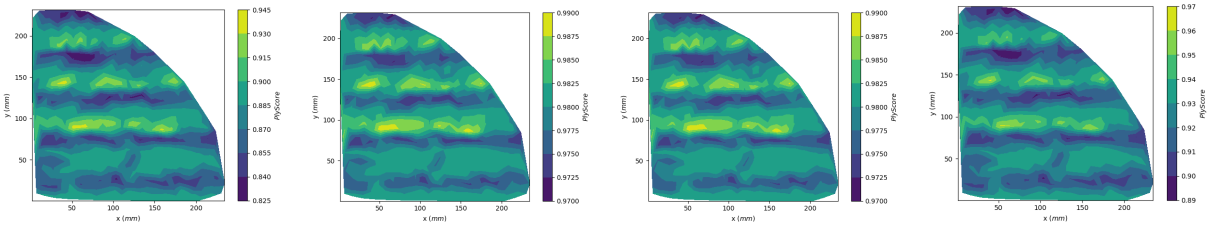

(a) Coverage (b) Angle Deviation (c) Excess Steering (d) Combined

Natural Strategy

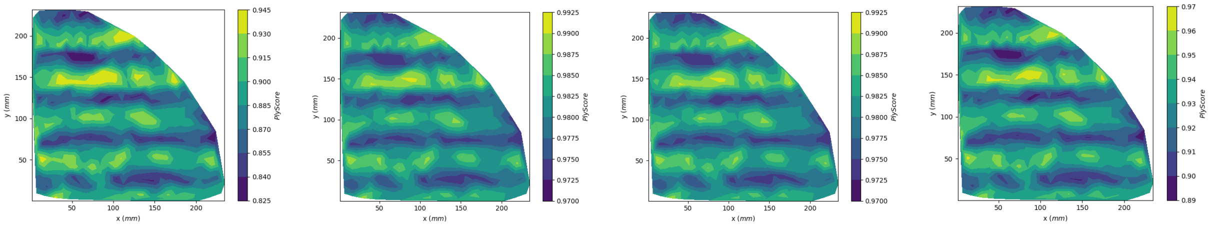

(e) Coverage (f) Angle Deviation (g) Excess Steering (h) Combined

Rosette-Parallel Strategy

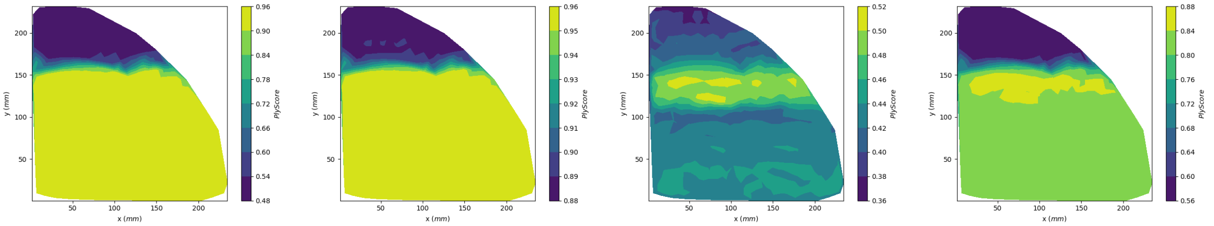

(i) Coverage (j) Angle Deviation (k) Excess Steering (l) Combined

Natural-Parallel Strategy

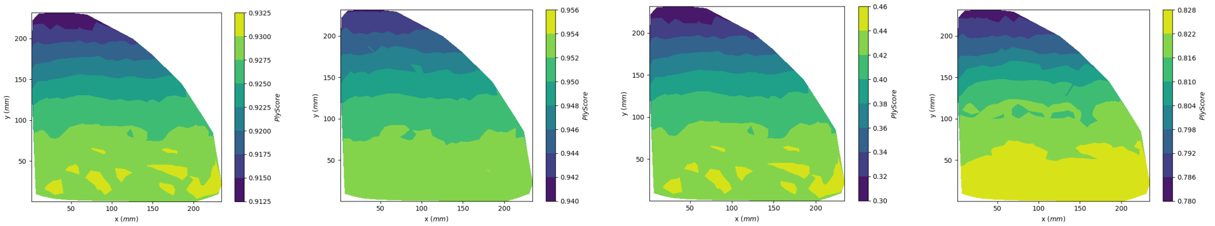

(m) Coverage (n) Angle Deviation (o) Excess Steering (p) Combined

Figure A.7 Score distributions of hyperbolic-paraboloid surface (variation 3 - $\theta = 0°$)

Rosette Strategy

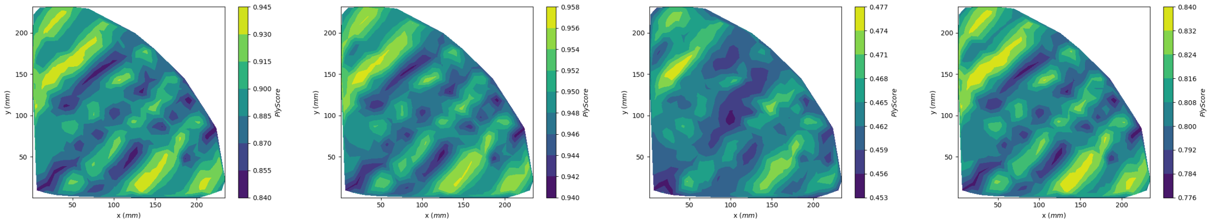

(a) Coverage (b) Angle Deviation (c) Excess Steering (d) Combined

Natural Strategy

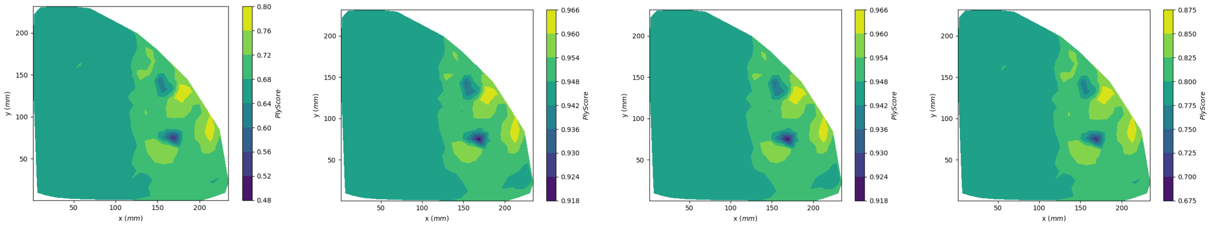

(e) Coverage (f) Angle Deviation (g) Excess Steering (h) Combined

Rosette-Parallel Strategy

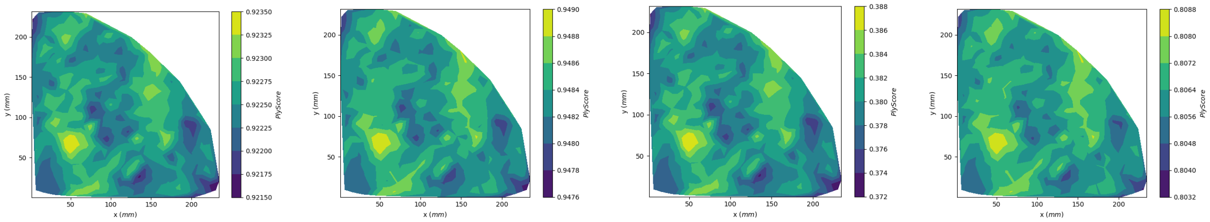

(i) Coverage (j) Angle Deviation (k) Excess Steering (l) Combined

Natural-Parallel Strategy

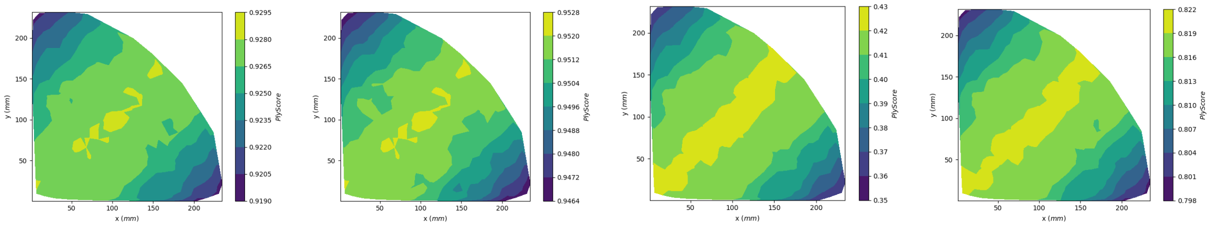

(m) Coverage (n) Angle Deviation (o) Excess Steering (p) Combined

Figure A.8 Score distributions of hyperbolic-paraboloid surface (variation 3 - $\theta = 45°$)

Rosette Strategy

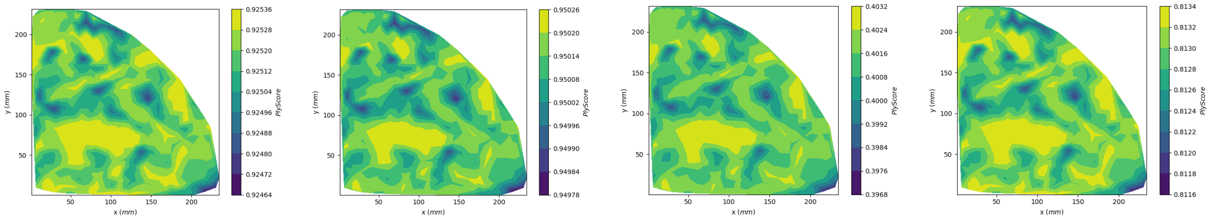

(a) Coverage (b) Angle Deviation (c) Excess Steering (d) Combined

Natural Strategy

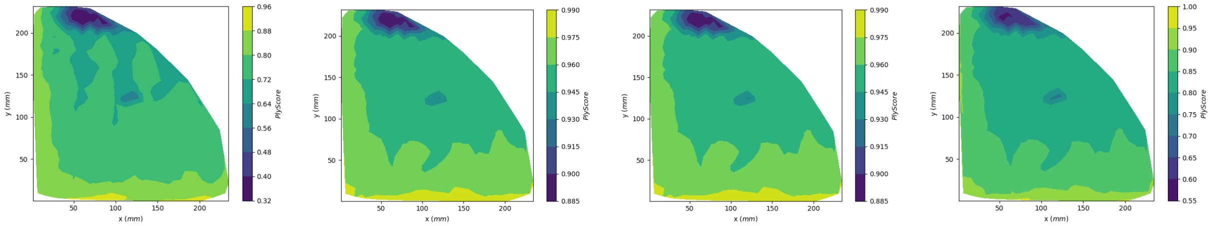

(e) Coverage (f) Angle Deviation (g) Excess Steering (h) Combined

Rosette-Parallel Strategy

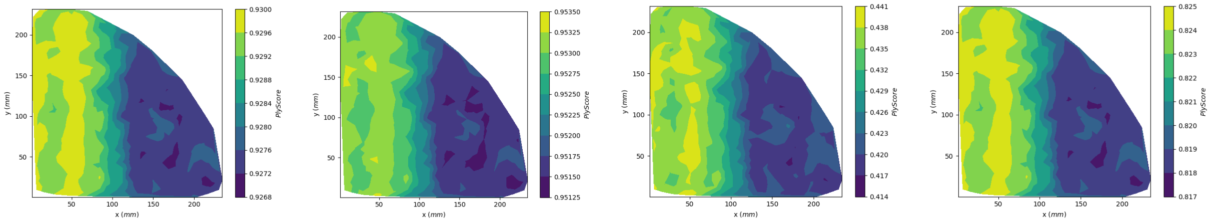

(i) Coverage (j) Angle Deviation (k) Excess Steering (l) Combined

Natural-Parallel Strategy

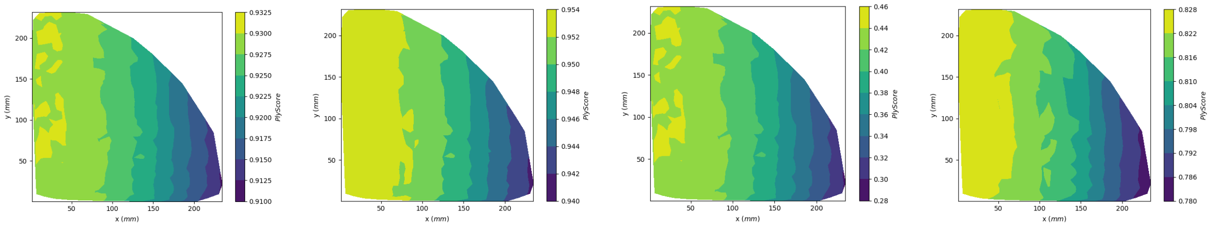

(m) Coverage (n) Angle Deviation (o) Excess Steering (p) Combined

Figure A.9 Score distributions of hyperbolic-paraboloid surface (variation 3 - $\theta = 90°$)

Variation 1

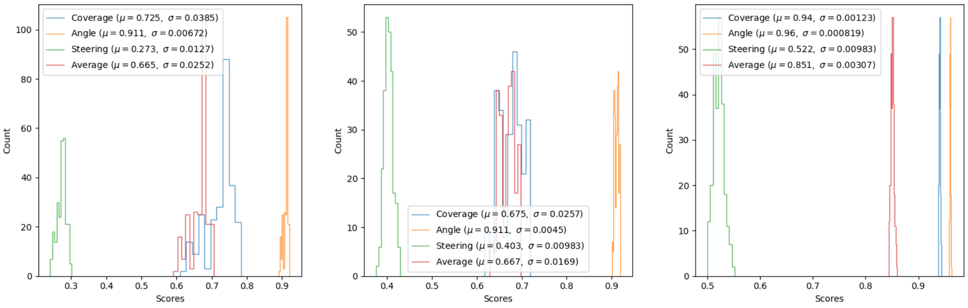

(a) $\theta = 0°$ (b) $\theta = 45°$ (c) $\theta = 90°$

Variation 2

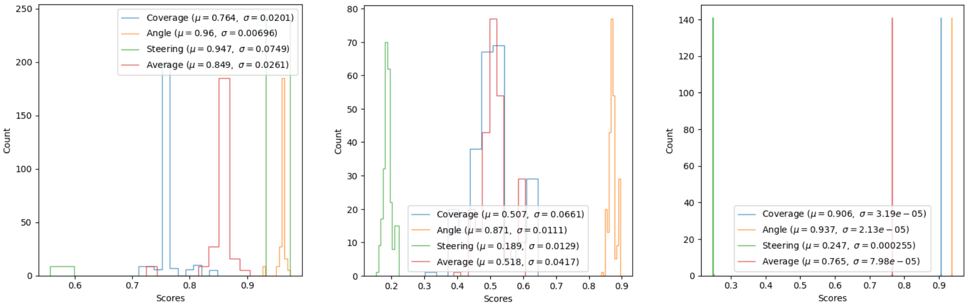

(d) $\theta = 0°$ (e) $\theta = 0°$ (f) $\theta = 90°$

Variation 3

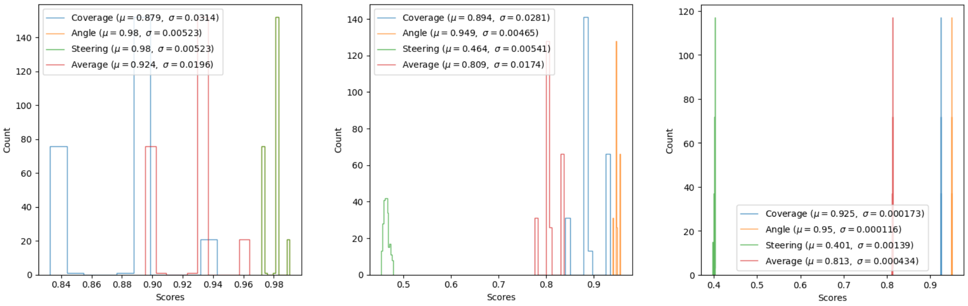

(g) $\theta = 0°$ (h) $\theta = 45°$ (i) $\theta = 90°$

Figure A.10 Score distributions of hyperbolic surface

Variation 1

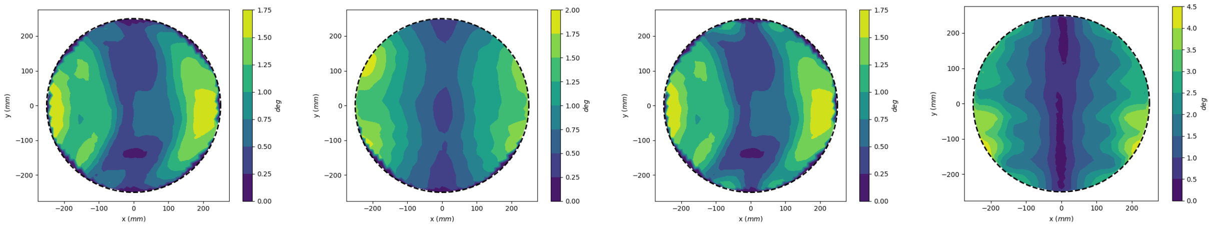

(a) Rosette (b) Natural (c) Rosette Parallel (d) Natural Parallel

Variation 2

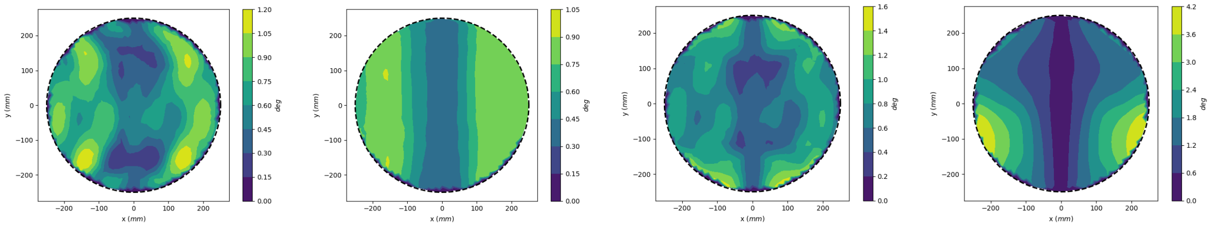

(e) Rosette (f) Natural (g) Rosette Parallel (h) Natural Parallel

Variation 3

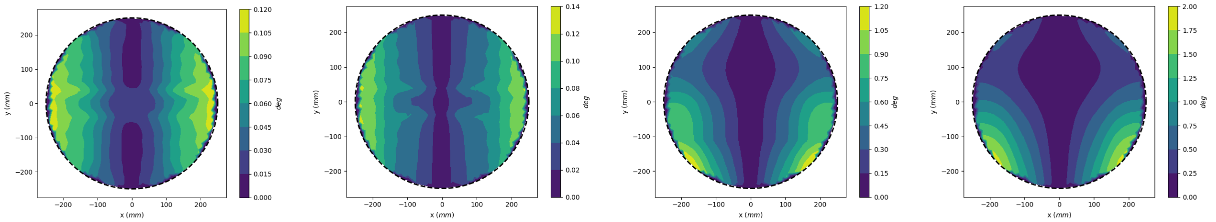

(i) Rosette (j) Natural (k) Rosette Parallel (l) Natural Parallel

Figure A.11 Aggregate average of excess angle deviation for hyperbolic surfaces ($\theta = 0°$)

Variation 1

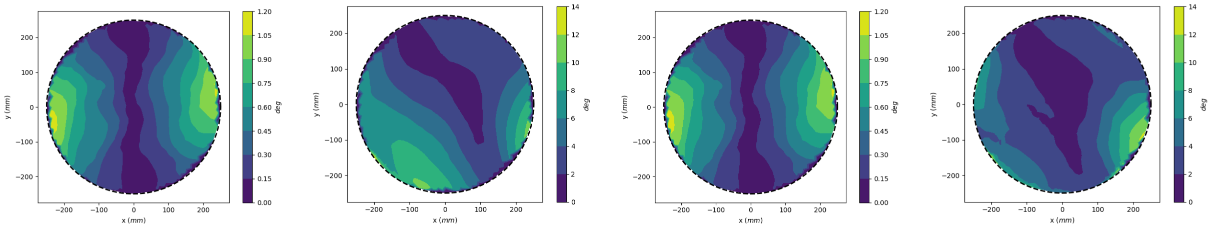

(a) Rosette (b) Natural (c) Rosette Parallel (d) Natural Parallel

Variation 2

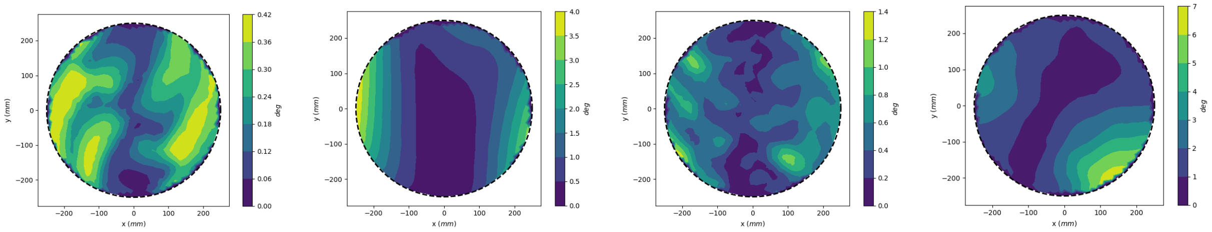

(e) Rosette (f) Natural (g) Rosette Parallel (h) Natural Parallel

Variation 3

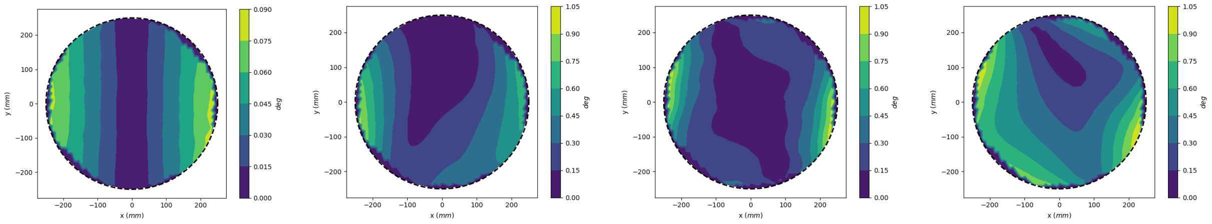

(i) Rosette (j) Natural (k) Rosette Parallel (l) Natural Parallel

Figure A.12 Aggregate average of excess angle deviation for hyperbolic surfaces ($\theta = 45°$)

Variation 1

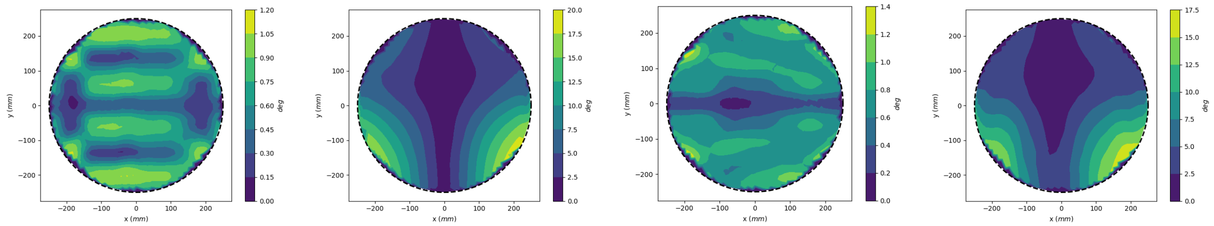

(a) Rosette (b) Natural (c) Rosette Parallel (d) Natural Parallel

Variation 2

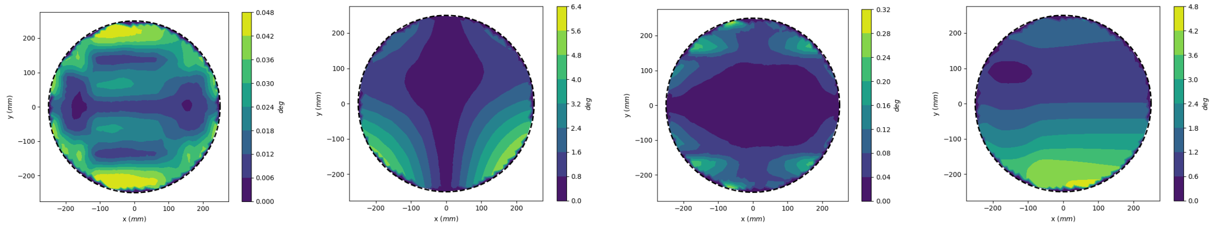

(e) Rosette (f) Natural (g) Rosette Parallel (h) Natural Parallel

Variation 3

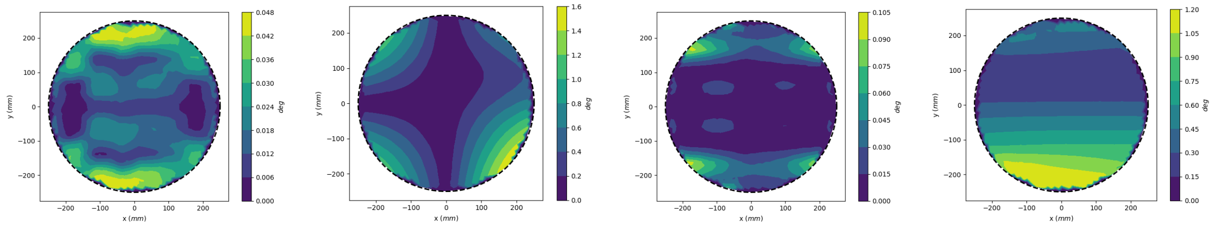

(i) Rosette (j) Natural (k) Rosette Parallel (l) Natural Parallel

Figure A.13 Aggregate average of excess angle deviation for hyperbolic surfaces ($\theta = 90°$)

Variation 1

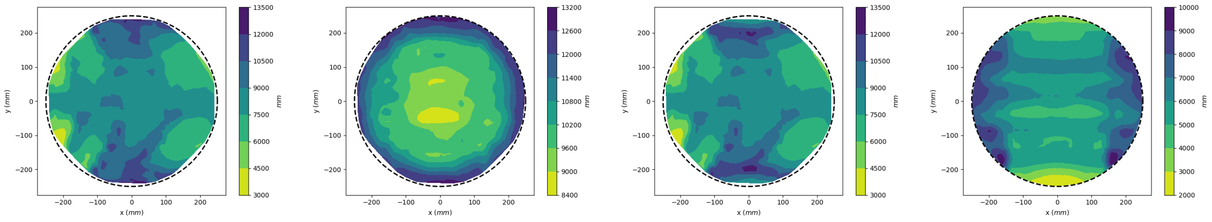

(a) Rosette (b) Natural (c) Rosette Parallel (d) Natural Parallel

Variation 2

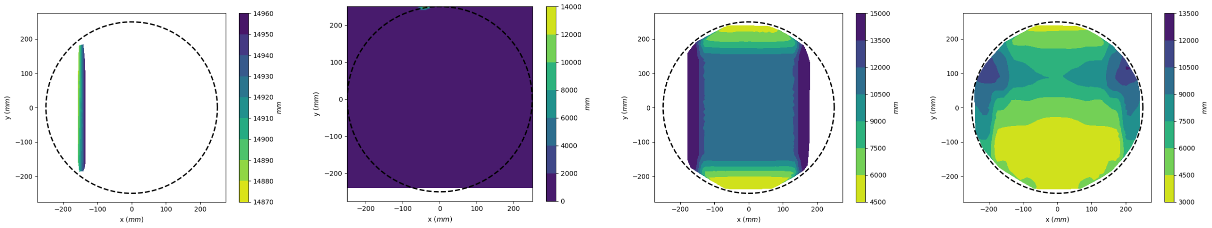

(e) Rosette (f) Natural (g) Rosette Parallel (h) Natural Parallel

Variation 3

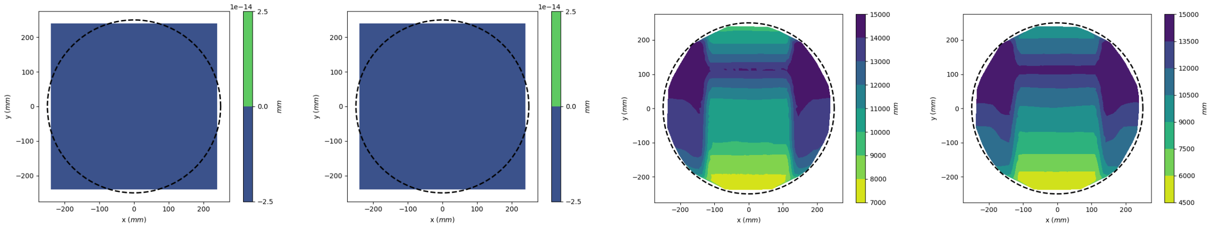

(i) Rosette (j) Natural (k) Rosette Parallel (l) Natural Parallel

Figure A.14 Aggregate average of excess steering radius for hyperbolic-paraboloid surfaces ($\theta = 0°$)

Variation 1

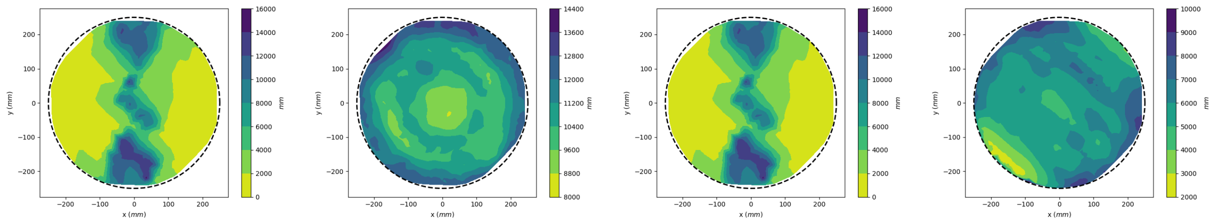

(a) Rosette (b) Natural (c) Rosette Parallel (d) Natural Parallel

Variation 2

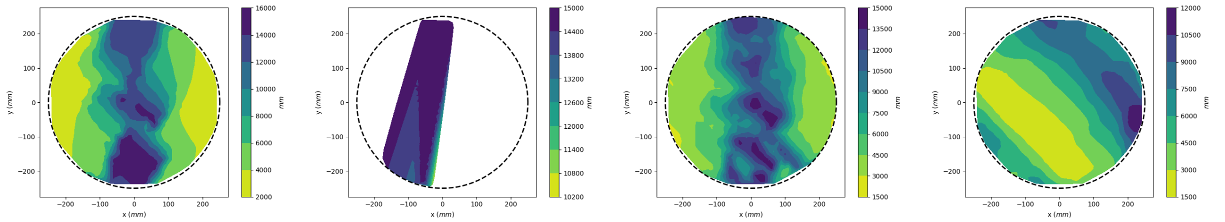

(e) Rosette (f) Natural (g) Rosette Parallel (h) Natural Parallel

Variation 3

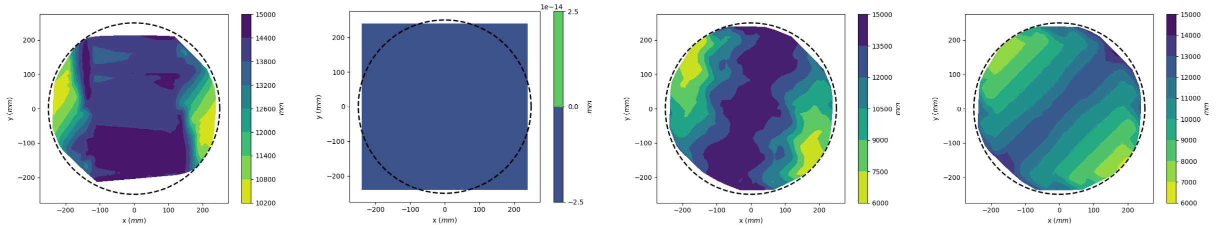

(i) Rosette (j) Natural (k) Rosette Parallel (l) Natural Parallel

Figure A.15 Aggregate average of excess steering radius for hyperbolic-paraboloid surfaces ($\theta = 45°$)

Variation 1

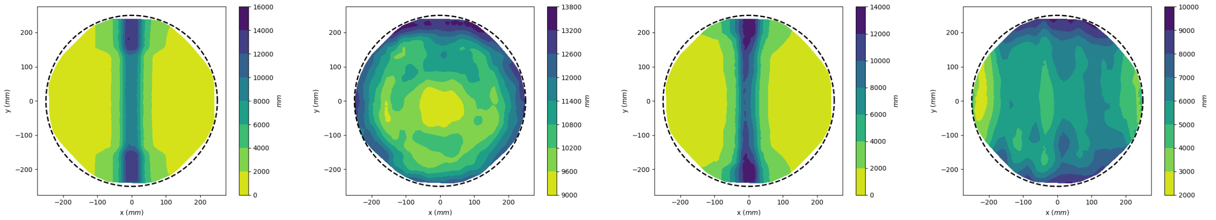

(a) Rosette (b) Natural (c) Rosette Parallel (d) Natural Parallel

Variation 2

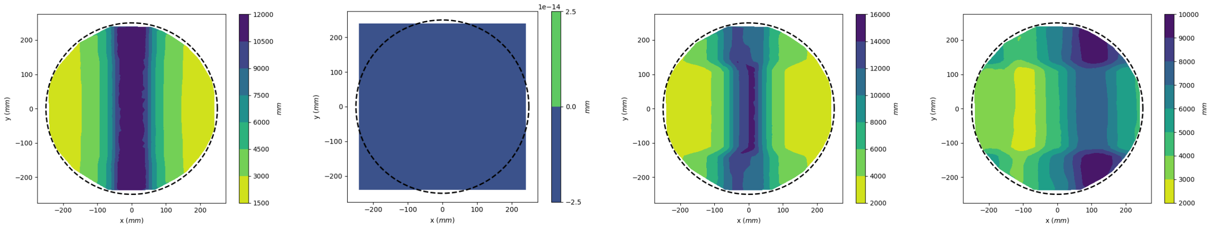

(e) Rosette (f) Natural (g) Rosette Parallel (h) Natural Parallel

Variation 3

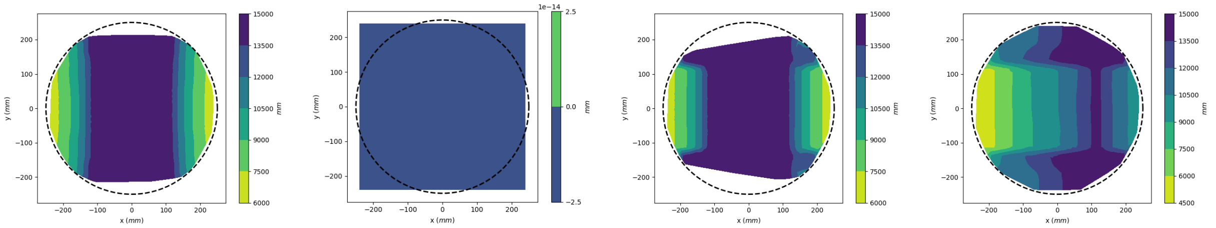

(i) Rosette (j) Natural (k) Rosette Parallel (l) Natural Parallel

Figure A.16 Aggregate average of excess steering radius for hyperbolid-paraboloid surfaces ($\theta = 90°$)

Variation 1

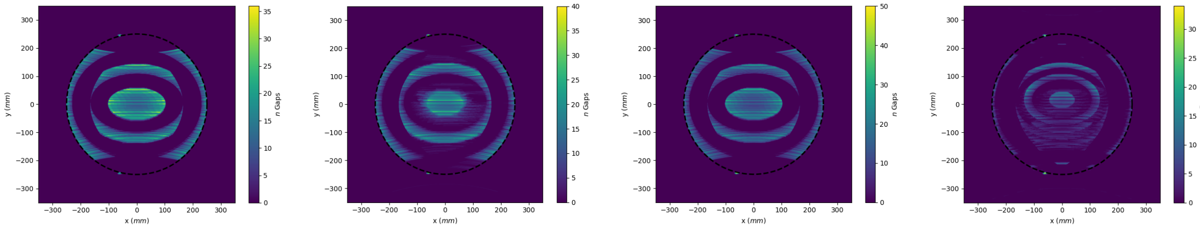

(a) Rosette (b) Natural (c) Rosette Parallel (d) Natural Parallel

Variation 2

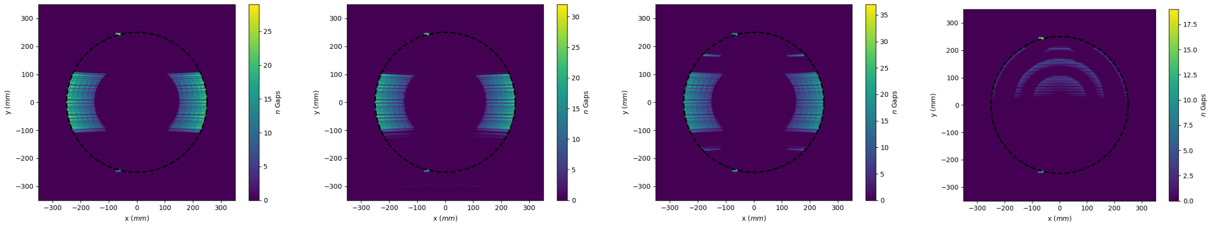

(e) Rosette (f) Natural (g) Rosette Parallel (h) Natural Parallel

Variation 3

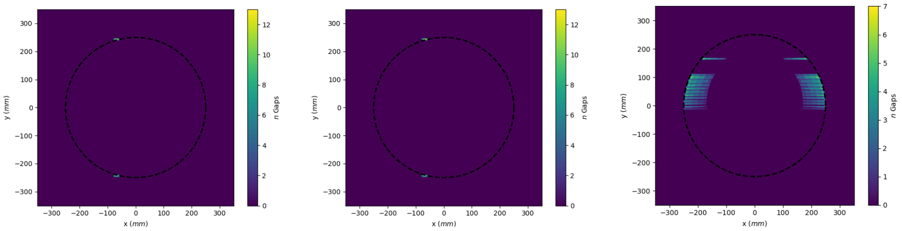

(i) Rosette (j) Natural (k) Rosette Parallel

Figure A.17 Aggregate of excess course-course gaps for hyperbolic-paraboloid surfaces ($\theta = 0°$)

Variation 1

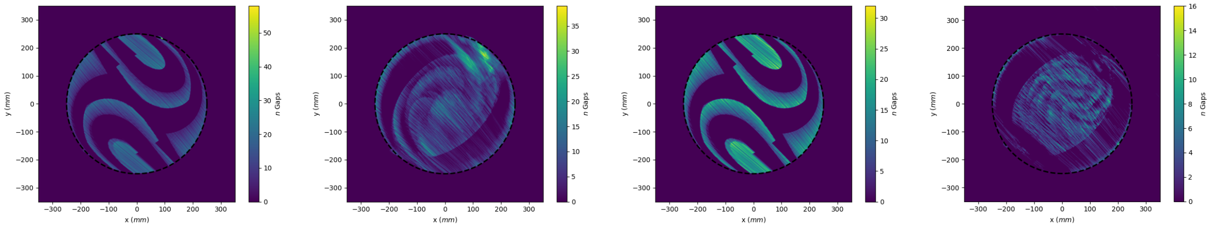

(a) Rosette (b) Natural (c) Rosette Parallel (d) Natural Parallel

Variation 2

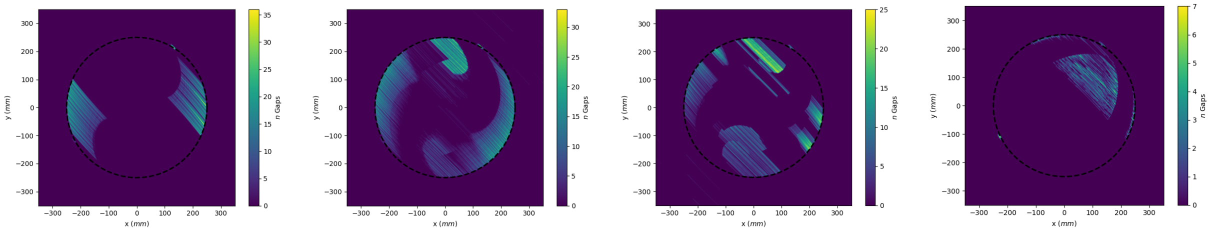

(e) Rosette (f) Natural (g) Rosette Parallel (h) Natural Parallel

Variation 3

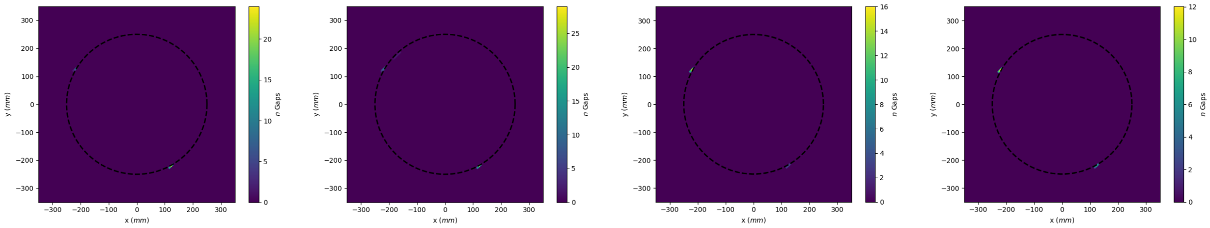

(i) Rosette (j) Natural (k) Rosette Parallel (l) Natural Parallel

Figure A.18 Aggregate of excess course-course gaps for hyperbolic-paraboloid surfaces ($\theta = 45°$)

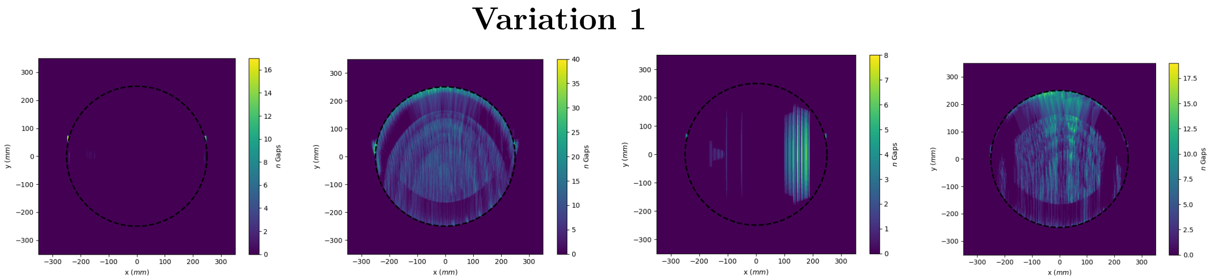
Variation 1

(a) Rosette (b) Natural (c) Rosette Parallel (d) Natural Parallel

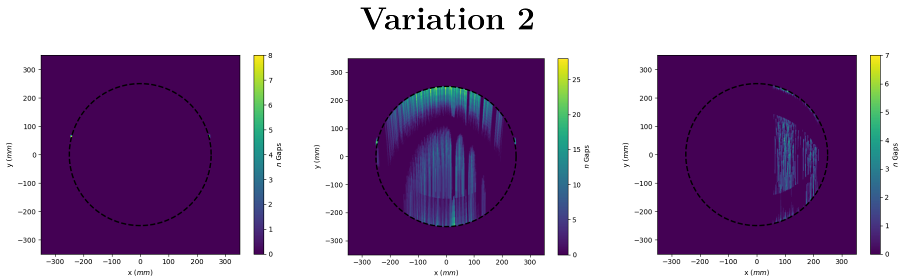
Variation 2

(e) Rosette (f) Natural (g) Natural Parallel

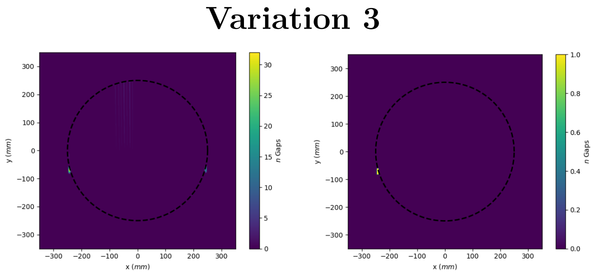
Variation 3

(h) Natural (i) Natural Parallel

Figure A.19 Aggregate of excess course-course gap for hyperbolic-paraboloid surfaces ($\theta = 90°$)

Variation 1

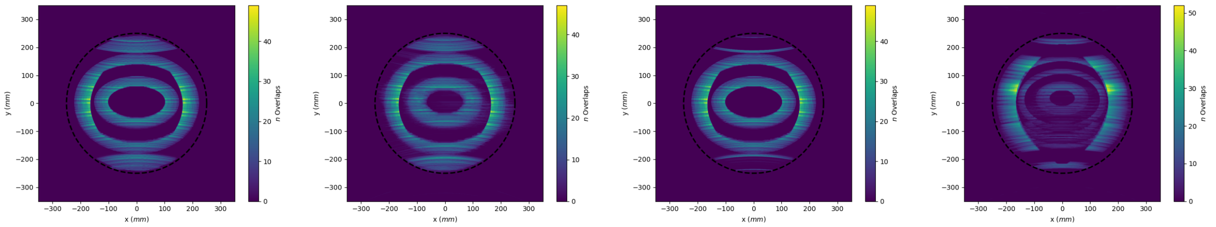

(a) Rosette (b) Natural (c) Rosette Parallel (d) Natural Parallel

Variation 2

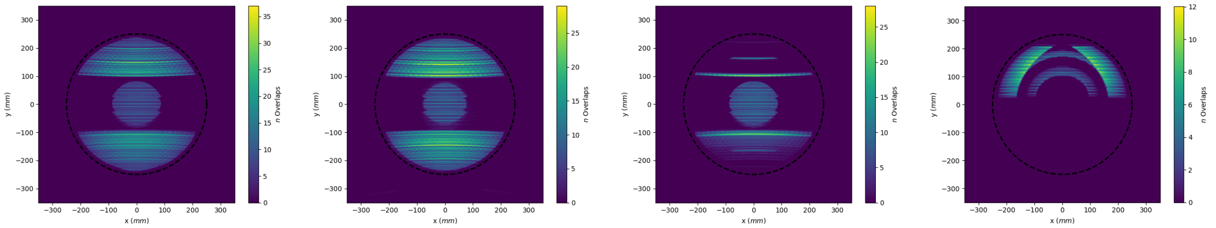

(e) Rosette (f) Natural (g) Rosette Parallel (h) Natural Parallel

Variation 3

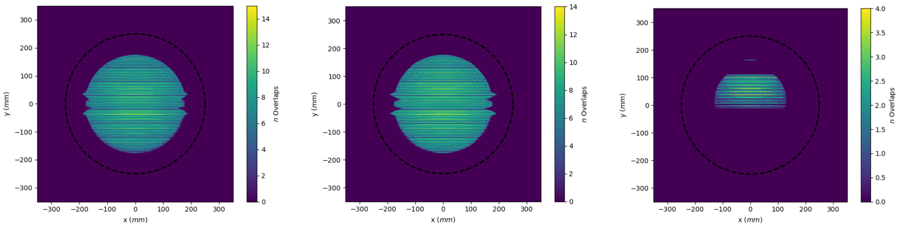

(i) Rosette (j) Natural (k) Rosette Parallel

Figure A.20 Aggregate of excess course-course overlaps for hyperbolic-paraboloid surfaces ($\theta = 0°$)

Variation 1

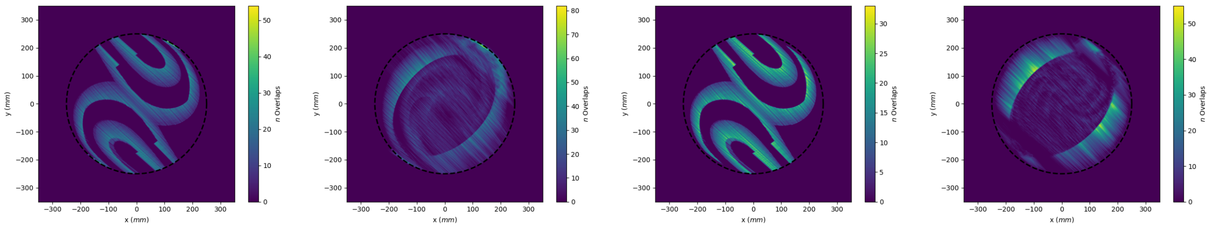

(a) Rosette (b) Natural (c) Rosette Parallel (d) Natural Parallel

Variation 2

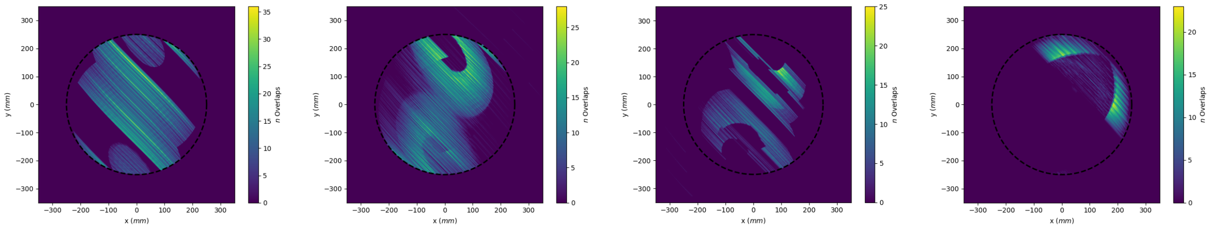

(e) Rosette (f) Natural (g) Rosette Parallel (h) Natural Parallel

Variation 3

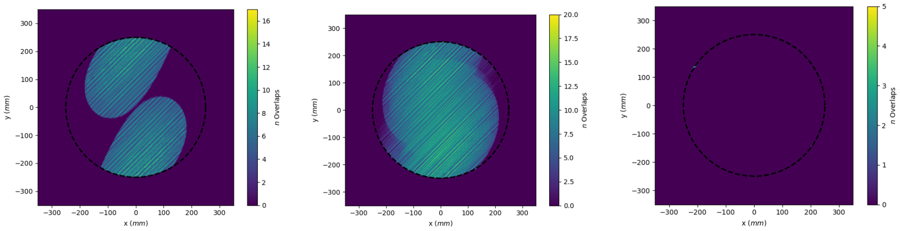

(i) Rosette (j) Natural (k) Rosette Parallel

Figure A.21 Aggregate of excess course-course overlaps for hyperbolic-paraboloid surfaces ($\theta = 45°$)

Variation 1

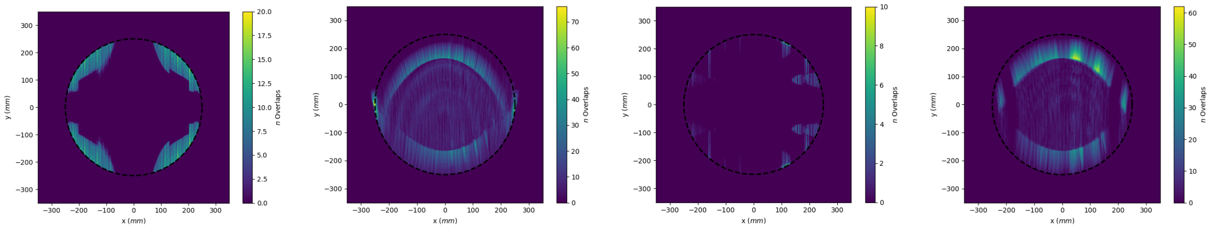

(a) Rosette (b) Natural (c) Rosette Parallel (d) Natural Parallel

Variation 2

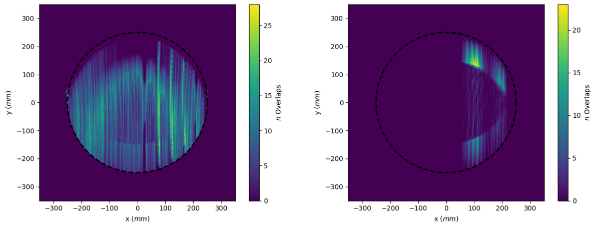

(e) Natural (f) Natural Parallel

Variation 3

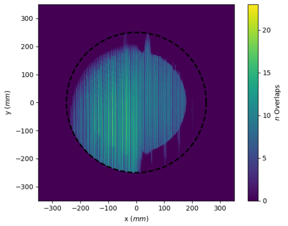

(g) Natural

Figure A.22 Aggregate of excess course-course overlaps for hyperbolic-paraboloid surfaces ($\theta = 90^\circ$)